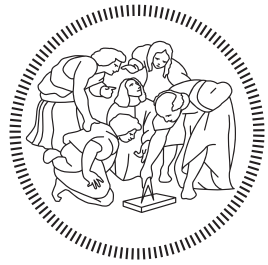

Politecnico di Milano
Department of Aerospace Science and Technology
Doctoral Programme in Aerospace Engineering

Absolute and Relative 6DOF Dynamics, Guidance and Control for Large Space Structures in Cislunar Environment

Doctoral Dissertation of:
Andrea Colagrossi

Supervisor:
Prof. Michèle Lavagna

Tutor:
Prof. James Douglas Biggs

Coordinator:
Prof. Pierangelo Masarati

Year 2018 – Cycle XXXI

And as we wind on down the road
Our shadows taller than our soul
There walks a lady we all know
Who shines white light and wants to show
How everything still turns to gold
And if you listen very hard
The tune will come to you at last
When all are one and one is all
To be a rock and not to roll
And she's buying the stairway to heaven.

— Jimmy Page, Robert Plant

Abstract

Future science and exploration missions will exploit cislunar environment as effective outpost to advance technology readiness in view of human presence beyond Earth. These ambitious space programmes entail modular large space infrastructures to be available in non-Keplerian orbits, to run manned and robotic activities in Moon vicinity. As ISS operations teach, in space outposts ask for complex logistic, which leans on rendezvous and docking/undocking capabilities between space segments, and embrace different engineering disciplines. So far, no mission performed autonomous and accurate proximity operations but in LEO. Conversely, several flown missions were operational on non-Keplerian orbits, exploiting the increased knowledge about n-body dynamics modelling for trajectory design. However, existing studies deeply investigating the 6 DOF absolute and relative dynamics in non-Keplerian orbits are somewhat missing; this area of investigation is now mandatory to support the cislunar infrastructure design and implementation, assessing and addressing practical solutions for guidance and control strategies, which shall be applicable to reliably manage proximity operations of the lunar gateway.

The dissertation, starting from the well-known restricted n-body problem formulation, presents analyses and results obtained by adding a coupled orbit-attitude dynamical model and the effects due to the large structure flexibility. The cislunar environment is accurately modelled, assessing the fidelity of various modelling approaches. Thus, the most relevant perturbing phenomena, such as the Solar Radiation Pressure and the Sun's gravity, are included in the Earth-Moon system model as well. A multi-body approach is preferred to represent

possible configurations of the large and flexible cislunar structure: interconnected simple structural elements - such as beams, rods or lumped masses linked by springs - build up the space segment.

The 6 DOF dynamical models are implemented to analyse absolute and relative dynamics in cislunar space. Moreover, efficient 6 DOF absolute and relative guidance and control methods are presented. In particular, single and dual-spin stabilisation are compared and the results are carefully analysed to highlight an attitude control strategy that is less resource consuming. Analogously, relative guidance and control functions are implemented for non Keplerian orbits proximity operations. Furthermore, additional guidance and control functions able to deal with flexible space systems are presented; classical control methods are deeply investigated, together with a preliminary assessment of a wave-based attitude control technique.

The outcomes of the research work presented in this dissertation are intended to highlight relevant results and drivers for cislunar outposts design, with the purpose to better leverage the coupled 6 DOF natural dynamics in computing effective and efficient trajectories, while addressing functional and performance requirements. On board resource limitations and mission reliability are highlighted in the analyses. Different case studies for large space structures in selected non-Keplerian orbits in the Earth-Moon system are discussed, to point out some relevant conclusions for the potential implementation of such a mission.

Acknowledgements

I spent the last two hours, still, in front of this page, looking for a good way to write the most important part of this dissertation and to condense in few words all the feelings and all the thoughts I had in the last three years of my life, along my Ph.D. path.

Everything began while I was living in the United States, enjoying new experiences, far from home, surrounded by new friends, missing the old ones, happy to learn many new things, serious and thoughtful about making my next big life decision. I never thought about doing a Ph.D., I planned to go abroad and work in a large aerospace company or in an important space agency. Luckily, life is so unpredictable and I like to follow the internal stream of feelings and sensations. For this reason, you are reading this: a doctoral dissertation, developed in the department of Aerospace Science and Technology of Politecnico di Milano, thanks to the Italian government funds, written in Milano and finalized in Viterbo. Home. However, the main reason why you are reading this and I was able to complete my Ph.D. is because I am fortunate to be surrounded by very special wonderful people who inspire me every day. It is difficult to find the right words to reveal my feelings, but I can clearly say that it is hard to think my life without you, and for this reason, thanks to you all.

The first mention goes to my supervisor and mentor Prof. Michèle Lavagna. I am immensely grateful to her for the opportunities she offered me, together with the trust she made me feel. She is an extraordinarily powerful source of motivation for me, a passionate teacher and a tireless worker. I must thank her for any academic and working achievement I might have reached.

I would like to thank my friend and colleague Vincenzo. We shared together the ups and downs, the good and the bad of the Ph.D. journey. We started together and we are finishing together. Despite the unpredictable future, I am sure, we will always be in touch. Moreover, we will never be just a couple of friends, but rather a part of a trio: Claudio, thanks to you too.

I am eager to thank Davide and Fabio. You are amazing friends and I am thankful to you for being fantastic mentors and for the support you gave me during the development, the finalization and the reviews of my master's and Ph.D. theses. I would like to thank also Prof. Josep Masdemont for his important contribution as a reviewer of this dissertation.

I owe special thanks to my awesome friends and colleagues at Politecnico di Milano: Andrea, Benny, Daniele, Diogene, Francesco, Lorenzo, Luca, Paolo, Stefano; and to those scattered across industries and universities all around the world: Alessandro, Betta, Emanuele, Francesco, Giuseppe, Marco, Pablo, Riccardo. Thanks to all the people, friends and colleagues I met and I worked with in Deimos Space. In particular, I am grateful to Miguel and Simone for their support during my working experience with them.

Life is not all about work and, particularly, mine would not have been the same without all the happy and unforgettable moments I spent with my friends in every corner of the globe. Thanks to you all. Nevertheless, particular mention is deserved to Groove Street, to all my everlasting friends in Viterbo, to Giacomo, Matteo, Silvio and to the awesome friends I have in Spain and in the United States.

At this point, a place of honor is reserved to those have been and will always be here with me. My family: Pierangelo, Maria Elena, Valentina and *i Nonni*. Your infinite love, trust, sacrifice and support have been fundamental for me and for my personal growth. I would have never reached this point without all of you. Thanks.

I wish to conclude this section with few words dedicated to a special person. Our paths crossed at the begin of our postgraduate experiences and my entire Ph.D. life has been supported and enhanced by you; with you I have already spent most of the best and happiest times of my life. My deepest gratitude is dedicated to you, Giulia.

This dissertation closes an extremely important chapter of my life, but it immediately opens to a fascinating world of new adventures and possibilities. I am ready and I feel cool thanks to you, all!

Andrea

Viterbo, Italy
December 24th, 2018

Table of Contents

List of Figures

List of Tables

List of Acronyms

ACS	Attitude control system.
BC4BP	Bicircular Four-body Problem.
CAM	Collision Avoidance Manoeuvre.
CR3BP	Circular Restricted Three-body Problem.
DOF	Degrees of freedom.
DPM	Distributed Parameters Model.
DRO	Distant Retrograde Orbit.
EJ2000	Ecliptic and equinox at date J2000.
EML	Earth-Moon Lagrangian point.
ER3BP	Elliptic Restricted Three-Body Problem.
FER3BP	Ephemeris Restricted Three-body Problem.
FER4BP	Ephemeris Restricted Four-body Problem.
FERnBP	Ephemeris Restricted n-body Problem.
FES	Functional Engineering Simulator.
FOV	Field of view.
GC	Guidance and Control.
GNC	Guidance Navigation and Control.
HOI	Halo Orbit Insertion.

ISECG	International Space Exploration Group.
ISS	International Space Station.
KOS	Keep-out-sphere.
LEO	Low Earth orbit.
LLO	Low Lunar orbit.
LMM	Lumped Masses Model.
LPM	Lumped Parameters Model.
LPO	Libration point orbit.
LQR	Linear-quadratic regulator.
LSM	Liquid Sloshing Model.
LTI	Linear Time Invariant.
LVLH	Local Vertical Local Horizontal.
MIMO	Multiple-Input and Multiple-Output.
MOI	Manifold Orbit Insertion.
NLP	Non-linear programming.
NRHO	Near Rectilinear Halo Orbit.
Ph.D.	Philosophiae Doctor.
PID	Proportional integral derivative.
R3BP	Restricted Three-body Problem.
R4BP	Restricted Four-body Problem.
RDV	Rendezvous.
RnBP	Restricted n-body Problem.
S/C	Spacecraft.
SISO	Single-Input and Single-Output.
SQP	Sequential quadratic programming.
SRP	Solar radiation pressure.
STM	State Transition Matrix.
TOF	Time of flight.
TPBVP	Two-points boundary value problem.
VSVO	Variable-step, variable-order.
WB	Wave-based.

ZVC Zero Velocity Curves.

CHAPTER 1

Introduction

> It is contrary to reason to say that there is a vacuum or a space in which there is absolutely nothing.
>
> — René Descartes

During the last decade of the twentieth century humanity posed the bases for prolonged human habitation in space. In fact, the International Space Station (ISS) program achieved marvellous objectives in Low-Earth orbit and allowed to better understand the effects of spaceflight on human body. In the meantime, robotic exploration of Solar System made huge leaps forward as well; many planets and numerous celestial objects were explored as never before. At present time, space exploration goals are increasingly ambitious and, in few years from now, manned and unmanned space missions will cooperate to bring mankind further and further away from its cradle.

The path to follow has been already outlined by the International Space Exploration Group (ISECG) in the global space exploration roadmap [1], which foresees a series of intermediate steps and progressive achievements to support

future space exploration programmes. Indeed, this fascinating and ambitious plan is based on the sustainability of the entire network of systems and operations to accomplish the established goals, which would not be possible without a solid support of preliminary missions and new technologies development.

One of the milestone of the ISECG roadmap is considered to be a modular and extended space system in deep-space, to run robotic activities in preparation of a safe and reliable operational habitat for humans to come. The specifications for this space system and its ideal staging location still have to be defined. Although, as a matter of fact, cislunar space is receiving a lot of attention from international space community, thanks to its peculiar dynamical environment. A space station in lunar vicinity is the current proposed solution to have a permanent human outpost in deep-space.

As ISS operations teach, in-space outposts ask for complex logistic, which leans on rendezvous (RDV) and docking/berthing capabilities between space segments and embrace different engineering disciplines. However, despite the available knowledge about proximity operations in low Earth orbit (LEO), the development of this kind of missions in cislunar space asks for new design methods. Recent studies are proposing different Keplerian and non-Keplerian orbit options to operate a space system in lunar vicinity, but orbits that exist only in the Restricted Three-body Problem (R3BP) seem the most promising ones [2]. For example, orbits about one of the collinear libration points, such as Earth-Moon Lagrangian point (EML) Halo orbits, have continuous line of sight coverage for communications and their Earth accessibility with existing transportation systems is good. Also other R3BP orbit types have appealing properties, such as the excellent orbit stability of Distant Retrograde Orbits (DROs) or the satisfactory ease of access from the Moon of Near Rectilinear Halo Orbits (NRHOs). In general, the non-Keplerian dynamics is able to boost and support the design of innovative space systems and infrastructures.

The feasibility of the whole project is strongly dependent from the improvements in new trajectory design and Guidance Navigation and Control (GNC) techniques that have to leverage Restricted n-body Problem (RnBP) dynamics, coupled orbit-attitude equations of motion, appropriate structural models and efficient control techniques. These enhanced methods are especially needed when dealing with a large and flexible space structure, such as a space station in the vicinity of the Moon.

1.1 Historical Heritage

Celestial phenomena intrigued humanity since the beginning of our presence on the Earth. Thousands of years ago, ancient astronomers started formulating the *law of the stars*, etymological meaning of Astronomy, looking at the sky

and trying to fit what they were seeing in empirical laws. Nevertheless, modern work on celestial motion began with Nicolaus Copernicus, who published *De Revolutionibus orbium coelestium* in 1543 [3], and continued with the fundamental astronomical observations made by, among the others, Galileo Galilei at the end of the 16th century [4]. In 1609, the german mathematician and astronomer Johannes Kepler postulated that the motion of celestial bodies evolves on conic orbits, as described in his laws of planetary motion published in *Astronomia Nova* [5]. At that time, the predictions made with the modern heliocentric model were by far superior than the forecasts made with the older geocentric Ptolemaic model in terms of accuracy and simplicity. However, modern astronomy had to wait more than 50 years to mathematically confirm all the previous models and intuitions, when Sir Isaac Newton, recognised as one of the most influential scientists of all time, formulated the universal theory of gravitation in its *Philosophiae Naturalis Principia Matematica* in 1687 [6]. Finally, celestial mechanics had a solid mathematical foundation and the motion of planets was related to geometrical arguments and physical laws.

The outcomes of Newton's theory allowed to explain the motion of natural celestial bodies with great accuracy, but few minor corrections were still necessary. In fact, the dynamical model used by both Kepler and Newton in their researches contemplated for only one main attractor at a time, consequently named *two-body problem* or Keplerian model. In the following centuries, the scientific community was interested in finding the complete description of motion under the influence of more than two bodies. Newton itself considered the gravitational presence of the Sun (third body) in the attempt of correcting the errors of the two-body model. Nevertheless, if more than two main bodies are considered, the general analytical description of the motion is not available anymore.

Particular equilibrium solutions in the Three-Body problem were found at the end of the 18th century by the italian mathematician Giuseppe Lodovico Lagrangia, in *Essai sur le Problème des Trois Corps* [7], and by the Swiss physicist Leonhard Euler. The former proved the existence of constrained analytical equilibrium solutions in the general three-body problem, when the three bodies compose an equilateral triangle or collinear formation. The latter introduced for the first time the idea of a synodic, or rotating, coordinate frame to formulate the Restricted Three-body problem, which assumes a particle moving under the gravitational attraction of two massive bodies without influencing their motion. In the following years, several mathematicians, physicists and astronomers continued to develop analytical theories to study problems of increasing complexity. Different techniques were developed to analyse some peculiarities of the motion in an arbitrarily complicated gravitational field, but a global analytical solution was never found. In 1836 Jacobi discovered the integral of motion associated to the R3BP. Few years later, in 1878, the physical meaning of the Jacobi integral was given by Hill, who introduced the concept of Zero Velocity Curves (ZVC).

These curves are associated to the energy of the particle, through the Jacobi constant, and they bound the feasible motion within the three-body system. In those years, the mathematical formulation of the R3BP was clearly defined and the research focus was intended to find solutions associated to this problem. However, the complexity of such chaotic dynamical system, required a different approach coming from the contribution of Jules Henri Poincaré. In *Les Méthodes Nouvelles de la Mécanique Céleste* [8], Poincaré showed that infinite periodic solutions exist in the R3BP and that the only integral of motion is the one founded by Jacobi. Furthermore, he understood that periodic solutions are the only way to made accessible the problem of the three bodies.

The most remarkable achievements about periodic orbits in R3BP were available in the 20th century. First, thanks to the works of Moulton [9] and Szebehely [10]. Then, thanks to the advent of numerical computing, which provided a greater capability in analysing complex dynamical systems. A great milestone in the R3BP studies was posed in 1970 by Farquhar [11], who highlighted three-dimensional periodic motions in the vicinity of collinear Lagrangian points: the Halo orbits. In the followings, more comprehensive works came from Farquhar and Kamel [12], Breakwell and Brown [13], Howell [14, 15], Howell and Breakwell [16], Richardson [17] and Hénon [18]. They developed new methods to compute different families of R3BP orbits, both around libration points and primaries. They extended the investigation to different values of mass ratio of the primaries and they also formulated analytical methods to find initial guesses for periodic orbit solutions.

First investigations about attitude dynamics in the restricted three-body problem assumed the spacecraft as artificially maintained close to the equilibrium points and only the stability of the motion was considered by Kane [19] and Robinson [20] in the 70s of the last century. Afterwards, Euler parameters were introduced to study the rotational dynamics of a single body located at one of the Lagrangian point by Abad [21]. More recently, Brucker [22], Peláez [23] and Wong [24] focused their attention on the attitude dynamics of a spacecraft in the vicinity of equilibrium points, using Poincarè maps, Lagrangian formulation and linear approximations of non-Keplerian orbits. In the second decade of the 21st century, the coupling between orbital and attitude motion was investigated by Guzzetti providing different families of orbit-attitude solutions in R3BP [25, 26, 27, 28]. Exploratory results about stability of attitude dynamics in non-Keplerian orbits was presented by Meng in the same years [29].

Studies about flexible structures in non-Keplerian orbits are quite recent. A method developed by Knutson in 2012 allows to investigate the full three-dimensional coupled motion for a generic multi-body spacecraft in the Earth-Moon system [30, 31]. Therefore, it would allow to model flexibility effects in R3BP orbits. In addition, preliminary investigations about this topic, with

simple flexible elements, were conducted by Guzzetti [32]. Still, large flexible spacecraft were studied in classical Keplerian orbits since the 1970 with the works of Ho [33] and Modi [34, 35, 36], among the others. In 1987, Kane proposed a new method to study the dynamics of flexible structure undergoing large overall motions [37]. Further developments of this method, by Yoo [38] and Invernizzi [39], simplified the procedure of formulating the derivation of the equations of motion and assessed the validity of linear approaches. In 2018, a convenient formulation able to effectively manage the control of a flexible spacecraft was proposed by Liu [40].

Researches dedicated to relative motion and rendezvous problem in cislunar space exist since the beginning of the Apollo Program, because of the concern over the loss of communications with the spacecraft as they went behind the Moon. Lunar Halo orbit relay satellites were proposed. Hence, the need to approach such target positions was felt. In 1971, Gerding formulated rendezvous equations in the vicinity of the second libration point of the Earth-Moon system [41]. Then, the study of proximity operations control in R3BP was applied to formation flying by Gurfil [42], Marchand [43] and Héritier [44]. In 2015, possible rendezvous strategies were proposed, with a target on a EML2 Halo orbit, by different authors [45, 46, 47]. More investigations about dynamical models and GNC strategies to support the design of rendezvous operations in non-Keplerian orbits were presented by Mand [48] and Bucci [49, 50].

1.2 The Research Problem

From previous literature studies, most of the existing solutions to deal with non-Keplerian environment are founded on dynamical models based on point-mass dynamics, which is sometimes not sufficient to carry out accurate analysis when a large space system, such as the cislunar space station, is considered. Indeed, when the attitude dynamics is coupled with the orbital motion in a non-Keplerian environment, the rotational behaviour of the interested body may have extremely complex evolutions. Nevertheless, under the chaotic appearance that is typical when more than one massive body is considered, there could be regular dynamical structures that may be exploited to design space missions, leveraging also the attitude dynamics to satisfy very complicated system and operational requirements.

Similarly, the knowledge about spacecraft relative dynamics and about rendezvous and docking/berthing in space is mainly developed in Keplerian orbits. Thus, it is not always suitable to address problems set in cislunar space. Actually, relative RnBP dynamics is quite different from the classical one considered to design RDV missions in LEO. Accordingly, the GNC design is largely affected by this unique dynamical environment. Non-Keplerian relative dynamics has

remarkable characteristics that can be exploited to design natural approaching or departure trajectories from a certain position on a libration point orbit (LPO). Furthermore, 6 degrees of freedom (DOF) relative dynamics is mandatory to deal with large cislunar infrastructures, because of their non negligible attitude dynamics, and it has been hardly addressed by previous studies.

An additional important aspect, rarely considered in previous researches, is the influence between the space structure flexibility and the orbital and attitude dynamics in non-Keplerian orbits. In fact, having in mind the structural properties of a ISS-like space structure, it is reasonable to investigate if it is possible to assume rigid body dynamics while modelling such kind of large space system. The information gathered from these analyses can be applied to highlight the validity range in assuming rigid body motion and to select the best GNC design capable to handle large flexible structures during RDV operations. In these regards, the verification of true closed loop stability or effective actuation of a control system designed for a large and flexible space structure in complex dynamical environments is fundamental.

Therefore, there is a legitimised reason to better understand the coupled interactions between orbital, attitude and flexible dynamics in non-Keplerian dynamical environments. In particular, this is relevant to design and shape the GNC functions able to deal with a space station in lunar vicinity.

1.3 Dissertation Overview

This research work focuses on analyses, methods, techniques and tools for studying absolute and relative orbit-attitude dynamics in cislunar environment, with the purpose to handle the guidance, navigation and control problem for rendezvous and proximity operations with large and flexible space systems in the Earth-Moon system.

Particular attention is dedicated to naturally periodic non-Keplerian orbit-attitude solutions. For example, naturally periodic motion could enable coarse pointing operational modes for data acquisition or communications without a relevant control action. Moreover, an important improvement in pointing accuracy or rendezvous and docking safety could be obtained knowing the natural attitude evolution of a spacecraft in complex dynamical environments. Yet in addition, control authority on attitude stability could be desired to increase the design freedom, the pointing capabilities and the rendezvous possibilities. The knowledge of non-Keplerian relative dynamics and the ability to compute natural or controlled 6DOF transfer trajectories is highlighted and is applied to RDV problems. In fact, this research is aimed also to analyse possible rendezvous missions, defining practical strategies that can be exploited to deal

with the assembly and the operations of the cislunar space station. GNC design is addressed considering both passive and active control methods, while example scenarios are discussed to apply the developed tools. The investigation is always supported by the analyses about the most appropriate dynamical model to investigate extended space systems in cislunar environment. Circular Restricted Three-body Problem (CR3BP) is compared with higher fidelity representation, such as Bicircular Four-body Problem (BC4BP) or Ephemeris Restricted n-body Problem (FERnBP). Linearised models can be helpful to design GNC functions, but their validity range is defined considering the characteristics of the operational environment. Analogously, perturbing effects, such as the second order deviations in the main gravitational attraction due to the finite extension of the spacecraft, or the solar radiation pressure (SRP), should be applied understanding their relevance and their effects on the system under investigation in this research. The flexibility effects on the large spacecraft dynamics are taken into account. Different structural models are compared and the capabilities of the multi-body approach are exploited to efficiently represent the system. Distributed parameters and lumped parameters models are applied to simulate internal forces, such as the fluid sloshing and the structural flexibility. Their influence on natural and on controlled motion is discussed. The GNC functions are designed in order to take care of these oscillatory phenomena and the obtained performances are verified with respect to example applications.

The work presented in this dissertation is organised as follows.

Chapter 2 deals with the background knowledge and recalls mathematical formulations of non-Keplerian dynamical models under study, both for absolute and relative dynamics. The formulation used to model the main perturbing effects related to the cislunar environment, such as the SRP, the n-body gravity and the variation in the gravitational attraction due to the finite dimension of the small body, is recalled. Flexible dynamics and fluid sloshing models are presented and discussed in this chapter as well.

Chapter 3 discusses absolute dynamics results in the Earth-Moon system. A multiple shooting algorithm is described and it is used to find solutions that are periodic in both the orbital and attitude states. Moreover, a method to generate initial guesses for periodic orbit-attitude solutions is presented. Attitude spin stabilisation methods are introduced and applied on reference periodic motions. Then, the stability properties of different orbit-attitude dynamics are critically analysed and relevant implications for operations are highlighted. Natural 6DOF dynamics associated with invariant orbit-attitude manifolds is presented, analysed and exploited to find relevant proximity trajectories.

Chapter 4 presents an analysis on relative dynamics in the Earth-Moon system. 6DOF guidance and control functions are discussed, starting from energy optimal rendezvous trajectories and getting to GNC operational functions. Natural

dynamics is considered also in this chapter, to underline the fruitful effects of the coupled 6DOF relative dynamics approach adopted for non-Keplerian environment design. In this chapter, the main families of non-Keplerian orbits are considered and discussed, but greater attention is dedicated to libration point Halo orbits, both with regular amplitude (Halo) or with large amplitude (NRHO), because of their applicative relevance with regards to the cislunar space station program.

Chapter 5 is dedicated to the problem of rendezvous with a large space infrastructure in non-Keplerian orbits. Functional and operational requirements are outlined, considering example rendezvous strategies. The proximity operations are categorised with respect to the distance from the target, and the GNC design is differentiated between *far range* and *close range* rendezvous, with particular attention to the safety of the latter. Cislunar environment characteristics are highlighted and exploited to enhance the relative trajectory design.

Chapter 6 considers the interactions between orbit-attitude and flexible dynamics. The effects of the flexibility coupling on the natural dynamics are discussed and the validity range in assuming rigid body motion is identified. Furthermore, Guidance and Control (GC) functions able to deal with flexible space systems are presented. Classical control methods (e.g. proportional integral derivative (PID) control) are thoroughly considered together with a preliminary assessment of an alternative control technique: wave-based (WB) control.

Final remarks, together with a possible roadmap for future research and development, are drawn in chapter 7.

1.4 Bibliographic Disclaimer

During the years of my Philosophiae Doctor (Ph.D.), I presented updates of my work in many conferences and I also had the possibility to publish part of them in peer reviewed journals. Therefore, most of the work in this dissertation has already been presented in different articles. The most significant are listed below.

- ◇ Colagrossi, A. and Lavagna, M., "Preliminary Results on the Dynamics of Large and Flexible Space Structures in Halo Orbits", *Acta Astronautica*, vol.134, pp. 355-367, 2017, doi:10.1016/j.actaastro.2017.02.020.
- ◇ Colagrossi, A. and Lavagna, M., "Dynamical Analysis of Rendezvous and Docking with Very Large Space Infrastructures in non-Keplerian Orbits", *CEAS Space Journal*, vol. 10, no. 1, pp. 87-99, 2018, doi:10.1007/s12567-017-0174-4.

- ◇ Bucci, L., Colagrossi, A., and Lavagna, M., "Rendezvous in lunar Near Rectilinear Halo Orbits", *Advances in Astronautics Science and Technology*, vol. 1, no. 1, pp 39-43, 2018, doi:10.1007/s42423-018-0012-6.
- ◇ Colagrossi, A. and Lavagna, M., "Cislunar non-Keplerian orbits rendezvous and docking: 6DOF guidance and control", in *Proceedings of the 69th International Astronautical Congress*, Bremen, Germany, 1-5 October 2018.
- ◇ Colagrossi, A. and Lavagna, M., "Assembly and Operations for a Cislunar Orbit Space Station", in *Proceedings of the 68th International Astronautical Congress*, Adelaide, Australia, 25-29 September 2017.
- ◇ Colagrossi, A. and Lavagna, M., "Dynamics and Control of Modular and Extended Space Structures in Cislunar Environment", in *Proceedings of the 26th International Symposium on Space Flight Dynamics*, Matsuyama, Japan, 3-9 June 2017.
- ◇ Colagrossi, A. and Lavagna, M., "Preliminary Results on the Dynamics of Large and Flexible Space Structures in Halo Orbits", in *Proceedings of the 67th International Astronautical Congress*, Guadalajara, Mexico, 26 - 30 September 2016.
- ◇ Colagrossi, A. and Lavagna, M., "Dynamical Analysis of Rendezvous and Docking with Very Large Space Infrastructures in Non-Keplerian Orbits", in *Proceedings of the 6th International Conference on Astrodynamics Tools and Techniques*, Darmstadt, Germany, 14-17 March 2016.

CHAPTER 2

Background

> If I have seen further, it is by standing on the shoulders of Giants.
>
> — Isaac Newton

Keplerian two-body model is still used to preliminarily study the motion of an artificial body in space, thanks to its simple mathematical formulation and its proven closed form solution. Nonetheless, modern astrodynamics often search for feasible solutions in complex non-Keplerian systems, with the purpose to enhance the capabilities of the trajectory design or to increase the accuracy of the dynamical models predictions. The most investigated dynamical systems are those set in the framework of CR3BP and Elliptic Restricted Three-Body Problem (ER3BP). In the CR3BP the main attractors move on circular orbits around their common barycentre, while the ER3BP is a generalisation of the circular problem for the case of elliptical orbits for the main bodies. These models allows to predict, with higher accuracy than Keplerian ones, the motion of observable celestial bodies (e.g. the motion of the Moon in the Sun-Earth system). CR3BP and ER3BP are valuable models for preliminary analysis of non-Keplerian orbits. Nevertheless, for certain applications, the very peculiar

regime of the Earth-Moon system requires that the true non-linear motions of the two primaries are taken into account, since their periodic and secular variations are not negligible in dictating the force field that maintains the periodicity of specific LPOs. In these cases, an Ephemeris Restricted n-body Problem (FERnBP) modelling approach can be applied.

Furthermore, the presence of the Sun plays a non-negligible role, in terms of both 4th body gravity and solar radiation pressure. For example, the periodic oscillations of NRHOs due to the Sun's gravitational pull are missed out in a CR3BP or ER3BP model. The dynamics in cislunar space can be also set within a Restricted Four-body Problem (R4BP) model. When the circular simplification is accepted, the cislunar space is idealised and modelled as a classical Bicircular Four-body Problem (BC4BP), where the orbits of the Earth and the Moon about their common centre of mass are assumed to be circular, and the centre of mass of the Earth-Moon system is assumed to revolve around the centre of mass of the Earth-Moon-Sun system in a circular, coplanar motion. When maximum modelling accuracy is sought, an ephemeris model can be considered: the position of Earth, Moon and Sun are obtained from numerical ephemerides. In this last case, the cislunar space is accurately modelled as a Ephemeris Restricted Four-body Problem (FER4BP), sub-product of FERnBP, neglecting just the minor perturbing effects.

A complete understanding of the suitable dynamical model is necessary to properly handle and design regular and controlled motions near Lagrangian points. This capability represents a step forward into the space mission design era: it opens to a complete new variety of solutions, able to meet complex space mission objectives and to promote innovative ideas for future mission opportunities.

In this chapter, the background knowledge needed to approach the present research work is recalled. The equations of motion of 6DOF absolute and relative dynamics related to the cislunar space are here formulated and discussed, including the perturbative effects influencing the dynamical environment. Finally, flexible dynamics and fluid sloshing models are presented.

2.1 Gravitational Field

The dynamics of a generic massive body B, in motion between two points in space, is influenced by the interaction with the surrounding gravitational field, which creates a force on the body itself. The work done by this force upon B is the same for any physically possible path between the two points, thus the gravitational field is said to be a conservative field.

From vector analysis, a necessary and sufficient condition that this work be independent from the physical path taken by the particle is that the force per unit mass, $\mathbf{g}$, be the gradient of a scalar function of position, $\mathbf{r}$:

$$\mathbf{g} = -\nabla V(\mathbf{r}), \tag{2.1}$$

where V is called the gravitational potential [58]. ∇ represents the three-dimensional gradient operator, whose Cartesian form is $\hat{\mathbf{i}}\frac{\partial}{\partial x} + \hat{\mathbf{j}}\frac{\partial}{\partial y} + \hat{\mathbf{k}}\frac{\partial}{\partial z}$.

The Newton's law is the generally used gravitational model to describe the force field due to any massive body. It states that any pair of particle masses attracts each other with a force that is directly proportional to the product of their masses and inversely proportional to the square of the distance between them. So, according to this law, the gravitational potential due to a point mass m is:

$$V = -G\frac{m}{r}, \tag{2.2}$$

where G is the gravitational constant and $r = \|\mathbf{r}\|$ is the distance of the body B from the mass m. Note that symbols in bold font represent vectors, while the scalars are indicated in normal font. If the same symbol is used in bold and normal font, the former is the vector and the latter is its norm.

2.2 Cislunar Space Dynamics

Cislunar space dynamics can be described exploiting restricted three-body problem modelling approach, which considers the body B, with mass m_B, and two other masses, m_1 and m_2, assuming $m_B \ll m_1, m_2$ and $m_2 < m_1$. m_1 and m_2 are denoted as primaries, and are assumed to be in motion about their common centre of mass. Within the *restricted* problem assumption, the motion of m_B does not affect the trajectories of the primaries. The equations of motion of B in cislunar space are conveniently expressed in a rotating reference frame, S, which is called *synodic* frame and is shown in figure 2.1. It is centred at the centre of mass of the system, O; the first axis, $\hat{\mathbf{x}}$, is aligned with the vector from m_1 to m_2; the third axis, $\hat{\mathbf{z}}$, is in the direction of the angular velocity of S, $\boldsymbol{\omega}_S = \omega_S\hat{\mathbf{z}}$; $\hat{\mathbf{y}}$ completes the right-handed triad. At time $t = 0$, the rotating frame S is aligned to the *inertial* frame I, which is centred in O and is defined by the axes $\hat{\mathbf{X}}$, $\hat{\mathbf{Y}}$ and $\hat{\mathbf{Z}}$. Note that the hat symbol (i.e. $\hat{}$) represents versors.

The dynamics equations of B can be derived starting from a Lagrangian formulation. The Lagrangian function is defined as:

$$\mathcal{L} = \mathcal{T} - \mathcal{V}, \tag{2.3}$$

where $\mathcal{T}$ is the kinetic energy and $\mathcal{V}$ is the generalised potential. The body B is now assumed to be a rigid body.

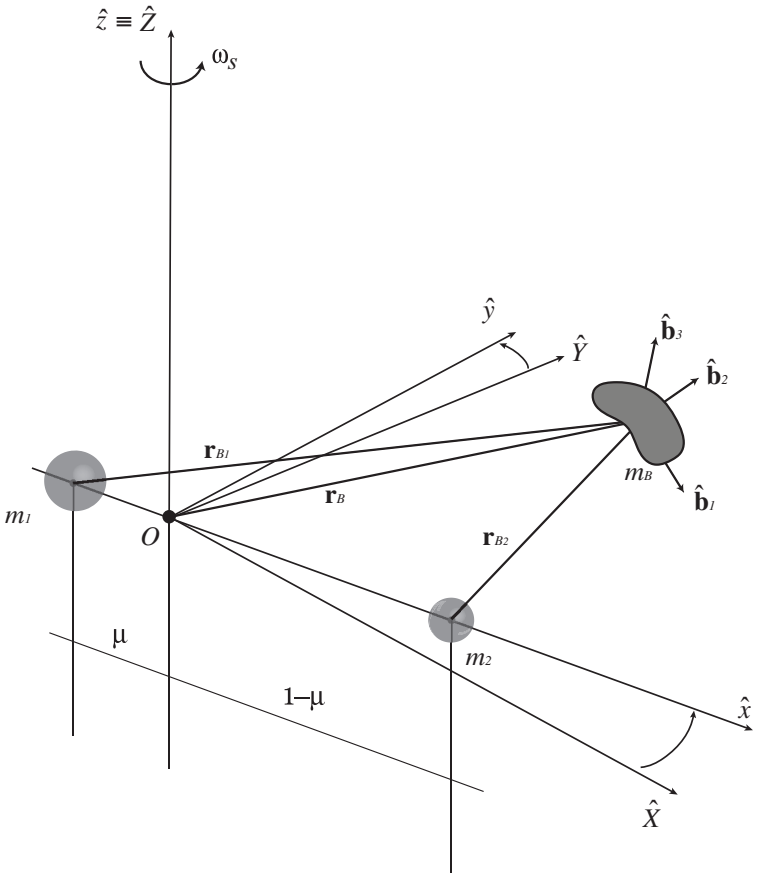

Figure 2.1: Orbit-attitude Absolute Dynamics (Synodic and Inertial Reference Frames).

The kinetic energy $\mathcal{T}$ of a rigid body can be expressed as the kinetic energy of the translational motion of the centre of mass plus the kinetic energy of the rotational motion around the centre of mass:

$$\mathcal{T} = \frac{1}{2} m_B \, \dot{\mathbf{r}}_B \cdot \dot{\mathbf{r}}_B + \frac{1}{2} \boldsymbol{\omega} \cdot \mathbb{I}_B \cdot \boldsymbol{\omega}, \tag{2.4}$$

where $\dot{\mathbf{r}}_B$ is the velocity of B, $\boldsymbol{\omega}$ is the angular velocity of the body relative to the S frame and $\mathbb{I}_B$ is the inertia tensor about the centre of mass, O_B.

The generalised potential $\mathcal{V}$ is related with the gravitational forces, with the perturbing forces and with the inertia forces, since the synodic frame S is a non-inertial reference frame rotating with the two primaries. It can be expressed as the sum of the ordinary gravitational potential, $V_g = V_{g_1} + V_{g_2}$, the generalised potential of the inertia forces, V_i, and the generalised potential of the perturbations, V_p.

The gravitational action exerted by the i-th spherical primary on the rigid body m_B, can be derived from:

$$V_{g_i} = -\frac{G m_i m_B}{r_{B_i}} + \frac{G m_i}{2\, r_{B_i}^3} \left[3(\hat{\mathbf{r}}_{B_i} \cdot \mathbb{I}_B \cdot \hat{\mathbf{r}}_{B_i}) - \mathrm{tr}(\mathbb{I}_B)\right], \tag{2.5}$$

where r_{B_i} and $\hat{\mathbf{r}}_{B_i}$ are respectively magnitude and direction of $\mathbf{r}_{B_i}$: position vector of m_B with respect to the i-th primary. Equation (2.5) is an expansion up to the second order of the gravitational potential generated by a spherical attractor on a small extended body [59].

The generalised potential of the inertia forces, needed to write the equations of motion in S, can be expressed as:

$$V_i = \frac{m_B}{2} \mathbf{r}_B \cdot [\boldsymbol{\omega}_S \times (\boldsymbol{\omega}_S \times \mathbf{r}_B) + 2\boldsymbol{\omega}_S \times \dot{\mathbf{r}}_B] - \frac{1}{2} \boldsymbol{\omega}_S \cdot \mathbb{I}_B \cdot (\boldsymbol{\omega}_S + 2\boldsymbol{\omega}). \tag{2.6}$$

At this point, combining equations (2.4) to (2.6) into equation (2.3), it is possible to derive the equations of motion of the body B in cislunar space as:

$$\frac{d}{dt}\left(\frac{\partial \mathcal{L}}{\partial \dot{q}_j}\right) - \frac{\partial \mathcal{L}}{\partial q_j} = \mathcal{F}_j, \tag{2.7}$$

where q_j with $j = 1, \ldots, 6$ are the generalised coordinates, associated with the orbit and attitude states, while $\mathcal{F}_j$ are the generalised forces due to different perturbing contributions. Remembering from the classical mechanics theory, a generalised force, $\mathcal{F}_j$, can be obtained from a generalised potential function $\mathcal{G}(\mathcal{P}_j, \dot{\mathcal{P}}_j)$ as:

$$\mathcal{F}_j = \frac{d}{dt}\left(\frac{\partial \mathcal{G}}{\partial \dot{\mathcal{P}}}\right) - \frac{\partial \mathcal{G}}{\partial \mathcal{P}_j}, \tag{2.8}$$

where $\mathcal{P}_j$ is a generalised coordinate and $\dot{\mathcal{P}}_j$ is the associated derivative.

The generalised potential of the perturbations, V_p, and the related generalised forces, are not explicitly defined here, but the effects of the perturbations will be discussed in section 2.3.1.

2.3 Absolute Orbit-Attitude Equations of Motion

Absolute orbit-attitude equations of motion are conveniently derived exploiting the Circular Restricted Three-Body Problem modelling approach. In this case, the three-body system can be univocally defined by the mass parameter,

$$\mu = \frac{m_2}{m_1 + m_2}, \tag{2.9}$$

the magnitude of the costant angular velocity of S,

$$\omega_S = \sqrt{\frac{G(m_1 + m_2)}{r_{12}^3}}, \tag{2.10}$$

and the distance between the two primaries r_{12}. The equations of motion are usually normalised such that r_{12}, ω_S and the total mass of the system, $m_T = m_1 + m_2$, are unitary in non-dimensional units. In this dissertation, these units are indicated with the symbol [nd]. As a consequence, after the normalisation, the universal constant of gravitation is $G = 1$, the period of m_1 and m_2 in their orbits about their centre of mass is $T = 2\pi$ and the time derivatives are taken with respect to the non-dimensional time $\tau = \omega_S t$: $\dot{\circ} = d \circ / d\tau$. The location of m_1 along $\hat{\mathbf{x}}$ is $-\mu$, whereas m_2 is located at $1 - \mu$. In the Earth-Moon system the parameters to normalise the equations of motion are $r_{12} = 384\,400\,\text{km}$, $m_T = 6.04 \times 10^{24}\,\text{kg}$ and $T = 2\pi/\omega_S = 27.28\,\text{d}$.

The body m_B is extended, three-dimensional and, in this section, is assumed to be rigid. Hence, it has six degrees of freedom: the position of its centre of mass in S, which is easily described by the position vector $\mathbf{r}_B$, and the orientation of the body reference frame B with respect to I or S. To define the orientation of one frame with respect to another, three parameters are the minimal set required, but in this model the instantaneous orientation of B is more conveniently described using the four-dimensional quaternion vector, also known as Euler parameters [60], as will be discussed in the following. The body-fixed frame B is centred at the centre of mass of m_B, O_B, and it is aligned with the body principal inertia directions, $\hat{\mathbf{b}}_1$, $\hat{\mathbf{b}}_2$ and $\hat{\mathbf{b}}_3$.

To simplify the present formulation, the orbital equations of motion of the body m_B can be written from equation (2.7) assuming circular motion of the primaries, (i.e. CR3BP), plus the contribution of the Solar Radiation Pressure, the fourth-body gravity of the Sun and the variation in the gravitational attraction due to the finite dimension of B, expressed with the second order term of the force exerted on a finite dimension body by a particle (i.e. second order term of the expansion in equation (2.5)). The resulting equations are written in normalised scalar form as:

$$\mathbf{f}_x = \begin{cases} \dot{x} = v_x \\ \dot{y} = v_x \\ \dot{z} = v_z \end{cases} \tag{2.11}$$

$$\mathbf{f}_v = \begin{cases} \dot{v}_x = x + 2v_y - \frac{(1-\mu)(x+\mu)}{r_{B_1}^3} - \frac{\mu(x-1+\mu)}{r_{B_2}^3} + a_{SRP_x} + a_{4th_x} + a_{1_x} + a_{2_x} \\ \dot{v}_y = y - 2v_x - \frac{(1-\mu)y}{r_{B_1}^3} - \frac{\mu y}{r_{B_2}^3} + a_{SRP_y} + a_{4th_y} + a_{1_y} + a_{2_y} \\ \dot{v}_z = -\frac{(1-\mu)z}{r_{B_1}^3} - \frac{\mu z}{r_{B_2}^3} + a_{SRP_z} + a_{4th_z} + a_{1_z} + a_{2_z}, \end{cases} \tag{2.12}$$

where x, y and z are the Cartesian coordinates of O_B expressed in terms of the synodic reference frame; v_x, v_y and v_z are the velocity components of the body m_B in S. The distances between the centre of mass of m_B and the two primaries are respectively $r_{B_1} = \sqrt{(x+\mu)^2 + y^2 + z^2}$ and $r_{B_2} = \sqrt{(x-1+\mu)^2 + y^2 + z^2}$, as can be easily noted from figure 2.1.

In the case the Elliptic Restricted Three-Body Problem (ER3BP) is considered, the primaries (i.e. Earth and Moon) are assumed to move on ellipses, with constant eccentricity, around the barycentre of the system. The equations of motion in the rotating frame are written considering that $\omega_S = \omega_S(t)$ is now time dependent, with $\dot{\omega}_S \neq 0$. In the synodic frame, the primaries are no longer in fixed positions, but they are oscillating along the $\hat{\mathbf{x}}$ axis. The instantaneous distance between the two primaries is now solution of the two-body problem between them:

$$r_{12}(t) = \frac{1 - e_S^2}{1 + e_S \cos\left(\nu_S(t)\right)}, \tag{2.13}$$

where e_S is the eccentricity and $\nu_S(t)$ is the true anomaly, function of time, describing the motion of the Earth-Moon system. Unlike CR3BP, this system depends on time and, thus, is not autonomous anymore. The equations of motion can be normalised considering both the rotation and the pulsation of the primaries along $\hat{\mathbf{x}}$. With this normalisation approach, equation (2.12) is formally valid also in the ER3BP but is expressed in a rotating-pulsating reference frame, $\tilde{S}$. ER3BP is based on the three-body environment and the assumed Keplerian elliptic motion of the primaries is only an approximation to the true motions with additional celestial bodies. Therefore, it is meaningless to extended the elliptic problem to four-body or n-body models.

As highlighted in the beginning of this chapter, the effects of the Sun cannot always be neglected in cislunar space and a R4BP approach can be more suitable than a R3BP. BC4BP can be applied to simplify the model formulation and FER4BP to achieve an high modelling accuracy. The hierarchy of dynamical models is therefore unmistakable [61]: highest accuracy for simulations and, for example, GNC design validation require full ephemeris restricted n-body models, while preliminary analyses and analytical investigations require the simple circular restricted three-body problem. In the middle, a great variety of astrodynamical models that can be useful to separately focus different physical

phenomena, like the eccentricity of the Earth-Moon system with ER3BP or the presence of the Sun with BC4BP.

The attitude dynamics of m_B allows to represent the orientation of the body reference frame B with respect to a different frame. In the present model, the equations of rotational motion are written with respect to the inertial frame, I, and the orientation of B with respect to S is computed with a simple frame transformation. The quaternion vector is used as attitude parameter and is denoted as:

$$\mathbf{q} = [q_1, q_2, q_3, q_4]^{\mathrm{T}}, \tag{2.14}$$

The components of the quaternion vector must satisfy the constraint:

$$q_1^2 + q_2^2 + q_3^2 + q_4^2 = 1; \tag{2.15}$$

therefore, just the first three components, $[q_1, q_2, q_3]^{\mathrm{T}}$, which identify the Euler axis of rotation, have to be defined to have a complete set of initial conditions. The fourth component, q_4, which gives information about the Euler angle, is automatically defined by the constraint in equation (2.15). The sign ambiguity that exist when q_4 is obtained from the quaternion constraint can be solved giving an initial condition for the sign of q_4 and enforcing the sign continuity during the numerical integration. The attitude parameters relate two reference frame and in this dissertation they are indicated as ${}^{C}\bullet^{D}$, where C and D are two generic reference frames and $\bullet$ is a generic attitude parameter. For example, the notation ${}^{I}\mathbf{q}^{B}$ means that the quaternion relates the frame B with respect to the frame I. Quaternions have been used as attitude parameters because they have no singularity condition and just three components are sufficient to define the attitude of m_B, thanks to equation (2.15). Moreover, the analysis of the quaternion subspace allows to highlight certain features of the considered dynamical system, as will be discussed in chapter 3.

The fundamental rules of attitude kinematics allow the propagation the rotational motion from the attitude dynamics. In fact, it is possible to evaluate the time rate of change of the quaternion vector from the body angular velocity as:

$$\mathbf{f}_q = \begin{cases} \dot{q}_1 = \frac{1}{2}(\omega_1 q_4 - \omega_2 q_3 + \omega_3 q_2) \\ \dot{q}_2 = \frac{1}{2}(\omega_1 q_3 + \omega_2 q_4 - \omega_3 q_1) \\ \dot{q}_3 = \frac{1}{2}(-\omega_1 q_2 + \omega_2 q_1 + \omega_3 q_4) \\ \dot{q}_4 = -\frac{1}{2}(\omega_1 q_1 + \omega_2 q_2 + \omega_3 q_3), \end{cases} \tag{2.16}$$

where ω_1, ω_2 and ω_3 are components of the angular velocity of the body relative to I and expressed in the body-fixed reference frame B, ${}^{I}\boldsymbol{\omega}^{B}$; q_1, q_2, q_3 and q_4 are the quaternion components of ${}^{I}\mathbf{q}^{B}$.

The angular velocity can be obtained integrating the equations for the rotational dynamics: the Euler equations of motion. Euler equations includes the gravity torques exerted by the two primaries, which can be computed as the fourth-body gravity torque with equation (2.23) on page 23. Moreover, the angular accelerations due to the Solar Radiation Pressure and to the gravity gradient of the fourth-body, Sun, are included in the model. They are obtained from the related torques described before and normalised for the CR3BP formulation. The resulting Euler dynamical equations for the attitude dynamics are expressed as:

$$\mathbf{f}_\omega = \begin{cases} \dot{\omega}_1 = \frac{I_3 - I_2}{I_1}\left(\frac{3(1-\mu)}{r_{B_1}^5} l_2 l_3 + \frac{3\mu}{r_{B_2}^5} h_2 h_3 - \omega_2\omega_3\right) + & \alpha_{SRP_1} + \alpha_{4th_1} \\ \dot{\omega}_2 = \frac{I_1 - I_3}{I_2}\left(\frac{3(1-\mu)}{r_{B_1}^5} l_1 l_3 + \frac{3\mu}{r_{B_2}^5} h_1 h_3 - \omega_1\omega_3\right) + & \alpha_{SRP_2} + \alpha_{4th_2} \\ \dot{\omega}_3 = \frac{I_2 - I_1}{I_3}\left(\frac{3(1-\mu)}{r_{B_1}^5} l_1 l_2 + \frac{3\mu}{r_{B_2}^5} h_1 h_2 - \omega_1\omega_2\right) + & \alpha_{SRP_3} + \alpha_{4th_3}, \end{cases} \tag{2.17}$$

where l_i are the direction cosines in the reference B of the unit position vector from m_1 to m_B, $\hat{\mathbf{r}}_{B_1}$; h_i are those related with $\hat{\mathbf{r}}_{B_2}$; $\alpha_{SRP_{1,2,3}}$ and $\alpha_{4th_{1,2,3}}$ are the components of the angular accelerations introduced before, respectively due to the SRP and to the presence of the Sun. I_1, I_2 and I_3 are the principal moments of inertia of m_B, $\mathbb{I}_B$.

For a classical spacecraft, the contribution of solar radiation torque and fourth-body gravity gradient torque is few orders of magnitude smaller than the gravity gradient torques generated by the two primaries. However, their effect should not be neglected to run accurate simulations, especially when dealing with long propagation of large space structures in lunar vicinity. For example, considering a spacecraft with mass and size of the ISS in a typical L1 orbit, the Earth and the Moon generate a gravity gradient torque respectively in the order of 10^{-4} Nm and 10^{-3} Nm, while the fourth-body effect is around 10^{-6} Nm. For what concern the solar radiation pressure, the magnitude of the torque depends also on the dimensions and the geometry of the spacecraft itself, but, again, for a ISS-like structure, the magnitude of this perturbing term is also in the order of 10^{-6} Nm.

Equations (2.11), (2.12), (2.16) and (2.17) complete the whole set of coupled equations of motion that is needed to describe the orbit-attitude dynamics of a rigid body in a restricted n-body problem environment plus the Solar Radiation Pressure. Moreover, including the second order term of the force exerted on the finite dimension body by a point-mass, the model is not limited to small rigid bodies and it can be applied to any kind of spacecraft in the Earth-Moon system. The complete set of non-linear differential equations is denoted as $\mathbf{f} = \{\mathbf{f}_x, \mathbf{f}_v, \mathbf{f}_q, \mathbf{f}_\omega\}$.

2.3.1 Perturbations

The variation in the gravitational attraction due to the finite dimension of the body, which is represented by the additional terms a_{1_x}, a_{1_y} and a_{1_z} for the first primary m_1, and by a_{2_x}, a_{2_y} and a_{2_z} for the second primary m_2, is due to the fact that the resultant gravity force on a particle and on an extended body are different. When a large space structure is taken into account, the gravitational attraction is also dependent from the relative orientation of m_B with respect to each primary. In fact, from equation (2.5), the force exerted on the extended body by the i-th primary is computed as a series expansion up to the second order:

$$\mathbf{\Gamma}_i \simeq -\nabla V_{g_i} = -\frac{Gm_i m_B}{r_{B_i}^2} \left(\hat{\mathbf{r}}_{B_i} + \mathbf{G}_{2_i}\right). \tag{2.18}$$

The full series expansion will be composed by an infinite number of terms, $\mathbf{G}_{j_i}$, of j-th degree in ρ/r_{B_i}: ρ is the distance of a generic point of m_B with respect to the centre of mass, O_B, and $\hat{\mathbf{r}}_{B_i}$ is the unit vector directed from the i-th primary towards O_B. The series expansion in equation (2.18) is valid and converges for a body that is small compared to the distance from the primary, such that $\rho/r_{B_i} \ll 1$. Obviously, the first element in the bracket is the usual point-mass contribution and it is already included in the nominal unperturbed equations, which are written in the first rows of each right-hand side of equation (2.12). Therefore, the variation in the gravitational attraction due to the finite dimension of the body is computed from $\mathbf{G}_{2_i}$:

$$\mathbf{G}_{2_i} = \frac{1}{m_B r_{B_i}^2} \left\{ \frac{3}{2} \left[\mathrm{tr}(\mathbb{I}_B) - 5\hat{\mathbf{r}}_{B_i} \cdot \mathbb{I}_B \cdot \hat{\mathbf{r}}_{B_i} \right] \hat{\mathbf{r}}_{B_i} + 3\mathbb{I}_B \cdot \hat{\mathbf{r}}_{B_i} \right\}. \tag{2.19}$$

This equation is computed at each integration step, knowing the position and the orientation of the body m_B with respect to each primary. In particular, the attitude dynamics is needed to find the direction cosines of the body reference frame B relative to a frame A_i, which has the first axis aligned as $\hat{\mathbf{r}}_{B_i}$ and the other two axes form a right-handed orthogonal coordinate frame: the second and third axis of A_i are chosen to be mutually perpendicular and orthogonal to $\hat{\mathbf{r}}_{B_i}$ and to $\hat{\mathbf{z}}$. In general, $\mathbf{G}_{2_i}$ is not parallel to $\hat{\mathbf{r}}_{B_i}$ and the resultant gravity force does not align with the vector from the primary to the body centre of mass. The acceleration term that is representing this variation can be obtained from equation (2.19) and equation (2.18), normalised for the applicable RnBP modelling approach formulation and inserted in equation (2.12) through $a_{1_{x,y,z}}$ and $a_{2_{x,y,z}}$, respectively valid for the first and the second primary. It important to note that these terms are not particularly relevant for realistic bodies when compared to other perturbing phenomena, such as the SRP or the Sun's gravity. For example, for a ISS-like spacecraft orbiting around L1, their contribution is 4 to 5 orders of magnitude smaller than the one determined by the other perturbations.

The presence of the Sun is another important aspect that should be considered, especially when an accurate model to propagate the motion at a significant distance from any primary gravitational attractor is sought. In this model, the Sun can be included both with its gravitational effect and its radiation contribution. In these regards, the model is maintained within the Earth-Moon synodic frame but the position of the Sun is computed in the inertial frame I and then rotated in S, exploiting the bicircular approximation (BC4BP) or an ephemeris model (FER4BP). In the latter model, however, the circular approximation is not considered to be significant anymore and the ephemerides of Earth and Moon are also considered: the cislunar space is accurately modelled neglecting just the minor perturbing effects. The ephemerides are obtained exploiting the SPICE Toolkit by NASA / JPL. The frame I is used to express the equations of motion in the FER4BP: I is centred in the Earth-Moon barycentre, O, as previously introduced, and it is assumed to be parallel to the Ecliptic and equinox at date J2000 (EJ2000) reference. When the positions of the primary bodies and of the Sun are known in I or S, the solar radiation pressure contribution and the fourth-body gravitational effect can be easily evaluated. These perturbations are modelled as typically done in astrodynamics literature [62, 63].

The solar radiation pressure is an expression for the interaction between incoming photons from the Sun and a surface that is invested by such a flux. The radiation can interact with a generic body by reflection or absorption, and since it carries momentum and energy, this interaction generates a pressure that perturbs the dynamics. The average pressure due to radiation can be computed using:

$$P_{SRP} = \frac{\Lambda_{SRP}}{c}, \tag{2.20}$$

where $c = 299\,792\,458\,\mathrm{m/s}$ is the speed of light, and Λ_{SRP} is the flux density of solar radiation at the distance of the body from the Sun. It can be computed with an inverse square law, knowing the flux of solar radiation at a certain location in Space. For example, in the Earth-Moon system $\Lambda_{SRP} \simeq 1350\,\mathrm{W/m^2}$. The fraction of radiation associated that can be absorbed, specularly reflected and reflected with diffusion is expressed by a coefficient of absorption, c_a, diffuse reflection, c_d, and specular reflection, c_r. The coefficients must sum to unity, $c_a + c_d + c_r = 1$, and in this work they are assumed to have the typical values for the materials used in the space system. The force that is generated by the solar radiation pressure interaction can be computed using the expression for the radiation pressure on a flat surface; no approximation is made in addition to the one of discretising the real body with a series of flat surfaces, and the self-shadowing effect can be taken into account with simple geometrical considerations [64, 65]. For the i-th body planar surface of area A_i, the solar radiation force

can be expressed as:

$$\mathbf{\Gamma}_{SRP_i} = -A_i P_{SRP} \left[(1 - c_r)\hat{\mathbf{s}} + 2 \left(c_r \cos(\alpha_i) + \frac{1}{3} c_d \right) \hat{\mathbf{n}}_i \right] \cos(\alpha_i)_{Sh}, \quad (2.21)$$

where $\hat{\mathbf{s}}$ and $\hat{\mathbf{n}}_i$ are, respectively, the Body-Sun direction and the surface normal direction in the body-fixed frame. The angle α is the angle between the Body-Sun and the normal to the surface directions, and $\cos(\alpha)$ can only assume positive values since, if $\hat{\mathbf{n}}_i \cdot \hat{\mathbf{s}}$ is negative, the surface is in shadow and is not illuminated by the Sun. This can be mathematically expressed with $\cos(\alpha_i)_{Sh} = \max(0, \cos(\alpha_i))$. Equation (2.21) is obtained assuming that the absorbed radiation acts in the Body-Sun direction, the specularly reflected radiation acts in the normal to the surface direction and the diffuse radiation acts in both directions. The whole solar radiation force can be computed summing up equation (2.21) for each face that is included in the model. The resulting acceleration is normalised for the CR3BP formulation and inserted in equation (2.12) through $a_{SRP_{x,y,z}}$. Similarly, for what concern rotational motion, the solar radiation torque can be obtained knowing the centroid of each planar face and its position vector, $\mathbf{r}_{A_i B}$, with respect to the centre of mass, O_B. In fact, the torque contribution of each face is directly computed as the moment produced by $\mathbf{\Gamma}_{SRP_i}$ about, O_B. The net solar radiation torque, $\mathbf{T}_{SRP}$, is the summation over all the planar faces and the related angular acceleration, $\boldsymbol{\alpha}_{SRP}$, is normalised and inserted in the attitude equation (2.17).

The fourth-body gravitational effect is determined by the presence of the Sun, while the gravitational forces of all the other planets are neglected in this model. The dynamics of m_B is influenced by the gravitational attraction of the two primaries, which are revolving around their centre of mass, as described by the first part of equation (2.12) written in the synodic frame. However, it is currently assumed that the whole Earth-Moon system is influenced by the gravity of the Sun and O is revolving according to the Bicircular or to the Ephemeris model around the centre of mass of the Solar System. In order to simplify the description of the overall motion, the S frame is used anyhow; when the position of the Sun is gathered from the ephemerides in I, it is subsequently rotated in S, where the Earth and Moon have fixed positions and the Sun is rotating clockwise around the barycentre of the Earth-Moon system. Note that, in the circular approximation, the assumed motion do not satisfy Newton's equations but previous works showed that, in some regions of phase space, BC4BP gives the same qualitative behaviour as the real system [66]. The fourth-body gravitational force can be computed as:

$$\mathbf{\Gamma}_S = -G m_S m_B \left(\frac{\hat{\mathbf{r}}_{B_S}}{r_{B_S}^2} - \frac{\hat{\mathbf{r}}_{O_S}}{r_{O_S}^2} \right), \quad (2.22)$$

where m_S is the mass of the Sun, $\hat{\mathbf{r}}_{B_S}$ and r_{B_S} are respectively direction and magnitude of the vector from the Sun to the centre of mass of the body, O_B, while

$\hat{\mathbf{r}}_{O_S}$ and r_{O_S} are those related with the vector from the Sun to the barycentre of the Earth-Moon system, O. The previous equation is composed by two terms: the first one models the effect of the Sun on the spacecraft, while the second one models the effect of the fourth-body on the Earth-Moon system. The latter is needed because the frame I is not really inertial, having its origin at the barycentre of Earth and Moon. The acceleration on m_B can be directly obtained from equation (2.22) and, after the normalisation for the CR3BP formulation, it can be inserted in equation (2.12) through $a_{4th_{x,y,z}}$. Particular attention is paid to numerical difficulties that might arise in computing equation (2.22), as typically discussed in the fundamental astrodynamics literature. For what concern rotational dynamics, also the gravitational effect of the Sun is not uniform and determines a gravity gradient torque on a non-symmetric body. The effect of the gravity gradient on the rotational dynamics of m_B can be expressed in the body-fixed frame, B, as:

$$\mathbf{T}_S = \frac{3Gm_S}{r_{B_S}^3} \begin{pmatrix} (I_3 - I_2)c_{S_2}c_{S_3} \\ (I_1 - I_3)c_{S_1}c_{S_3} \\ (I_2 - I_1)c_{S_1}c_{S_2} \end{pmatrix}, \tag{2.23}$$

where c_{S_1}, c_{S_2} and c_{S_3} are the direction cosines of the Sun-Body direction, $\hat{\mathbf{r}}_{B_S}$, in principal inertia axes. The resulting angular acceleration, $\boldsymbol{\alpha}_{4th}$, is inserted, after the normalisation, in the attitude equations of motion that will be examined next. Again, as already discussed in section 2.3, the gravity gradient torque of the Sun is in general few orders of magnitude smaller than the gravity gradient torques generated by the two primaries, but it is here reported for sake of completeness.

2.4 Relative Orbit-Attitude Equations of Motion

The relative orbit-attitude dynamical model in cislunar space is based on the absolute dynamics discussed in the previous section. The relative dynamics between two bodies of generic masses m_T and m_C, shown in figure 2.2, is conveniently expressed in the inertial reference frame I. For analogy with absolute dynamics analyses, certain results can be also expressed in the rotating synodic reference frame, S.

The absolute orbit-attitude dynamics of the extended and three-dimensional bodies m_T, target, and m_C, chaser, is modelled as in section 2.3 and is applied to two different bodies. Hence, the absolute orbit-attitude dynamics is parametrised using the positions of the centres of mass of the bodies m_T and m_C, described by the position vectors $\mathbf{r}_T$ and $\mathbf{r}_C$, and the four-dimensional quaternion unit vectors, $\mathbf{q}_T$ and $\mathbf{q}_C$, which relates the body frames B_T and B_C with respect to the inertial frame I. The body-fixed frames B_T and B_C are centred at the centre of mass of the two bodies and are aligned with their principal inertia directions.

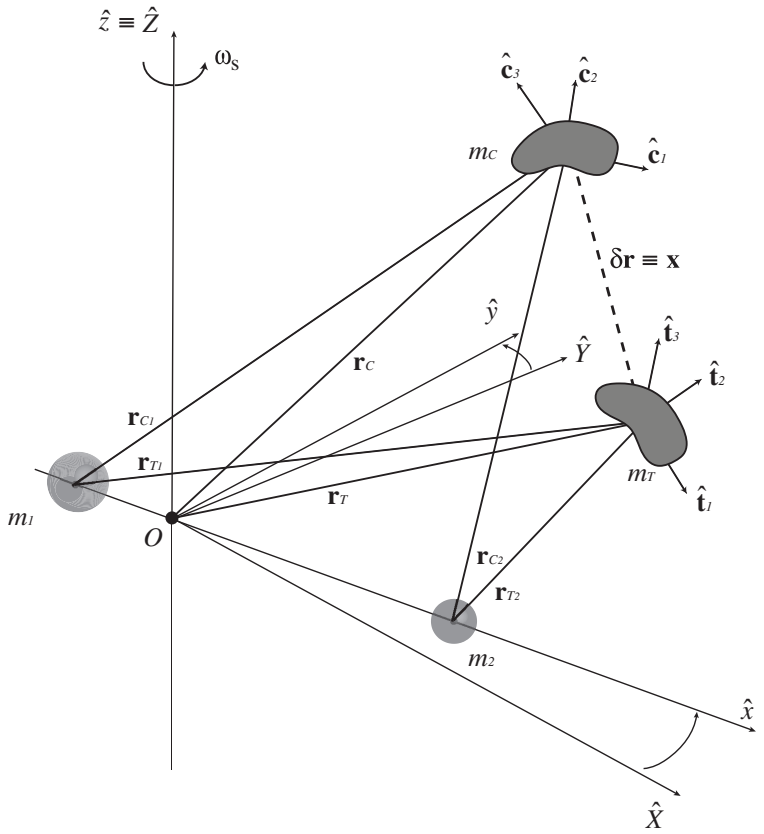

Figure 2.2: Orbit-attitude Relative Dynamics.

The relative translational dynamics is immediately available from the definition of the relative position vector, $\mathbf{x}$, expressed in the frame I:

$$\mathbf{x} \equiv \delta\mathbf{r} = \mathbf{r}_C - \mathbf{r}_T, \tag{2.24}$$

which, in the inertial reference frame, can be straightforwardly differentiated in time obtaining:

$$\ddot{\mathbf{x}} = \ddot{\mathbf{r}}_C - \ddot{\mathbf{r}}_T, \tag{2.25}$$

where $\ddot{\mathbf{r}}_C$ and $\ddot{\mathbf{r}}_T$ are the absolute acceleration vectors of chaser and target (i.e. the reference), available from the absolute dynamics equations. For readers' convenience, from equation (2.12), the absolute dynamics of the target is reported here in the frame I and in dimensional form :

$$\ddot{\mathbf{r}}_T = -\frac{\mu_E}{r_{T_E}^3}\mathbf{r}_{T_E} - \frac{\mu_M}{r_{T_M}^3}\mathbf{r}_{T_M} + \mathbf{a}_{T_{4th}} + \mathbf{a}_{T_{SRP}}, \tag{2.26}$$

where the subscript 1 of the larger primary has been substituted with E (i.e. Earth) and the subscript 2 of the smaller primary with M (i.e. Moon). $\mu_E =$

Gm_E and $\mu_M = Gm_M$ are the dimensional mass parameters. The terms $\mathbf{a}_{T_{4th}}$ and $\mathbf{a}_{T_{SRP}}$ are the perturbing accelerations vectors due to the gravitational presence of the Sun and due to the SRP. They are, as already remarked, the most relevant perturbations to be considered for the dynamics on Earth-Moon libration point orbits, since they have a noticeable effect also in a short time scale for relative dynamics. In these regards, orbital eccentricity and orbital inclination of the primaries (i.e. FERnBP), solar gravitation and solar radiation pressure shall be taken into account, while second order of the gravitational potential generated by a spherical attractor on an extended body can be neglected, as will be highlighted in chapter 4.

The relative attitude dynamics requires more attention with respect to the translational one. In fact, it describes the rotational motion of the chaser relative to the target frame, or the other way around; in both cases, the relative attitude dynamics is expressed with respect to a non-inertial reference frame. First of all, a relative quaternion from B_T to B_C has to be defined as:

$$\delta\mathbf{q} = \mathbf{q}_C \times \mathbf{q}_T^{-1} = \begin{bmatrix} \boldsymbol{\chi}(\mathbf{q}_T)\mathbf{q}_C \\ \\ \mathbf{q}_T^{\mathrm{T}}\mathbf{q}_C \end{bmatrix}. \tag{2.27}$$

The matrix $\boldsymbol{\chi}(\mathbf{q}_T)$ is a 3×4 matrix defined as:

$$\boldsymbol{\chi}(\mathbf{q}_T) = \begin{bmatrix} q_{T_4}\mathbf{I}_{3\times 3} - [\mathbf{q}_{T_{123}}\times] & -\mathbf{q}_{T_{123}} \end{bmatrix}, \tag{2.28}$$

where $\mathbf{q}_{T_{123}} = [q_{T_1}, q_{T_2}, q_{T_3}]^{\mathrm{T}}$ is the column vector part and q_{T_4} is the scalar part of the target quaternion $\mathbf{q}_T$; $\mathbf{I}_{3\times 3}$ is the 3×3 identity matrix; $[\mathbf{q}_{T_{123}}\times]$ is the 3×3 skew-symmetric cross-product matrix, defined for a generic column vector, $\mathbf{u} = [u_1, u_2, u_3]^{\mathrm{T}}$, as:

$$[\mathbf{u}\times] = \begin{bmatrix} 0 & -u_3 & u_2 \\ u_3 & 0 & -u_1 \\ -u_2 & u_1 & 0 \end{bmatrix}. \tag{2.29}$$

The rotation matrix $\mathbf{R}$, which transform a vector from the target reference frame, B_T, to the chaser reference frame, B_C, can be expressed in terms of the relative quaternion $\delta\mathbf{q}$ as:

$$\mathbf{R}(\delta\mathbf{q}) = \begin{bmatrix} \delta\mathbf{q}_1^2 - \delta\mathbf{q}_2^2 - \delta\mathbf{q}_3^2 + \delta\mathbf{q}_4^2 & 2(\delta\mathbf{q}_1\delta\mathbf{q}_2 - \delta\mathbf{q}_3\delta\mathbf{q}_4) & 2(\delta\mathbf{q}_1\delta\mathbf{q}_3 + \delta\mathbf{q}_2\delta\mathbf{q}_4) \\ 2(\delta\mathbf{q}_1\delta\mathbf{q}_2 + \delta\mathbf{q}_3\delta\mathbf{q}_4) & -\delta\mathbf{q}_1^2 + \delta\mathbf{q}_2^2 - \delta\mathbf{q}_3^2 + \delta\mathbf{q}_4^2 & 2(\delta\mathbf{q}_2\delta\mathbf{q}_3 - \delta\mathbf{q}_1\delta\mathbf{q}_4) \\ 2(\delta\mathbf{q}_1\delta\mathbf{q}_3 - \delta\mathbf{q}_2\delta\mathbf{q}_4) & 2(\delta\mathbf{q}_2\delta\mathbf{q}_3 + \delta\mathbf{q}_1\delta\mathbf{q}_4) & -\delta\mathbf{q}_1^2 - \delta\mathbf{q}_2^2 + \delta\mathbf{q}_3^2 + \delta\mathbf{q}_4^2 \end{bmatrix}. \tag{2.30}$$

At this point, the relative angular velocity can be defined with respect to I as:

$$\delta\boldsymbol{\omega}^I = \boldsymbol{\omega}_C^I - \boldsymbol{\omega}_T^I = \mathbf{A}_{I\,B_C}(\boldsymbol{\omega}_C^{B_C} - \mathbf{R}\,\boldsymbol{\omega}_T^{B_T}), \tag{2.31}$$

where $\mathbf{A}_{I\,B_C} = \mathbf{A}_{B_C I}^{\mathrm{T}}$ is the attitude matrix from the chaser frame B_C to the inertial frame I. Note that chaser and target angular velocities $\boldsymbol{\omega}_C^I$ and $\boldsymbol{\omega}_T^I$ are expressed in the inertial frame, while $\boldsymbol{\omega}_C^{B_C}$ and $\boldsymbol{\omega}_T^{B_T}$ are expressed in the body-fixed frames. Consequently, the relative angular velocity in B_C is simply:

$$\delta\boldsymbol{\omega}^{B_C} = \boldsymbol{\omega}_C^{B_C} - \mathbf{R}\,\boldsymbol{\omega}_T^{B_T}. \tag{2.32}$$

Finally, it is possible to express the relative attitude motion of the chaser with respect to the target, deriving the dynamics in the body-fixed frame B_C, as:

$$\begin{aligned}\delta\dot{\boldsymbol{\omega}}^{B_C} = \mathbb{I}_C^{-1}\Big\{ &- [\delta\boldsymbol{\omega}^{B_C}\times]\mathbb{I}_C\delta\boldsymbol{\omega}^{B_C} - [\delta\boldsymbol{\omega}^{B_C}\times]\mathbb{I}_C\mathbf{R}\,\boldsymbol{\omega}_T^{B_T} \\ &+ \mathbb{I}_C[\delta\boldsymbol{\omega}^{B_C}\times]\mathbf{R}\,\boldsymbol{\omega}_T^{B_T} - [\mathbf{R}\,\boldsymbol{\omega}_T^{B_T}\times]\mathbb{I}_C\delta\boldsymbol{\omega}^{B_C} + \mathbf{n}_C \\ &- \mathbf{R}\Big[(\mathbf{R}^{\mathrm{T}}\mathbb{I}_C\mathbf{R} - \mathbb{I}_T)\mathbb{I}_T^{-1}(\mathbf{n}_T - [\boldsymbol{\omega}_T^{B_T}\times]\mathbb{I}_T\boldsymbol{\omega}_T^{B_T}) \\ &+ [\boldsymbol{\omega}_T^{B_T}\times](\mathbf{R}^{\mathrm{T}}\mathbb{I}_C\mathbf{R} - \mathbb{I}_T)\boldsymbol{\omega}_T^{B_T}\Big] - \mathbf{R}\,\mathbf{n}_T\Big\},\end{aligned} \tag{2.33}$$

where $\mathbb{I}_C$ and $\mathbb{I}_T$ are the inertia tensors of chaser and target in principal axes; $\mathbf{n}_C$ and $\mathbf{n}_T$ are the external torque vectors acting on the rigid bodies, respectively expressed in B_C and B_T [67]. It is worth remembering that, the relevant external torques in cislunar space are: the gravity gradient torques of Earth and Moon, and the solar radiation pressure torque. Furthermore, in this work, also the gravity gradient torque of the Sun can be taken into account as an external torque perturbation.

From the relative attitude dynamics, which allows to compute the time evolution of the relative angular rates, the derivation of the attitude kinematics is immediate. In fact, the kinematic equation for the relative quaternion is:

$$\delta\dot{\mathbf{q}} = \frac{1}{2}\boldsymbol{\Omega}(\delta\boldsymbol{\omega}^{B_C})\delta\mathbf{q}, \tag{2.34}$$

where all the used variables are function of time and the matrix $\boldsymbol{\Omega}$ is a 4×4 skew-symmetric matrix defined as:

$$\boldsymbol{\Omega}(\boldsymbol{\omega}) = \begin{bmatrix} -[\boldsymbol{\omega}\times] & \boldsymbol{\omega} \\ -\boldsymbol{\omega}^{\mathrm{T}} & 0 \end{bmatrix}. \tag{2.35}$$

Knowing the relative orbit-attitude dynamics between target and chaser and assuming to have available the absolute orbit-attitude dynamics of the target (i.e. the reference), it is possible to have a complete understanding of both absolute and relative orbit-attitude dynamics involving two bodies in cislunar space.

For practical operational applications, both absolute (in equations (2.12) and (2.17)) and relative (in equations (2.25) and (2.33)) orbit-attitude dynamics can be

propagated in-time with on-board software. In particular, the aforementioned dynamics is useful to increase the navigation accuracy with filters to better estimate the states available from sensors measurements. An example of navigation implementation is briefly discussed considering a chaser spacecraft equipped with sensors able to measure its relative state with respect to the target: a navigation filter, exploiting the developed relative orbit-attitude dynamics in non-Keplerian orbits, is applied to improve the accuracy of relative navigation, enabling the guidance functions to work in relative frames and compute the best trajectories for rendezvous and docking between the two spacecraft. For what concern absolute navigation, it should be supported by ground-tracking (e.g. DSN), or, in order to have full on-board autonomy, alternative navigation techniques should be exploited (e.g. liaison navigation). However, when one of the two spacecraft have accurate information about its absolute and relative states, the estimation of the absolute state of the other spacecraft is straightforward from the relations available.

Guidance and control functions, similarly to what has been discussed for the navigation functions, require the dynamics equations to be implemented. In this research work, 6DOF relative GNC functions to perform rendezvous and docking in cislunar non-Keplerian orbits are discussed and, thus, equation (2.25) and equation (2.33) are of interest. These are exploited to compute the reference trajectories connecting chaser and target. Then, the control profile is needed in order to have the chaser moving on the desired rendezvous path. This work is not considering the control actuation and, hence, the discussion about 6DOF guidance and control is concluded when the nominal control acceleration profiles are available. In fact, the output of the control functions is a vector of linear accelerations in inertial frame I and a vector of angular accelerations in chaser body-fixed frame B_C. These control acceleration vectors, respectively $\mathbf{a}_C$ and $\boldsymbol{\alpha}_C$, are summed to the chaser absolute orbit-attitude dynamics. As a consequence, considering the formulation of equations (2.25) and (2.33), the controlled relative orbit-attitude dynamics equation are:

$$\ddot{\tilde{\mathbf{x}}} = \ddot{\mathbf{x}} + \mathbf{a}_C, \tag{2.36}$$

$$\delta\dot{\boldsymbol{\omega}}^{B_C} = \delta\dot{\boldsymbol{\omega}}^{B_C} + \boldsymbol{\alpha}_C. \tag{2.37}$$

2.4.1 Linearised relative dynamics

Guidance and control functions can be developed exploiting linear techniques and, in general, a linear formulation of the dynamics can be helpful. Therefore, to set up the framework for linear control design, a linearisation of the relative dynamics about the target (i.e. reference) spacecraft state can be performed.

Translational relative dynamics can be linearised assuming the relative distance between chaser and target to be small compared to the distance between the target and the primaries: $\|\mathbf{x}\| \ll r_{T_E}$ and $\|\mathbf{x}\| \ll r_{T_M}$. In this way, a first order expansion of equation (2.25) is possible obtaining [68]:

$$\begin{bmatrix} \dot{\mathbf{x}} \\ \ddot{\mathbf{x}} \end{bmatrix} \approx \begin{bmatrix} \mathbf{0} & \mathbf{I}_{3\times3} \\ \boldsymbol{\Xi}(t) & \mathbf{0} \end{bmatrix} \begin{bmatrix} \mathbf{x} \\ \dot{\mathbf{x}} \end{bmatrix}, \tag{2.38}$$

where $\boldsymbol{\Xi}(t)$ is a term dependent from the position of the target spacecraft. Hence, it is a term depending, as a function of time, on the known absolute orbital state of the target:

$$\begin{aligned} \boldsymbol{\Xi}(t) = &- \left(\frac{\mu_E}{r_{T_E}^3} + \frac{\mu_M}{r_{T_M}^3} \right) \mathbf{I}_{3\times3} + 3\frac{\mu_E}{r_{T_E}^3} \left[\hat{r}_{T_E} \hat{r}_{T_E}^{\mathrm{T}} \right] \\ &+ 3\frac{\mu_M}{r_{T_M}^3} \left[\hat{r}_{T_M} \hat{r}_{T_M}^{\mathrm{T}} \right], \end{aligned} \tag{2.39}$$

where the result of a first order expansion linearisation is evident. Note that the relative perturbation terms due to the Sun's gravity and to the SRP are negligible in the linearisation process, compared to the gravity field of the primaries. Even if their linearisation is straightforward, these effects are treated as perturbations also in the linearised dynamic model, in order to avoid an eccessive computational burden. Equation (2.39) can be easily adapted to work with the circular restricted model or with the ephemeris model, since the differences stay only in the definition of the position vectors of the primaries: as sinusoidal circle functions or as numerical ephemerides. Analogously, the modification from dimensional units to normalised non-dimensional ones is immediate. As a last comment, equation (2.38) and equation (2.39) can be modified also to be formulated in synodic non-inertial reference frame: the matrix $\boldsymbol{\Xi}(t)$ requires only to be rotated from I to S, while the linear system in equation (2.38) has to take into account the non-inertial terms due to centrifugal and Coriolis effects. When the control is applied, considering also the relative perturbations, the linear dynamics equations become:

$$\begin{aligned} \begin{bmatrix} \dot{\tilde{\mathbf{x}}} \\ \ddot{\tilde{\mathbf{x}}} \end{bmatrix} \approx &\begin{bmatrix} \mathbf{0} & \mathbf{I}_{3\times3} \\ \boldsymbol{\Xi}(t) & \mathbf{0} \end{bmatrix} \begin{bmatrix} \tilde{\mathbf{x}} \\ \dot{\tilde{\mathbf{x}}} \end{bmatrix} + \begin{bmatrix} \mathbf{0} \\ \mathbf{I}_{3\times3} \end{bmatrix} \mathbf{a}_C \\ &+ \begin{bmatrix} \mathbf{0} \\ \mathbf{I}_{3\times3} \end{bmatrix} (\delta\mathbf{a}_S + \delta\mathbf{a}_{SRP}), \end{aligned} \tag{2.40}$$

where $\delta\mathbf{a}_S$ and $\delta\mathbf{a}_{SRP}$ are respectively the differential gravitational perturbation of the Sun and the differential perturbation due to solar pressure.

The relative attitude dynamics can be linearised similarly to translation motion. However, in this case, the assumptions is to have small attitude errors (i.e.

$\delta\mathbf{q} \approx [0,0,0,1]^{\mathrm{T}}$) and small angular rates (i.e. $\boldsymbol{\omega}_C \approx \mathbf{0}$ and $\boldsymbol{\omega}_T \approx \mathbf{0}$). The first assumption allows to approximate the rotation matrix from B_T to B_C as $\mathbf{R} \approx \mathbf{I}_{3\times3}$, while the second assumption allows to neglect the cross angular rate terms as second order effects. Then, equation (2.37) becomes in the frame B_C:

$$\delta\dot{\boldsymbol{\omega}}^{B_C} \approx \mathbb{I}_C^{-1}\left\{\mathbf{n}_C - \mathbf{n}_T - \left[\mathbb{I}_C - \mathbb{I}_T\right]\mathbb{I}_T^{-1}\mathbf{n}_T\right\} + \boldsymbol{\alpha}_C, \tag{2.41}$$

which obviously reduces to

$$\delta\dot{\boldsymbol{\omega}}^{B_C} \approx \mathbb{I}_C^{-1}\mathbf{n}_C - \mathbb{I}_T^{-1}\mathbf{n}_T + \boldsymbol{\alpha}_C, \tag{2.42}$$

where the external torque vectors are computed considering all the aforementioned external contributions within the assumptions of the linearised model. Accordingly, the linearised attitude kinematics becomes:

$$\delta\dot{\mathbf{q}} \approx \frac{1}{2}\begin{bmatrix}\delta\boldsymbol{\omega}^{B_C \cong B_T} \\ 0\end{bmatrix}. \tag{2.43}$$

Note that with these assumptions the target and chaser body frames, B_C and B_T, are approximately equivalent.

2.5 Flexible Dynamics

Flexible dynamics models are necessary further steps to understand the coupled orbital, attitude and flexible dynamics in non-Keplerian dynamical environments. These models are needed to represent flexible elements within the space systems, which are dynamically coupled to the rigid body motion described in the previous sections. The main reason is to highlight possible interactions between orbit-attitude dynamics and flexible dynamics. In fact, orbital and rotational motion of the cislunar space station may be perturbed by the natural vibrations of the flexible structure or, inversely, the frequencies associated to the non-Keplerian dynamics may be an issue with respect to possible resonances of the flexible system.

Moreover, additional internal perturbations sources can be modelled, like the fluid sloshing. As a matter of fact, large spacecraft in cislunar space require a substantial mass of fuel to perform orbit corrections for prolonged times and to execute trajectory transfers. When the fuel tanks are only partially filled and under roto-translational accelerations, large quantities of fuel move uncontrollably inside the tanks and generate sloshing perturbations, which are extremely dangerous for attitude stability [63, 62].

The structural mode equations for the flexible elements and the sloshing modes can be expressed in a canonical form of second order dynamics, with known

eigenfrequencies and damping coefficients. Thus, the flexibility modelling techniques described in this section can be applied to both vibrational modes. The developed flexibility coupling terms allow to augment the dynamics equations of rigid-body motion with structural and sloshing model dynamics.

2.5.1 Flexible Elements Models

The flexible elements models within the extended body m_B are based on simple and generic structural elements: flexible beams, lumped masses, springs, dampers and, eventually, flexible plates. In this way, it is possible to further extend the space system to more complex configurations, with a Multi-Body technique [69].

Flexible structural elements are included in the model with a Lumped Masses Model (LMM), or with a Lumped Parameters Model (LPM) or with a Distributed Parameters Model (DPM). In the first case, lumped masses are connected to a rigid structure with a massless spring; in a way to have an equivalent spring-mass system, able to represent a pseudo-mode of vibration [70]. In the second technique rigid elements are interconnected with lumped stiffness or damping parameters in order to compose a more complex flexible multi-body system. Lastly, with DPM the flexible elements are represented by approximate finite-dimensional models of the flexible structures [71].

Considering LMM, the spring-mass systems are attached to the rigid body in arbitrary points at a fixed distance from O_B. Their motion is excited from the dynamics of B itself. Their effect is inserted in the equations of motion through $\mathbf{\Gamma}_{LMM}$ and $\mathbf{T}_{LMM}$, in fact the spring generates a force on the rod and therefore a torque with respect to centre of mass of the rigid body. Each i-th spring-mass system, represented in figure 2.3, is located at a distance l_i from the barycentre of B, and it is defined by a pseudo-modal mass $\widetilde{m}_i$ and an equivalent stiffness $\widetilde{k}_i$. All the modal masses are scaled to 1, and each pseudo-mode is entirely represented through $\widetilde{k}_i$. From the natural frequency of each mode of the structure, $\widetilde{\omega}_i$, the stiffness can be computed as:

$$\widetilde{k}_i = \widetilde{\omega}_i^2 \widetilde{m}_i. \tag{2.44}$$

The motion of the spring-mass systems can be constrained to be orthogonal to certain surface, in order to simulate only bending modes or axial modes. The elongation of the spring, with respect to the linking point, is $\widetilde{\mathbf{z}}_i$. The acceleration of the linking point is $\ddot{\widetilde{\mathbf{y}}}_i$, and it can be easily computed knowing the dynamics of the body m_B. Also in this case, the equations of motion can be normalised with same process that has been described for the rigid body dynamics, even if, to avoid numerical problems, the normalisation is differently scaled according to the typical dimensions of the flexible dynamics. For each spring mass system it

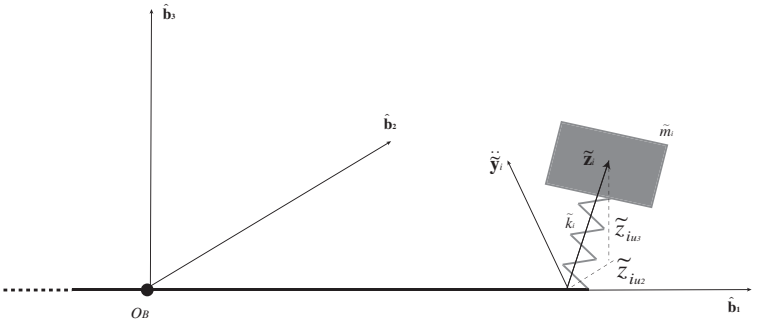

Figure 2.3: Lumped Masses Model (LMM).

is possible to write:

$$\widetilde{m}_i(\ddot{\widetilde{\mathbf{z}}}_i + \ddot{\widetilde{\mathbf{y}}}_i) + \widetilde{k}_i\widetilde{\mathbf{z}}_i = 0. \tag{2.45}$$

The force exerted on B is directly available from equation (2.45), while the associate torque, with respect to the centre of mass O_B, by a single spring-mass system is:

$$\mathbf{T}_{LMM_i} = l_i\hat{\mathbf{b}}_1 \times \widetilde{k}_i\widetilde{\mathbf{z}}_i. \tag{2.46}$$

The LMM is particularly useful to model the sloshing dynamics, in particular, when dampers are inserted in the spring-mass systems.

The more complex flexible models, LPM and DPM, are founded on the pioneering work of Kane, who studied the dynamics of flexible structure undergoing large overall motions [37]. In fact, a non-linear strain measure and a change of coordinates allow to automatically include numerous motion-induced effects, such as centrifugal stiffening or vibrations induced by Coriolis force, which are usually neglected by the canonical structural techniques based on linear Cartesian modelling approaches. A quadratic form of the strain energy helps to obtain an accurate model, which produces exact simulations and can be easily implemented for numerical computation through a Rayleigh-Ritz method to approximate the involved variables. The theoretical foundation of the developed model has been gathered from the work of Yoo [38] and Invernizzi [39].

The lumped parameters model, LPM, produces less precise results than DPM, but is less expensive in terms of computational load and allows an easier and faster investigation of space structures composed by many simple elements. In fact, LPM is developed exploiting a multi-body formulation that, with reference to figure 2.4, is based on rigid rods, lumped masses, springs and dampers to represent the inertia and flexibility properties of a given extended flexible body. In this research work, an algorithm has been developed by the author to automatically write the analytical equations of motion of the system, once the list of the various

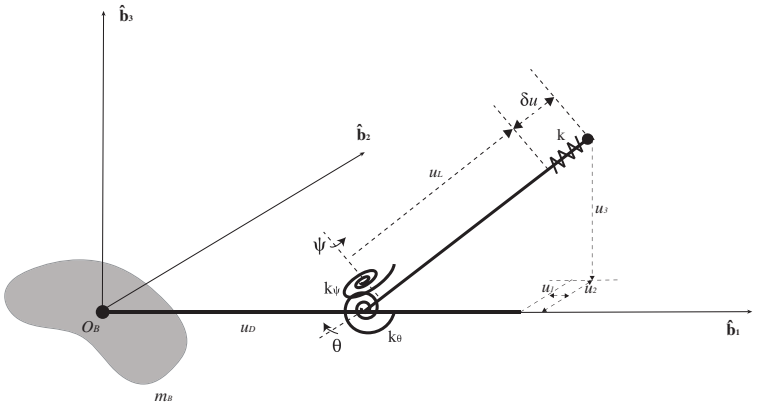

Figure 2.4: Lumped Parameters Model (LPM).

elementary structural components and the mutual connection between them have been specified. The different elements are assembled exploiting rotation matrices between the local coordinate systems of each part of the structure and satisfying the imposed constraints. The resulting dynamic equations are obtained with a Lagrangian approach, starting from the Lagrangian function of the multi-body system. Practically, equation (2.7) is formulated taking into account the kinetic energy related with the flexible deformations:

$$\begin{aligned}\mathcal{T} = &\frac{1}{2} m_B \, \dot{\mathbf{r}}_B \cdot \dot{\mathbf{r}}_B + \frac{1}{2} \boldsymbol{\omega} \cdot \mathbb{I}_B \cdot \boldsymbol{\omega} \\ &+ \frac{1}{2} \sum_{i=1}^{n_{flex}} \int_{flex_i} \dot{\mathbf{u}}_i \cdot \dot{\mathbf{u}}_i \, dm_{flex_i} + \frac{1}{2} \sum_{i=1}^{n_{LMM}} \widetilde{m}_i \, \dot{\widetilde{\mathbf{z}}}_i \cdot \dot{\widetilde{\mathbf{z}}}_i.\end{aligned} \tag{2.47}$$

where n_{flex} is the number of flexible elements, n_{LMM} is the number of lumped masses and $\dot{\mathbf{u}}_i$ is the velocity of the differential flexible element, dm_{flex_i}. Similarly, also the potential energy associated to the deformable structures is taken into account to compute the Lagrangian function:

$$V_{flex_i} = \frac{1}{2} \boldsymbol{\zeta}_i \cdot \mathbf{K}_{flex_i} \cdot \boldsymbol{\zeta}_i, \tag{2.48}$$

$$V_{LMM_i} = \frac{1}{2} \widetilde{k}_i \, \widetilde{\mathbf{z}}_i \cdot \widetilde{\mathbf{z}}_i, \tag{2.49}$$

where $\boldsymbol{\zeta}_i$ represents the generalised coordinates associated with the vibration degrees of freedom, modelled in the LPM or in the DPM, and $\mathbf{K}_{flex_i}$ is the modal stiffness matrix of the i-th deformable element.

DPM is able to model generic flexible structures attached to the centre of mass of the body m_B under the effects of the coupled orbit-attitude dynamics in cislunar space, displayed in figure 2.5 for the simple case of the cantilever beam. This model allows further extensions: different beams or plates may be attached

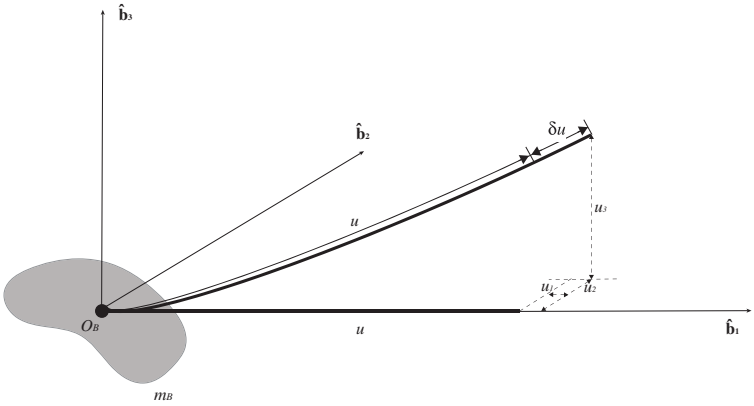

Figure 2.5: Distributed Parameters Model (DPM).

to the same rigid body within the same modelling techniques. All the non-linear strain terms due to the large motion of the flexible structure are retained, while the inertia forces are linearised to obtain the final equations of motion for the present modelling method, which can also be referred as foreshortening approach. The distributed parameters technique can be exploited as a reference for the less refined but effective LPM, as will be discussed in chapter 6.

2.5.2 Sloshing Models

The motion of liquids, such as fuel, in partially filled tanks must be taken into account in a spacecraft model, in particular with manoeuvres that excite the lateral motion of the fluid. The effect of the liquid on the spacecraft can be replaced by a linear mechanical model. In fact, it is assumed that the sloshing is linear: both a pendulum model and a spring-mass model are equivalent in representing the linear sloshing phenomena. The spring-mass model does not require the use of kinematic constraints, leaving the equations of motion of the different bodies to be independent; the reason because this latter model is preferred in this research.

Thus, the Liquid Sloshing Model (LSM) dynamics has been analytically derived applying the Lumped Masses Model (LMM) assumptions. However, the parameters of the mass-spring-damper slosh model have to be tuned properly in order to correctly represent a real liquid sloshing in the spacecraft tanks. The correct parameters to be used have been retrieved from available literature studies and models [72, 73]. In table 2.1, the definition and the formulation of the parameters to set-up the sloshing model are reported for a cylindrical tank with diameter d and height h, in [m], filled with a liquid of density ρ_{liq}, in [kg/m^3]. The acceleration influencing the sloshing dynamics, g, is the dynamically-induced

Table 2.1: Slosh Model Parameters for a Cylindrical Tank.

Definition	Symbol	Value	Units
Geometric Coefficient	σ	1.841	$[-]$
Damping Ratio	ϵ	0.05	$[-]$
Tank Acceleration	g	$f(\mathbf{r}_B, \mathbf{q}, \mathbf{f}_v, \mathbf{f}_\omega)$	$[\mathrm{ms}^{-2}]$
Liquid Mass	m_{liq}	$\frac{\pi}{4} d^2 h \rho_{liq}$	[kg]
Sloshing Mass	m_1	$m_{liq}\left[\frac{d\tanh\left(2\sigma\frac{h}{d}\right)}{\sigma(\sigma^2-1)h}\right]$	[kg]
Rigidly Attached Mass	m_0	$m_{liq} - m_1$	[kg]
Sloshing Mass Position	h_1	$\frac{h}{2} - \frac{d}{2\sigma}\tanh\left(2\sigma\frac{h}{d}\right)$	[m]
Rigidly Attached Mass Position	h_0	$\frac{m_{liq}}{m_0}\left[\frac{h}{2} - \frac{d^2}{8h}\right] - \frac{m_1}{m_0} h_1$	[m]
Stiffness Coefficient	$k_\xi = k_\eta$	$m_{liq}\frac{2g}{(\sigma^2-1)h}\tanh^2\left(2\sigma\frac{h}{d}\right)$	$[\mathrm{kgs}^{-2}]$
Damping Coefficient	$c_\xi = c_\eta$	$2m_1\epsilon\sqrt{\frac{k_\xi = k_\eta}{m_1}}$	$[\mathrm{kgs}^{-1}]$

acceleration acting along the axis of the tank; for practical applications, it can be selected to be equal to the average gravitational acceleration along the orbital motion.

2.5.3 Flexible Equations of Motion

Flexibility coupling with orbit-attitude dynamics can be derived from the Lagrangian formulation in equation (2.7). Nevertheless, the most relevant interaction between flexible and rigid body dynamics is mainly on rotational motion. In fact, the vibrational dynamics evolving from flexible elements and internal fuel sloshing interferes strongly with the attitude dynamics, and it can reduce the achievable performances of the attitude control system (ACS).

The absolute attitude dynamics equations in equation (2.17) can be reformulated to include flexibility effects. For example, assuming to have a spacecraft with two solar panels modelled with LPMs, as in figure 2.4, and an internal fluid sloshing represented by two LMM mass-spring-damper systems, as in figure 2.6,

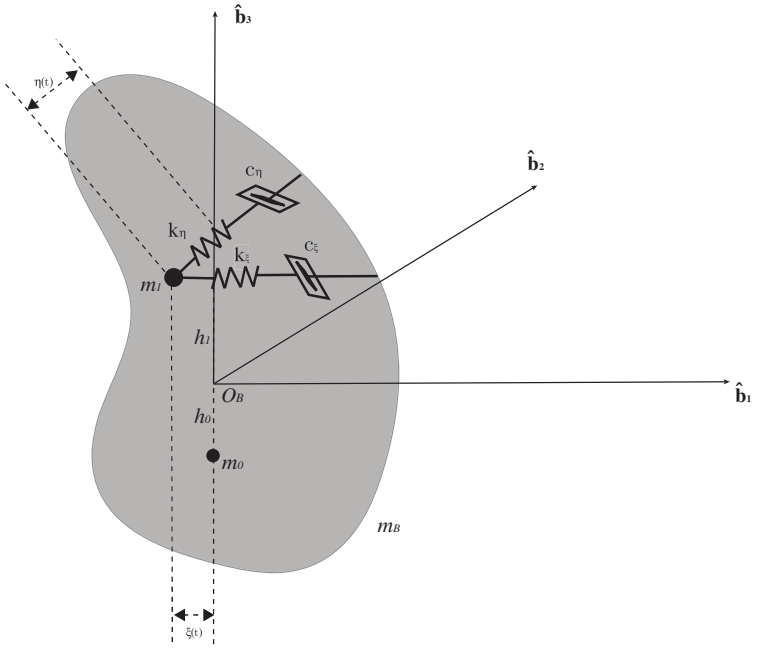

Figure 2.6: Liquid Sloshing Model (LSM).

the kinetic energy in equation (2.47) is:

$$\begin{aligned}\mathcal{T} = &\frac{1}{2}\boldsymbol{\omega}\cdot\mathbb{I}_{B_f}\cdot\boldsymbol{\omega} + \frac{1}{2}\left(\boldsymbol{\omega}+\boldsymbol{\omega}_W\right)\cdot\mathbb{I}_W\cdot\left(\boldsymbol{\omega}+\boldsymbol{\omega}_W\right)\\ &+\frac{1}{2}\dot{\mathbf{p}}\cdot\mathbb{M}_P\cdot\dot{\mathbf{p}} + \boldsymbol{\omega}\cdot\mathbb{P}\cdot\dot{\mathbf{p}} + \frac{1}{2}\dot{\mathbf{s}}\cdot\mathbb{M}_S\cdot\dot{\mathbf{s}} + \boldsymbol{\omega}\cdot\mathbb{S}\cdot\dot{\mathbf{s}},\end{aligned} \tag{2.50}$$

where $\mathbf{p} = [\theta_1, \psi_1, \theta_2, \psi_2]^{\mathrm{T}}$ represents the generalised coordinates associated with the vibration degrees of freedom of the solar panels, θ_i and ψ_i with $i = 1, 2$, and $\mathbf{s} = [\xi, \eta]^{\mathrm{T}}$ represents the generalised sloshing coordinates, ξ and η. The axial deformation of the flexible appendages is ignored with respect to the bending ones, assuming $\delta u = 0$, and the rigid part of the solar panels is not considered: $u_D = 0$. Moreover, the sloshing is assumed to be constrained on the $\hat{\mathbf{b}}_1 - \hat{\mathbf{b}}_2$ plane and the panels are aligned along the $\hat{\mathbf{b}}_1$-axis.

The matrix $\mathbb{I}_{B_f}$ includes the slosh mass moment of inertia and the flexible appendages moments of inertia in the non-deformed configuration, plus the elastic displacement contribution to the moments and products of inertia:

$$\mathbb{I}_{B_f} = \mathbb{I}_B + \mathbb{I}_{P_1}\left(\theta_1(t), \psi_1(t)\right) + \mathbb{I}_{P_2}\left(\theta_2(t), \psi_2(t)\right) + \mathbb{I}_S\left(\xi(t), \eta(t)\right). \tag{2.51}$$

It should be noted that the rigidly attached slosh mass, m_0, is accounted inside the moment of inertia associated with the liquid sloshing, $\mathbb{I}_S$, which is is divided in a constant term, $\mathbb{I}_{S_{m_0}}$, and in a variable term, $\mathbb{I}_{S_{m_1}}\left(\xi(t), \eta(t)\right)$.

The matrix $\mathbb{M}_P$ is the modal mass matrix of the solar panels and the matrix $\mathbb{M}_S$ is the generalised mass matrix of the slosh:

$$\mathbb{M}_P = \begin{bmatrix} m_{P_1} u_{L_1}^2 & 0 & 0 & 0 \\ 0 & m_{P_1} u_{L_1}^2 \cos^2(\theta_1(t)) & 0 & 0 \\ 0 & 0 & m_{P_2} u_{L_2}^2 & 0 \\ 0 & 0 & 0 & m_{P_2} u_{L_2}^2 \cos^2(\theta_2(t)) \end{bmatrix}, \quad (2.52)$$

$$\mathbb{M}_S = \begin{bmatrix} m_1 & 0 \\ 0 & m_1 \end{bmatrix}, \quad (2.53)$$

where $u_{L_1} = u_{L_2}$ are the lengths of the solar panels, $m_{P_1} = m_{P_2}$ their masses in the LPM and m_1 is the oscillating mass in the slosh model.

The matrix $\mathbb{P}$ denotes the coupling coefficient matrix between the attitude motion and the vibration of the two panels:

$$\mathbb{P} = \begin{bmatrix} \mathbb{P}_1 & \mathbb{P}_2 \end{bmatrix}, \quad (2.54)$$

where

$$\mathbb{P}_i = m_{P_i} u_{L_i}^2 \begin{bmatrix} -\sin(\psi_i(t)) & \cos(\psi_i(t)) \cos(\theta_i(t)) \sin(\theta_i(t)) \\ \cos(\psi_i(t)) & \sin(\psi_i(t)) \cos(\theta_i(t)) \sin(\theta_i(t)) \\ 0 & \cos^2(\theta_i(t)) \end{bmatrix}, \quad (2.55)$$

with $i = 1, 2$.

The matrix $\mathbb{S}$ denotes the coupling coefficient matrix between the attitude motion and the sloshing mass motion:

$$\mathbb{S} = \begin{bmatrix} 0 & -h_1 \\ h_1 & 0 \\ -\eta(t) & \xi(t) \end{bmatrix}, \quad (2.56)$$

where h_1 is the sloshing arm with respect to the centre of mass, O_B.

The flexible dynamical model includes the presence of reaction wheels as actuators. The matrix $\mathbb{I}_W$ is the reaction wheels inertia matrix and the angular velocity of the wheels $\boldsymbol{\omega}_W$ is relative to the angular velocity of m_B, $\boldsymbol{\omega}$. In this research work, the mounting configuration of the wheels is neglected and it is assumed to have one wheel aligned with each principal inertia axis.

This model formulation with DPM, LPM and LMM allows further extensions and different beams or plates may be attached to the same rigid body with minor modifications. Moreover, the exploitation of lumped models produces acceptable results with a lower computational load. The potential energy associated to the

deformable elements is computed from equations (2.48) and (2.49) according to the used flexible model formulation, as will be explained in the following of this section. The dynamical environment is represented in terms of all the external forces and perturbations, including the gravity gradients of the two primaries, which are included in the final equations of motion. The resulting dynamic equations are obtained with the aforementioned Lagrangian approach for quasi-coordinates, $\boldsymbol{\omega}$ and $\boldsymbol{\omega}_W$, and for flexible coordinates, $\mathbf{p}$ and $\mathbf{s}$:

$$\frac{d}{dt}\left(\frac{\partial \mathcal{L}}{\partial \boldsymbol{\omega}}\right) + [\boldsymbol{\omega}\times]\frac{\partial \mathcal{L}}{\partial \boldsymbol{\omega}} = \mathbf{T}_{env}, \tag{2.57}$$

$$\frac{d}{dt}\left(\frac{\partial \mathcal{L}}{\partial \boldsymbol{\omega}_W}\right) + [\boldsymbol{\omega}_W\times]\frac{\partial \mathcal{L}}{\partial \boldsymbol{\omega}_W} = \mathbf{T}_W, \tag{2.58}$$

$$\frac{d}{dt}\left(\frac{\partial \mathcal{L}}{\partial \dot{\mathbf{p}}}\right) - \frac{\partial \mathcal{L}}{\partial \mathbf{p}} = 0, \tag{2.59}$$

$$\frac{d}{dt}\left(\frac{\partial \mathcal{L}}{\partial \dot{\mathbf{s}}}\right) - \frac{\partial \mathcal{L}}{\partial \mathbf{s}} = 0, \tag{2.60}$$

where $\mathbf{T}_{env}$ is the external environmental torque and $\mathbf{T}_W$ is the torque applied to reaction wheels (i.e. the control torque).

The fully coupled equations of attitude-flexible motion are:

$$\begin{aligned}
&\mathbb{I}_{B_f}\cdot\dot{\boldsymbol{\omega}} + \mathbb{P}\cdot\ddot{\mathbf{p}} + \mathbb{S}\cdot\ddot{\mathbf{s}} + \mathbb{I}_W\cdot(\dot{\boldsymbol{\omega}} + \dot{\boldsymbol{\omega}}_W) = \\
&\qquad + \mathbf{T}_{env} - \boldsymbol{\omega}\times\left[\mathbb{I}_{B_f}\cdot\boldsymbol{\omega} + \mathbb{I}_W\cdot(\boldsymbol{\omega}+\boldsymbol{\omega}_W) + \mathbb{P}\cdot\dot{\mathbf{p}} + \mathbb{S}\cdot\dot{\mathbf{s}}\right] \\
&\qquad - \dot{\mathbb{I}}_{B_f}\cdot\boldsymbol{\omega} - \dot{\mathbb{P}}\cdot\dot{\mathbf{p}} - \dot{\mathbb{S}}\cdot\dot{\mathbf{s}},
\end{aligned} \tag{2.61}$$

$$\begin{aligned}
&\mathbb{M}_P\cdot\ddot{\mathbf{p}} + \mathbb{P}^{\mathrm{T}}\cdot\dot{\boldsymbol{\omega}} + \mathbf{C}_P\cdot\dot{\mathbf{p}} + \mathbf{K}_P\cdot\mathbf{p} = \\
&\qquad - \dot{\mathbb{M}}_P\cdot\dot{\mathbf{p}} - \dot{\mathbb{P}}^{\mathrm{T}}\cdot\boldsymbol{\omega} \\
&\qquad + \frac{1}{2}\boldsymbol{\omega}\cdot\frac{\partial \mathbb{I}_{B_f}}{\partial \mathbf{p}}\cdot\boldsymbol{\omega} + \frac{1}{2}\dot{\mathbf{p}}\cdot\frac{\partial \mathbb{M}_P}{\partial \mathbf{p}}\cdot\dot{\mathbf{p}} + \boldsymbol{\omega}\cdot\frac{\partial \mathbb{P}}{\partial \mathbf{p}}\cdot\dot{\mathbf{p}},
\end{aligned} \tag{2.62}$$

$$\begin{aligned}
&\mathbb{M}_S\cdot\ddot{\mathbf{s}} + \mathbb{S}^{\mathrm{T}}\cdot\dot{\boldsymbol{\omega}} + \mathbf{C}_S\cdot\dot{\mathbf{s}} + \mathbf{K}_S\cdot\mathbf{s} = \\
&\qquad - \dot{\mathbb{S}}^{\mathrm{T}}\cdot\dot{\boldsymbol{\omega}} + \frac{1}{2}\boldsymbol{\omega}\cdot\frac{\partial \mathbb{I}_{B_f}}{\partial \mathbf{s}}\cdot\boldsymbol{\omega} + \boldsymbol{\omega}\cdot\frac{\partial \mathbb{S}}{\partial \mathbf{s}}\cdot\dot{\mathbf{s}},
\end{aligned} \tag{2.63}$$

$$\mathbb{I}_W\cdot\left(\dot{\boldsymbol{\omega}} + \dot{\boldsymbol{\omega}}_W\right) = \mathbf{T}_W. \tag{2.64}$$

The matrices $\mathbf{C}_P$, $\mathbf{K}_P$, $\mathbf{C}_S$ and $\mathbf{K}_S$ are diagonal and, respectively, the damping and the stiffness matrices of the solar panels and of the fluid sloshing. The solar panels parameters such as mass, rigidity and damping are determined assuming a desired natural frequency of the vibration modes. The damping ratio is selected from typical damping coefficients values for flexible spacecraft appendages. For what concern the sloshing parameters, they are obtained from the models present in literature and discussed in section 2.5.2.

2.5.3.1 Linearised Flexible Dynamics

Linearised dynamics can be helpful during the design of guidance and control functions dealing with the attitude-flexible motion. Even if non-linear control of space systems with liquid sloshing and flexible appendages can be designed exploiting Lyapunov stability theory or other non-linear methods, the typical vibrational motion is small compared to the orbit-attitude one. Therefore, second order small quantities in equations (2.61) to (2.64) can be neglected for linearisation, allowing the development of GC functions exploiting linear control techniques.

A variable substitution method is exploited to linearise sloshing and flexible motions around their equilibrium conditions [40]:

$$\boldsymbol{\gamma} = \dot{\mathbf{p}} + \mathbb{M}_P^{-1}\,\mathbb{P}^{\mathrm{T}} \cdot \boldsymbol{\omega} \tag{2.65}$$

$$\boldsymbol{\varphi} = \dot{\mathbf{s}} + \mathbb{M}_S^{-1}\,\mathbb{S}^{\mathrm{T}} \cdot \boldsymbol{\omega}. \tag{2.66}$$

Thus, the linearised version of the attitude-flexible equations motion in equations (2.61) to (2.64) is expressed as:

$$\begin{aligned}\dot{\boldsymbol{\omega}} = \mathbb{I}_{B_l}^{-1}\Big\{ & \mathbf{T}_{env} - \mathbf{T}_W - \boldsymbol{\omega} \times \left[\mathbb{I}_{B_l} \cdot \boldsymbol{\omega} + \mathbb{I}_W \cdot (\boldsymbol{\omega} + \boldsymbol{\omega}_W) + \mathbb{P} \cdot \boldsymbol{\gamma} + \mathbb{S} \cdot \boldsymbol{\varphi}\right] \\ & + \mathbb{P}\,\mathbb{M}_P^{-1}\left[\mathbf{K}_P \cdot \mathbf{p} + \mathbf{C}_P \cdot \boldsymbol{\gamma} - \mathbf{C}_P \mathbb{M}_P^{-1}\,\mathbb{P}^{\mathrm{T}} \cdot \boldsymbol{\omega}\right] \\ & + \mathbb{S}\,\mathbb{M}_S^{-1}\left[\mathbf{K}_S \cdot \mathbf{s} + \mathbf{C}_S \cdot \boldsymbol{\varphi} - \mathbf{C}_S \mathbb{M}_S^{-1}\,\mathbb{S}^{\mathrm{T}} \cdot \boldsymbol{\omega}\right]\Big\},\end{aligned} \tag{2.67}$$

$$\dot{\mathbf{p}} = \boldsymbol{\gamma} - \mathbb{M}_P^{-1}\,\mathbb{P}^{\mathrm{T}} \cdot \boldsymbol{\omega}, \tag{2.68}$$

$$\dot{\boldsymbol{\gamma}} = -\mathbb{M}_P^{-1}\left[\mathbf{K}_P \cdot \mathbf{p} + \mathbf{C}_P \cdot \boldsymbol{\gamma} - \mathbf{C}_P \mathbb{M}_P^{-1}\,\mathbb{P}^{\mathrm{T}} \cdot \boldsymbol{\omega}\right], \tag{2.69}$$

$$\dot{\mathbf{s}} = \boldsymbol{\varphi} - \mathbb{M}_S^{-1}\,\mathbb{S}^{\mathrm{T}} \cdot \boldsymbol{\omega}, \tag{2.70}$$

$$\dot{\boldsymbol{\varphi}} = -\mathbb{M}_S^{-1}\left[\mathbf{K}_S \cdot \mathbf{s} + \mathbf{C}_S \cdot \boldsymbol{\varphi} - \mathbf{C}_S \mathbb{M}_S^{-1}\,\mathbb{S}^{\mathrm{T}} \cdot \boldsymbol{\omega}\right], \tag{2.71}$$

with

$$\mathbb{I}_{B_l} = \mathbb{I}_{B_f} - \mathbb{P} \cdot \mathbb{M}_P^{-1} \cdot \mathbb{P}^{\mathrm{T}} - \mathbb{S} \cdot \mathbb{M}_S^{-1} \cdot \mathbb{S}^{\mathrm{T}}. \tag{2.72}$$

The validation of the linear model in equations (2.67) to (2.71) has been carried out comparing its result with respect to the full non-linear model in equations (2.61) to (2.64). The linear model loses some of the cross-coupling between slosh and flexible appendages. Moreover, it tends to smooth the flexible-sloshing behaviour, but it is very reliable in the attitude output. The validation results are presented in chapter 6.

CHAPTER 3

Absolute Dynamics

> There are no eternal facts, as there are no absolute truths.
>
> — Friedrich Nietzsche

Absolute dynamics for large space structures in cislunar space is influenced by the n-body dynamical environment introduced in chapter 2. In particular, the orbit-attitude coupling is relevant to understand the complete 6DOF dynamics and exploit design techniques able to leverage the fully coupled motion of spacecraft, in order to achieve enhanced mission performances.

In this chapter, the absolute orbit-attitude dynamics in cislunar space is investigated with the purpose to highlight periodic motions that can be exploited to naturally stage large space structures in lunar vicinity, with lower difficulties and improved operational capabilities. In these regards, the complete space of orbit-attitude solutions is analysed and a brief survey of different orbital families is reported. The results obtained with different modelling approaches (e.g. CR3BP, ER3BP, FER4BP) are shown. Moreover, attitude stabilisation

methods (i.e. single and dual-spin stabilisation) are presented, compared and discussed.

Natural dynamics existing in the n-body dynamical environments is remarkably relevant to compute natural proximity operations trajectories and to understand the feasibility of efficient low-cost control methods for rendezvous missions. This part of the dissertation is also dedicated to discuss the methods to compute natural 6DOF trajectories, and the available results are critically analysed having in mind possible applications.

3.1 Orbit-Attitude Periodic Motion

The equations of motion presented in chapter 2 do not have an analytical solution space, as it is generally true for the dynamics propagated in a CR3BP environment. Therefore, equations (2.11), (2.12), (2.16) and (2.17) have to be numerically integrated to analyse the motion evolution of m_B. However, the solutions are extremely sensitive to the set of initial conditions and a numerical targeting algorithm is needed, if one wants to highlight a particular behaviour or obtain a certain final condition. A very common method to find specific solutions in non-Keplerian environments is employed in this research, following the idea introduced in the last decades of the twentieth century and presented also in the work of Guzzetti [25, 27]. In fact, a multiple shooting scheme, together with a multi-variable Newton-Raphson solver, is exploited to find orbit-attitude periodic solutions.

3.1.1 Differential Correction Method

The idea of this numerical method is founded on the possibility to propagate the dynamics in the vicinity of reference solution. In fact, considering a generic non-linear set of equations of motion and a reference solution, $\bar{\mathbf{x}}$, it is possible to perturb the reference initial state vector, $\bar{\mathbf{x}}_0$, by a small quantity, $\delta\mathbf{x}_0$. Then, the linear evaluation for the behaviour of the variation, $\delta\mathbf{x} = \mathbf{x}(\bar{\mathbf{x}}_0 + \delta\mathbf{x}_0, t) - \bar{\mathbf{x}}(\bar{\mathbf{x}}_0, t)$, relative to the reference motion can be obtained using the Jacobian of the original non-linear system, $J(t) = \frac{\partial \mathbf{f}}{\partial \mathbf{x}}$, where the state vector is composed by: $\mathbf{x} = [x; y; z; v_x; v_y; v_z; q_1; q_2; q_3; w_1; w_2; w_3]$. Note that only three components of the quaternion have to be defined to completely define the system $\mathbf{f}$. In fact, the first-order variational equation can be written as:

$$\delta\dot{\mathbf{x}} = J(t)\delta\mathbf{x}. \tag{3.1}$$

At this point, the effect of variations in the initial state on $\delta\mathbf{x}$ can expressed in a linear sense as:

$$\delta\mathbf{x} = \left(\frac{\partial\mathbf{x}}{\partial\mathbf{x}_0}\right)\delta\mathbf{x}_0. \tag{3.2}$$

The linear differential relationship between initial and final state, $\frac{\partial\mathbf{x}}{\partial\mathbf{x}_0}$, which is known as State Transition Matrix (STM) and is denoted as $\Phi(t,t_0)$, can be related to a first-order differential equation governing its evolution. In fact, from equations (3.1) and (3.2) after some manipulations, it is possible to write:

$$\dot{\Phi}(t,t_0) = J(t)\Phi(t,t_0), \tag{3.3}$$

where the elements of the matrix $\Phi(t,t_0)$ represent the partial derivatives of the state, $\mathbf{x}$, at time t with respect to the initial state, $\mathbf{x}_0$, at time t_0 that are integrated simultaneously with the equations of motion to produce the STM at any time along the integrated trajectory relative to a reference solution. Obviously, a variation in the initial state vector can only influence itself if the equations are not integrated and just evaluated at $t = t_0$. Hence, the initial condition for the STM in equation (3.3), is the identity matrix:

$$\Phi(t_0,t_0) = \mathcal{I}. \tag{3.4}$$

In order to integrate equation (3.3), the time-variant Jacobian of the system must be computed. It contains the partial derivatives of the system $\mathbf{f}$ with respect to the state vector $\mathbf{x}$:

$$J(t) = \begin{bmatrix} \frac{\partial\mathbf{f}_x}{\partial\mathbf{x}_B} & \frac{\partial\mathbf{f}_x}{\partial\mathbf{v}_B} & \frac{\partial\mathbf{f}_x}{\partial{}^I\mathbf{q}_B^B} & \frac{\partial\mathbf{f}_x}{\partial{}^I\boldsymbol{\omega}_B^B} \\ \frac{\partial\mathbf{f}_v}{\partial\mathbf{x}_B} & \frac{\partial\mathbf{f}_v}{\partial\mathbf{v}_B} & \frac{\partial\mathbf{f}_v}{\partial{}^I\mathbf{q}_B^B} & \frac{\partial\mathbf{f}_v}{\partial{}^I\boldsymbol{\omega}_B^B} \\ \frac{\partial\mathbf{f}_q}{\partial\mathbf{x}_B} & \frac{\partial\mathbf{f}_q}{\partial\mathbf{v}_B} & \frac{\partial\mathbf{f}_q}{\partial{}^I\mathbf{q}_B^B} & \frac{\partial\mathbf{f}_q}{\partial{}^I\boldsymbol{\omega}_B^B} \\ \frac{\partial\mathbf{f}_\omega}{\partial\mathbf{x}_B} & \frac{\partial\mathbf{f}_\omega}{\partial\mathbf{v}_B} & \frac{\partial\mathbf{f}_\omega}{\partial{}^I\mathbf{q}_B^B} & \frac{\partial\mathbf{f}_\omega}{\partial{}^I\boldsymbol{\omega}_B^B} \end{bmatrix}, \tag{3.5}$$

where $\mathbf{x}_B$, $\mathbf{v}_B$, ${}^I\mathbf{q}_B^B$ and ${}^I\boldsymbol{\omega}_B^B$ are the elements of the state vector $\mathbf{x}$, respectively related with the orbital position, the orbital velocity, the attitude parameters and the angular velocity of the body m_B. It must be noted that for the coupled orbit-attitude dynamics without perturbations $\frac{\partial\mathbf{f}_x}{\partial\mathbf{x}_B}$, $\frac{\partial\mathbf{f}_x}{\partial{}^I\mathbf{q}_B^B}$, $\frac{\partial\mathbf{f}_x}{\partial{}^I\boldsymbol{\omega}_B^B}$, $\frac{\partial\mathbf{f}_v}{\partial{}^I\mathbf{q}_B^B}$, $\frac{\partial\mathbf{f}_v}{\partial{}^I\boldsymbol{\omega}_B^B}$, $\frac{\partial\mathbf{f}_q}{\partial\mathbf{x}_B}$, $\frac{\partial\mathbf{f}_q}{\partial\mathbf{v}_B}$ and $\frac{\partial\mathbf{f}_\omega}{\partial\mathbf{v}_B}$ are equal to null matrices. However, when the previously introduced perturbations are included, the orbital motion is directly influenced by the orientation of the body and the partial $\frac{\partial\mathbf{f}_v}{\partial{}^I\mathbf{q}_B^B}$ is not equal to zero anymore.

The coupled orbit-attitude motion is described by 13 equations of motion contained in the system $\mathbf{f}$. Still, having in mind the constraint equation (2.15), only

12 equations are actually independent, because one of the kinematic relations in equation (2.16) is not necessary to completely describe the dynamics of the system: the fourth component of the quaternion vector can be derived from the Euler parameters constraint. Anyway, the modification of the system of differential equations $\mathbf{f}$ is not practical and it is maintained as described in section 2.3, but the Jacobian and the STM are reduced to a 12 by 12 matrix, relating only the independent variables. This is done expressing the partials of the Jacobian relative to the quaternions as:

$$\frac{\mathrm{d}\mathbf{f}_i}{\mathrm{d}q_j}(q_1, q_2, q_3, q_4(q_1, q_2, q_3)) = \frac{\partial \mathbf{f}_i}{\partial q_j} - \frac{q_j}{q_4}\frac{\partial \mathbf{f}_i}{\partial q_4}, \tag{3.6}$$

which can be derived from the variational expression of equation (2.15). Therefore, considering the 13 equations of motion and the 12×12 linear differential relationships between initial and final state, there are 157 differential equations to be integrated in order to find orbit-attitude periodic solutions.

The Jacobian in equation (3.5) has been derived analytically for the coupled orbit-attitude dynamics with the CR3BP or BC4BP modelling approaches. The analytical expression of the partials has been obtained also for the variation in the gravitational attraction due to the finite dimension of the body. The effort in deriving such analytical expressions is justified by a relevant reduction in the computational cost of the algorithms that exploits that matrix. When the ephemeris models are used, the terms in the Jacobian are instead computed numerically. In practice, when terms related with non-analytic formulations are included, the State Transition Matrix is numerically obtained applying a small perturbation with respect to a reference initial condition, then the finite difference between the reference and the perturbed final state is available and the terms in the matrix can be numerically computed. This operation is done for each partial and the complete STM is finally assembled, even though it is not the real State Transition Matrix but just a numerical approximation. To assess the accuracy of this numerical STM, the result is continuously matched with the analytical STM for circular approximations.

With the availability of the State Transition Matrix, an algorithm able to find periodic solutions in both the orbital and attitude state can be implemented. In fact, it is possible to obtain a periodic motion in the rotating reference frame by iteratively correcting a reference path, but a good initial guess is needed. In this work, the targeting scheme is based on a multiple shooting strategy, which is very common in modern astrodynamics for the computation of periodic orbits. The idea is to find a solution that is continuous between the final and initial states in both the translational and rotational components, which is a typical two-point boundary value problem. However, the presented approach solves many Initial Value Problems where the different initial states are iteratively corrected, with a Newton approach, until the constraints at given patch points are satisfied, within

a certain tolerance. In practice, the trajectory is discretised in N patch points, which are associated with $N-1$ arcs. In the orbit-attitude coupled problem, each i-th patch point is the 12-dimensional state vector, $\mathbf{x}_i = [\mathbf{x}_{B_i}; \mathbf{v}_{B_i}; {}^I\mathbf{q}^B_{B_i}; {}^I\boldsymbol{\omega}^B_{B_i}]$. The first and last patch points are respectively the initial and final conditions. Each arc has the same time of flight, T_a, and therefore the complete solution has time of flight $T_t = (N-1)T_a$.

The problem has a free variables vector that includes the state vector in each patch point, plus the time of flight of a single arc:

$$\boldsymbol{\nu} = [\mathbf{x}_1; \ldots; \mathbf{x}_i; \ldots; \mathbf{x}_N; T_a]. \tag{3.7}$$

Hence the dimension of the problem is $n = 12N + 1$ and the free variables vector has to be corrected to satisfy a set of m_B given constraints, collected in the vector $\boldsymbol{\mu}$. The periodic solution is identified as a set of $\bar{\boldsymbol{\nu}}$ that satisfies the constraint equations:

$$\boldsymbol{\mu}(\bar{\boldsymbol{\nu}}) = [\mu_1(\bar{\boldsymbol{\nu}}); \ldots; \mu_m(\bar{\boldsymbol{\nu}})] = \mathbf{0}. \tag{3.8}$$

This is done expanding the constraint function $\boldsymbol{\mu}$ about an initial guess $\boldsymbol{\nu}_0$ in a Taylor series to the first order:

$$\boldsymbol{\mu}(\boldsymbol{\nu}) \simeq \boldsymbol{\mu}(\boldsymbol{\nu}_0) + J_\mu(\boldsymbol{\nu}_0)(\boldsymbol{\nu} - \boldsymbol{\nu}_0), \tag{3.9}$$

where J_μ is the Jacobian of the constraint function with respect to the free variables ν. Equation (3.9) is set equal to zero and iteratively solved for $\bar{\boldsymbol{\nu}}$.

Usually there are more free variables than constraint equations and so a minimum norm solution is exploited to produce the updated free variables vector. In fact, at the k-th iteration, the new solution is found as:

$$\boldsymbol{\nu}_{k+1} = \boldsymbol{\nu}_k - J_\mu(\boldsymbol{\nu}_k)^{\mathrm{T}} \left[J_\mu(\boldsymbol{\nu}_k) J_\mu(\boldsymbol{\nu}_k)^{\mathrm{T}}\right]^{-1} \boldsymbol{\mu}(\boldsymbol{\nu_k}). \tag{3.10}$$

This equation is recursively applied to update the free variables vector. When the equation (3.8) is solved within a certain numerical tolerance, the algorithm is stopped and the current solution $\boldsymbol{\nu}_k$ is the desired periodic solution $\bar{\boldsymbol{\nu}}$.

In this research, the constraint vector $\boldsymbol{\mu}$ is strongly related with the desired coupled orbit-attitude behaviour. The multiple shooting algorithm iteratively finds a solution that is periodic in both attitude and orbital state, has internal continuity at patch points between the different arcs and is sufficiently close to the desired initial guess. The periodicity is sought in the rotating synodic reference, but note that the attitude dynamics is expressed in the inertial frame. Hence, the quaternion ${}^I\mathbf{q}^B$ has to be transformed in the synodic reference, ${}^S\mathbf{q}^B$, prior to enforce periodicity. There is no need to transform the angular velocity of the body m_B in the synodic reference, because the difference between the angular velocity measured in the inertial frame and in the rotating one is just a

constant offset, which is not an issue for what concern periodicity: the periodicity constraints for the angular velocity can be expressed in both rotating and inertial frames. The orbital states do not need any addition modification since they are already expressed in S. Moreover, only 5 translational states have to be periodic; the remaining one is implicitly continuous because of the existence of an integral of motion, which is known as Jacobi constant. The presented coupled orbit-attitude dynamical model preserves this constant and the whole algorithm is continuously assessed checking its value. One additional constraint is needed to fix a coordinate in the trajectory and phase all the orbits of a given family. Therefore, the constraint vector which is used in the algorithm is:

$$\boldsymbol{\mu}(\boldsymbol{\nu}) = \begin{bmatrix} (\mathbf{x}_1)_{T_a} - \mathbf{x}_2 \\ \vdots \\ (\mathbf{x}_{N-1})_{T_a} - \mathbf{x}_N \\ \\ x_N - x_1 \\ z_N - z_1 \\ v_{x_N} - v_{x_1} \\ v_{y_N} - v_{y_1} \\ v_{z_N} - v_{z_1} \\ \\ y_1 \\ \\ {}^{S}\mathbf{q}^{B}_{B_N} - {}^{S}\mathbf{q}^{B}_{B_1} \\ \\ {}^{I}\boldsymbol{\omega}^{B}_{B_N} - {}^{I}\boldsymbol{\omega}^{B}_{B_1} \end{bmatrix}, \tag{3.11}$$

where the continuity at patch points, the periodicity of 5 orbital states, the phasing of the family and the periodicity of attitude states are respectively listed. The result is a total of $m = 12N$ constraint equations composing the vector $\boldsymbol{\mu}$, which has to be nulled to find a periodic orbit-attitude solution.

3.1.2 Continuation Method

The differential corrector method, presented in section 3.1.1, is used to obtain a single periodic solution corresponding to an individual trajectory, which satisfies a particular problem defined via the constraint equations in equation (3.8), such as periodic orbit-attitude LPOs discussed in this dissertation. Once a converged solution is found, it can be used to generate a dynamical family of other periodic

orbits, which are useful to explore the whole subspace of solutions existing in the interested dynamical environment.

The techniques available to obtain families of periodic motions are typically named numerical continuation methods. These continuation processes are needed to create new initial guesses, which can be obtained just modifying one parameter to the existing periodic solution or expanding in the direction of the null space of a reference Jacobian matrix, $J_\mu(\bar{\boldsymbol{\nu}})$. Both methods are well-known continuation schemes; the former is called single-parameter continuation, while the latter is the pseudo-arclength continuation, which is used in this research.

The pseudo-arclength continuation scheme is intended to continue a family of periodic orbit-attitude motions in the direction tangent to their exact nonlinear variations along the space of solutions [74]. The tangential direction is evaluated from the null space of the Jacobian matrix of the last converged solution, $\bar{\boldsymbol{\nu}}$:

$$\boldsymbol{\kappa} = \ker(J_\mu(\bar{\boldsymbol{\nu}})). \tag{3.12}$$

The tangential direction, $\boldsymbol{\kappa}$, has the same dimensions of the free variable of the problem, $\boldsymbol{\nu}$. Thus, the new member of the family, $\boldsymbol{\nu}^*$, is shifted along $\boldsymbol{\kappa}$ from the last reference solution, $\bar{\boldsymbol{\nu}}$, with an arclength step size ds. This condition is obtained appending an additional equation to the constraint vector equation (3.11), defining an augmented constraint function:

$$\boldsymbol{\mu^*}\left(\boldsymbol{\nu}^*\right) = \begin{bmatrix} \boldsymbol{\mu}\left(\boldsymbol{\nu}^*\right) \\ (\boldsymbol{\nu}^* - \bar{\boldsymbol{\nu}}) \cdot \boldsymbol{\kappa} - ds \end{bmatrix}. \tag{3.13}$$

The derivative of $\boldsymbol{\mu^*}\left(\boldsymbol{\nu}^*\right)$ yields to an augmented Jacobian matrix:

$$J_{\mu^*} = \begin{bmatrix} J_\mu \\ \boldsymbol{\kappa}^{\mathrm{T}} \end{bmatrix} \tag{3.14}$$

The new member of the family is obtained via simple iterative update process:

$$\boldsymbol{\nu}^*_{k+1} = \boldsymbol{\nu}^*_k - J_{\mu^*}(\boldsymbol{\nu}^*_k)^{-1}\boldsymbol{\mu^*}(\boldsymbol{\nu}^*_k) \tag{3.15}$$

The advantage of the pseudo-arclength continuation with respect to the single-parameter continuation is that it does not require a previous knowledge of the user about the family evolution. This strategy is reasonably robust and exploits a continuation parameter which is neutral with respect to the problem definition. Moreover, it generally avoids possible jumps to other families during the continuation process.

3.1.3 Initial Guess Generation

The search for periodic solutions needs an initial guess that is sufficiently close to the desired motion. Existing literature presents several methods able to

provide approximation of the desired coupled dynamics, but many of them tries to find the geometry of the spacecraft that makes periodic a certain set of initial conditions. In this research a different method has been developed: starting from a given mass distribution of the body and, therefore, fixing its inertia parameters, the initial guess is generated with two distinct global optimisation techniques, which are applied one after the other. In this way, it is possible to find a certain periodic orbit-attitude solution for a given mass distribution, instead of studying which is the body that can have a periodic motion on given orbit-attitude dynamics. Moreover, this method is faster and less demanding in computational resources than a standard search of periodic behaviours in a Poincarè map, requiring typically less than 1 min on a standard personal computer. The mass distribution of the body can be mathematically defined from the moments of inertia of the spacecraft or a combination of them. In this research, the ratio between the maximum moment of inertia and the minimum one is used.

The developed method begins with the definition of the inertia properties of the body, then the family and the period of the non-Keplerian orbit is introduced to identify the initial conditions for periodic orbital dynamics. At this point, the algorithm asks for the angular rate and the initial orientation of the attitude dynamics; these values do not have to generate a periodic motion, but they bind the inspection in a certain region of the attitude subspace. This step is fundamental to drive the algorithm in the desired direction and a bit of knowledge of the considered dynamical environment is necessary in order to have a fast convergence of the method. Next, the search for the initial guess is started, first with a genetic algorithm that optimises the orbit-attitude initial conditions, then a pattern search algorithm refines the output of the genetic optimisation. The goal of the two optimisation techniques is to reduce the sum of the difference in all the orbit-attitude states, $\mathbf{x}$, at the starting point and after one period: the periodicity error. The search for the initial guess is stopped when the periodicity error is below a given tolerance, which is low enough to allow the convergence of the multiple shooting Newton-Raphson solver.

The variables of the genetic algorithm are the 6 initial attitude states, while the initial orbital states are fixed and related to a given periodic orbit. The population is composed by 150 individuals, and it is initially generated with uniform distribution around a given initial guess. This user defined starting point, together with the bounds for the variables, confines the search space within the attitude subspace. Between two consecutive generations 5 best individuals are maintained and the crossover fraction of the remaining individuals is 70%. The maximum number of allowed generations is 175 and the stopping criteria are met when the periodicity error goes below 5×10^{-2} nd. Then, a pattern search algorithm is started from the best solution found by the genetic algorithm, which has only to be refined. In fact, the tolerances for the search are very tight

and the feasible poll points remains in the vicinity of the output of the previous optimisation step. This further optimisation step usually reduces the periodicity error between 1×10^{-2} nd and 1×10^{-3} nd, allowing a very fast convergence of the multiple shooting algorithm. On a 2.5 GHz quad core processor that runs the optimisation algorithms in parallel, the initial guess is usually found in about 20 s, if good starting point and bounds are provided. The search needs few minutes in the worst conditions, which are caused by highly sensitive orbital families (e.g. NRHO) and random starting point without bounds. Then, on the same processor, the multiple shooting algorithm usually runs in about 10 s to reduce the periodicity error down to 1×10^{-10} nd.

The developed method is based on global optimisation techniques to search for an initial guess with heuristic strategies. The focus has not been directed on a particular optimisation technique and the genetic algorithm has just proven to work well. No comparison with other heuristic optimisation techniques has been carried out. In the same way, the refinement step accomplished by the pattern search method has just resulted in a faster convergence of the Newton-Raphson correction scheme. Further investigations might be of interest to compare different optimisation methods in order to find the best ones in terms of computational speed and quality of the initial guess.

In figure 3.1 an initial guess is confronted with the relative periodic orbit-attitude solution for an example Halo orbit. From the picture, it is possible to understand that the initial guess solution must be very close to the periodic one, in order to have a good and fast convergence of the algorithm. Moreover, focusing on the coupled orbit-attitude periodic dynamics, it is evident that the passage close to the Moon generates a relevant angular acceleration, which is obviously due to the intense gravity gradient action exerted by the second primary on the body m_B. The orbit reported in figure 3.1a is a L1 Halo with period of 10.5 d; the distribution of mass for m_B is the one of a disk-like body with ratio between the maximum moment of inertia (I_{max}) and the minimum one (I_{min}) equal to 1.5. The initial conditions for the genetic algorithm are set to find an initial guess close to a simple spin dynamics around the body axis $\hat{\mathbf{b}}_3$, with the body reference frame and the inertial frame aligned at $t = 0$. The obtained initial guess is shown in figures 3.1a, 3.1c and 3.1e, while the periodic solution, output of the multiple shooting Newton-Raphson correction algorithm, is reported in figures 3.1b, 3.1d and 3.1f. The quaternions are shown as computed in the rotating synodic reference and, in order to simplify the notation, the quaternion ${}^{S}\mathbf{q}^{B}$ has been denoted as $\mathbf{q}_r$ in the plots. From figure 3.1d, it is possible to see that in the reported dynamics, the body m_B is just librating and performs no overall rotation in S. The results shown in figure 3.1 have been obtained in a CR3BP model without the additional perturbing terms in the dynamical model. In table 3.1 the numerical values of the quaternion shown in figure 3.1d

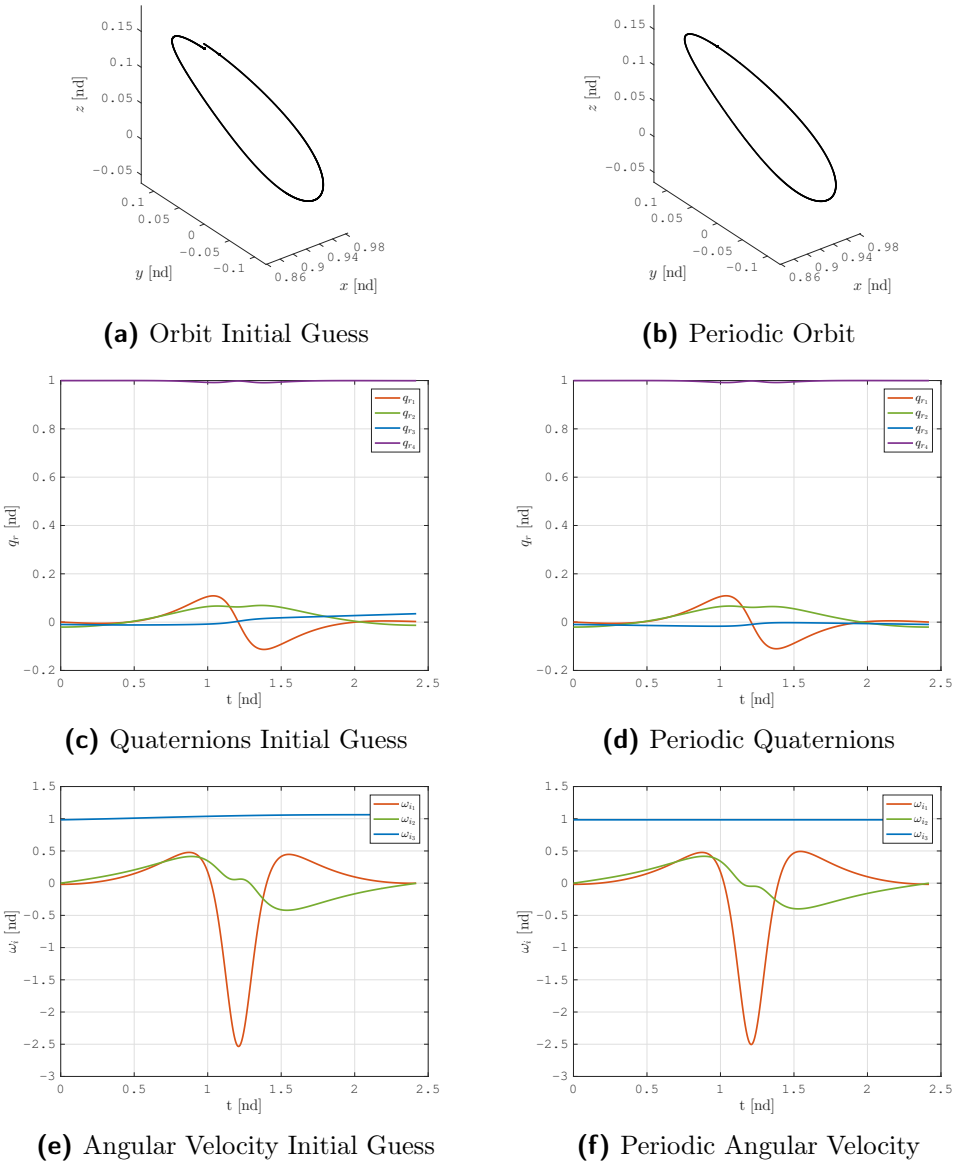

(a) Orbit Initial Guess

(b) Periodic Orbit

(c) Quaternions Initial Guess

(d) Periodic Quaternions

(e) Angular Velocity Initial Guess

(f) Periodic Angular Velocity

Figure 3.1: Initial guess and periodic orbit-attitude dynamics. (EML1 Halo Orbit: $T_t = 10.5\,\mathrm{d}$ - $I_{max}/I_{min} = 1.5$).

are reported for $t = 0$, $t = T_t/2$ and $t = T_t$, in order to accurately asses the periodicity of the solution and the fulfilment of the constraint equation (2.15).

Table 3.1: Numerical Values of Periodic Orbit-Attitude Dynamics Quaternions. (cf. figure 3.1d).

	$\mathbf{q}_r$
$t = 0$	$[+0.000197, -0.020475, -0.009622, +0.999744]$
$t = T_t/2$	$[-0.000797, +0.061167, -0.009594, +0.998081]$
$t = T_t$	$[+0.000197, -0.020475, -0.009622, +0.999744]$

3.1.4 Periodic Solutions

Many other periodic solutions, for any kind of planar and spatial family of orbits in the n-body environment, were generated exploiting the presented multiple-shooting algorithm applied to the coupled orbit-attitude model.

Figure 3.2 shows the family of periodic orbit-attitude dynamics in L1 Halo Orbits generated from the periodic solution in figure 3.1. The pseudo-arclength continuation develops the Halo family decreasing the distance of the orbits from the Moon, looking at figure 3.2a from the dark blue lines to the yellow one. The continuation would have been possible in the other direction changing the sign of the step size, ds. The reduced distance with respect to the moon is associated to a shorter orbital period and to a larger gravity gradient acceleration due to the close perilune passage, as evident in figures 3.2b and 3.2c going from darker to lighter colours. The quaternion subspace in figure 3.2d is representative of the attitude motion associated with the family without overall rotation during the orbital period (i.e. librating attitude motion).

Figure 3.3 shows different periodic orbit-attitude dynamics in L1 Lyapunov Orbits, which were found to be remarkably sensitive to out-of-plane perturbations. In fact, the perturbations due to the Sun have been neglected and the orbit-attitude motion has been constrained on the x-y plane. The investigations performed for Sun-perturbed Lyapunov orbits, within the employed ephemeris model, determined that an orbit-attitude control action is necessary in real applications. However, the presented naturally periodic solutions reports three dissimilar rotational motions for a disk-like spacecraft, with moment of inertia ratio equal to 5. They are related to Lyapunov Orbits with period equal to 12.1 d, 14.1 d and 18.88 d. The attitude dynamics analysed in the quaternion subspace allows to point out and uniquely characterise the various dynamical families, which have different behaviours according to the orbital period and, therefore, the energy of the orbit. These results can be explained, as already highlighted by Guzzetti [26], considering the dynamical bifurcations and the changes in the stability of the motion along the family. With respect to the previous studies, the presence of the second order term of the gravity exerted on a finite dimension body barely modifies the results of the current research

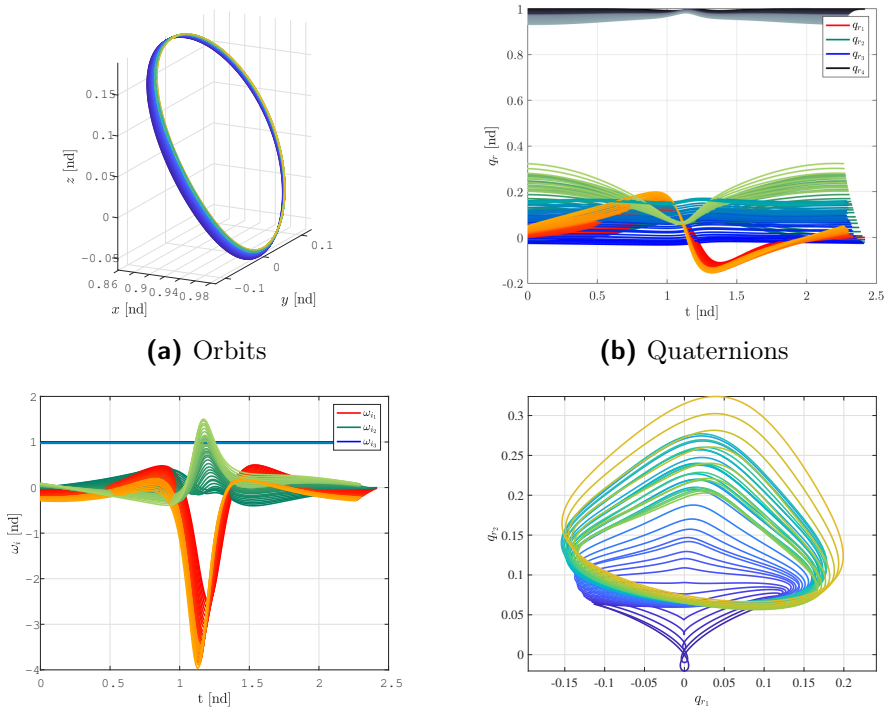

(a) Orbits **(b)** Quaternions

(c) Angular velocities **(d)** Quaternion subspace

Figure 3.2: Family of Halo orbit-attitude periodic dynamics. (EML1 Halo Orbits: $I_{max}/I_{min} = 1.5$).

work, as evident in figure 3.4. In fact, analysing the results for a spacecraft with different sizes (e.g. from 0m to 100m), the differences in the periodic attitude are minimal, as expected from the magnitude of the related acceleration discussed in section 2.3.1.

The previous results identify a strong connection between the size of the orbit and the associated periodic attitude motion, which is quite typical for this class of problems. Looking at the differences between the three different attitude families in figures 3.3b to 3.3d, it is evident that for a certain energy level of a specific orbital motion there exists a single family of attitude solutions associated to a set of inertia properties. In fact, in the vicinity of each orbit shown in figure 3.3a, the allowed periodic rotational solutions share similar dynamical properties, such as the stability level or the quaternion subspace shape. Obviously, a minor change in the orbit would result in a small variation in the rotational motion. However, if the energy gap between two similar orbits is large enough to move across a bifurcation point, the attitude dynamics could have the features of distinct dynamical families. This example is representative of the coupling between orbital and attitude dynamics in non-Keplerian environment,

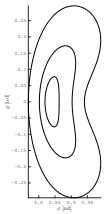

(a) Lyapunov orbit

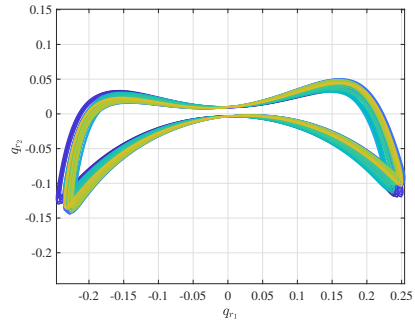

(b) Quaternions - Family 1

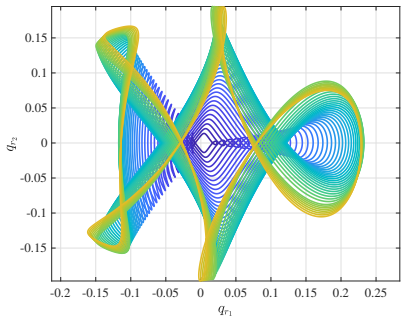

(c) Quaternions - Family 2

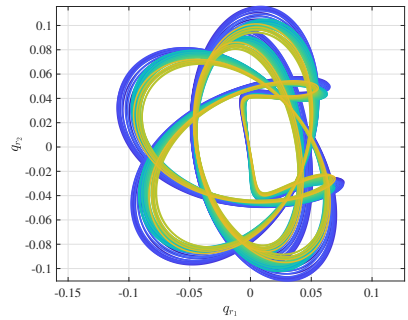

(d) Quaternions - Family 3

Figure 3.3: Family of Lyapunov orbit-attitude periodic dynamics - Quaternion subspace, components 1 and 2. (EML1 Lyapunov Orbits: $T_{t_1} \simeq 12\,\mathrm{d}$, $T_{t_2} \simeq 14\,\mathrm{d}$ and $T_{t_3} \simeq 19\,\mathrm{d}$ - $I_{max}/I_{min} = 5$).

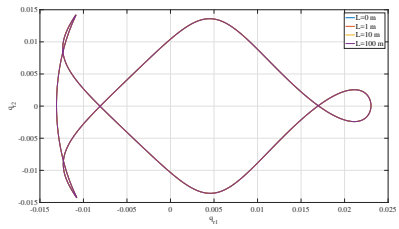

(a) Quaternions subspace

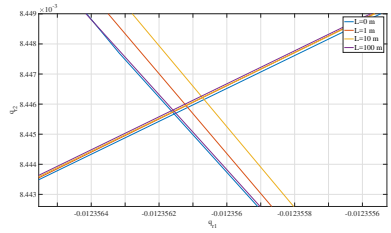

(b) Enlarged detail

Figure 3.4: Effect of second order term of the gravity exerted on a finite dimension body. (cf. EML1 Lyapunov Orbits: $T_t = 13.8\,\mathrm{d}$ in figure 3.3c).

but further investigation is warranted to understand the weight of this dynamical pairing.

An additional family of very important and useful planar orbits is the DRO family. DRO are remarkably stable in the long-term and can be reached at a reasonable

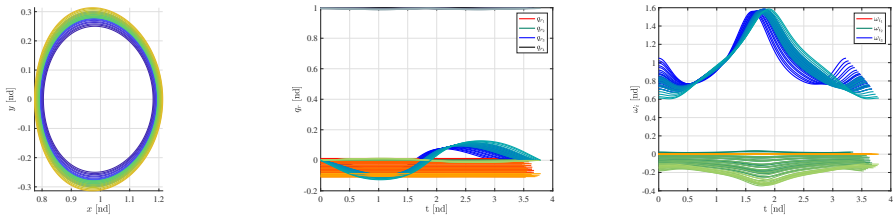

(a) Orbits **(b)** Quaternions **(c)** Angular velocities

Figure 3.5: Family of DRO orbit-attitude periodic dynamics. (EM DRO: $T_t \simeq 15\,\mathrm{d}$ - $I_{max}/I_{min} = 2.5$).

cost. For these reasons, they may be exploited for many interesting applications around the Moon. An example of DRO family is reported in figure 3.5 for a rod like mass distribution with ratio between maximum and minimum inertia moments equal to 2.5.

The different elements of the family share the same orbit, which has a period of 14 d, but they differ for the number of overall rotations of m_B in the synodic frame. In fact, the attitude dynamics in figure 3.6b shows 2 overall clockwise rotations in S, while figure 3.6c and figure 3.6d perform just one rotation per orbital period, respectively clockwise and counterclockwise. A particular scenario is represented by figure 3.6a, where the body is not spinning in S, but it is just librating about the equilibrium condition. Numerous periodic solutions of a single dynamical family with diverse spinning conditions open to a wide set of operational opportunities. In fact, the distinct attitude alternatives allow to exploit a single orbit, which may be constrained from several requirements coming from the mission design, for various operational phases. For example, the librating solution could facilitate the telecommunication subsystem, while the fast spinning one can be exploited to reduce the attitude station-keeping effort, since a spinning platform behaves better, with respect to the librating configuration, in terms of perturbations counteracting.

3.2 Optimal Staging Location for a Cislunar Space Station: NRHO

As already discussed in chapter 1, LPOs seem the most promising staging locations for a cislunar space station [2]. In particular, EML NRHOs have the most interesting properties for such an application, thanks to their continuous line of sight coverage for communications and the good Earth accessibility with existing transportation systems. Moreover, they guarantee significant ease of access from the Moon surface. The NRHO family derives as a section of the Halo family [16]; as the orbits get closer to the Moon, their shape tends to elongate, hence the name of the sub-family. They are classified in North and

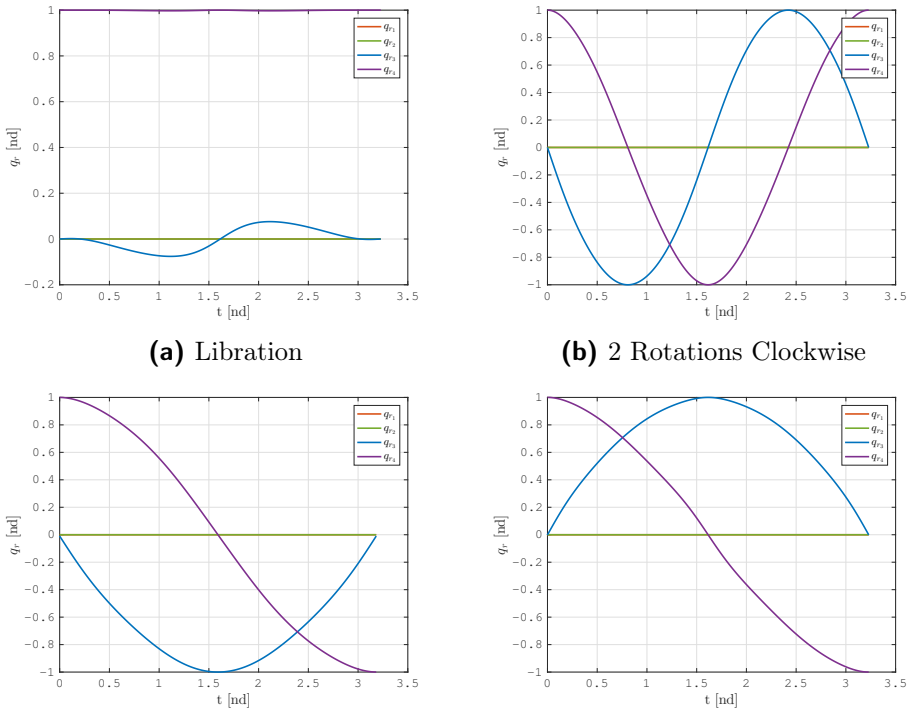

(a) Libration

(b) 2 Rotations Clockwise

(c) 1 Rotation Clockwise

(d) 1 Rotation Counterclockwise

Figure 3.6: Family of DRO orbit-attitude periodic dynamics, different spinning velocities - Quaternions with respect to time. (EM DRO: $T_t = 14\,\mathrm{d}$ - $I_{max}/I_{min} = 2.5$).

South NRHOs, according to the position of the apolune with respect to the Moon surface. Note that, being the orbits non-Keplerian, the definition of apolune does not correspond to the classic Keplerian one. International literature vastly adopts, nevertheless, such term, to define the point farthest from the Moon. This nomenclature is selected for this dissertation as well; conversely, the already mentioned perilune denotes the point closest to the Moon at every revolution.

NRHOs belongs to the collinear Lagrangian points $L1$ or $L2$. $L1$ NRHOs are obtained through continuation of the $L1$ Halo family, approaching the Moon,

Table 3.2: NRHO Families Characterization.

	$L1$ Family	$L2$ Family
Orbit Period [d]	$7.8 - 8.5$	$6 - 7.5$
Perilune Altitude [km]	$10 - 2500$	$10 - 3000$
Apolune Altitude [km]	$84000 - 95000$	$66000 - 75000$

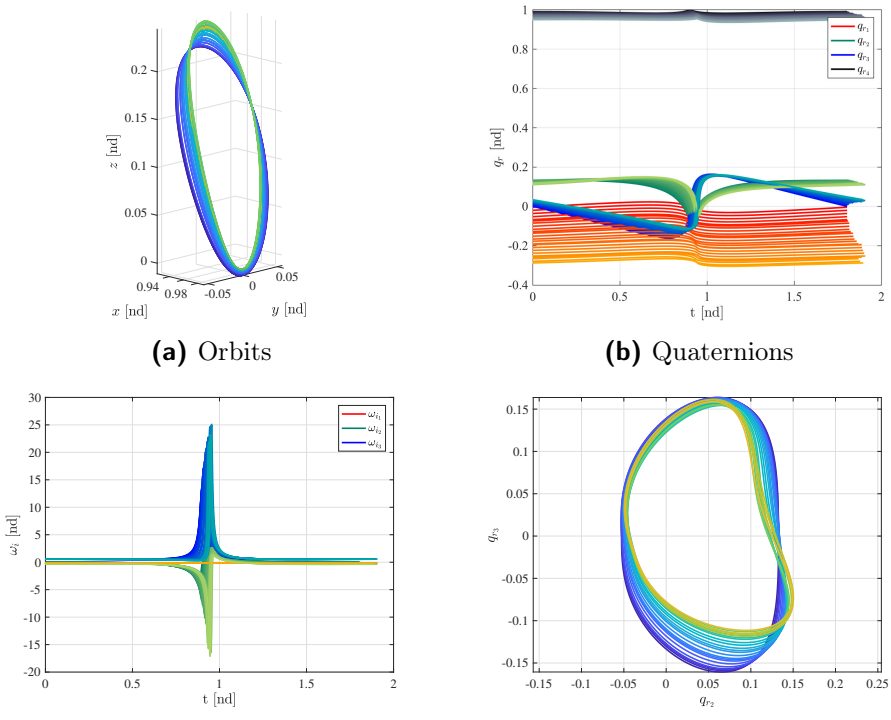

(a) Orbits **(b)** Quaternions

(c) Angular Velocities **(d)** Quaternion Subspace

Figure 3.7: Family of NRHO orbit-attitude periodic dynamics. (EML1 NRHO: $I_{max}/I_{min} = 1.5$).

while $L2$ NRHOs are obviously obtained from $L2$ Halo orbits. A peculiar behaviour is observed on the orbital period trend: as the $L1$ family approaches the Moon, from the Lagrangian point, the period decreases, reaches a value of about 7.8 d, and then increases again. This is not observed in the $L2$ family, whose period decreases roughly linearly getting closer to the Moon. This aspect offers some advantages in trajectory definition and operational scheduling, providing a rough correlation between orbit period, amplitude, and energy. Table 3.2 summarises the most important features of the NRHO family.

An example family of periodic orbit-attitude solutions is shown in figure 3.7 for a NRHO. In this case, the period of the orbit is around 8.5 d and the mass distribution is the same that has been used to generate the Halos of figures 3.1 and 3.2. This case is particularly representative for all the NRHO, since it shows the huge angular acceleration that exists during the passage very close to the Moon. Here, the gravity gradient influence of the second primary, already noted for the Halo periodic solution, is extremely emphasised and determines this typical behaviour for NRHOs, which may pose problems for the structural integrity of a spacecraft orbiting in this class of orbits. A real extended space

structure may experience difficulties in bearing the abrupt angular velocity variation shown in figure 3.7c. Moreover, the attitude stability for this kind of periodic orbit-attitude dynamics is poor and particular counter-measurements must be applied, as will be discussed in section 3.5.

From figure 3.7, it is evident the strong relations between NRHO and normal Halo orbits: they belong to the same dynamical family, even if the dynamics on the NRHOs is peculiar because of the extremely low perilune passage. As already noted, the orbit-attitude motion experiences a very fast dynamics at the NRHO's perilune, with a large acceleration and successive deceleration. Such passage may be interpreted as a quasi-gravity assist with the Moon. From the inertial point of view, this perilune passage exploits the gravity of the Moon to produce the correct curvature, in order to continuously follow the primary body in the inertial space. Hence, NRHOs have a large difference in velocities and accelerations between perilune and apolune.

Any orbit-attitude family is dependent by the inertia properties of the considered spacecraft; the periodic solutions are extremely sensitive to the changes in the inertia moments, and the attitude dynamics stability is also dependent on the shape of the orbiting body. For example, a rod-like spacecraft is more sensitive to perturbations and initial errors with respect to a disk-like one, and this is particularly true on NRHOs. In general, a given set of orbit-attitude initial conditions is valid only for a particular inertia tensor, which can be parametrised by certain relations between the values of the inertia moments. In this research work, the ratio between the maximum moment of inertia and the minimum one is often used. However, an additional inertia parameter can be defined as:

$$K_3 = \frac{I_2 - I_1}{I_3}, \tag{3.16}$$

which defines the shape of the body with respect to $\hat{\mathbf{b}}_3$. A value of K_3 close to zero indicates a body that is axis-symmetric about $\hat{\mathbf{b}}_3$, while other values stand for a preferential elongation along $\hat{\mathbf{b}}_1$ or $\hat{\mathbf{b}}_2$.

The correlation between attitude initial conditions and inertia properties of the spacecraft are dependent from the orbit-attitude families, and they are helpful to understand the particular dynamical environment and to have parametrised information about possible operative applications. For instance, the attitude initial conditions for different K_3 ratios are mapped as a function of the orbital period for $L2$ South NRHOs, in figure 3.8. Note that, the associated initial conditions for North NRHOs can be obtained changing the sign to the initial values of z and ω_1: $z_{South}(t_0) = -z_{North}(t_0)$ and $\omega_{1_{South}}(t_0) = -\omega_{1_{North}}(t_0)$. From this and other similar maps, the periodic orbit-attitude dynamics related to a certain spacecraft is available. This knowledge can be exploited to link different natural periodic motions for changing inertia properties of the orbiting body. In the case of the cislunar space station, the inertia ratios are expected to

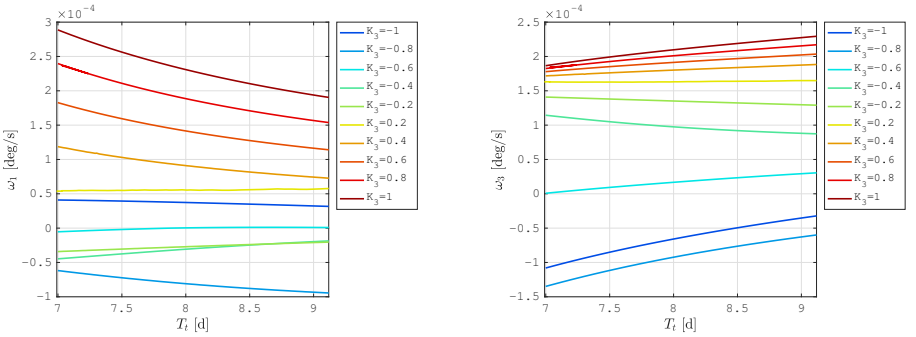

(a) ω_1 map **(b)** ω_3 map

Figure 3.8: Map of attitude initial Conditions, ω_1 and ω_3, as a function of the orbital period, T_t, and the inertia ratio, K_3 on EML2 South NRHO Families.

change during the on-orbit assembly. Assuming to maintain a fixed orbit (i.e. fixed orbital period T_t), the angular velocities of the station have to be modified as indicated in figures 3.8a and 3.8b to maintain the periodic motion with a different K_3 value.

In this thesis, the NRHOs will be extensively exploited as application scenario for analyses about the cislunar space station. However, from the absolute orbit-attitude dynamics discussed in this chapter, a first outcome about this family of non-Keplerian orbits is available. In fact, perilune passage in NRHOs poses many difficulties from the dynamical point of view, because of the fast orbit-attitude dynamics, the badly conditioned numerical problem and the weak stability for attitude and relative motion. These last two issues will be deeply investigated in the followings of this dissertation. Furthermore, the risk of structural instability in the extended space structures is not negligible. Therefore, NRHO's perilune is not convenient for proximity operations, such as rendezvous and docking manoeuvres, and NRHO's apolune is the safe region where complex operations shall take place.

3.3 Comparison of Selected Modelling Approaches

Dynamics in cislunar space can be analysed using different modelling formulations, which can be compared to understand the level of accuracy of the used models. Circular approximations, like CR3BP or BC4BP, can be compared to more refined models, like the elliptic three-body problem or the full ephemeris one. This analysis is needed to understand the range of validity for the given modelling approaches while studying the absolute orbit-attitude dynamics in lunar vicinity.

For sure, the analytical insight that is possible thanks to the CR3BP is a valuable tool for preliminary analyses of the dynamical environment and for initial assessment of the operational trajectories. However, the GNC functions and the refined design of the operations shall consider the real environment to get to the required accuracy while carrying out proximity operations.

In particular, NRHO dynamics is strongly dependent on the cislunar four-body environment, influenced by the gravitational attraction of the Earth, the Moon and the Sun, and the non-inertial terms due to the motion of the Earth and the Moon around their common barycentre and around the Sun. Moreover, the very peculiar regime of NRHOs, requires that the true non-circular motion of the Earth and the Moon is taken into account, since their relative eccentricity is not negligible in dictating the force field that maintains the periodicity of the non-Keplerian orbit. Furthermore, the gravity of the Sun plays a non- negligible role as well; in fact, the periodic oscillations of the NRHO due to the Sun's gravitational pull are missed out in a CR3BP model. These oscillations are in the order of $\sim 5 - 10\,\text{deg}$ in inertial frame, corresponding to an absolute error of $\sim$ 6000km at the apolune.

Elliptic model is based on the three-body environment and the assumed Keplerian elliptic motion of the primaries is not theoretically compatible with the presence of additional celestial bodies. Therefore, it is meaningless to extend the elliptic problem to 4-body or n-body models, and this limitation lead to inaccuracies in describing the motion on NRHOs. Moreover, ER3BP assumes the two main bodies to have a constant eccentricity; in reality, the orbit of the Moon itself is subject to perturbations, and its eccentricity varies between 0.04 and 0.09. Using a constant eccentricity model results in an absolute error of about $\sim$ 11000km. In addition, ER3BP equations are analytically more complex than the Full Ephemeris ones. In fact, the latter are set in an inertial reference frame without the need to have a time varying variable transformation (i.e. rotating-pulsating frame of ER3BP). The dynamics equations are straightforward: only the Newtonian gravitational terms have to be computed having the positions of the n celestial bodies. Table 3.3 summarises the results with different modelling approaches, highlighting the gradual increase in fidelity, but underlining the

Table 3.3: Absolute Dynamics Error in the Coordinate of the NRHO Apolune with respect to FER4BP.

Model	Absolute error [km]	Relative error [%]
CR3BP	30000	40
ER3BP	11000	15
FER3BP	6000	8

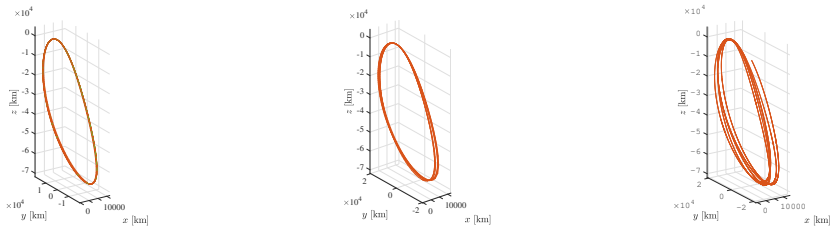

(a) CR3BP **(b)** ER3BP **(c)** FER4BP

Figure 3.9: Comparison of selected modelling approaches on EML2 South NRHO, $T_t = 7$d.

importance of the full ephemeris four-body model in order to grasp the peculiar NRHO dynamics. In figure 3.9 an EML2 South NRHO with period $T_t = 7$d is shown when computed with 3 different modelling approaches. In this dissertation, ER3BP is typically not used, CR3BP is exploited for all the analytical discussions and FER4BP is used in *GNC* problems and operative applications.

The comparisons between different modelling approaches are possible also with other orbital families. In figure 3.10 a single DRO, with period $T_t \simeq 24$d, is simulated in CR3BP and in FER4BP. The the remarkable stability of this particular periodic orbit-attitude motion is evident: the dynamics is simulated for almost 5 periods, and also the attitude motion remains bounded despite the non-perfect resonance with the Sun. This would have not been possible with other dynamical families, which suffer of a low attitude dynamics stability and require an exact periodicity of the complete 6DOF motion with respect to the environment. For practical applications, it is not always possible to exploit a complete periodic orbit-attitude state. In fact, it might be necessary to orbit a FER4BP NRHO, without the constraints imposed by the attitude periodicity with the Moon's gravity gradient and with the Sun effects. For this reason, there is a well-founded necessity to implement attitude control strategies and to look for stable attitude motions over periodic orbits in perturbed non-Keplerian environments.

3.4 Attitude Control Strategies

Naturally periodic orbit-attitude motions in cislunar environment do exist and, in some case, they are also remarkably stable (i.e. DRO in figure 3.10). However, again, an attitude control strategy can be desired to be actuated on-board of an extended space structure in lunar vicinity for a series of reasons. For instance, there might be the need to increase the stability of a certain configurations, or to manoeuvre the spacecraft or even to bring the system in unstable conditions with the purpose to excite some natural dynamics able to drive large slewing

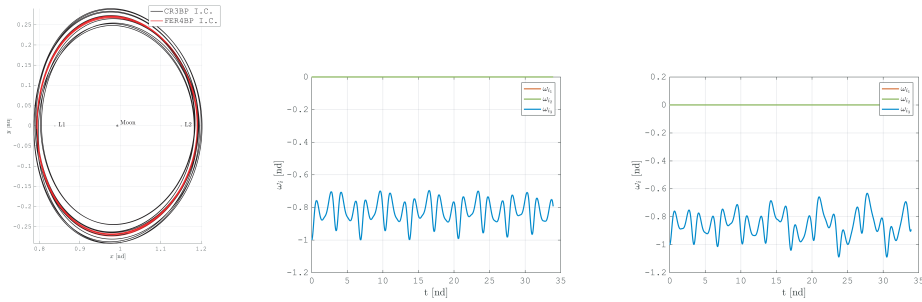

(a) Orbital Dynamics

(b) CR3BP Attitude Dynamics

(c) FER4BP Attitude Dynamics

Figure 3.10: Comparison of selected modelling approaches on DRO, $T_t \simeq 24$d.

manoeuvres. The constraint that should be enforced while designing the attitude control system imposes a strong limitation in active consumption of resources while controlling the dynamics. In fact, the cislunar space station will be operative for a long time, with limited supplies and conservative power budget, relatively to its dimensions and its tasks to be accomplished. For these reasons, this section focus its attention on single-spin or dual-spin attitude control techniques, which are more precisely referred to as attitude stabilisation techniques. Indeed, the stabilisation action with spinning spacecraft or with constant speed momentum wheels is remarkably efficient in terms of energy consumption.

Spin stabilisation techniques are based on the gyroscopic effect of the angular momentum stored within the body m_B. In single-spin stabilisation method, the whole spacecraft is spinning and the rotating mass of the spacecraft acts as attitude stabilising system. While, dual-spin stabilisation methods are based on momentum wheels that are able to store an important amount of angular momentum, needed to stabilise the system. Nevertheless, they can have a different rotation speed with respect to the main body and, thus, there is one additional degree of freedom that can be exploited while designing the mission operations. Furthermore, momentum wheels can be easily controlled in spinning rate or direction, and this feature opens to the possibility of attitude manoeuvres and enhanced control capabilities.

The additional stored angular momentum, which is eventually due to the presence of momentum wheels, affects the dynamic of the system as if the internal angular momentum were:

$$\mathbf{h} = \mathbb{I}_B \boldsymbol{\omega}_B^B + \mathbf{h}_W, \tag{3.17}$$

where the inertia tensor of the spacecraft, $\mathbb{I}_B$, takes into account the moments of inertia of the momentum wheels, and $\mathbf{h}_W$ is the angular momentum of the momentum wheels expressed relative to the body reference frame. Assuming the

presence of three different momentum storage devices, aligned with the principal axes of the body m_B, the angular momentum of the wheels is:

$$\mathbf{h}_W = [I_{1_W}\omega_{1_W}, I_{2_W}\omega_{2_W}, I_{3_W}\omega_{3_W}]^{\mathrm{T}}, \tag{3.18}$$

where I_{1_W}, I_{2_W}, I_{3_W} are the moments of inertia of the rotors respectively aligned with $\hat{\mathbf{b}}_1$, $\hat{\mathbf{b}}_2$ and $\hat{\mathbf{b}}_3$; ω_{1_W}, ω_{2_W} and ω_{3_W} are the relative angular velocities of three momentum wheels with respect to the body frame.

Therefore, equation (2.17) has to be modified with the additional terms due to the presence of the rotating momentum wheels that can be evaluated as described in classic literature about rigid body dynamics:

$$\boldsymbol{\eta}_W = \boldsymbol{\omega}_B^B \times \mathbf{h}_W = \begin{bmatrix} 0 & -\omega_3 & \omega_2 \\ \omega_3 & 0 & -\omega_1 \\ -\omega_2 & \omega_1 & 0 \end{bmatrix} \begin{bmatrix} I_{1_W}\omega_{1_W} \\ I_{2_W}\omega_{2_W} \\ I_{3_W}\omega_{3_W}. \end{bmatrix} \tag{3.19}$$

The three components, η_{1_W}, η_{2_W} and η_{3_W} of the vector $\boldsymbol{\eta}_W$ are then respectively divided by the moments of inertia of the body m_B. The resulting terms η_{1_W}/I_1, η_{2_W}/I_2 and η_{3_W}/I_3 are successively subtracted from the right-hand side of equation (2.17). In this section, the momentum wheels are assumed to be operated with constant spinning rate and axis and, thus, no additional term, such as derivative of the angular momentum of the rotors $\dot{\mathbf{h}}_W$ has to be included in the present model. Moreover, the additional equations of motion for the momentum wheels in $\mathbf{f}$ are trivial, being:

$$\dot{\omega}_{i_W} = 0 \longleftrightarrow \omega_{i_W} = const, \quad \text{with} \quad i = 1, 2, 3. \tag{3.20}$$

It must be noted that the differential correction scheme described in section 3.1.1 should be slightly modified. In fact, the Jacobian of the system now contains the terms due to the presence of the momentum wheels. Hence, the State Transition Matrix is a bit different from the basic coupled orbit-attitude dynamical model. On the contrary, the constraint vector is unmodified because the periodicity is not sought in the dynamics of the momentum wheels.

Single-spin attitude stabilisation can be analysed with this model, just considering the momentum wheels as non-rotating devices or as zero inertia rotors (e.g. $\omega_{i_W} = 0$ or $I_{i_W} = 0$ with $i = 1, 2, 3$).

3.4.1 Single-spin Attitude Stabilisation

The single-spin attitude stabilisation is a very simple and effective technique to increase the stability of the rotational motion. Even though the details about

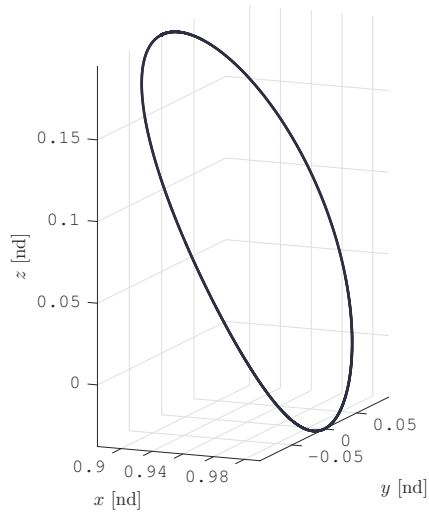

Figure 3.11: Reference EML1 NRHO: $T_{NRHO} = 2.07\,\text{nd} = 8.98\,\text{d}$, $A_{z_{Max}} = 0.195\,\text{nd} = 7.49 \times 10^4\,\text{km}$.

attitude stability will be discussed later, the general characteristics of single-spin periodic dynamics are introduced in this section.

Periodic orbit-attitude motion in cislunar environment has to satisfy periodicity constraints in both orbital and attitude variables and, moreover, the attitude evolution should be compatible and periodic with the gravity gradient torques due to the presence of the primaries and with all the perturbing forces. In fact, the effects of the gravitational attraction on the rotational motion strongly characterises the periodic dynamics. This is true in particular for non-Keplerian orbits with a low perilune altitude with respect to the lunar surface, such as large amplitude Lyapunov orbits, elongated Halo orbits or NRHOs. The latter are among the ones with the lowest perilune passage and, therefore, experience the largest gravity gradient torque that determines a relevant angular acceleration on the extended body, which is a source of instability for the attitude dynamics. For this reason, a NRHO around the Earth-Moon L1 point (EML1) is used as a reference orbit to analyse the features of single-spin attitude stabilisation. Details about the reference NRHO are reported in figure 3.11.

Several attitude periodic motions are possible on the same orbit, but only few examples are shown here to highlight the general features of the stabilised orbit-attitude periodic motions. The reference dynamics is the one that is not spin stabilised, being just librating around the equilibrium position. As can be seen in figure 3.12, the body m_B performs zero overall rotations in synodic frame (figure 3.12b) and the librational motion is due to the gravity gradient torque of

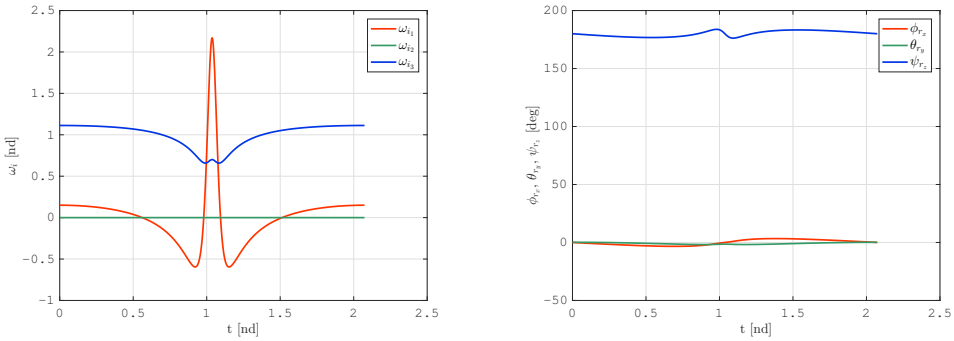

(a) Angular rates. **(b)** Euler angles.

Figure 3.12: Periodic librating (0-spin) attitude dynamics on the reference EML1 NRHO (figure 3.11): $K_3 = 0.2$.

the primaries. The presented solution has been obtained for a body with inertia parameter $K_3 = 0.2$. In figure 3.12a, the noticeable angular acceleration at the perilune passage is evident in the middle of the simulation. In that point, the spacecraft must be correctly oriented in order to remain stable on the naturally periodic motion, otherwise the large gravity gradient torque, different from the nominal one, generates the unstable dynamics. Moreover, since the spacecraft has not stored angular momentum, a fast departure from the reference condition is likely to happen. The angular velocity reported in the figures is evaluated with respect to the inertial reference frame, and the component along $\hat{\mathbf{z}}$ has an offset of 1 in non-dimensional units because of the rotational motion of the synodic frame with respect to the inertial one. Thus, a velocity component $\omega_{I_z} = 1\,\text{nd}$ in inertial frame is equivalent to $\omega_{S_z} = 0\,\text{nd}$ in synodic frame.

The single-spin dynamics on the reference EML1 NRHO are shown in figure 3.13. These all have similar features because of the attitude that is initialised as in the reference librating solution and the inertia parameter of the body is $K_3 = 0.2$. The only difference is the spinning rate around $\hat{\mathbf{b}}_3$ that, in the first case in figure 3.13a, allows one overall rotation along one orbit, while in the other two simulations in figures 3.13c and 3.13e determines, respectively, two and three overall rotations in one orbital period. The angular accelerations due to the gravity gradient of the Moon is evident also in these situations, but the effect is weaker if compared to the global magnitude of the angular velocity. Furthermore, the increasing stored angular momentum makes the spinning body less influenced by external perturbations and the resulting attitude dynamics more stable and stiff. The increase in attitude stability will be formally discussed in section 3.5 but, from a general overview of the attitude evolution for increasing spinning rates, presented in figure 3.13, it is evident how the attitude dynamics is less affected by the gravity gradient torque at perilune. On the other hand, such a

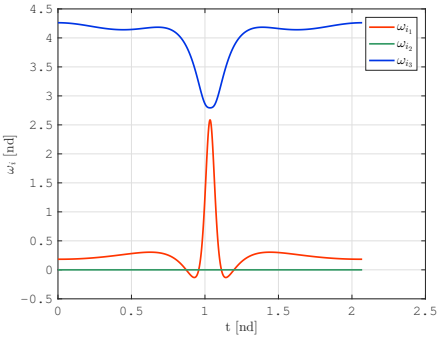

(a) 1-spin periodic angular rates.

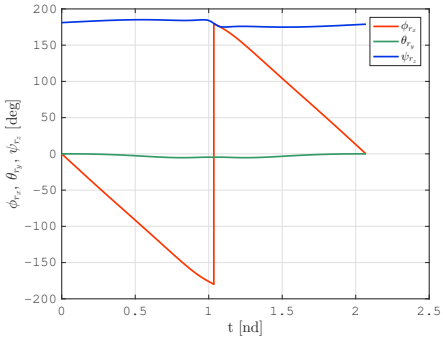

(b) 1-spin periodic Euler angles.

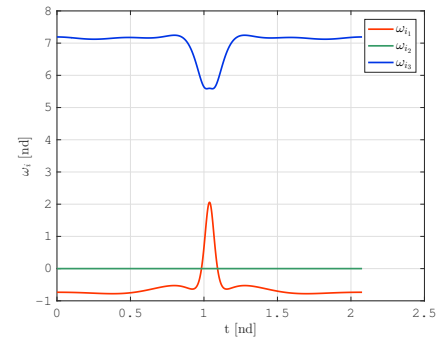

(c) 2-spin periodic angular rates.

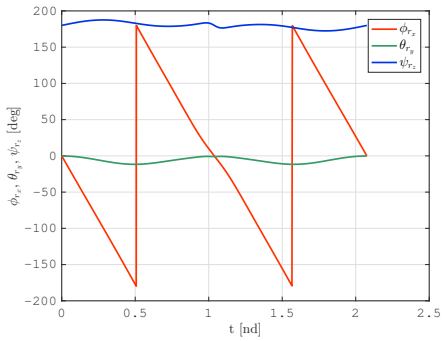

(d) 2-spin periodic Euler angles.

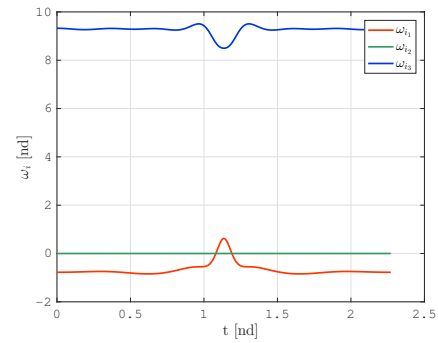

(e) 3-spin periodic angular rates.

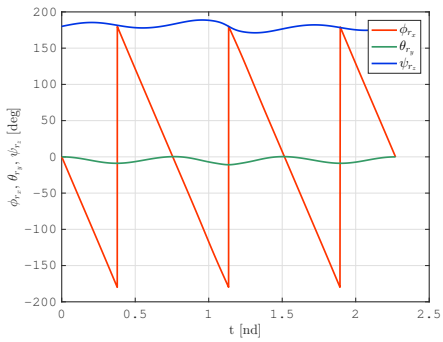

(f) 3-spin periodic Euler angles.

Figure 3.13: Periodic single-spin attitude dynamics on the reference EML1 NRHO (figure 3.11): $K_3 = 0.2$.

spinning condition, may be problematic in terms of operations and other mission constraints. For example, telecommunications or docking activities may be more complex in the case the cislunar station is rotating with large angular rate.

Single-spinning attitude stabilisation solutions are available also for other orbital families. For instance, single-spin attitude solutions on DROs are shown in figure 3.6 but, the large stability of DROs also in the librating solution, together with the very small gravity gradient torque generated by the primaries, makes them not so interesting in terms of attitude control. Nevertheless, if enhanced stability properties or different operational requirements are sought along DROs, single-spin stabilisation is possible and periodic spinning solutions are easily available.

3.4.2 Dual-spin Attitude Stabilisation

The operational constraints imposed by the single-spinning attitude stabilisation methods can be easily overcome with a separate angular momentum storage device, which can be spun at a different angular rates with respect to the main body. Thus, there is one additional degree of freedom that can be exploited to stabilise the attitude dynamics without inserting additional operational constraints. In this section, the spinning momentum wheels mounted on the body m_B are used at a constant spinning rate. The increased angular momentum of the whole space system is the foundation for the dual-spin attitude stabilisation technique.

The periodic solutions shown in figure 3.14 refer to three distinct angular rates of the spinning momentum wheel, leading to as many dual-spin attitude periodic dynamics. They have been initialised on the reference EML1 NRHO, starting from the librating attitude solution in figure 3.12 and considering a body with inertia parameter $K_3 = 0.2$. Hence, they all share comparable characteristics in order to correlate the two attitude stabilisation methods. In the analysed dual-spin solutions there is only one spinning momentum wheel, which is the one along the principal inertia axis $\hat{\mathbf{b}}_3$. In this way, there is a direct connection between the single-spin and the dual-spin with spinning direction along the same body axis. Furthermore, an increased angular momentum along $\hat{\mathbf{b}}_3$ is the one that is needed to make possible and stabilise the attitude dynamics for the given orbit and initial orientation. The momentum wheel has moment of inertia $I_{3_W} = \frac{I_3}{100}$.

The three proposed periodic solutions differ for the spinning rate of the momentum wheel. In the first case, figure 3.14a, the wheel is slowly spinning with $\omega_{3_W} = 500\,\mathrm{nd}$ and the stabilisation effect is not so evident, except for the additional rotational motion around $\hat{\mathbf{b}}_2$ due to the gyroscopic coupling. The dual-spin behaviour starts to be more evident with an higher angular velocity

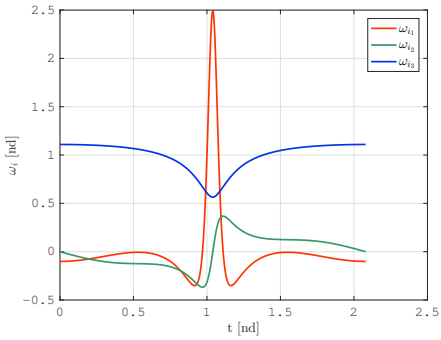

(a) Slow spinning wheel periodic angular rates ($\omega_{3_W} = 500\,\text{nd}$).

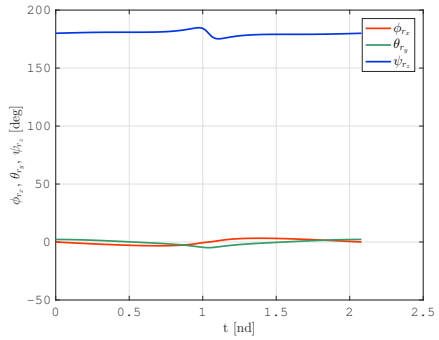

(b) Slow spinning wheel periodic Euler angles ($\omega_{3_W} = 500\,\text{nd}$).

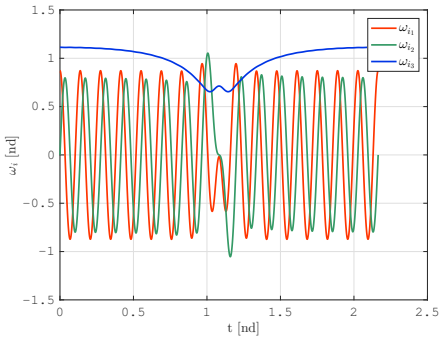

(c) Medium spinning wheel periodic angular rates ($\omega_{3_W} = 5000\,\text{nd}$).

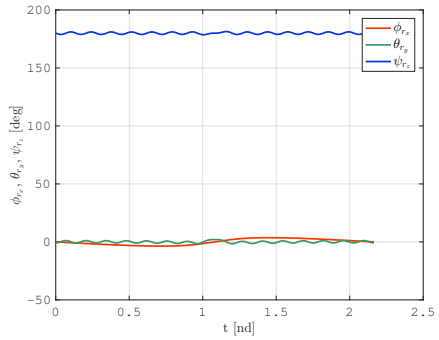

(d) Medium spinning wheel periodic Euler angles ($\omega_{3_W} = 5000\,\text{nd}$).

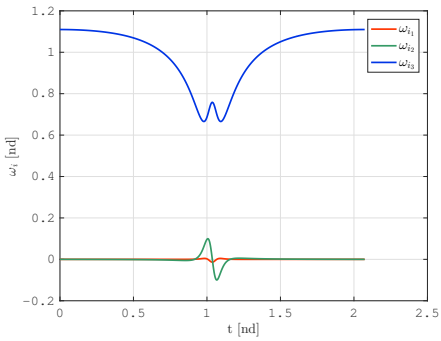

(e) Fast spinning wheel periodic angular rates ($\omega_{3_W} = 50\,000\,\text{nd}$).

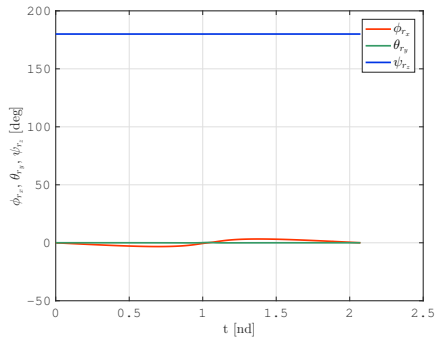

(f) Fast spinning wheel periodic Euler angles ($\omega_{3_W} = 50\,000\,\text{nd}$).

Figure 3.14: Periodic dual-spin attitude dynamics on the reference EML1 NRHO (figure 3.11): $K_3 = 0.2$.

of the momentum wheel in figure 3.14c. In this case, the increased angular momentum makes the system more stiff and the gyroscopic coupling frequency is high, with fast oscillations around the rotation axis of the body. The effect due to the large gravity gradient of the Moon is mitigated and the attitude is stable in its pulsating evolution. However, a great improvement in attitude stabilisation is obtained further increasing the spinning rate of the momentum wheel. In figure 3.14e the momentum wheel is spinning at a fast rate, $\omega_{3_W} = 50\,000\,\mathrm{nd}$, and the attitude dynamics is greatly stabilised with limited angular acceleration at the perilune. With dual-spin attitude stabilisation is therefore possible to stabilise the attitude, limiting the effect of the gravity gradient torque, with the body that is no more rotating in the Synodic reference frame. In fact, comparing figure 3.14f and figure 3.13f, a spinning momentum wheel allows to greatly increase the performance of the attitude dynamics, while maintaining the cislunar station just librating around an equilibrium condition. Thus, no additional mission constraints are imposed and the space system can be operated more easily with respect to the case in which the whole spacecraft is rotating with large angular rate. Moreover, the proposed stabilisation can be practically implemented since the $\omega_{3_W} = 50\,000\,\mathrm{nd}$ corresponds in dimensional units to $\omega_{3_W} = 0.133\,\mathrm{rad/s} = 1.27\,\mathrm{RPM}$.

3.5 Attitude Stability

At this point, the necessity to introduce a precise definition of attitude stability is needed. In fact, assuming the body on its operational orbit with imposed attitude dynamics in order to achieve a coupled periodic motion, it is interesting to quantify the dynamical properties of the orbit-attitude motion. Many consideration are possible on the coupled stability, as well as the mutations of the dynamical behaviour along a family of orbit-attitude periodic solution (e.g. bifurcations in the dynamical structure of the family of periodic solutions).

The considerations presented in this section are based on some outcomes of the Floquet theory, similarly to what has been already done by other authors in previous orbit-attitude and restricted three-body problem literature [26, 29] . In particular, the first consideration is based on the fact that solutions in the vicinity of a periodic reference are linearly approximated by the modes of the monodromy matrix (i.e. the state transition matrix over one period). These linear modes allow to investigate the linear stability properties along the periodic solution.

For a periodic orbit in the orbit-attitude system $\boldsymbol{f}$, the monodromy matrix $\mathbf{M}$ of a periodic orbit-attitude LPO is defined as the State Transition Matrix after a full period T_t.

$$\mathbf{M} = \Phi(T_t + t_0, t_0). \tag{3.21}$$

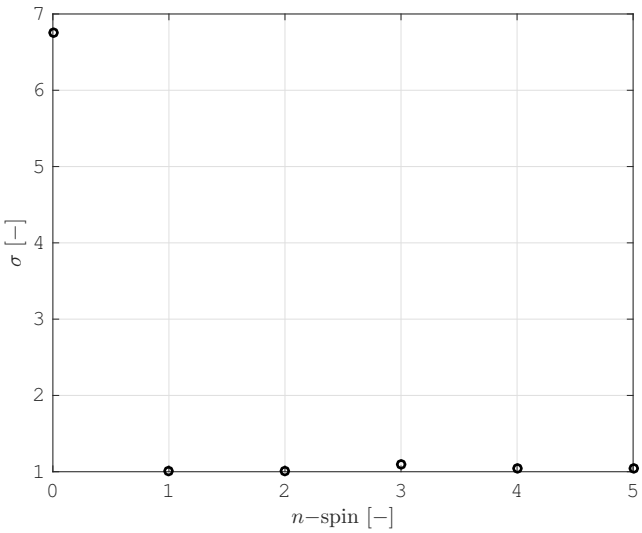

Figure 3.15: Stability index for single-spin attitude stabilisation solutions. (cf. figure 3.13).

In order to focus the analysis on the attitude stability, only the attitude part of the monodromy matrix, $\mathbf{M}_{Attitude}$, is taken into account (i.e. the submatrix where only attitude variables are involved):

$$\mathbf{M}_{Attitude} = \begin{bmatrix} M_{qq} & M_{q\omega} \\ M_{\omega q} & M_{\omega\omega} \end{bmatrix}. \tag{3.22}$$

It should be noted that the monodromy matrix shall be transformed into the synodic rotating frame, even though the state variables are expressed with respect to the inertial frame I. In fact, The periodicity of the attitude states is seen in the quaternion of the body respect to the rotating frame, and the monodromy matrix has to be written in S in order to catch the actual eigenstructure around the orbit-attitude LPO seen from a rotating observer.

Linear attitude modes are therefore associated to the eigenstructure of $\mathbf{M}^{S}_{Attitude}$, which is composed by 6 eigenvalues $\lambda_{Attitude_i}$. Those with magnitude less than one are related to linear stable modes, while those with magnitude greater than one correspond to linear unstable modes. Attitude eigenvalues with $\|\lambda_{Attitude_i}\| = 1$ are paired to marginally stable modes. As a consequence, if $\|\lambda_{Attitude_i}\| \leq 1$ for any i, the periodic attitude solution is stable (or marginally stable) in the linear approximation. On the contrary, if at least one $\|\lambda_{Attitude_i}\| > 1$, the periodic solution is unstable.

Furthermore, according to what has been already introduced by Guzzetti [27], a stability index, σ, can be defined in order to simplify the stability analyses. In

particular, this quantity is defined as:

$$\sigma = \frac{1}{2}\left(\lambda_{Attitude_{Max}} + \frac{1}{\lambda_{Attitude_{Max}}}\right), \tag{3.23}$$

where $\lambda_{Attitude_{Max}} = \max \|\lambda_{Attitude_i}\|$ is the magnitude of the dominant eigenvalue. According to this definition, $\sigma = 1$ is associated to marginally stable attitude dynamics, while $\sigma > 1$ represent unstable attitude solution and a larger stability index can be related to a faster departure from the periodic motion. Stable dynamics are associated to $\lambda_{Attitude_{Max}} < 1$.

Analysing for example the stability index for different single-spin attitude solutions, reported in figure 3.15, it is evident the stability improvement due to the spinning stabilisation methods. Indeed, the stability index, which is equal to 6.81 for the librating solution, approaches the value 1 for all the spinning dynamics. Small deviations towards instability are possible, looking for example at the 3−spin periodic motion, but σ is always very close to 1, meaning that the spinning solution departs from the periodic motion slowly.

The same analysis is possible for dual-spin attitude stabilisation. In fact, similarly to the figure for single-spin dynamics, the attitude stability increases for an increasing stored angular momentum due to the presence of a faster wheel. However, the progressive evolution of σ along a family of periodic solutions with different angular rates of the momentum wheel is more interesting for dual-spin dynamics.

For instance, figure 3.16 reports the stability index and the magnitude of attitude eigenvalues for different dual-spin solutions, $\omega_{3_W} \in [-250, 300\,\text{nd}]$, on a reference EML1 Halo orbit, whose details are reported in the caption of figure 3.16. From figure 3.16a is evident the general increase in stability (i.e. σ decreases) for increasing angular rate of the wheel. Moreover, the evolution of the magnitude of $\lambda_{Attitude_i}$, in figure 3.16b, highlights the presence of distinct bifurcation points. These points are associated with a change in the eigenstructure of the periodic solution, as evident in figure 3.16b for $\omega_{3_W} \simeq -175\,\text{nd}$, where a saddle point appears in place of two eigenvalues on the unit circle that disappears.

This fact opens to the possibility to facilitate the manoeuvres between different periodic attitude families by varying the amount of stored angular momentum in the wheel. In practice, when the system is at a bifurcation point, a small perturbation in the direction of the desired bifurcating family could enable a variation in the attitude motion. However, it should be noted that the stability properties of the bifurcating solution may be not satisfactory and, thus, the system may be naturally inclined towards the most stable dynamics. In this perspective, the bifurcation points should be just exploited to begin a desired manoeuvre, which has to be correctly driven in order to acquire a precise periodic attitude motion. Furthermore, having in mind again that the cislunar

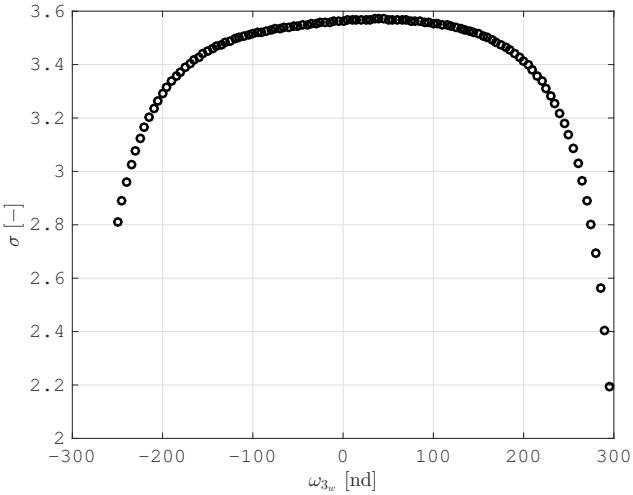

(a) Stability index, σ.

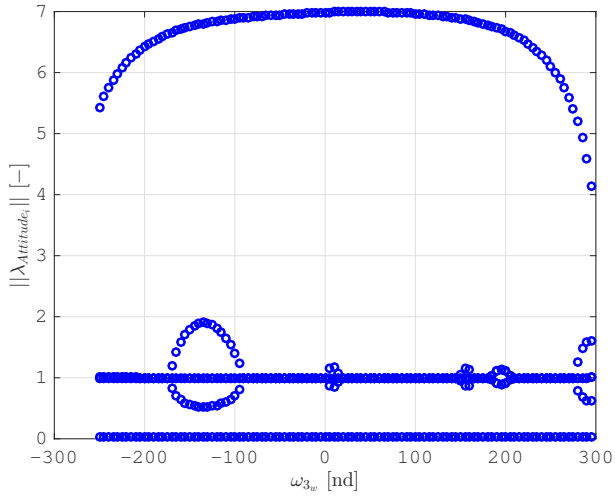

(b) Magnitude of eigenvalues, $\|\lambda_{Attitude_i}\|$.

Figure 3.16: Dual-spin stability analysis for attitude family on reference EML1 Halo orbit: $T_{Halo} = 2.30\,\text{nd} = 9.98\,\text{d}$, $A_{z_{Max}} = 0.18\,\text{nd} = 6.9 \times 10^4\,\text{km}$, $K_3 = 0.2$ and $\omega_{3_W} \in [-250, 300\,\text{nd}]$.

space station will be assembled on-orbit, through many docking and undocking operations with massive modules, the inertia parameters of the system can vary in time. Hence, bifurcating solutions may be exploited in order to connect two stable periodic attitude dynamics associated with the different inertia properties of the modular space station.

An additional analysis on the considered framework is possible looking at the stability properties of another dynamical family. Figure 3.17 shows stability index and the magnitude of attitude eigenvalues for several dual-spin solutions, $\omega_{3_W} \in [-300, 300\,\text{nd}]$, on a reference DRO defined in the caption. Distant retrograde orbits are highly stable planar trajectories around both the collinear points L1 and L2, associated to smooth and stable periodic attitude solutions. In general, the whole orbit-attitude dynamics on DROs is remarkably stable, as ca be also understood looking at the stability index in figure 3.17a, especially in comparison with the stability analysis for the Halo presented in figure 3.16.

In this case, the unstable solution may be of interest with the purpose to excite some natural dynamics able to drive large attitude manoeuvres or fast slewing operations. In fact, when an unstable mode exists it can be excited in order to move the system along a natural trajectory that evolves towards a desired final condition. Dual-spin stabilisation is effective also in this situation, where the space system is orbiting along a DRO with librating rotational motion in synodic reference frame. The angular velocity of the body m_B associated with this particular attitude dynamics is, in inertial frame, $\omega_3 = 1\,\text{nd}$. Hence, a counter-spinning wheel able to cancel the stored angular momentum of the system can decrease the stability level of the whole system. In figure 3.17a, the largest stability index (i.e. the highest instability) is at $\omega_{3_W} = -237\,\text{nd}$, because the inertia of the rotors is $I_{3_W} = \frac{I_W}{237}$. For this particular spinning rate of the momentum wheel, the system has internal angular momentum along $\hat{\mathbf{b}}_3$ equal to zero and, therefore, null gyroscopic stiffness. The resulting motion is not stable and the presence of unstable modes can be exploited for the aforementioned operative applications. The existing instability for slow spinning momentum wheel, $\omega_{3_W} \in (0, 110\,\text{nd}]$ is due to the cross-coupling between the stored angular momentum along $\hat{\mathbf{b}}_3$ and the attitude dynamics around $\hat{\mathbf{b}}_1$ and $\hat{\mathbf{b}}_2$. Indeed, the slow spinning wheel is not sufficient to spin stabilise the system, but the cross-coupling makes the dynamics sensitive to perturbations perpendicular to the $xy-$plane and, thus, slightly unstable.

3.6 Attitude Control for a Cislunar Space Station

The analyses presented in section 3.5 provides general results that can be exploited to drive the design of modular and extended space structures in cislunar environment, such as the cislunar space station. The size of this kind of space system imposes a strong consideration about the attitude dynamics and its stability. Many dedicated analyses can be carried out with this purpose, having in mind that the main driver while designing such a complex mission is related to a maximum reduction of the maintenance and station-keeping costs.

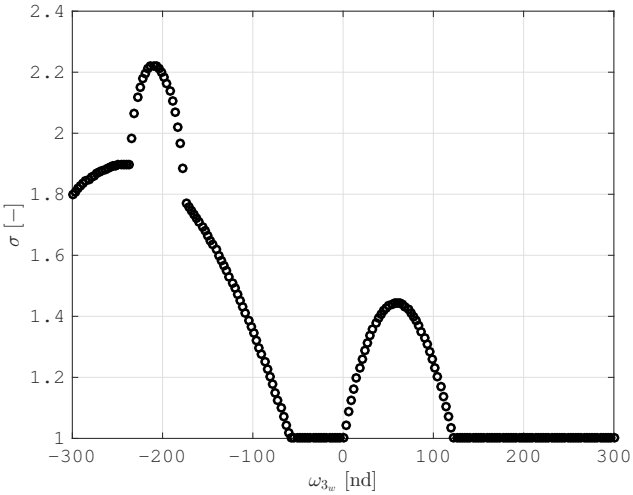

(a) Stability index, σ.

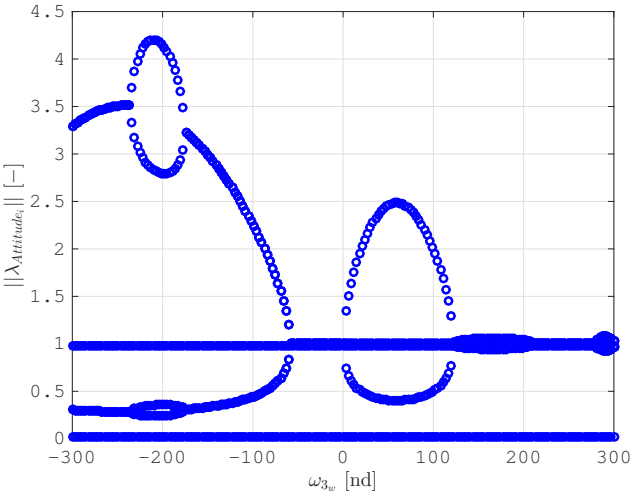

(b) Magnitude of eigenvalues, $\|\lambda_{Attitude_i}\|$.

Figure 3.17: Dual-spin stability analysis for attitude family on reference DRO: $T_{DRO} = 3.37\,\text{nd} = 14.63\,\text{d}$, $K_3 = 0.2$ and $\omega_{3_W} \in [-300, 300\,\text{nd}]$.

Moreover, the progressive on-orbit assembly of the modular structure must be carefully planned in order to minimise risks and costs.

A first analysis is possible looking at a family of orbit-attitude periodic solutions with dual-spin attitude stabilisation, presented in figure 3.18. In this case a family of EML2 Halo orbits is generated starting from a periodic solution with orbital period $T_{Halo_1} = 3.35\,\text{nd}$, maximum $\hat{\mathbf{z}}$ elongation $A_{z_{Max_1}} = 0.083\,\text{nd}$, angular rate and moment of inertia of the spinning wheel respectively $\omega_{3_W} = 100\,\text{nd}$

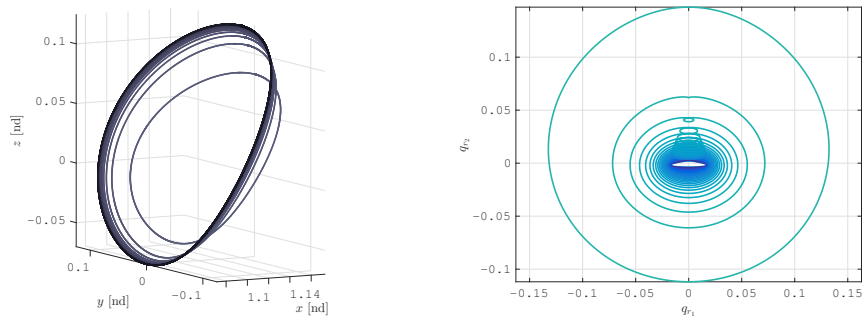

(a) Orbital trajectories along the family.

(b) Quaternions subspace, components q_1 and q_2 along the family.

Figure 3.18: Periodic orbit-attitude family on EML2 Halo orbits with dual-spin attitude stabilisation: $T_{Halo_1} = 3.35\,\text{nd} = 14.57\,\text{d}$, $A_{z_{Max_1}} = 0.083\,\text{nd} = 3.18 \times 10^4\,\text{km}$, $K_3 = 0.2$ and $\omega_{3_W} \in [-100, 100\,\text{nd}]$.

and $I_{3_W} = \frac{I_3}{100}$. The family is continued decreasing the spinning rate ω_{3_W} down to $-100\,\text{nd}$. At the beginning of the family, the orbit closest to the Moon, associated with the darker line in figure 3.18a, and the dual-spin attitude stabilisation determine the convergence of the periodic solution with a fast quaternion dynamics influenced by the gravity gradient torque, associated to the sharp corner and the double inner loop in the quaternion subspace (darkest line in figure 3.18b). Decreasing the spinning stabilisation, the convergence to a periodic solution is possible at a greater distance from the moon. The related attitude dynamics is influenced by a lower gyroscopic stiffness and a weaker gravity gradient torque, resulting in larger and smoother loop in figure 3.18b. When the family reaches the point of momentum wheel with $\omega_{3_W} = -100\,\text{nd}$ and, thus, a null gyroscopic stiffness, the converged periodic solution is at the largest distance from the Moon, where the librating attitude dynamics of the overall system is less affected by the gravity gradient.

A similar family of orbit-attitude periodic dynamics can be obtained fixing the angular rate of the momentum wheel at a constant value and continuing the family along the inertia parameters of the system. Therefore, a certain periodic attitude motion, for a modular station with changing inertia properties, can be maintained by varying the attitude stabilisation level. Otherwise, for constant attitude stabilisation effort and different inertia parameters, the periodic motion can be achieved on a distinct orbit-attitude periodic solution.

The increased operational capabilities when attitude stabilisation techniques are exploited on extended and modular cislunar spacecraft are evident in figure 3.19, where a spacecraft with $K_3 < 0$ is considered. According to classical attitude stability analyses [29], pitch motion is stable only for positive inertia parameter

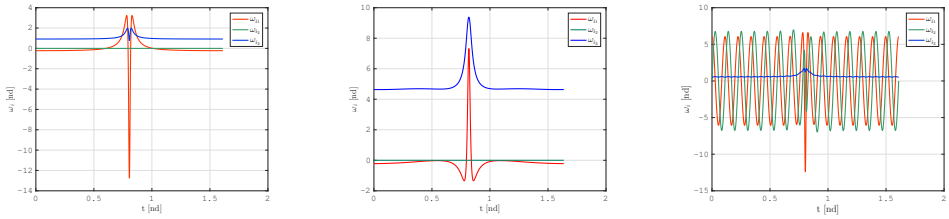

(a) Non-spin stabilised.

(b) Single-spin stabilised (1-spin).

(c) Dual-spin stabilised ($\omega_{3_W} = 5000\,\text{nd}$, $I_{3_W} = \frac{I_3}{100}$).

Figure 3.19: Periodic orbit-attitude solutions on EML2 South NRHO with $K_3 < 0$: $T_{S-NRHO} = 1.77\,\text{nd} = 7.68\,\text{d}$, $A_{z_{Max}} = -0.192\,\text{nd} = -7.41 \times 10^4\,\text{km}$, $K_3 = -0.2$.

K_3. In fact, for the currently analysed case with $K_3 = -0.2$, the resulting periodic motion in figure 3.19a is extremely unstable with stability index, σ, equal to 21.5. Thus, an attitude stabilisation method is fundamental in order to correctly operate the given space system in a EML2 South NRHO with period $T_{S-NRHO} = 1.77\,\text{nd}$ and maximum $\hat{\mathbf{z}}$ elongation $A_{z_{Max}} = -0.192\,\text{nd}$. The performance of single-spin and dual-spin attitude stabilisation techniques are compared in figures 3.19b and 3.19c, with details in the relative captions. Both solutions are effective in stabilising the spacecraft, determining a stability index respectively equal to $\sigma_{single} = 1.02$ for single-spin and $\sigma_{dual} = 2.16$ for dual-spin. The stabilised attitude evolution is completely transformed and the resulting dynamics has some analogies with the previously presented solution for a body with $K_3 = 0.2$. Therefore, for a modular space station that is progressively assembled, the situation in which a large attitude instability arises can be managed through a proper selection of the attitude stabilisation parameters.

3.6.1 Artificial Gravity Generator

One of the main goals of the space station in cislunar environment will be achieved when astronauts from all over the world will have the possibility to stay for prolonged time in deep space. This accomplishment will be fundamental to perform complex operations and activities in the vicinity of the Moon and towards the interplanetary space. However, despite the advances obtained with the experience of the International Space Station, the possibility to have living conditions similar to those on Earth is extremely important.

In this section, spin stabilisation methods are applied to generate an artificial gravity field. In principle, this is possible considering both single-spin and dual-spin attitude stabilisation methods. Nevertheless, in the second case the

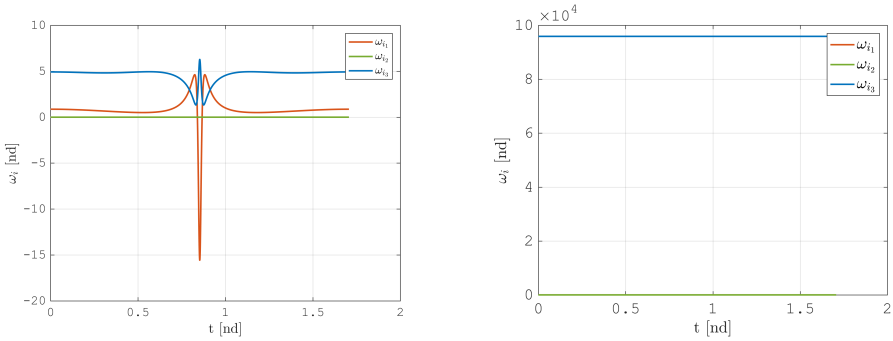

(a) 1-spin periodic solution. **(b)** 1/6 g single-spin periodic solution.

Figure 3.20: Artificial gravity generator with single-spin dynamics.

station architecture is more complex because there would be the need of large rotors capable to host astronauts inside or, in alternative, the station should be subdivided in a rotating and a non-rotating side. For this reason, the simpler idea to spin the whole space station is here considered.

Assuming a space station with spinning radius $r = 25\,\text{m}$ the angular rates to obtain artificial gravity levels of practical interest for future space missions are reported in table 3.4. Even to obtain 1/6 g, approximately equal to the gravitational acceleration on the surface of the Moon, the station has to spin at $2.44\,\text{rpm} = 0.256 rad/s$ equal to 9.59×10^4 in CR3BP normalised units.

Looking at figure 3.20, where an example case is considered, the slow spinning solution for an extended spacecraft with $K_3 = 0.4$ in a EML2 NRHO with period $T = 7.5$ [nd] is compared with a fast single-spin solution able to generate an artificial gravity level of 1/6 g. The fast spinning rate determines a great attitude stability. In fact, the noticeable angular acceleration at the perilune passage, which is evident in the middle of the simulation in figure 3.20a, is negligible for the gravity generation solution in figure figure 3.20b. Moreover, the increasing stored angular momentum makes the spinning body less influenced by external perturbations and the resulting attitude dynamics more stable and stiff. Obviously, the same conclusion is valid also for larger artificial gravity levels.

Table 3.4: Spinning Rates to Achieve Relevant Artificial Gravity Levels.

Artificial Gravity Level [g]	Spinning Rate [rpm]
1	5.98
4/5	5.35
1/3	3.45
1/6	2.44

Thus, the possibility to create a non-negligible gravitational acceleration inside the space station is important for the life-support capabilities of the cislunar mission, but is helpful as well in terms of the dynamical characteristics of the orbit-attitude motion.

3.7 Natural 6DOF Dynamics

Rendezvous and proximity operations in space involves a spacecraft already in an operational orbit, which is commonly called target, and a spacecraft that is approaching to it, chaser. The different phases of a generic rendezvous consist of a series of orbital manoeuvres and controlled trajectories, which have to progressively bring the chaser into the vicinity of the target. They will be defined and addressed with more attention in chapter 5. Anyhow, the absolute n-body dynamics offers interesting recommendation for the design of rendezvous trajectories in lunar vicinity. In fact, since the cislunar station will be assembled by means of many automated rendezvous activities and will rely on a complex infrastructure of automated transfer vehicles, it is fundamental to find an efficient, autonomous and reliable method to move several objects back and forth from the station. The natural dynamics existing in n-body environments are suitable for this scope: as a matter of fact, stable and unstable manifolds ensure affordable and robust approaching and departure trajectories from most periodic orbits in cislunar space, which are favourable locations to keep and operate the proposed space station.

The attitude constraints imposed by the rendezvous with a large space structure naturally evolving on periodic orbit-attitude dynamics are an additional aspect to be managed in the currently considered scenario. In fact, the large space station will be rotating according to an imposed attitude dynamics that will be selected to satisfy certain requirements related to long-term stability, telecommunications and much-more. Coupled orbit-attitude dynamics in cislunar space allows to investigate orbit-attitude manifolds. They exist in the space of states associated with orbital and rotational dynamics and can be considered an extension of the usual invariant manifolds existing in the CR3BP. Natural orbit-attitude trajectories can be exploited to easily guide and control the chaser that is approaching or departing from the operational orbit of the target. The advantage of exploiting manifolds to design rendezvous operations is related to the fact that since they are associated to natural dynamics, they require negligible control action. It should be noted that the manifolds are invariant only in autonomous systems, like CR3BP. In FERnBP, or other non-autonomous systems, manifolds are no more invariant. Nevertheless, they can be computed exploiting the initial guesses obtained from the approximated autonomous models. Hence, the method to compute invariant orbit-attitude methods is of general interest for this research, regardless the selected modelling approach.

3.7.1 Floquet's Theory for Periodic Orbits

Orbit-attitude manifolds are obtained similarly to the classical orbital CR3BP manifolds. According to Floquet's theory, they are strictly linked to the eigenvalues λ_i of the Monodromy matrix, $\mathbf{M}$, in equation (3.21). Considering the system of orbit-attitude differential equations, $\mathbf{f}$, the dynamical flow $\phi_t(\mathbf{x}) = \phi(\mathbf{x}, t)$ is the flow driven by $\mathbf{f}$ and passing through a generic point $\mathbf{x}$. A periodic orbit, Γ, of period T_t, can be defined as:

$$\Gamma : \mathbf{x} = \boldsymbol{\gamma}(t) = \phi_t(\mathbf{x}_0) \text{ with } 0 \leq t \leq T_t, \tag{3.24}$$

meaning that any point of the orbit can be determined from the initial point $\mathbf{x}_0$ and the time t. The latter is the time needed to reach $\mathbf{x}$, on the periodic orbit, through the flow ϕ_t starting from the point $\mathbf{x}_0$. The linearization of the non-linear system $\mathbf{f}$ about Γ is defined by the non-autonomous linear system in the first-order variational equation (3.1) and by the STM, $\Phi(t)$, which represents the linear mapping of the variational evolution about a reference flow ϕ_t.

For a periodic orbit, the Floquet's Theorem says that, for any time $t > t_0$, any fundamental solution matrix of the system $\mathbf{f}$ can be expressed as:

$$\Phi(t) = Q(t)\, e^{Bt}\, Q^{-1}(t_0), \tag{3.25}$$

where $Q(t)$ is a non-singular differentiable matrix with period T_t, and B is a constant matrix. Furthermore, if $\Phi(t_0) = \mathcal{I}$ then also $Q(t_0) = \mathcal{I}$. It follows that after a full period $Q(T_t) = \mathcal{I}$ and, as a consequence, the definition of monodromy matrix is obtained as:

$$\mathbf{M} = \Phi(T_t) = e^{B\,T_t}. \tag{3.26}$$

Therefore, the eigenvalues λ_i of the monodromy matrix $\mathbf{M}$ are directly related to the eigenvalues ϵ_i of the matrix B:

$$\|\lambda_i\| = e^{\epsilon_i T_t}. \tag{3.27}$$

The eigenvalues ϵ_i are called characteristic exponents of the periodic orbit Γ, while the eigenvalues λ_i are called characteristic multipliers of Γ. Let now apply the following transformation of coordinate to the variational state vector:

$$\mathbf{y} = Q^{-1}(t)\delta\mathbf{x}, \tag{3.28}$$

which reduces equation (3.1) to an autonomous linear system with constant coefficients:

$$\dot{\mathbf{y}} = B\mathbf{y}. \tag{3.29}$$

The knowledge of eigenvalues and eigenvectors of the matrix B allows to diagonalise the system (3.29), as well as the fundamental relation (3.25):

$$\Phi(t) = E(t)\, e^{Dt}\, E^{-1}(t_0), \tag{3.30}$$

where D is a constant matrix which diagonal components corresponds to the ϵ_i eigenvalues of B. The matrix $E(t)$ is called Floquet's Modal matrix and is non-singular, differentiable and with period T_t. The columns $\mathbf{e_i}$ of the matrix $E(t)$ represents a six-dimensional, non-orthogonal basis to describe the linear system in equation (3.1) and are defined as Floquet's modes. The columns of $E(t_0)$ are constituted from the real and the imaginary part of the eigenvectors of the monodromy matrix. Equation (3.30) shows that the characteristic exponents ϵ_i describe the rate of departure from the neighbourhood of the orbit Γ, qualitatively proportional to an exponential function. Therefore, the monodromy matrix is so important for non-linear system analysis because it gives access to the stability information of the orbit via its eigenvalues. Moreover, the eigenvectors of the monodromy matrix allow to decompose the relative motion in the vicinity of the orbit $\Gamma(t)$ through the Floquet's modes.

3.7.2 Orbit-attitude Manifolds

Let consider the periodic orbit Γ in the non-linear system $\mathbf{f}$. If the set of the characteristic exponents has at least one eigenvalue ϵ_i with negative real part, then there exists a neighbourhood N_δ of the orbit Γ such that

$$S(\Gamma) = \{\gamma x \in N_\delta(\Gamma) \mid \Delta(\phi_t(\gamma x), \Gamma) \to 0 \ \ as \ \ t \to \infty \ \ and \ \ \phi_t(\gamma x) \in N_\delta(\Gamma) \ \ for \ \ t \geq t_0\}. \tag{3.31}$$

The stable manifold $S(\Gamma)$ of the orbit Γ describe an n_S-dimensional space which is positively invariant under the flow ϕ_t, where n_S is equal to the number of stable eigenvalues ϵ_i.
If the set of the characteristic exponents has at least one eigenvalue ϵ_i with positive real part, then there exists a neighbourhood N_δ of the orbit Γ such that

$$U(\Gamma) = \{\gamma x \in N_\delta(\Gamma) \mid \Delta(\phi_t(\gamma x), \Gamma) \to 0 \ \ as \ \ t \to -\infty \ \ and \ \ \phi_t(\gamma x) \in N_\delta(\Gamma) \ \ for \ \ t \leq t_0\}. \tag{3.32}$$

The unstable manifold $U(\Gamma)$ of the orbit Γ describe a n_U-dimensional space which is negatively invariant under the flow ϕ_t, where n_U is equal to the number of unstable eigenvalues ϵ_i.

The motion along trajectories on the flows belonging to stable or unstable manifolds is synchronised with the motion along the corresponding orbit Γ through a given asymptotic phase at t_0. Moreover, the stable and the unstable manifolds intersect transversally the orbit Γ. The local stable manifold $S(\Gamma)$ and the local unstable manifold $U(\Gamma)$ can be exploited to generate the corresponding global stable manifold $W^S(\Gamma)$ and the global unstable manifold $W^U(\Gamma)$. The global stable and unstable manifolds are defined respectively as

$$W^S(\Gamma) = \bigcup_{t \leq t_0} \phi_t(\gamma x) \ \ with \ \ \gamma x \in S(\Gamma), \tag{3.33}$$

$$W^U(\Gamma) = \bigcup_{t \geq t_0} \phi_t(\gamma x) \;\; with \;\; \gamma x \in U(\Gamma). \tag{3.34}$$

The local invariant manifolds are directly linked to the subspace of the monodromy matrix $\mathbf{M} = \Phi(T_t)$. In fact, according to the stable manifold theorem for periodic orbit [75], the local stable and unstable manifolds $W^S(\Gamma)$ and $W^U(\Gamma)$ are tangent to the corresponding stable and the unstable subspaces $E^S(\Gamma)$ and $E^U(\Gamma)$. Therefore, the eigenvectors of the monodromy matrix allows to numerically approximate the local stable and unstable manifolds. Then, the global stable and unstable manifolds can be numerically propagated as shown in equations (3.33) and (3.34). Finally, considering again the periodic orbit Γ in the system γf of dimension n, with n_S characteristic exponents with negative real part and n_U characteristic exponents with positive real part. There will be $n_C = n - n_S - n_U$ characteristic exponents with zero real part. Then, a n_C-dimensional centre manifold of the periodic orbit $W^C(\Gamma)$ exists.

The eigenvalues and the eigenvectors of the monodromy matrix are related to the characteristic exponents that measure the rate of departure from the reference orbit given an initial small perturbation, allowing to numerically approximate the local stable, unstable and centre invariant manifolds. Hence, the knowledge of the eigenstructure of the monodromy matrix allows to determine the local geometry of the state space around the periodic orbit (i.e. the behaviour of trajectories in the neighbourhood of the periodic orbit). Looking at the case of coupled orbit-attitude dynamics, the monodromy matrix can be subdivided in 4 sub-monodromy matrices as:

$$\mathbf{M} = \begin{bmatrix} \mathbf{M}_{Orb} & \mathbf{M}_{OrbAtt} \\ \mathbf{M}_{AttOrb} & \mathbf{M}_{Att} \end{bmatrix}, \tag{3.35}$$

where each sub-matrix is a 6×6 block: $\mathbf{M}_{Orb}$ is referred to orbital dynamics $\{\mathbf{f}_x, \mathbf{f}_v\}$ and orbital state $\mathbf{x}_{Orb}$; $\mathbf{M}_{AttOrb}$ to attitude dynamics $\{\mathbf{f}_q, \mathbf{f}_\omega\}$ and orbital state $\mathbf{x}_{Orb}$; $\mathbf{M}_{Att}$ to attitude dynamics $\{\mathbf{f}_q, \mathbf{f}_\omega\}$ and attitude state $\mathbf{x}_{Att}$. Without additional perturbations, such as Solar Radiation Pressure or second order deviations in the main gravitational attraction due to the finite extension of the spacecraft, there is no cross-coupling between attitude states and orbital dynamics and, thus, $\mathbf{M}_{OrbAtt} = \mathbf{0}$. Since this effect is small compared to the other cross-coupling directions, the assumption that led to have the upper right block of the matrix equal to zero is acceptable in the vast majority of the applications. It should be noted that the upper and lower diagonal 6×6 sub-matrices refer separately to the orbit dynamics and to the attitude dynamics. The eigenstructure of the sub-matrices of $\mathbf{M}$ can be associated with the de-coupled orbit and attitude manifolds as well.

The algorithm to find and propagate manifolds trajectories works as usual in classical CR3BP. Several fixed points along the periodic orbit-attitude dynamics

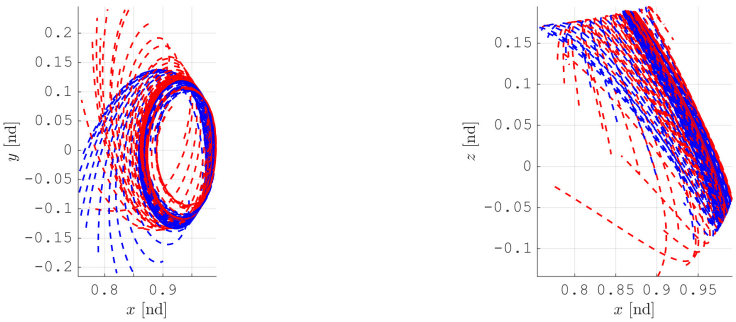

(a) x-y view. **(b)** (b) x-z view.

Figure 3.21: Orbit-attitude manifold from Halo orbit: orbital dynamics (blue is stable - red is unstable).

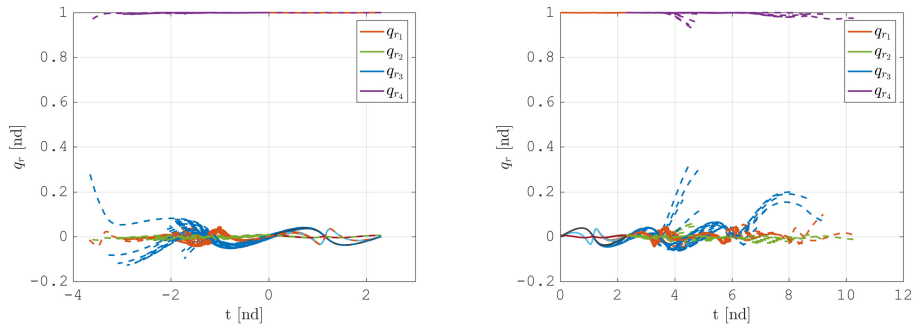

(a) Stable **(b)** Unstable

Figure 3.22: Orbit-attitude manifold from Halo orbit: attitude dynamics

are selected and the monodromy matrices associated to any of these points are computed. When stable and unstable eigenvectors are obtained from the eigenstructure of each matrix $\mathbf{M}$, the state vectors at the selected fixed points are slightly perturbed in direction of the stable or unstable eigenvectors. The perturbed state at each selected fixed point is the initial condition for the trajectory along stable and unstable manifolds. Then, stable manifold trajectories are generated using reverse-time integration, while unstable manifold trajectories are obtained by employing forward-time integration. It must be noted that in orbit-attitude dynamics the eigenvectors have dimension 12: 6 associated to the orbit state $\mathbf{x}_{Orb}$ and 6 to the attitude state $\mathbf{x}_{Att}$. The full state vector of each selected point has to be expressed in synodic reference to perturb along the stable or unstable directions. The attitude part is then converted in inertial reference I for integration, since equations (2.16) and (2.17) are developed in this frame.

Figure 3.21 shows the orbital dynamics associated with the orbit-attitude manifolds of an Halo orbit. In this case, it has been considered an EML1 Halo orbit with period $T = 2.38$ [nd]. The spacecraft is just librating in S (i.e. no spinning motion in synodic reference). The inertia parameter of the spacecraft is $K_3 = 0.2$. The orbit-attitude manifolds result in a slightly different set of trajectories with respect to usual CR3BP Halo manifolds, with slow departing and approaching trajectories. Stable (blue) and unstable (red) trajectories must be considered together with the coupled attitude dynamics associated to the orbit-attitude manifolds. In figures 3.22a and 3.22b the quaternion manifold trajectories are reported respectively approaching and departing from the periodic quaternion evolution along the orbit. The single manifold trajectory is remarkably influenced from the starting point. For example, a closer perilune passage, during the manifold trajectory, determines a sudden variation of the rotational motion because of the stronger Moon's gravity gradient torque (e.g. the unstable attitude trajectories diverging for $t \simeq 4$ [nd] in figure 3.22b). Therefore, a careful planning of approaching and departing orbit-attitude trajectories, while proximity operations are carried out, is needed to achieve the desired mission objectives. Eventual spinning attitude stabilisation would allow a precise tuning and control of the attitude dynamics along natural rendezvous trajectories.

3.8 Natural 6DOF Trajectories for a Cislunar Space Station

Rendezvous trajectories that are possible exploiting manifolds subspace are interesting because they allow a natural and efficient system of transportation. Departing and approaching trajectories are easily obtained, but they still have to be carefully analysed in order to design and optimise the GNC during proximity operations with a large space structure in cislunar space.

One application example is the possibility to depart from a parking orbit that guarantees an easy access to the Moon surface, like the L1 North NRHO reported in figure 3.23. The orbit has a period equal to $T = 2.1$ [nd] and the spacecraft is again librating in the synodic frame, S, with dual-spin attitude stabilisation. The momentum wheel is rotating around the body axis $\hat{\mathbf{b}}_3$ with wheel moment of inertia $I_{3_W} = \frac{I_3}{100}$. The inertia parameter of the spacecraft is $K_3 = \frac{I_2 - I_1}{I_3} = 0.2$.

The departing trajectories begin at the perilune, which in general is not a good point to start a manoeuvre, because of the large gravity gradient acceleration due to the Moon that can be an issue for the attitude dynamics of the spacecraft along its motion. However, it has been here reported to show the influence of different dual-spinning conditions on the natural dynamics of the system. In fact, as reported in figure 3.24, for various angular rates of the momentum wheel the attitude manifold is different, as evident from the related attitude trajectories here analysed. This means that, for the same orbit manifold, it is

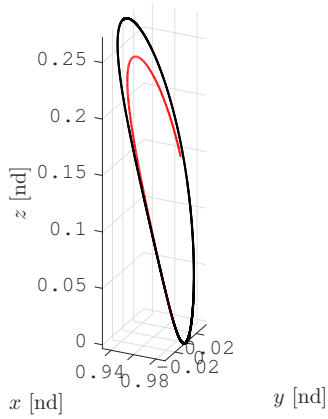

Figure 3.23: Departing trajectory from NRHO: orbital dynamics.

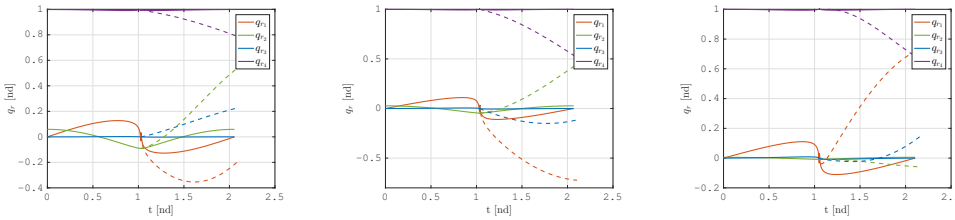

(a) Momentum wheel $\omega_{3_W} = -100$ [nd].

(b) Momentum wheel $\omega_{3_W} = 0$ [nd].

(c) Momentum wheel $\omega_{3_W} = 100$ [nd].

Figure 3.24: Departing trajectory from NRHO: attitude dynamics.

possible to obtain many coupled attitude manifolds according to the attitude stabilisation level. Obviously, this is because of the assumption to neglect the coupling between attitude states and orbital dynamics. Nevertheless, again, the orbit to attitude coupling direction has proven to be not negligible with respect to the attitude to orbit cross-coupling.

Looking at the attitude departing trajectories in figure 3.24, the trajectories have a fast departure from the periodic motion. However, when the final approaching part of the rendezvous operations is considered, the requirements might change with respect to the undocking and departure phase. In fact, there might be interest in having a trajectory that slowly approaches the rendezvous point and, thus, to the cislunar station. The velocity associated with the manifold departure or approach to the periodic orbit can be associated to the stability level of the periodic motion. With this in mind, the dual-spin method can be effectively used to increase the stability of the attitude dynamics and have a slow departure or approach to the nominal trajectory. In figure 3.25, the NRHO described before is used to analyse an approaching phase, with the rendezvous

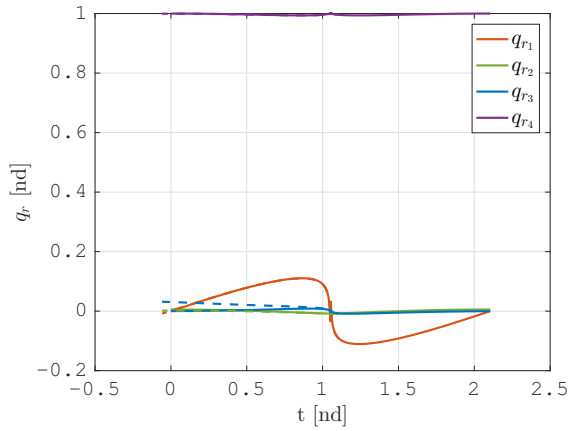

Figure 3.25: Attitude dynamics approaching the periodic motion.

assumed to occur at perilune. The momentum wheel is now assumed in a fast spinning mode and the stability level is higher with respect to the previous case. Indeed, the stable manifold trajectory now approaches the perilune very smoothly, allowing a safe and natural proximity phase before docking. It is here reminded that low perilune in NRHO is not a safe place to carry out rendezvous and close proximity operations. However, this example is intended to show the enhanced capabilities that are possible exploiting natural orbit-attitude rendezvous trajectories together with attitude stabilisation devices.

Completely different analyses are possible considering DRO. Distant retrograde orbits are characterised by remarkably stable orbit-attitude dynamics. Stable or unstable manifolds do not exist in these cases. For example, looking at figure 3.26, perturbations applied to orbit just result in a slightly perturbed dynamics in the vicinity of the DRO, without any stable or unstable behaviour. The DRO here considered has a period $T = 3.37$ [nd] and the simulated dynamics is without additional stored angular momentum (i.e. spinning wheel is not rotating). The same considerations are possible also looking at the coupled attitude dynamics in figure 3.27. In fact, both the stable ($t > 3.37$ [nd]) and unstable ($t < 0$ [nd]) attitude trajectories remain very close to the nominal periodic motion (0 [nd] $< t < 3.37$ [nd]). This is true for spacecraft not suffering the typical pitch instability related to gravity gradient (i.e. $K_3 > 0$ as discussed in section 3.6). Nevertheless, when a different configuration of the space station is considered, the pitch instability associated to negative inertia ratio (i.e. $K_3 < 0$) makes the attitude dynamics unstable and the manifold trajectories, both stable and unstable, depart from the nominal periodic motion. This condition is of interest when a natural rendezvous with a DRO is sought in terms of attitude dynamics. It must be remarked that unstable attitude motions can be obtained also with a stable inertia configuration ($K_3 > 0$), but in that case the momentum

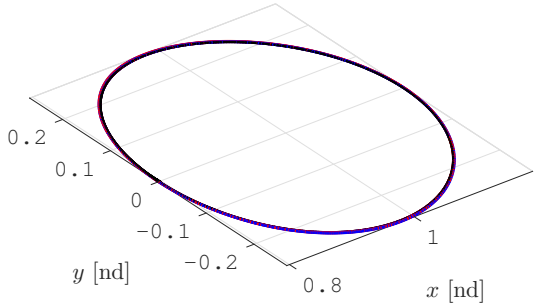

Figure 3.26: Orbital dynamics in the vicinity of DRO.

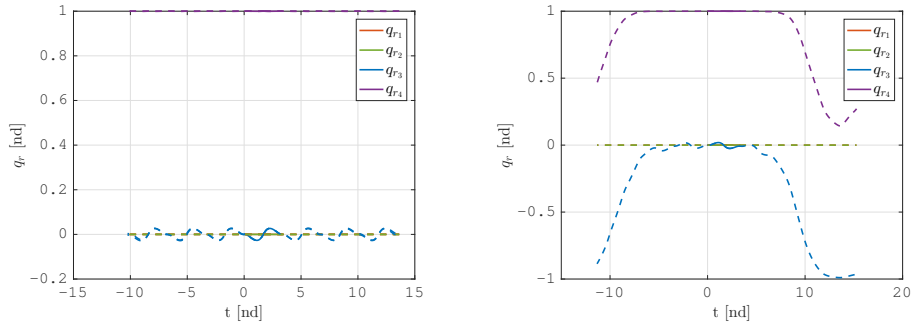

(a) $K_3 > 0$. **(b)** $K_3 < 0$.

Figure 3.27: Attitude dynamics in the vicinity of DRO

wheel has to be counter-spun in order to cancel any gyroscopic stiffness of the space station, as discussed in section 3.5.

CHAPTER 4

Relative Dynamics

> Everything is relative; and only that is absolute.
>
> — Auguste Comte

Relative dynamics for large space structures in cislunar space is derived from the absolute orbit-attitude dynamics discussed and applied in chapter 3, obtaining the relative equations of motion described in section 2.4. The free relative motion between two spacecraft is here noticeably different from the one it is experienced in Keplerian orbits, as described for instance in the Clohessy-Wiltshire equations for circular orbits [76]. An extensive knowledge about coupled 6DOF relative dynamics in non-Keplerian orbits is therefore fundamental to design GNC functions capable to handle the rendezvous problem in cislunar space.

In this chapter, the relative orbit-attitude dynamics in cislunar space is investigated with the purpose to highlight natural motions that can be associated with particular operational capabilities. Then, 6DOF guidance and control functions are discussed, starting from energy optimal relative trajectories and getting to a

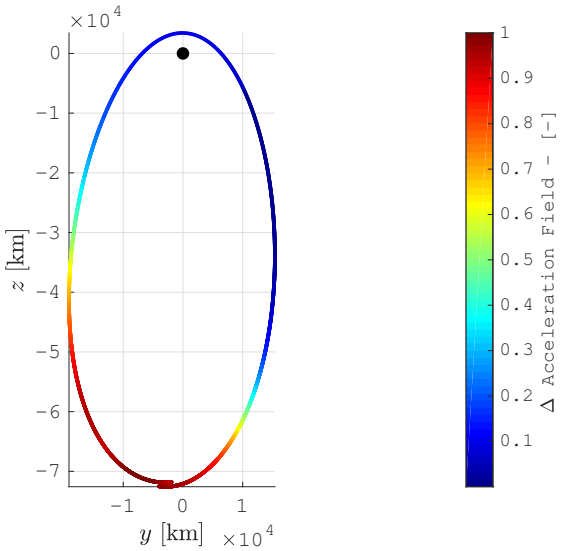

Figure 4.1: Circular restricted (CR3BP) and ephemeris (FER4BP) models comparison in relative dynamics modelling on NRHOs. (Results are normalised with respect to the maximum difference in the relative CR3BP acceleration).

control parametrisation that is useful to implement functional and operational requirements in the proximity trajectories.

Moreover, given the interest for practical applications, the present investigation is started with the assessment of the accuracy level of different modelling approaches (e.g. CR3BP, ER3BP, FER4BP) in dealing with the relative orbit-attitude non-Keplerian dynamics.

4.1 Comparison of Selected Modelling Approaches

Circular restricted and other approximated models are valuable for preliminary analysis of non-Keplerian orbits. Nevertheless, the very peculiar regime of the Earth-Moon system is strongly dependent from the true motion of Earth and Moon, since their orbital eccentricity is not negligible in dictating the force field that maintains the periodicity of non-Keplerian orbits. In particular, for what concern relative dynamics, even in the short period, the ephemeris four-body model is the model to correctly represent the peculiar regime of relative motion in cislunar space.

For example, when a Near Rectilinear Halo Orbit is considered, in figure 4.1, the error between circular restricted model and ephemeris model is particularly

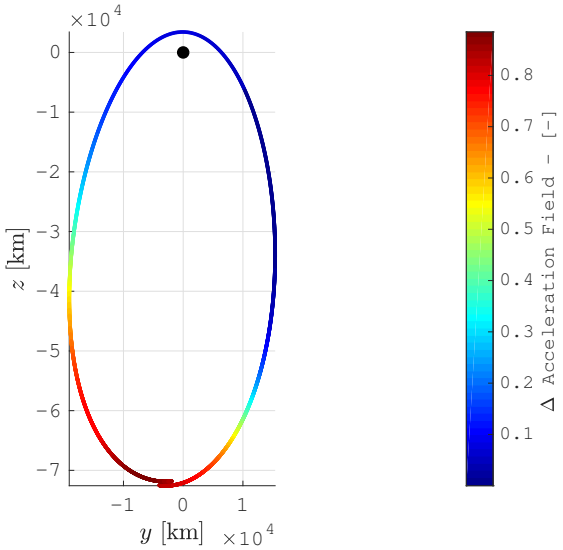

Figure 4.2: Elliptic restricted (ER3BP) and ephemeris (FER4BP) models comparison in relative dynamics modelling on NRHOs. (Results are normalised with respect to the maximum difference in the relative CR3BP acceleration, cf. figure 4.1).

relevant whenever the distance of the target from the Moon is above a certain value: at the apolune of the example orbit, the error in the relative acceleration is 30% in magnitude and 20° in direction. On the contrary, at the perilune of the orbit there is a little deviation, because the close vicinity to the Moon makes all the effects not considered in the circular model of minor importance with respect to the gravitational pull of the Moon, which is well represented in both models. A NRHO has been chosen to perform this comparison because it spans a wide range of distances from the Moon, it is non-planar and it is of great interest for practical applications, as already discussed in this research work and in literature [2]. Hence, this family of non-Keplerian orbits is in the focus for the analyses presented in this section, because of their applicative relevance. Moreover, they allow to highlight several peculiarities of relative dynamics in the Earth-Moon system, and the outcomes here discussed can be easily extended to the other families of cislunar orbits.

The same error comparison can be carried out for the Elliptic Restricted Three-body Problem (ER3BP). In figure 4.2 the error between elliptic restricted and ephemeris models is reported normalised with respect to the maximum error in the CR3BP model, shown in figure 4.1. Note that the error with the ER3BP is, at the apolune, about the 80% of the error obtained with the CR3BP; in general, the qualitative behavior is the same in the two models, but the scale of the magnitude is different.

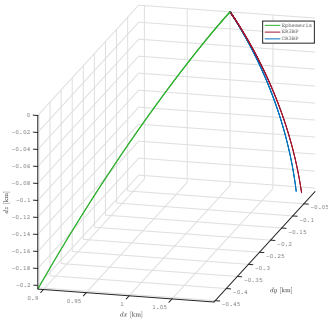

(a) Apolune

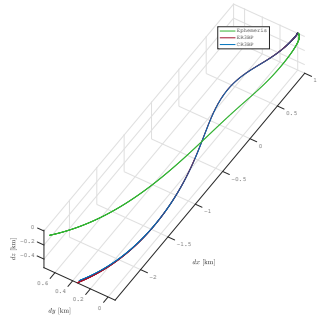

(b) Perilune

Figure 4.3: Relative dynamics comparison from apolune or perilune of NRHO: $\|\mathbf{x}(t_0)\| = 1\,\text{km}$ and $T = 2\,\text{d}$.

The relative dynamics in CR3BP or ER3BP approximates with low accuracy the full ephemerides 4-body model relative dynamics, in particular at the NRHO apolune (i.e. selected location for the RDV operations). The comparison results are shown in figure 4.3a starting the relative dynamics simulation at the apolune and in figure 4.3b starting at the perilune of the NRHO. The relative motion is initialised at close distance between target and chaser (e.g. $\|\mathbf{x}(t_0)\| = 1\,\text{km}$). At the perilune, the relative dynamics in CR3BP and ER3BP approximates with sufficient accuracy just the trend of the full ephemerides model, but then the three motions diverge, and the modelling error is in the order of $\sim 100\,\text{m}$. At the apolune, the three models are strongly in disagreement from the beginning and even in the short period the CR3BP and ER3BP relative dynamics are not valid. Moreover, the differences between CR3BP and ER3BP are more evident at the apolune, even if the two models are quite in accordance, but with great error with respect to the full ephemerides 4-body model (e.g $\sim 500\,\text{m}$). In fact, at the apolune the effects of Earth-Moon eccentricity and of the Sun have a less negligible influence on the relative dynamics compared to the perilune, where

the gravity of the Moon gets the lead in dictating the force field. In table 4.1 the relative dynamics errors with respect to the full ephemeris model are reported for a simulation time $T = 2\,\mathrm{d}$.

This proves that, although the ER3BP introduces an improvement with respect to the CR3BP, both are nevertheless unsuitable to generally represent the dynamics in cislunar space, in particular when NRHOs are considered. The weak points of CR3BP and ER3BP, in terms of environment representations, analysed for absolute dynamics in section 3.3 and for relative dynamics in the present section, may be summarised as follows:

- ◇ Zero or constant eccentricity of the primaries, which does not correctly represent the Earth-Moon system, where the relative eccentricity is not small and has non-negligible variations in time;
- ◇ Lack of the Sun gravity, which is proved in literature to have a significant effect on NRHOs [50, 77].

The addition of the Sun in the ER3BP would overcome this last point with a preliminary approximation of the Earth-Moon eccentricity, but the great increase in complexity of the dynamical equations favours a full ephemeris model, with the gravities of the Earth, the Moon and the Sun.

The approximated models (e.g. CR3BP, ER3BP, BC4BP) do not provide generally valid approximations of the relative dynamics in the Earth-Moon system and their validity should be assessed for each particular case that is analysed. Therefore, they are not considered in the followings of this dissertation. The model that provides the best results to investigate the relative dynamics in cislunar space is the ephemeris four-body model with perturbations.

4.1.1 Validity of Linearised Relative Dynamics

The relative dynamics in cislunar space can be linearised about the orbital motion of the target. In fact, the assumptions behind the linearised translational equations of motions are very simple and it is easy to check if they are satisfied. However, those associated with linearised relative attitude dynamics are very

Table 4.1: Relative Dynamics Error with respect to FER4BP. (cf. figure 4.3).

Model	Orbital Position	Absolute error [m]	Relative error [%]
CR3BP	Perilune	650	20.6
ER3BP	Perilune	640	20.3
CR3BP	Apolune	470	45.9
ER3BP	Apolune	410	40.1

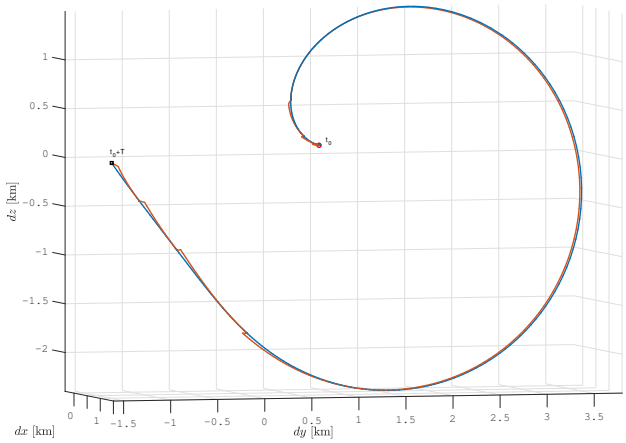

Figure 4.4: Non-Keplerian orbit relative dynamics: non-linear (blue) and linearised with update time 1 d (red). Example orbit EML1 Halo, $\|\mathbf{x}\| \sim 1\,\text{km}$ and t_0 at perilune.

strict and it is very difficult to respect them during operational scenarios or, even during simple simulated settings. They are useful for certain applications like, for instance, stability studies and linear control analyses. Anyhow, linearised relative attitude dynamics will not be employed in the following applications discussed in this dissertation. On the contrary, linearised relative translational dynamics is valid whenever the relative distance between chaser and target is small when compared to the distance between target and primaries. This condition is likely to be satisfied at all times during typical rendezvous operations. In fact, when the relative distance, $\|\mathbf{x}\|$, is below $10^2 - 10^3\,\text{km}$, depending on the target orbital state, the linearised equations (2.38) and (2.40) are valid [50].

Therefore, the linearised dynamics is valid to approximate relative trajectories during rendezvous phases and it can be used to propagate the relative dynamics, updating the relative state vector with a certain frequency. In figure 4.4 the relative dynamics with $\|\mathbf{x}\| \sim 1\,\text{km}$ is simulated for an orbital period, T_t, along an example L1 Halo orbit, comparing the full non-linear dynamics with the linearised one; the simulation is started at the perilune of the orbit and the relative state is updated every day. The ephemeris positions of Earth, Moon and Sun are used to run the models.

Figure 4.5 shows the error trend in synodic reference frame. The update time of the linearised model to maintain the error with respect to the full dynamics below 10 cm is of $\sim 3\,\text{h}$ at apolune and $\sim 40\,\text{s}$ at the perilune of the reference orbit. The acceptable duration of propagation time depends on GNC requirements. In the region close to the apolune (i.e. $t \sim 0\,\text{h}$), the divergence is mainly along the

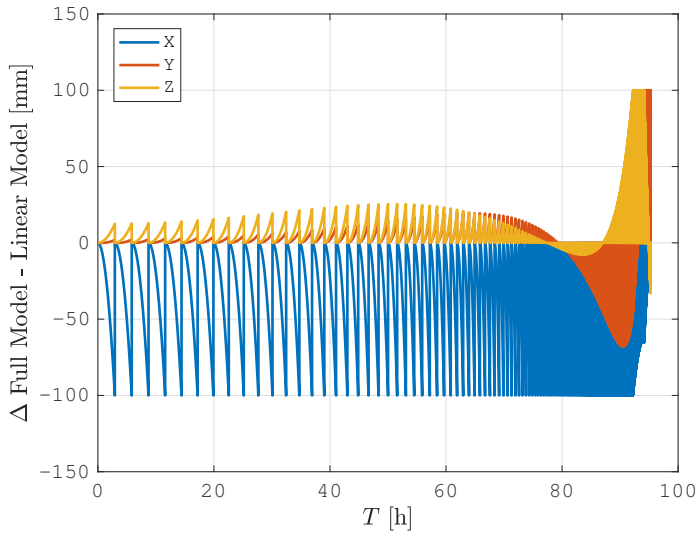

Figure 4.5: Linearisation error trend in synodic reference frame to meet error requirement below 10 cm. Example orbit EML2 NRHO, $\|\mathbf{x}\| \sim 10^2$ km and t_0 at apolune.

x-axis, meaning that linearised model mainly fails in representing the curvature of the NRHO. Close to the perilune (i.e. $t \sim 100$ h), the error is mainly in the direction towards the Moon. The linearisation error is now due mainly to the gravity modelling inaccuracies. From this example, it is evident that the propagation error has an evolution trend that is dependent on the point along the orbit: at the apolune (i.e. $r_{T_M} \sim 10^4$ km) the linearised model gives acceptable results for a longer time with respect to the perilune (i.e. $r_{T_M} \sim 10^3$ km). At the apolune, the assumption to have the relative distance much smaller than the distance of the target from the primaries is definitely valid, with greater tolerance with respect to the perilune.

The linearised full ephemerides relative dynamics is thus valid to compute trajectories in GNC algorithms, assuming to have the relative distance between the two spacecraft below 100 km and to update the relative state vector with a certain frequency, according to the operational requirements.

4.2 Natural Relative 6DOF Dynamics

Natural dynamics in cislunar space, under the influence of the non-Keplerian environment, is of great interest because of the dynamical properties that can be exploited to execute relative transfers and rendezvous trajectories with an extremely limited control cost. The study of natural dynamics (i.e. invariant

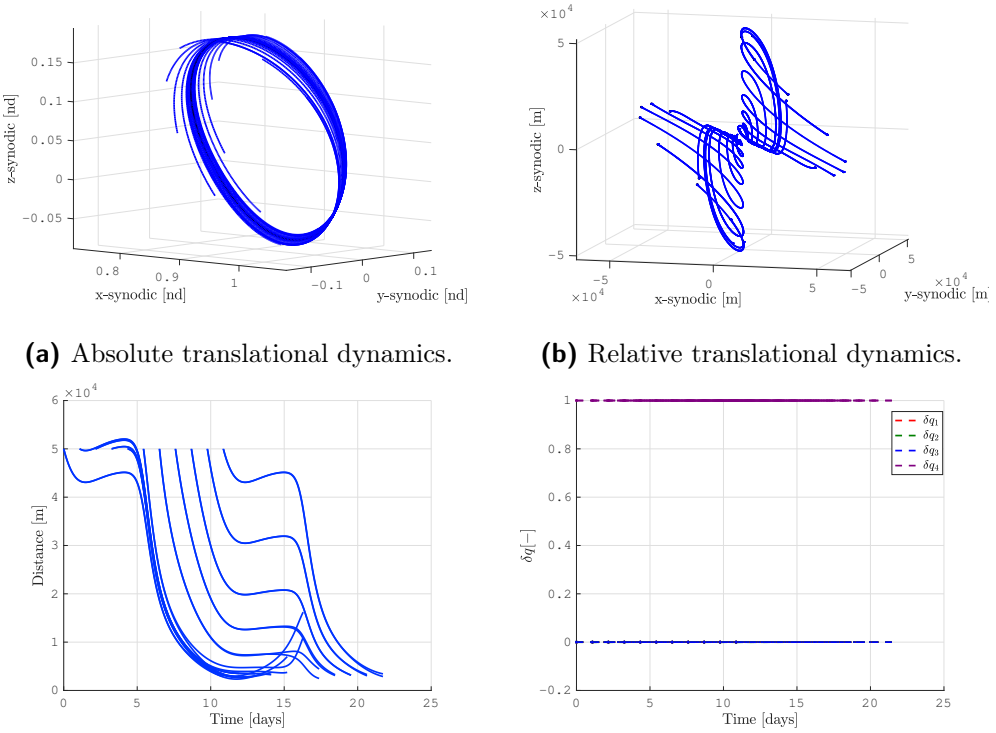

(a) Absolute translational dynamics.

(b) Relative translational dynamics.

(c) Relative distance.

(d) Relative attitude dynamics.

Figure 4.6: Natural approaching 6DOF relative dynamics on an EML1 Halo orbit.

manifolds fo CR3BP) in the three-body environments is very well known from many literature studies: as a matter of fact, stable and unstable manifolds ensure affordable and robust approaching and departure trajectories from most periodic orbits in cislunar space.

In the applications discussed here, the interest is directed towards 6DOF natural dynamics. According to what has been discussed in section 3.8, the coupled orbit-attitude dynamics in cislunar-space allows to compute orbit-attitude manifolds. They are of particular interest in the relative dynamics during a rendezvous phase. In fact, the natural orbit-attitude trajectories can be exploited to easily guide the chaser during its approach to the operational orbit of the target.

This research work considers the possibility to connect controlled trajectories with a final natural drift rendezvous path. In figure 4.6 is shown the 6DOF relative dynamics on a stable manifold approaching the orbit-attitude state of the target in vicinity of the apolune region of a EML1 Halo Orbit. Figure 4.6a shows the classical manifold trajectories approaching to the target orbit. The

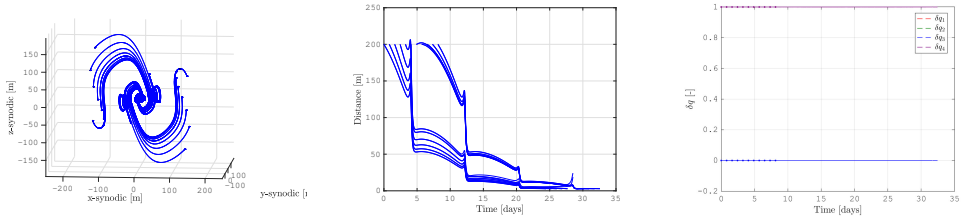

(a) Relative translational dynamics.

(b) Relative distance.

(c) Relative attitude dynamics.

Figure 4.7: Natural approaching 6DOF relative dynamics on an EML1 NRHO.

relative dynamics is of great interest: the relative trajectories in figure 4.6b have a spiral motion toward the target that naturally bring the chaser at close distance from the matching point ($\sim 1\,\text{km}$). A final controlled 6DOF motion can complete the proximity operation. This is done for safety reasons (i.e. avoid natural trajectories up to zero relative distance), and because natural trajectories in FER4BP are just an approximation of CR3BP invariant manifolds. Hence, the real natural dynamics is not perfectly matching up to the end with the stable manifolds trajectory.

During the proximity operations, the natural trajectory can be approached with an active control, which is driving the chaser up to the matching points (i.e. black dots in figure 4.6b), at a distance of ($\sim 50\,\text{km}$) from the target. Then, the rendezvous manoeuvre can be completed with a gentle close-loop control over the natural rendezvous trajectory. This is needed just to correct eventual navigation errors, perturbations and injection inaccuracies. However, the most interesting result is reported in figure 4.6d: the attitude dynamics over an orbital manifold is matched with the one of the target (note that this is true both for unstable and stable manifolds). In practice, orbit manifolds have no relative attitude component: the chaser can be controlled to have a zero relative attitude with respect to the target at the matching point. Then, it will naturally have an absolute attitude dynamics that is continuously matching the target attitude motion up to the docking point, when the two spacecraft will be correctly oriented, naturally. For this reason, as will be discussed in section 4.3.1, simple final relative attitude boundary conditions (e.g. zero relative attitude states at t_f) are relevant also for practical applications.

In figure 4.7 the 6DOF relative dynamics approaching to EML1 NRHO is reported. The trajectories are considered for different target positions, starting from a relative distance of 200 m, and are tuned to arrive in close proximity of the target in $\sim 20\,\text{d}$. As expected, the NRHOs show analogies with the classical Halo orbits, as evident comparing figure 4.7a with figure 4.6b and figure 4.7b with figure 4.6c. In fact, in both cases the approaching trajectories are spiraling

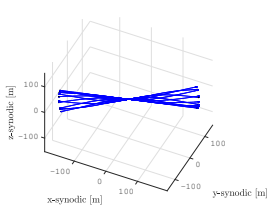

(a) Relative translational dynamics.

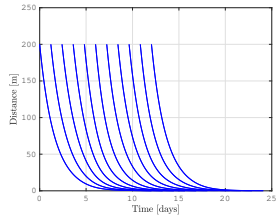

(b) Relative distance.

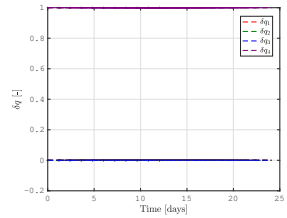

(c) Relative attitude dynamics.

Figure 4.8: Natural approaching 6DOF relative dynamics on an EML1 Lyapunov orbit.

toward the target with sharp variations in relative distance at the perilune of the orbit. Obviously, this fact is extremely emphasised for the NRHO, where also the spiral motion is more complex, with faster lobes when the two spacecraft are close to the Moon. Therefore, it is important to remark that, for NRHOs, a meaningful discussion about proximity operations is possible if the rendezvous point is far from the perilune of the orbit, being in a region close to the apolune of the orbit. In fact, at the perilune of a NRHO, the large gravity of the Moon creates a strong perturbations on the relative dynamics. This effect can be understood looking at figure 4.6c, where steep variations in the relative distance are associated to the perilune passage. Also in this case, a natural dynamics with no relative attitude component exists and the proximity operations can be designed with zero relative attitude at the beginning of the approaching trajectory.

A different condition can be discussed considering planar Lyapunov orbits, as in figure 4.8. Similar discussions to those previously carried out for relative natural dynamics in Halo orbits and NRHOs are possible also in this case. However, the peculiarities of this non-Keplerian family are related to the planarity of the absolute motion, reflected also in the approaching natural dynamics. Furthermore, the large distance from the primaries guarantees very smooth trajectories. The zero relative attitude, in figure 4.8c, highlights again a general outcome for relative natural dynamics in cislunar space: the excitation of orbital manifolds in 6DOF relative non-Keplerian dynamics guarantees no attitude component along the approaching or departing natural dynamics.

A last remark about cislunar natural dynamics is possible considering the central manifold, which is associated with neither approaching nor departing trajectories. In fact, centre subspace characterises the dynamics hovering about a point in non-Keplerian environment. With more details, the hovering motion can exist on the same orbit or on a trajectories remaining always in close vicinity to the original one. In the first case, shown in figure 4.9 for a EML1 Halo orbit,

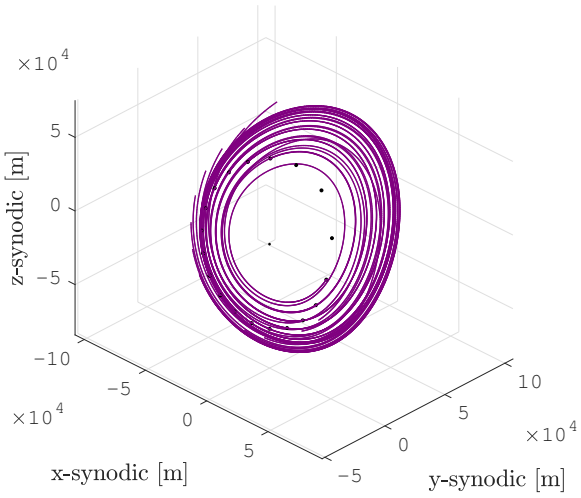

Figure 4.9: Natural periodic trajectories on EML1 Halo orbit.

the chaser position has just an offset in time on the same orbit, resulting in almost circular relative trajectories. The different sizes of the trajectories in figure 4.9 are related to the variation of the central manifold components along the orbit. In the second case, shown in figure 4.10 for the same orbit, the relative motion is set on a proper central manifolds, resulting in a real hovering three-dimensional dynamics, whose shape is connected to the absolute dynamics on the originating orbit. Similarly to stable and unstable dynamics, central subspace can be designed to have zero relative attitude components by exciting only the orbit part of the 6DOF manifolds. In particular, the natural motion in figures 4.9 and 4.10 is associated to null relative attitude dynamics.

The features of stable, unstable and central manifolds can be exploited during the design of proximity operations to satisfy functional and operational requirements. These concepts will be extensively addressed and explained in chapter 5.

4.3 Relative Orbit-attitude Guidance and Control Design

Relative orbit-attitude guidance and control (GC) design shall be based on full non-linear relative dynamics equations (2.36) and (2.37). However, a first insight about the possibilities to control the relative dynamics between two spacecraft in non-Keplerian orbits is available exploiting the linearised translational dynamics together with the full rotational dynamics; they are implemented with the ephemeris four-body model with perturbations.

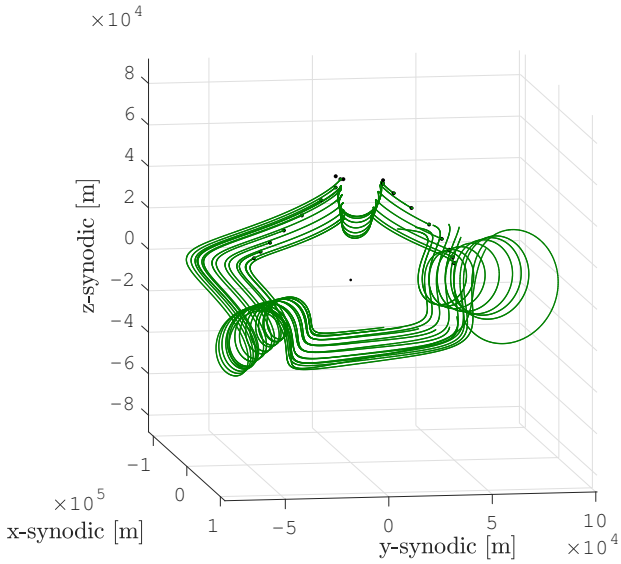

Figure 4.10: Natural central trajectories on EML1 Halo orbit.

4.3.1 Energy optimal 6DOF guidance and control

The requirements for the sustainability of the entire network of systems and operations to realise the forthcoming space programmes in cislunar space and beyond impose a certain attention while analysing and designing the elements that will compose the whole mission scenario. For this reason, this research work starts investigating the relative GC functions to be operated in cislunar space under the framework of energy optimal applications. Obviously, other alternatives are equally valid, like, for example, time optimal or sub-optimal robust solutions. Analogously, different optimality criterions can be foreseen during the design of guidance and control functions or, additional operational and functional requirements can force the design out of the classical optimal control concepts. Hints about possible operational implementations of rendezvous functions will be discussed in chapter 5.

Anyhow, an energy optimal control design is here discussed. In fact, the optimal rendezvous problem can be solved because the absolute dynamics of the chaser is controlled by a control variable,

$$\mathbf{u} = \left[\frac{a_{C_x}}{a_{C_x max}}, \frac{a_{C_y}}{a_{C_y max}}, \frac{a_{C_z}}{a_{C_z max}}, \frac{\alpha_{C_1}}{\alpha_{C_1 max}}, \frac{\alpha_{C_2}}{\alpha_{C_2 max}}, \frac{\alpha_{C_3}}{\alpha_{C_3 max}} \right]^{\mathrm{T}}, \quad (4.1)$$

which is representative of the 6DOF normalised control accelerations, respectively defined in the inertial frame and in the chaser body-fixed frame. Both are expressed in cartesian coordinates, as the relative equations of motion in equations (2.37) and (2.40). For sake of simplicity, it is assumed that $a_{C_i max} = 1\,\mathrm{ms}^{-2}$

and $\alpha_{C_j max} = 1\,\mathrm{rads}^{-2}$, for $i = x, y, z$ and $j = 1, 2, 3$. All six controls are bounded: $-\mathbf{1} \leq \mathbf{u} \leq \mathbf{1}$.

The analysis starts solving the optimal rendezvous problem with a constrained indirect optimisation.

4.3.1.1 Objective Function

The objective function is written according to Lagrange's problem formulation:

$$J = \int_{t_0}^{t_f} \mathcal{L}\, dt, \tag{4.2}$$

where t_0 and t_f are respectively the initial and final time of the rendezvous phase, while $\mathcal{L}$ is the Lagrangian of the problem, whose analytical expression depends on the particular optimisation problem to be solved. Again, in this work the minimum energy problem (i.e. minimum quadratic control) is addressed. Hence, the Lagrangian function is:

$$\mathcal{L} = \frac{1}{2}\left(\mathbf{u} \cdot \mathbf{u}\right), \tag{4.3}$$

where $\mathbf{u}$ is the 6DOF control variable.

4.3.1.2 Boundary Conditions

The boundary conditions of the problem are defined in a way that the overall optimal rendezvous problem would be as simple as possible. However, these boundary conditions are effective to have a well posed problem. The target and chaser initial states and, thus, the relative state at $t = t_0$ are fully assigned:

$$\mathbf{x}(t_0) = [x_0, y_0, z_0]^{\mathrm{T}}, \tag{4.4}$$

$$\dot{\mathbf{x}}(t_0) = [v_{x_0}, v_{y_0}, v_{z_0}]^{\mathrm{T}}, \tag{4.5}$$

$$\delta\mathbf{q}(t_0) = [\delta q_{1_0}, \delta q_{2_0}, \delta q_{3_0}, \delta q_{4_0}]^{\mathrm{T}}, \tag{4.6}$$

$$\delta\boldsymbol{\omega}^{B_C}(t_0) = \left[\delta\omega_{1_0}^{B_C}, \delta\omega_{2_0}^{B_C}, \delta\omega_{3_0}^{B_C}\right]^{\mathrm{T}}. \tag{4.7}$$

At final time $t = t_f$ the rendezvous has to be completed. The relative state is, accordingly:

$$\mathbf{x}(t_f) = [0, 0, 0]^{\mathrm{T}}, \tag{4.8}$$

$$\dot{\mathbf{x}}(t_f) = [0, 0, 0]^{\mathrm{T}}, \tag{4.9}$$

$$\delta\mathbf{q}(t_f) = [0, 0, 0, 1]^{\mathrm{T}}, \tag{4.10}$$

$$\delta\boldsymbol{\omega}^{B_C}(t_f) = [0, 0, 0]^{\mathrm{T}}. \tag{4.11}$$

All the boundary conditions are direct for a total of 26 direct explicit boundary conditions. In this section, the state variables are always related with the control variable.

Further investigations about attitude rendezvous boundary conditions are discussed in chapter 5; in particular, the possibility to have different attitude boundary conditions is addressed. However, as evident from section 4.2, relative attitude states equal to zero at final time is of importance also for practical applications that take into account natural dynamics. Finally, it should be noted that, in real cases, the position vector of the docking points with respect to the centres of mass is not zero. In these situations, docking-enabling conditions should be defined taking into account the coupled orbit-attitude relative dynamics: the boundary conditions at $t = t_f$ are coupled with all the six degrees of freedom.

4.3.1.3 Hamiltonian Function

The general formulation for the Hamiltonian of the system with the state vector $\mathbf{v} = [\mathbf{x}^{\mathrm{T}}\ \dot{\mathbf{x}}^{\mathrm{T}}\ \delta\mathbf{q}^{\mathrm{T}}\ \delta\boldsymbol{\omega}^{B_C\,\mathrm{T}}]^{\mathrm{T}}$, the control vector $\mathbf{u}$, the costate vector $\boldsymbol{\lambda} = [\boldsymbol{\lambda}_{\mathbf{x}}^{\mathrm{T}}\ \boldsymbol{\lambda}_{\dot{\mathbf{x}}}^{\mathrm{T}}\ \boldsymbol{\lambda}_{\delta\mathbf{q}}^{\mathrm{T}}\ \boldsymbol{\lambda}_{\delta\boldsymbol{\omega}^{B_C}}^{\mathrm{T}}]^{\mathrm{T}}$ and the Lagrangian $\mathcal{L}$, associated with the objective function in equation (4.2), is:

$$
\begin{aligned}
&H(\mathbf{v},\mathbf{u},\boldsymbol{\lambda}) = \mathcal{L} + \boldsymbol{\lambda}\cdot[\dot{\mathbf{x}}^{\mathrm{T}}\ \ddot{\mathbf{x}}^{\mathrm{T}}\ \delta\dot{\mathbf{q}}^{\mathrm{T}}\ \delta\dot{\boldsymbol{\omega}}^{B_C\,\mathrm{T}}]^{\mathrm{T}} \\
&= \mathcal{L} + \boldsymbol{\lambda}_{\mathbf{x}}^{\mathrm{T}}\dot{\mathbf{x}} + \boldsymbol{\lambda}_{\dot{\mathbf{x}}}^{\mathrm{T}}\Big(\boldsymbol{\Xi}(t)\mathbf{x} + \delta\mathbf{a}_S + \delta\mathbf{a}_{SRP} + \mathbf{a}_C\Big) \\
&+ \boldsymbol{\lambda}_{\delta\mathbf{q}}^{\mathrm{T}}\Big(\frac{1}{2}\boldsymbol{\Omega}(\delta\boldsymbol{\omega}^{B_C})\delta\mathbf{q}\Big) \\
&+ \boldsymbol{\lambda}_{\delta\boldsymbol{\omega}^{B_C}}^{\mathrm{T}}\Bigg(\mathbb{I}_C^{-1}\Big\{-[\delta\boldsymbol{\omega}^{B_C}\times]\mathbb{I}_C\delta\boldsymbol{\omega}^{B_C} - [\delta\boldsymbol{\omega}^{B_C}\times]\mathbb{I}_C\mathbf{R}\,\boldsymbol{\omega}_T^{B_T} \\
&+ \mathbb{I}_C[\delta\boldsymbol{\omega}^{B_C}\times]\mathbf{R}\,\boldsymbol{\omega}_T^{B_T} - [\mathbf{R}\,\boldsymbol{\omega}_T^{B_T}\times]\mathbb{I}_C\delta\boldsymbol{\omega}^{B_C} + \mathbf{n}_C \\
&- \mathbf{R}\Big[(\mathbf{R}^{\mathrm{T}}\mathbb{I}_C\mathbf{R} - \mathbb{I}_T)\mathbb{I}_T^{-1}(\mathbf{n}_T - [\boldsymbol{\omega}_T^{B_T}\times]\mathbb{I}_T\boldsymbol{\omega}_T^{B_T}) \\
&+ [\boldsymbol{\omega}_T^{B_T}\times](\mathbf{R}^{\mathrm{T}}\mathbb{I}_C\mathbf{R} - \mathbb{I}_T)\boldsymbol{\omega}_T^{B_T}\Big] - \mathbf{R}\,\mathbf{n}_T\Big\} + \boldsymbol{\alpha}_C\Bigg).
\end{aligned}
\tag{4.12}
$$

The part of the Hamiltonian that depends on the controls, $\mathbf{u}$, is:

$$
H^*(\mathbf{u},\boldsymbol{\lambda}) = \frac{1}{2}(\mathbf{u}\cdot\mathbf{u}) + \boldsymbol{\lambda}_{\dot{\mathbf{x}}}^{\mathrm{T}}\mathbf{a}_C + \boldsymbol{\lambda}_{\delta\boldsymbol{\omega}^{B_C}}^{\mathrm{T}}\boldsymbol{\alpha}_C, \tag{4.13}
$$

where the physical dimensions are uniformed because of the costate dimensions definition (i.e. normalised non-dimensional Hamiltonian function, according to the control variable expression in equation (4.1)).

4.3.1.4 Optimal Control Problem

Optimal control problem solved through indirect methods, which are based on the calculus of variation, requires a strong analytical effort to derive all the necessary quantities for the solution of the problem itself.

The costate dynamics adjoint equations are obtained as:

$$\dot{\boldsymbol{\lambda}} = -\left(\frac{\partial H}{\partial \mathbf{v}}\right). \tag{4.14}$$

It can be noted how the costates dynamics is intimately related to the state dynamics and the results are obviously dependent from the formulation of the relative dynamics itself. For example, the dynamics of the costates associated with translational dynamics result to be linear because of the linear dependance from $\mathbf{x}$ and $\dot{\mathbf{x}}$ in the relative dynamics, equation (2.40). Thus, when the Hamiltonian is differentiated with respect to these state variables the dependance from the state itself is lost: the translational costates evolution is just a function of the translational costates themselves and of the target (i.e. reference) trajectory in time. This is not the case for the costates related with the rotational motion, which is formulated through non-linear equations. Here, the attitude states are directly influencing the rotational costates dynamics that, in general, is non-linear.

For what concern the control equations for the minimum energy problem (in equation (4.3)), the 6 controls enters the Hamiltonian quadratically and, therefore, the optimal control results to be linearly dependent from the costates. In particular, control equations can be derived from:

$$\left(\frac{\partial H}{\partial \mathbf{u}}\right) = \left(\frac{\partial H^*}{\partial \mathbf{u}}\right) = 0. \tag{4.15}$$

The result of the previous equations states that the control actions have a magnitude defined by the magnitude of the costates associated with the velocities and a direction parallel and opposite to it:

$$\mathbf{u} = [-\boldsymbol{\lambda}_{\dot{\mathbf{x}}}^{\mathrm{T}}, -\boldsymbol{\lambda}_{\delta\boldsymbol{\omega}^{B_C}}^{\mathrm{T}}] \text{ with } \|\mathbf{u}\| < u_{max}. \tag{4.16}$$

4.3.1.5 Optimality and Transversality Conditions

The solution of the optimal control problem requires additional constraints with respect to the boundary conditions on the state at $t = t_0$ and $t = t_f$. In fact, the number of variables involved is definitely increased.

Optimality conditions, given the complete set of 26 direct boundary conditions on the initial and finale states, results in trivial conditions. In fact, the terms

$d\mathbf{x}(t_0)$ and $d\mathbf{x}(t_f)$ are zero, and the costates at initial time, $\boldsymbol{\lambda}(t_0)$, and at final time, $\boldsymbol{\lambda}(t_f)$, are free.

Transversality conditions, which are additional necessary conditions for optimality, are dependent only from the Hamiltonian, given again the complete set of 26 direct boundary conditions on the initial and final states. The initial Hamiltonian, $H(t_0)$, is free because t_0 is assigned. On the contrary, the final time t_f is not assigned, because it is unknown: in the considered rendezvous problem, the time of flight (TOF) is free. Hence, the transversality condition at the final time states $H(t_f)dt_f = 0$, constraining the Hamiltonian evaluated at t_f as:

$$H(t_f) = 0. \tag{4.17}$$

4.3.1.6 Numerical implementation

The numerical implementation of the optimal control problem is based on a Matlab code. A finite difference code based on collocation (three-stage Lobatto IIIa formula) integrated into Matlab is applied to solve the two-points boundary value problem (TPBVP) associated with the indirect methods for the optimal control.

The initial guess for the costates is chosen as a set of zeros in the minimum energy problem. The differential equations are integrated with a variable-step, variable-order (VSVO) Adams-Bashforth-Moulton solver.

To solve the optimal control problem with a free final time exploiting this numerical implementation, the final time must be included as an unknown parameter. This is accomplished by non-dimensionalising the time variable as:

$$\tau = \frac{t}{t_f} \rightarrow \frac{\mathrm{d}}{\mathrm{d}\tau} = t_f \frac{\mathrm{d}}{\mathrm{d}t} \text{ with } \tau \in [0, 1]. \tag{4.18}$$

4.3.1.7 Example Optimal Control Results

An example result about the optimal control 6DOF rendezvous is shown, to prove the capabilities of the developed method, in figures 4.11 and 4.12. Initial relative states are random, while the target is moving with the periodic orbit-attitude dynamics close the apolune of a EML1 NRHO. The control output is reported in terms of forces and torques in figures 4.11c and 4.12c. The chaser has a mass $m_C \sim 10^3\,\mathrm{kg}$ and the inertia moments $\mathbb{I}_C \sim 10^4\,\mathrm{kgm}^2$. The control action, as expected, is large only at departure point and arrival point: consequently, the required control energy is minimised. Note that, the control force is linear in time, while the control torque has an evident non-linear trend. The relative

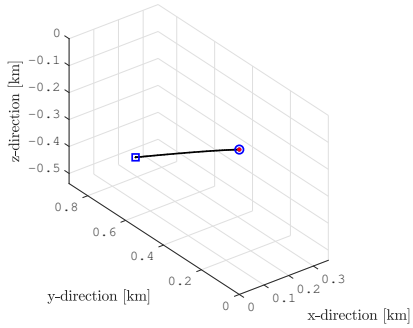

(a) Relative trajectory (t_0 blue square, t_f blue circle).

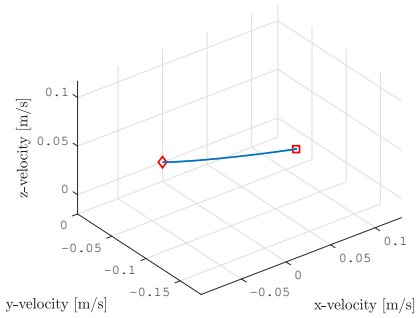

(b) Relative velocity (t_0 red square, t_f red diamond).

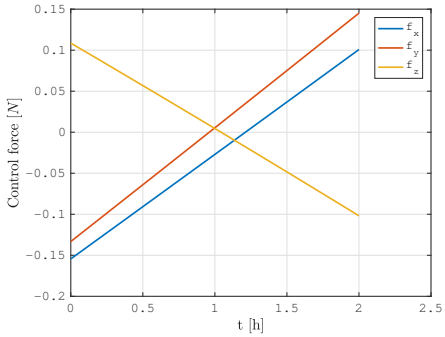

(c) Control force. Chaser mass: $m_C \sim 10^3$ kg.

Figure 4.11: Optimal control for 6DOF relative dynamics: translational dynamics. TOF: $t_f = 2$ h. Initial relative states random.

velocities in figures 4.11b and 4.12b are extremely small and to minimise the control effort the required time is long.

The algorithm provides an optimal solutions of the problem, in terms of quadratic control effort, but it requires quite few analyses to select a good initial guess for the costates. In particular, that is necessary when the initial relative states are complex and the rendezvous trajectories are not straightforward. For simple rendezvous scenarios, as the one discussed in this section, a vectors of zeros works decently as initial guess for the costates.

4.3.2 Direct Transcription of the Rendezvous Problem

Indirect methods rely on analytical relations and the conditions for optimality require the solution of a two-point boundary value problem. It is well known

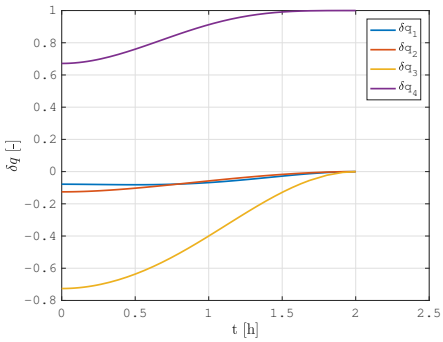

(a) Relative quaternion.

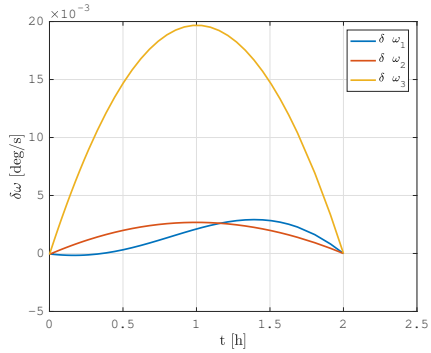

(b) Relative angular velocity.

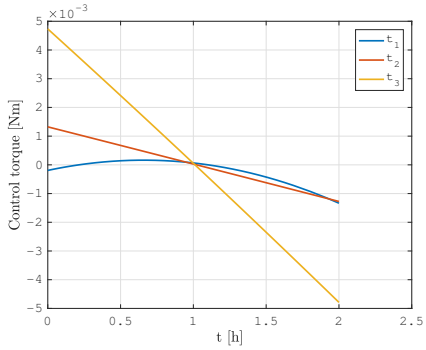

(c) Control torque. Chaser inertia moments: $\mathbb{I}_C \sim 10^4\,\mathrm{kgm}^2$.

Figure 4.12: Optimal control for 6DOF relative dynamics: rotational dynamics. TOF: $t_f = 2\,\mathrm{h}$. Initial relative states random.

that indirect methods ensures rapid convergence of good starting guesses, but most of the difficulties are related to the high sensitivity to the initial costates. As previously noted, it is difficult and time consuming to select a good initial guess for the costates. Their lack of physical meaning makes also difficult to have insights about their behaviour, in order to understand which could be a possibile good initial guess from previously converged solutions. In particular, these difficulties arise when a solution in the full non-linear relative dynamics is sought.

For the applications investigated in this research work, a more robust method is needed: the optimal rendezvous problem is now solved with direct methods, parametrising only the control variable and converting the optimal control problem into a non-linear programming (NLP) problem, with a direct transcription process. Direct methods requires often a large computation effort but they are usually robust and can accommodate path constraints.

The solution of a generic non-linear programming problem is a vector of n variables, $\mathbf{p}$, that minimises a scalar objective function:

$$\min_{\mathbf{p}} F(\mathbf{p}), \tag{4.19}$$

subject to m equality or inequality constraints:

$$\mathbf{b}_l \leq \mathbf{c}(\mathbf{p}) \leq \mathbf{b}_u, \tag{4.20}$$

and bounds:

$$\mathbf{p}_l \leq \mathbf{p} \leq \mathbf{p}_u. \tag{4.21}$$

The equality constraints are obtained imposing $\mathbf{b}_l = \mathbf{b}_u$.

With direct methods, the differential dynamic constraints of the indirect optimal rendezvous problem are converted into a set of algebraic constraints.

4.3.2.1 Control Parametrisation

From the results available, which have been discussed in section 4.3.1, it is possible to select a parametrisation for the control variable that is as close as possible from the available solution of the optimal rendezvous problem solved with indirect methods: linear control for the translational dynamics and polynomial control for the rotational dynamics.

However, now the 6DOF dynamic is fully non-linear and the solution for a general rendezvous problem has to be found. For this reason, more flexibility in the control variable parametrisation is sought, without discretising the rendezvous path in multiple arches connected by patch points, and without increasing too much the complexity of the control actions. Different parametrisation possibilities have been analysed, but the best results have been obtained with polynomials and Fourier series representations. Fourier series are known to have good convergence properties and polynomials are simple and effective, especially considering the optimal control available from indirect optimisation methods.

Practically, polynomials up to the third degree and Fourier series up to the fourth order are used. The limitations in the degree of the expansions are imposed to limit the number of involved parameters, thus, the dimension n of the NLP problem. These possible parametrisation options proved to have acceptable convergence properties and allowed to find a solution for the general rendezvous problem. As example, the control parametrisation with a second degree polynomial for the translational control and a with a fourth order Fourier series for the rotation control results in:

$$\mathbf{a}_C(t) = \mathbf{a}_0 + \mathbf{a}_1 \left(\frac{t}{t_{ref}}\right) + \mathbf{a}_2 \left(\frac{t}{t_{ref}}\right)^2, \tag{4.22}$$

$$\boldsymbol{\alpha}_C(t) = \frac{\boldsymbol{\alpha}_0}{2} + \sum_{k=1}^{4} \left[\boldsymbol{\alpha}_k \cos\left(k\boldsymbol{\tau} \frac{t}{t_{ref}} \right) + \boldsymbol{\beta}_k \sin\left(k\boldsymbol{\tau} \frac{t}{t_{ref}} \right) \right], \tag{4.23}$$

where $\mathbf{a}_i$, $\boldsymbol{\alpha}_i$, $\boldsymbol{\beta}_i$ and $\boldsymbol{\tau}$ are 3×1 parameters vectors defined, respectively, in the reference frames I and B_C. The physical dimensions of these parameters are defined according to the physical quantity they are parametrising. These parameters compose the vector of unknown variables, $\mathbf{p} = \left[\mathbf{a}_i^{\mathrm{T}}, \boldsymbol{\alpha}_i^{\mathrm{T}}, \boldsymbol{\beta}_i^{\mathrm{T}}, \boldsymbol{\tau}^{\mathrm{T}}, t_f \right]^{\mathrm{T}}$, to be found solving the problem in equation (4.19). The reference time, t_{ref}, is needed to non-dimensionalise the time, t, in the parametrised control functions. The choice of a reference time equal to the rendezvous TOF has proved to work well.

The dimension n of the NLP associated to the energy optimal rendezvous problem depends from the selected parametrisation of the control functions $\mathbf{a}_C(t)$ and $\boldsymbol{\alpha}_C(t)$. For example, in the case the selected parametrisation is the one shown in equations (4.22) and (4.23), the vector $\mathbf{p}$ has a dimensions of 40: 9 are the parameters for $\mathbf{a}_C(t)$, 30 are the parameters for $\boldsymbol{\alpha}_C(t)$ and 1 parameter is the rendezvous TOF: t_f. Again, note that the selection of $t_{ref} = t_f$ allows a smooth convergence of the control parametrisation.

The constraints in equation (4.20) are obtained from numerical integration of the controlled rendezvous dynamics. In fact, given a generic vector $\bar{\mathbf{p}}$ the relative dynamics has a certain evolution; the relative states at the end of the particular rendezvous simulations have to satisfy the imposed boundary conditions at the final time in equations (4.8) to (4.11). For example, the boundary conditions on the relative position is enforced as:

$$\mathbf{x}|_{\bar{\mathbf{p}}}(\bar{t}_f) = [0, 0, 0]^{\mathrm{T}}, \tag{4.24}$$

where $\mathbf{x}|_{\bar{\mathbf{p}}}$ is the relative position state, output of the relative dynamics, in equation (2.36), with $\mathbf{a}_c|_{\bar{\mathbf{p}}}(t)$.

The bounds in equation (4.21) are imposed to respect the physical meanings of the parameters. For example, the bounds on t_f are:

$$0 \leq t_f \leq t_{f_{Max}}, \tag{4.25}$$

where $t_{f_{Max}}$ is the imposed time limit to complete the rendezvous. The bounds on the remaining parameters are selected in order to have $\|\mathbf{u}(t)\| < u_{max}$ for any $t_0 \leq t \leq t_f$.

The optimality in terms of minimum energy control (i.e. minimum quadratic) is achieved defining the scalar objective function in equation (4.19) as:

$$F(\bar{\mathbf{p}}) = \frac{1}{2} \int_{\bar{t}} \mathbf{u}|_{\bar{\mathbf{p}}}^{\mathrm{T}}(t)\ \mathbf{u}|_{\bar{\mathbf{p}}}(t)\, dt, \tag{4.26}$$

where $\bar{t}$ is the rendezvous time from t_0 to $\bar{t}_f$. The integral is computed numerically, from the control parametrisation functions, knowing just the value of $\bar{\mathbf{p}}$. Therefore, the computation of the objective function is extremely fast. Equation (4.26) is the analogous, in the direct transcription of the optimal rendezvous problem, to equation (4.2), in the Lagrange's formulation of the optimal control problem.

4.3.2.2 Numerical Implementation

The numerical implementation of the optimal control problem is based on a Matlab code. A constrained minimisation algorithm that is integrated into Matlab is applied to solve the non-linear programming problem associated with the direct transcription of the optimal control. The algorithm exploits sequential quadratic programming (SQP) method to solve the rendezvous.

The initial guess for the parameters in the vector $\mathbf{p}$ is random, normally distributed within the bounds for the parameters. The initial guess for the rendezvous TOF is given according to the desired order of magnitude for t_f. The differential equations are integrated with a VSVO Adams-Bashforth-Moulton solver. The numerical evaluation of the objective function is performed with a trapezoidal numerical integration algorithm over a vector equally spaced in time from t_0 to t_f.

4.3.2.3 Example Direct Transcription Results

An example result about the direct transcription control for 6DOF rendezvous is shown, to prove the capabilities of the developed method, in figures 4.13 and 4.14. Initial relative states are random, while the target is moving with the periodic orbit-attitude dynamics close the apolune of a EML1 NRHO. The control output is reported in terms of forces and torques in figures 4.11c and 4.12c. The chaser inertia properties are the same of the previous example about optimal control. The control has been parametrised according to the example functions in equations (4.22) and (4.23). Again, the control action is larger at departure point and arrival point: consequently, the required control energy is minimised. Note that, the control force is almost linear in time, despite it has been parametrised through a quadratic function. In fact, in this case, the minimisation algorithm reduces almost to zero the parameters $\mathbf{a}_2$, related with the second order term. This result is expected and prove the correct convergence to a solution close to the one that could have been available with the indirect optimal control method. Note that since the close relative distance of the chaser with respect to the target, the differences between linear and non-linear translational dynamics are limited.

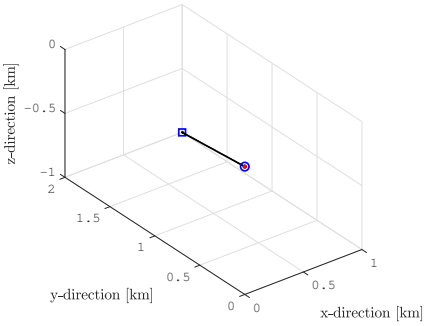

(a) Relative trajectory (t_0 blue square, t_f blue circle).

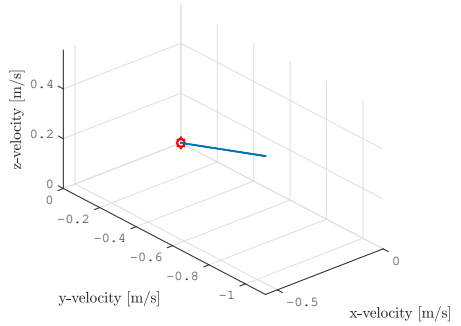

(b) Relative velocity (t_0 red square, t_f red diamond).

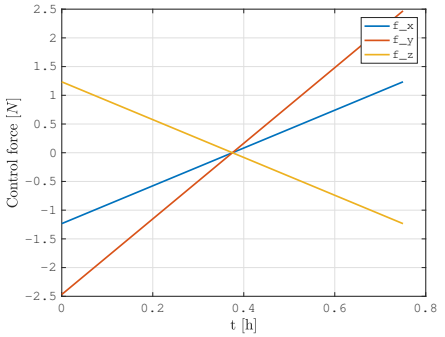

(c) Control force. Chaser mass: $m_C \sim 10^3$ kg.

Figure 4.13: Direct transcription control for 6DOF relative dynamics: translational dynamics. TOF: $t_f = 0.8$ h. Initial relative states random.

The control torque is evidently exploiting the parametrisation capabilities of the Fourier series. The attitude control torque has a regular behaviour, which is again almost linear to minimise the quadratic objective function. The Fourier series parametrisation of the attitude control requires little more time to converge, but it is usually providing better results in terms of control cost. In fact, from the analyses carried out, a simpler polynomial parametrisation for $\boldsymbol{\alpha}_C$ is quick to converge but provides worse solution in terms of cost. Typically, the difference resulted to be in the order of $10 - 20\%$. For what concern, the translational control parametrisation, $\mathbf{a}_C$, there have been no advantages in using the Fourier parametrisation. Thus, the quadratic function discussed in this section proved its effectiveness and efficiency for the direct transcription of the optimal translation rendezvous problem in cislunar space.

The algorithm is highly robust and converges quite easily, except for situations where the requested TOF for the rendezvous is out of the control capabilities

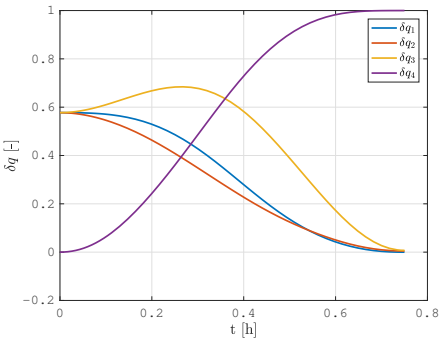

(a) Relative quaternion.

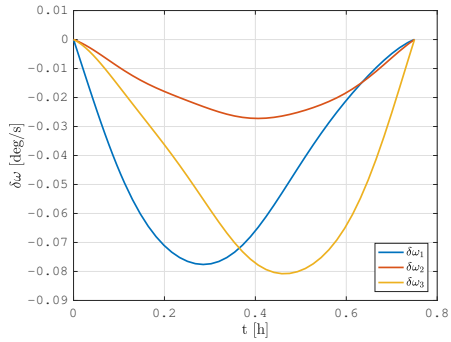

(b) Relative angular velocity.

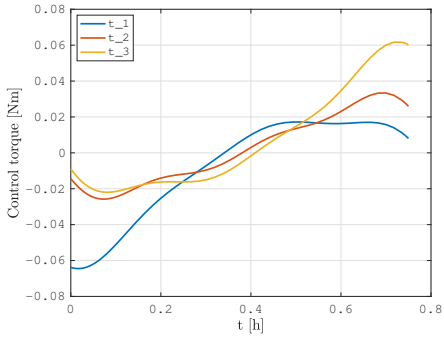

(c) Control torque. Chaser inertia moments: $\mathbb{I}_C \sim 10^4\,\mathrm{kgm}^2$.

Figure 4.14: Direct transcription control for 6DOF relative dynamics: rotational dynamics. TOF: $t_f = 0.8\,\mathrm{h}$. Initial relative states random.

(e.g. too short) or extremely long. In fact, the NLP solver has the authority to change t_f but, in general, the solution stays in proximity of the given initial guess for the TOF. The reason can be sought in the fact that changing the TOF creates a large discontinuities in the value of the objective function and the SQP algorithm avoid to continue the minimisation in that direction. An evidence, of the algorithm robustness is given in figure 4.15, where it is shown the relative trajectory associated with the initial guess in the control parametrisation of the example case reported in figures 4.13 and 4.14. Obviously, the initial guess does not solve the rendezvous problem and the final relative state is not the desired one.

The relative attitude dynamics control has good convergence properties if the constraints on the final relative quaternion is not enforced in vectorial form, but in scalar form. Therefore, the boundary condition on the final relative quaternion is expressed as:

$$\delta q_4^2(t_f) - 1 = 0. \tag{4.27}$$

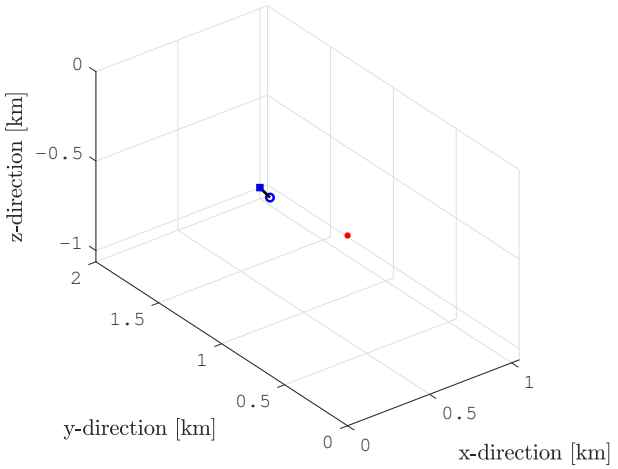

Figure 4.15: Relative trajectory for the initial guess, $\bar{\mathbf{p}}_0$, of control parametrisation. Note that it does not solve the rendezvous problem.

As a final remark, the direct transcription is capable to solve also very complex and long rendezvous problems. They are not very useful for practical application, but they can be of interest to test the performances of the developed method. An example scenario is shown in figure 4.16, where an extremely long and cost effective rendezvous scenario on a L1 Halo orbit is simulated. The control optimality is guaranteed from its linear evolution, analogous to the one available from the indirect methods. However, the direct method provided the solution in a very short time and without any analytical effort.

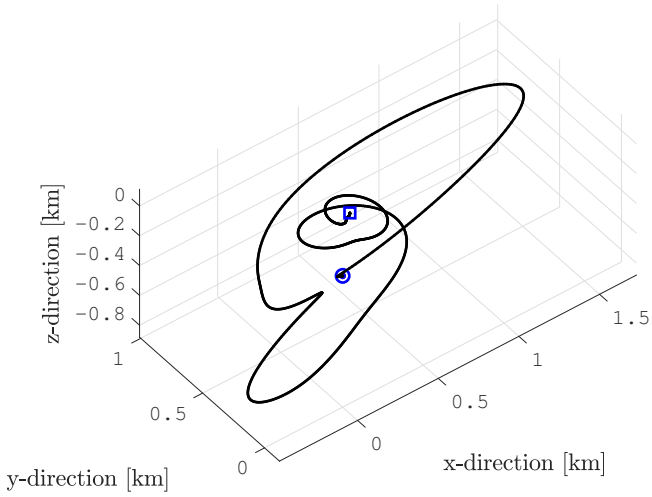

Figure 4.16: Direct transcription control for a test rendezvous scenario: translational dynamics. TOF: $t_f = 10\,\mathrm{d}$.

CHAPTER 5

Rendezvous

> Somebody said . . . when you come to within three miles, you've rendezvoused. If anybody thinks they've pulled a rendezvous off at three miles, have fun!
>
> — Wally Schirra

Rendezvous in space involves a spacecraft already in a operational orbit, which is commonly called target, and a spacecraft that is approaching to it, chaser. The different phases of a generic rendezvous mission have been extensively studied in the past, since the development of the programs Vostok and Gemini. They consist of a series of orbital manoeuvres and controlled trajectories, which have to progressively bring the chaser into the vicinity of the target [78].

This chapter is dedicated to the problem of rendezvous in non-Keplerian Cislunar orbits, exploiting the coupled 6DOF relative dynamics, guidance and control discussed in chapter 4. Rendezvous mission examples are presented and discussed, applying the theoretical findings presented in the previous chapters. Functional and performance GNC requirements are highlighted, together with the numerical

quantities characterising rendezvous operations in such an environment. All the different rendezvous phases are considered: from the phasing, passing through the far-range transfer, up to the close-range trajectories and the final approach.

5.1 Rendezvous Definition

The rendezvous between two spacecraft on Earth orbits within the framework of the restricted two-body problem, is nowadays well studied and tested, thanks to the experience of the ISS. However, this delicate phase is strongly supported by the direct control of the astronauts. The technology to support completely automated rendezvous operations has not yet reached a high level of maturity. Moreover, if the autonomous rendezvous operations have to be conducted in lunar vicinity, the studies are even more preliminary and not completely developed. Furthermore, as already said, studies in literature about rendezvous in non-Keplerian orbits were always limited to point-mass spacecraft.

Possible rendezvous strategies with a large space structure in cislunar space have been recently proposed by different authors [45, 46, 47]. Two operative examples involving relevant families of operational orbits are presented in this chapter, in accordance with the existing feasibility studies about the cislunar space station. The automated transfer vehicles (i.e. chaser) will have to reach the cislunar space station (i.e. target) from different locations, such as the Earth, the Moon or a different non-Keplerian orbit, within a reasonable time and cost. Therefore, a preliminary analysis involves the design of a trajectory connecting the departure point with the desired rendezvous location.

Rendezvous operations that are presented in this work are composed by different phase:

- ◇ *Starting Phase*: the chaser and the target are staged in orbits characterised by different set of orbital parameters. In particular, the target is orbiting in its operational orbit and the chaser is on a loitering trajectory, waiting to start rendezvous operations;
- ◇ *Departure*: the chaser is injected in the transfer trajectory with a first manoeuvre at t_0;
- ◇ *Transfer Phase*: the chaser performs a series of manoeuvres to arrive in the far-range rendezvous region (i.e. $\|\mathbf{x}\| \sim 10^2 - 10^3\,\mathrm{km}$). The details of this phase are dependent from the selected transfer strategy;
- ◇ *Approach Phase*: the chaser arrives in the far-range rendezvous region and acquires an holding point position, before the beginning of the close-range proximity operations. The relative distance between chaser and target is maintained within safety standards and requirements;

- ◇ *Closing phase*: the chaser is injected in the approaching trajectory to arrive in the close-range rendezvous region (i.e. $\|\mathbf{x}\| \sim 1 - 10^1$ km). The characteristics of the approaching trajectories depend on the selected proximity operations plan (e.g. the number of holding points is a design variable). This phase starts after the chaser has entered in the field of view of the target;
- ◇ *Final approach*: a series of manoeuvres progressively reduces the relative distance between the two spacecraft. The orientation of the chaser is maintained aligned with the target, which is rotating in its operational orbit;
- ◇ *Mating phase*: a final continuous manoeuvre is performed to reduce to zero the relative distance between the two spacecraft and brings the chaser at the mating point, before the final contact (i.e. docking or berthing).

5.2 Cislunar Rendezvous Operations

The methods and techniques applied to the cislunar rendezvous problem, discussed in this chapter, are capable to solve the 6DOF guidance and control problem. They have been developed having in mind practical applications and operations. From the results presented in chapter 4, it is evident how much is important to take into account the coupled 6DOF relative dynamics for non-Keplerian GNC design. Furthermore, practical operations and realistic mission scenarios have to consider many other aspects, such as safety of the manoeuvres, navigation performances and system constraints, among the others.

5.2.1 LLO to NRHO Rendezvous

The first operative example of proximity operations in cislunar space assume the target in motion on a L2 South NRHO, with an orbital period of ~ 7 d, an apolune distance from the lunar surface of $\sim 7 \times 10^4$ km and a perilune distance of $\sim 4 \times 10^3$ km. The departure point for the chaser is on a low Lunar orbit (LLO). The target is moving with an orbit-attitude periodic motion as described in chapter 3. This peculiar target orbit-attitude dynamics is characterised by large difference in orbit-attitude velocities between perilune and apolune, and symmetry with respect to the $\hat{\mathbf{x}} - \hat{\mathbf{z}}$ plane. This orbit has been selected as settings for this example rendezvous scenario because of the applicative relevance of NRHOs. In fact, as already said, an eventual space station in cislunar space will be probably staged on a NRHO. This selection can be explained because NRHOs are, among other advantageous characteristics, always visible from Earth and they have long visibility windows over lunar south pole [2].

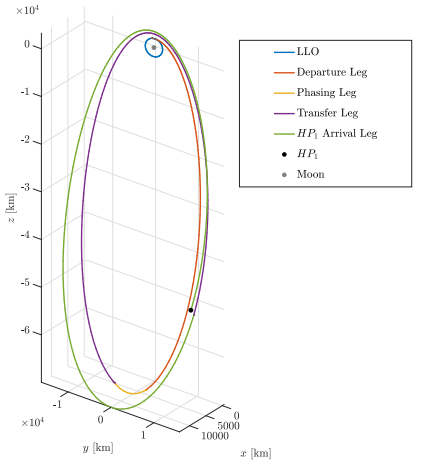

Figure 5.1: Transfer from LLO to HP_1, with intermediate NRHO. Phasing leg duration ~ 1.5 d.

The rendezvous operations, to go from a circular low Lunar orbit with radius 100 km up to the docking conditions with the target, are characterised by the following requirements:

- ◇ Final rendezvous and docking shall be performed in proximity of the apolune of the selected NRHO ($\pm 50°$ of mean anomaly);
- ◇ The overall rendezvous trajectory shall be optimised to minimise the total control energy;
- ◇ The rendezvous trajectory shall pass through designed holding points, HP_i;
- ◇ Passive safety shall be ensured at all time: the holding points HP_i shall lie on the central or unstable manifold of the NRHOs. This allows, in case of misfiring or no firing at all, to remain at bounded distance from the target, without getting in closer proximity, on the central manifold; or to drift away, minimising the risk of any possible risk of collision, on the unstable manifold. In order to have subsequent opportunities to perform the transfer, slow natural dynamics shall be selected. Note that, since the manifolds of the FER4BP NRHO change in time, the rendezvous analysis is strictly coupled with the phasing trajectory analysis [79];
- ◇ Active safety collision avoidance manoeuvre shall be designed as backwards rendezvous trajectories;

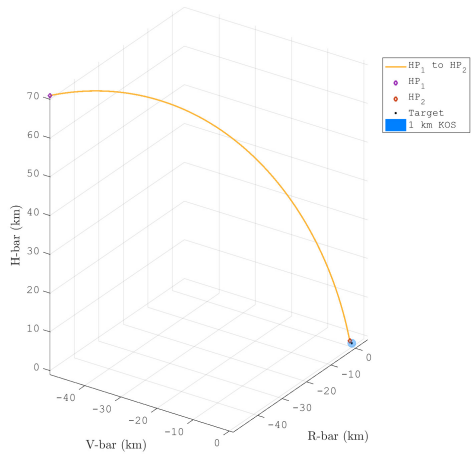

Figure 5.2: Relative dynamics in far-range rendezvous from HP_1 to HP_2. Expressed in LVLH relative to the target.

◇ The last holding point HP_n is set on the border of the keep-out-sphere (KOS) with radius of 1 km;

◇ The docking alignment path point shall lie on the negative R-bar direction, at ~ 100 m from the target;

◇ The navigation cameras and the docking port shall be mounted with an angular offset of 90° in chaser body frame. Hence, the rendezvous trajectory has to perform a proper rotation: to align the docking port at $t = t_f$ and to maintain the target in the camera field of view. This rotation is performed between the last holding point, HP_n, passage and the docking alignment path point.

Table 5.1: Transfer from LLO to HP_1 Parameters.

Transfer Phase	t_{Leg} [d]	Δv [m/s]
LLO Loitering	1	0
Departure Leg	3.03	621
Phasing Leg	1.38	0
Transfer Leg	4.34	53
HP_1 Arrival Leg	6.95	0
Total	16.7	674

In figure 5.1 is shown the transfer of the chaser from a LLO to the first holding point, HP_1, considering absolute FER4BP dynamics. The phases represented in this picture have been obtained according to the research work of Bucci [80]. After a loitering period on the LLO, the chaser is injected in the departure leg, connected to the phasing trajectory, which in the example application has a duration of $\sim 1.5\,\mathrm{d}$. Then, in the transfer phase, intermediate transfer orbits are exploited to arrive at far-range rendezvous distance: $\|\mathbf{x}\|_{HP_1} = 10^2\,\mathrm{km}$. First, the proper transfer leg is used to reduce the relative distance between the two spacecraft. Then, the HP_1 arrival leg is necessary to reach the desired holding point (i.e. approach phase). Trajectory legs are separated by impulsive leg injection manoeuvres, which are reported, together with the leg durations, in table 5.1. Indirect transfer, with phasing and more transfer legs, is longer than a direct ascent trajectory. Nevertheless, intermediate transfer orbits are necessary in order to have a time window to perform trajectory correction manoeuvres and orbit/attitude determination.

After orbit transfer, the chaser arrives at HP_1, situated $10^2 km$ away from the target in the negative along-track direction. At this point, the proximity operations are begun and, since their operative implementation purpose, they are represented in the target centred relative Local Vertical Local Horizontal (LVLH) frame, as defined in figure 5.12, and with absolute Euler $XYZ-$angles with respect to the inertial frame I. The first holding point lies on the central manifold of the NRHO, as per rendezvous design requirements. The consequences of this selection are discussed in section 5.2.1.1.

The closing phase is characterised by far-range rendezvous operations. These are initiated with a transfer arch from HP_1 to a second holding point, HP_2, at the border of the KOS: $\|\mathbf{x}\|_{HP_2} = 1\,\mathrm{km}$. In figure 5.2 the far-range rendezvous arc in the relative LVLH frame, target centred, is shown. The chaser approaches the target from the negative V-bar, with a free drift motion in the 3-dimensional LVLH space. This picture is relevant to understand the relative distance between LAE and DSG during far range rendezvous phase. The HP_2 holding point selection is driven by the preferred strategy for passive safety: HP_2 is set on the NRHO unstable manifold ensuring that if the burn to stop at HP_2 is not performed, or misfired, the chaser will start to safely drift away from the target. It is here remarked that if the close-range rendezvous phase is not started immediately after the completion of the far-range rendezvous phase, an active station keeping action must be performed to avoid the departure of the chaser in the unstable manifold direction. The far-range rendezvous trajectory is energy optimal, obtained applying the optimal guidance and control discussed in section 4.3.1. Nevertheless, the point HP_2 can be also approached with a slightly controlled natural drift on the stable manifold, or with a classical impulsive manoeuvres trajectory. In this phase, the attitude of the chaser is maintained always aligned with the target in order to have the field of view (FOV) of the

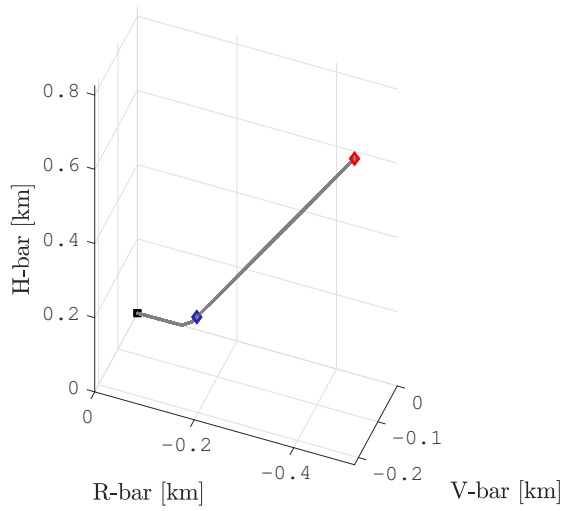

(a) Rendezvous in relative LVLH frame.

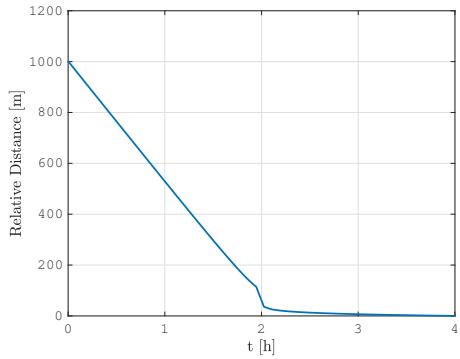

(b) Relative distance.

Figure 5.3: Close-range rendezvous trajectory from the holding point HP_2, (red diamond), to docking, (black dot). Alignment with the docking port axis at a distance of $\sim 100\,\mathrm{m}$ (blue diamond).

sensors correctly oriented for navigation purposes. The required Δv for the far-range rendezvous is $2.68\,\mathrm{m/s}$ and the corresponding TOF is $20\,\mathrm{h}$. This last value is selected because the time of flight shall be long enough to allow state determination and stabilisation of errors.

The close-range rendezvous phase is performed inside the KOS and is composed by a series of manoeuvres capable to reduce the relative distance between chaser and target (i.e. final approach phase). In the simulated application of the developed guidance and control algorithms, the close-range rendezvous is initiated after the holding point $HP_2 = HP_n$ at the border of the KOS. The

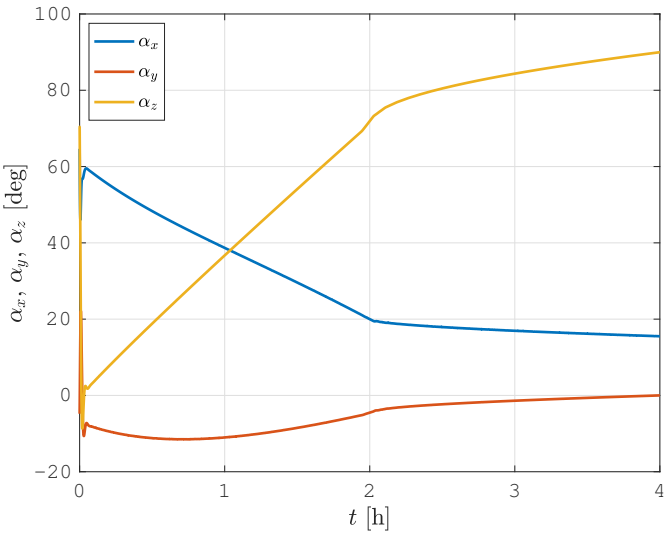

Figure 5.4: Attitude rendezvous trajectory from the holding point HP_2. Absolute attitude dynamics of the chaser, expressed in Euler $XYZ-$angles with respect to the inertial frame I.

final docking approach is designed to occur from the negative R-bar direction to bring the chaser at the docking port, as in figure 5.3a. The control trajectory has been designed imposing the passage through a docking alignment path point (blue diamond in figure 5.3a), in order to connect the holding point HP_2 with the imposed path constraints. In fact, in this example, the direct transcription control moves the chaser away from HP_2 and brings it progressively at the docking alignment point: positioned at $\sim 100\,\text{m}$ from the target, on the unstable manifold approach corridor, mainly aligned with the R-bar direction. The forced translation is maintained within a cone approach corridor defined by the NRHO unstable manifold, again, for strong passive safety enforcement. In fact, in case of problems in the control functions, the unstable manifold guarantees a drift away from the target, but the time scale is slow enough to allow recovery of the nominal operations. Then, from the docking alignment point to the final rendezvous point, the control produces a straight trajectory along the R-bar direction. The relative distance reduction during this last mating phase is very slow, as in figure 5.3b, for safety reasons. The required Δv to perform this rendezvous phase is: $\Delta v \simeq 0.3\,\text{m/s}$ with TOF of $4\,\text{h}$.

The 6DOF trajectories are computed along all the rendezvous phases. During transfer and approach phase the chaser is spinning perpendicular to Sun direction to fulfil power and attitude stability requirements. During far and close-range rendezvous phases the chaser is target pointing, for relative navigation purposes. Moreover, in the final approach phase, the chaser has to align its docking

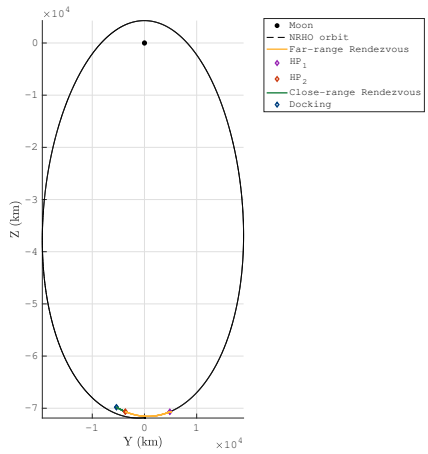

Figure 5.5: Rendezvous operations in Synodic reference frame.

port with the one of the target. The guidance is computed in order to switch from spinning attitude to target pointing to docking alignment, with attitude manoeuvres that are performed in a way there is a smooth transient between the attitude modes. In figure 5.4 the absolute attitude of the chaser is reported during the final approach rendezvous phases. The chaser has to rotate of approximately 55° around one axis to align the docking port and to maintain the target in the supposed camera field of view. In fact, while approaching from HP_2, the chaser is reducing its H-bar distance with respect to the target and a rotation is necessary to maintain the desired alignment. After the docking alignment point, the motion is almost only along R-bar and, therefore, the attitude dynamics is almost coincident with the target nominal periodic attitude. The attitude guidance profile is obtained with the developed direct transcription methods, to minimise the required control energy. The simulation in figure 5.4 is initialised from a random attitude state to verify the robustness of GC functions and, hence, the control system first achieves the optimal attitude profile, then maintains the chaser on the desired path.

An overall glimpse on the overall set of proximity operations is possible analysing the rendezvous trajectories in absolute reference frame. In accordance with the aforementioned requirements, the global rendezvous phase takes place in arc of $\pm 50°$ degrees of mean anomaly around the apolune, setting thus a boundary for the position of HP_1. The far-range rendezvous - yellow line in figure 5.5 - starts at HP_1 before the NRHO apolune, purple circle in figure 5.5, and ends at HP_2, red circle. Figure 5.5 shows also the close-range trajectory between HP_2 and the docking point (docking alignment point is omitted in this figure for clarity). The overall rendezvous from LLO to the target on NRHO require a $\Delta v \simeq 677\,\mathrm{m/s}$

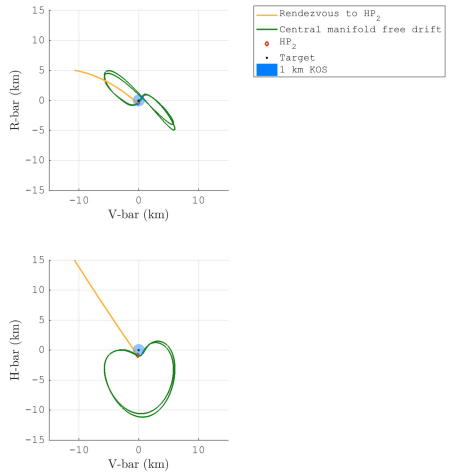

Figure 5.6: HP_2 position in relative LVLH with holding point on the central manifold of the NRHO and following free drift trajectory simulated for 2 NRHO periods.

and a TOF of 17.7 d. The numerical values of both quantities are mainly due to the transfer phase.

5.2.1.1 Passive Safety

Passive safety shall be enforced at all times and, to satisfy this requirement, the rendezvous trajectory has been designed exploiting the features of the relative 6DOF dynamics in cislunar environment. This possibility is allowed by the proposed direct transcription control, through a proper selection of the constraints verified with the numerical simulation of the relative non-Keplerian dynamics.

The holding point (i.e. HP_i) settling on the central manifold entails that, if the control function is not working and the rendezvous manoeuvres are not performed, the chaser remains hovering around the target with a periodic motion. In figure 5.6, the chaser is naturally hovering in proximity of the 1 km KOS, with enough time to have the control system working back again. In this case, weak passive safety is enforced at HP_2.

Nevertheless, if strong passive safety is sought, as inside the KOS, the holding point shall be set on the unstable manifold. In fact, in the example application, HP_2 is settled on the NRHO unstable manifold ensuring a safe drift away from the target in case of failures, as in figure 5.7. Moreover, also the approach

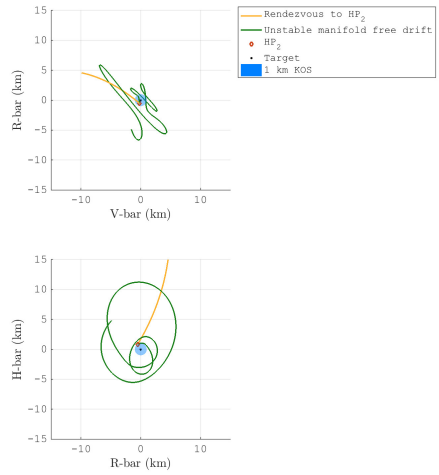

Figure 5.7: HP_2 position in relative LVLH with holding point on the unstable manifold of the NRHO and following free drift trajectory simulated for 2 NRHO periods.

corridor from HP_2 to the the docking alignment point is designed on the unstable manifold, which guarantees natural collision avoidance if a problem occurs.

5.2.1.2 Active Safety

Contingency operations can be managed exploiting active safety enforcement and, in particular, Collision Avoidance Manoeuvres (CAMs) are planned for the chaser to minimise the collision risk with the target when a problem occurs. Collision avoidance manoeuvres are to be intended in addition to nominal passive safety enforcement at all times of the rendezvous and docking operations. If a non-nominal condition occurs, the chaser, after the CAM execution, is retreated to a safe hold point.

The CAMs can be computed with the direct transcription control method, setting a safe 6DOF relative state as a final boundary condition for the algorithm. The CAMs can be designed from any point along the rendezvous trajectories to any safe holding point. In figure 5.8, an example CAM trajectory is shown. The TOF is imposed to be twice the nominal rendezvous time, in a way that no large control action is required. Thus, assuming that the system is undergoing non-nominal operations, in the worse case scenario, even a wrongly commanded CAM manoeuvre can be recovered.

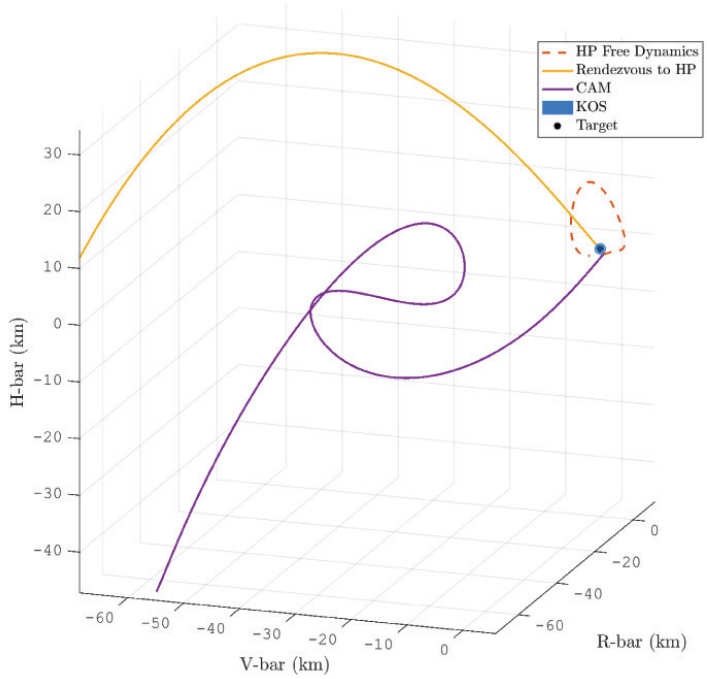

Figure 5.8: Active safety: CAM manoeuvre from HP.

5.2.2 Halo to Halo Rendezvous

The second operative example of proximity operations in cislunar space involves a target's operational EML2 North Halo orbit with $A_z = 10\,000$ km in positive direction. The chaser's parking orbit is a different EML2 North Halo orbit with $A_z = 8000$ km. The rendezvous operations contain a natural heteroclinic transfer between the two orbits on the same side of the Moon, with a connection point on the orbital manifolds. According to the definition introduced by Koon [66], this kind of rendezvous can be denoted as Halo Orbit Insertion (HOI), being the chaser on a different Halo orbit when the sequence of manoeuvres is started. The other type of rendezvous is called Stable Manifold Orbit Insertion (MOI), because in that case, the chaser is travelling from the Earth, or the Moon, and is directly inserted in the stable manifold of the operational orbit.

By assuming the cislunar space station on the selected EML2 Halo orbit, it is reasonable to have the injection point of the stable manifold in the vicinity of the Moon. In this way, it is possible to find many injection points that can be easily reached from different operational scenarios: a LEO, a LLO, the Lunar surface or a safe non-Keplerian parking orbit, similarly to the case discussed

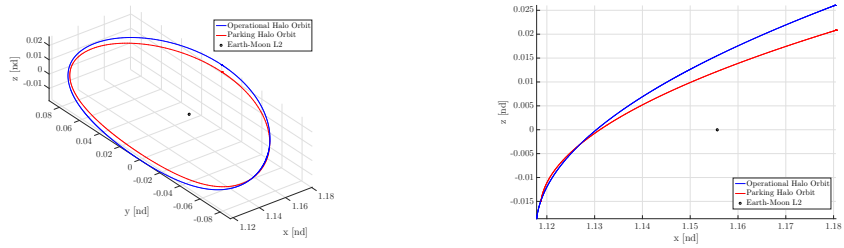

(a) 3D view. **(b)** x-z view.

Figure 5.9: Operational and Parking Halo orbits in normalised S.

in this section. A vast literature addresses the problem of injection in natural transfers, and many solutions were proposed to solve it. For example, in the work of Bernelli [81], a spacecraft is injected on a stable manifold, which is progressively converging to an operational non-Keplerian orbit, from the apogee of an highly eccentric orbit reached from a low Earth orbit (LEO) or a LLO.

The Rendezvous phases discussed in the beginning of this chapter are detailed for this example operational scenario as:

- ◇ *Departure*: the chaser is injected in an unstable manifold of the parking orbit with a first manoeuvre, Δv_1.
- ◇ *Transfer switching manoeuvre*: the chaser is injected in the stable manifold of the target operational orbit. The injection point is at the intersection of the unstable and the stable manifolds. A second manoeuvre, Δv_2, is needed.
- ◇ *Approach phase*: the chaser arrives in proximity of the target and, with a third manoeuvre, Δv_3, is moved very close to the operational Halo orbit.
- ◇ *Closing phase*: a fourth manoeuvre, Δv_4, aligns the chaser with the docking axis of the space station.
- ◇ *Final approach*: a series of manoeuvres, Δv_5 and Δv_{51}, progressively reduces the relative distance between cargo and space station.
- ◇ *Mating phase*: a continuous manoeuvre, Δv_6, is performed to reduce to zero the relative distance between the two spacecraft..

The transfer switching point is assumed to be in the vicinity of the Moon, in the space between Earth and Moon: $x_{SP} < 1 - \mu$. This choice is motivated from the willing to simulate a possible cyclic chaser that is continuously transferring between the operational and the parking orbit; the passage between Earth and Moon allows an easy encounter with a cargo coming from the Earth, the Moon

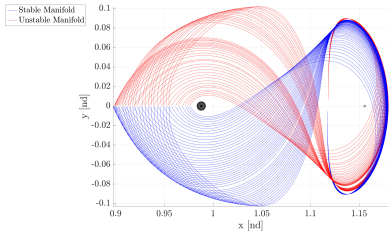

(a) Sub-optimal connections.

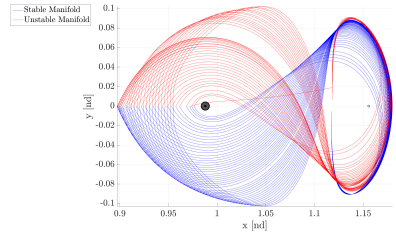

(b) Corrected sub-optimal connections.

Figure 5.10: Possible Heteroclinic connections for $x_{SP} < 1 - \mu$.

or a Low Lunar orbit. The halo orbits considered in this work are shown in figure 5.9, with data reported in table 5.2

First of all, it is important to find an heteroclinic connection between the two Halo orbits: the *transfer trajectory*. In this work, it has been assumed that the chaser and the target are approximately phased in their own orbits according to the chosen transfer, i.e. the target needs the time of the transfer, $t_{transfer}$, to move from its starting point to the ending point of the heteroclinic connection. Such requirement can be always satisfied with a Phasing Phase to be conducted before the Starting Phase of the rendezvous operations; moreover, the proximity operations after the heteroclinic transfer are able to correct some errors in the phasing of chaser and target.

The heteroclinic connection is individuated, computing the unstable manifold of the parking orbit and the stable manifold of the operational orbit. Manifolds can be computed from the eigenvectors of the Monodromy Matrix, $\mathbf{M}$, which is reminded to be the State Transition Matrix, $\mathbf{\Phi}$, evaluated after one orbital period, T_t. The intersections of the two manifolds are analysed on a Poincarè section and different sub-optimal solutions are located for $x_{SP} < 1 - \mu$. Then, a correction procedure is applied to all the sub-optimal solutions, in order to exactly connect in position starting point, switching point and ending point. In figure 5.10 the sub-optimal solutions are shown before and after the correction procedure. Among the selected sub-optimal solution the best one is chosen as the one with the smallest $\Delta v_{transfer} = \Delta v_1 + \Delta v_2 + \Delta v_3$. This best sub-optimal transfer is then optimised with an optimisation algorithm.

Table 5.2: Operational and Parking Halo Parameters.

Name	A_z [km]	T [d]	C [nd]
Operational Halo	10000	14.808	3.149
Parking Halo	8000	14.813	3.150

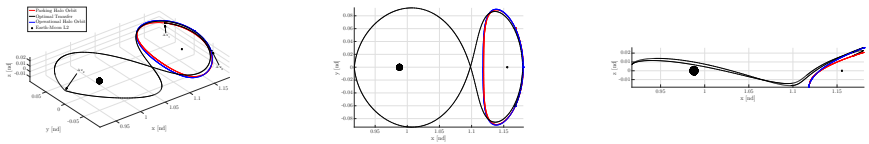

(a) 3D view. **(b)** x-y view. **(c)** x-z view.

Figure 5.11: Optimal transfer.

The transfer optimisation algorithm starts from the already mentioned sub-optimal connection and slightly varies the state vector of the chaser at the starting point, $\mathbf{x}_{Start} = [x_{Start}, y_{Start}, z_{Start}, v_{x_{Start}}, v_{y_{Start}}, v_{z_{Start}}]^{\mathrm{T}}$. The starting position, $\mathbf{r}_{B_{Start}} = [x_{Start}, y_{Start}, z_{Start}]$, is constrained to lie on the Halo orbit. Moreover, also the state vector at the switching point can be varied with the constraint to preserve the continuity in position with the stable manifold of the operational Halo orbit. The algorithm is based on a constrained multiple-shooting corrector with a multi-variable Newton methods [82]. The optimum solution is searched with a derivative-free method. The result of the transfer optimisation algorithm is shown in figure 5.11, and the characteristics of the best heteroclinic transfer are reported in table 5.3. From these data, the low-cost transfer capabilities of invariant manifolds are evident, but the time of flight during this connection can be somewhat too long for certain applications, e.g. humans transportation or emergency cargos. However, this is only a limit for transfers that have to pass between Earth and Moon; in fact, for $x_{SP} > 1 - \mu$, the typical time of transfer is in the order of few days.

After Δv_3 the relative distance between chaser and target is usually in the order of few hundreds of kilometers; in the presented example $|\mathbf{x}| \simeq 150\,\mathrm{km}$. In the following phases, the dynamical tool performs more convenient analyses exploiting a LVLH reference frame. The LVLH reference frame is centred at the barycentre B of the target; $\hat{\mathbf{z}}_{LVLH}$ (R-bar) is always directed towards the Lagrangian point associated to the studied Halo; $\hat{\mathbf{y}}_{LVLH}$ is opposite to the direction of the orbital momentum vector; $\hat{\mathbf{x}}_{LVLH}$ (V-bar) completes the right-handed frame as shown in figure 5.12.

When the chaser enters in view of the target along the R-Bar, Δv_4 is performed to align the chaser with the docking axis of the space station. After this closing phase manoeuvre, the chaser is maintained always aligned with the docking

Table 5.3: Optimal Transfer Parameters.

$t_{transfer}$ [d]	Δv_1 [m/s]	Δv_2 [m/s]	Δv_3 [m/s]	$\Delta v_{transfer}$ [m/s]
26.14	5.49	152.29	0.51	158.29

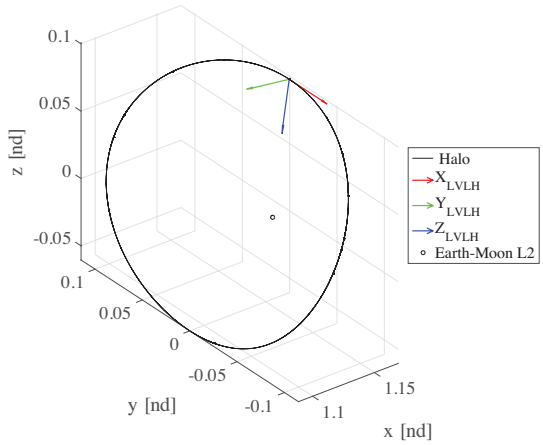

Figure 5.12: LVLH Reference Frame.

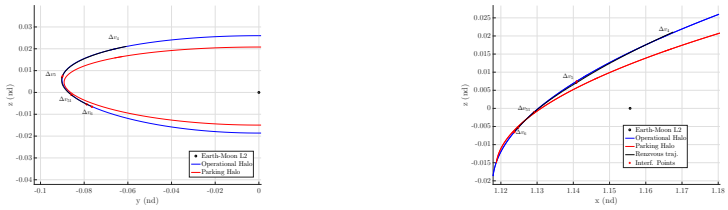

(a) y-z view. **(b)** x-z view.

Figure 5.13: Proximity Operations in Synodic Frame.

axis of the target, within the field of view. During the final approach phase, this alignment is checked at different interface points; the first is at a distance of 200 km from the target, the second at 10 km and the third at 500 m. These interface points are needed to break the rendezvous trajectory with some check-and-go points, in order to have a more gradual and safe final approach.

The different phases after the transfer are computed and optimised with a constrained optimisation algorithm. The cost of the manoeuvre at each interface point and the difference in velocity between chaser and target at the end of the arc, as a preliminary measure of the next Δv, are the objective functions of an optimisation algorithm. In this way, the rendezvous path is evaluated minimising the cost of all the proximity manoeuvres. The constraint is used to reduce the relative distance and maintain the alignment between chaser and target. Thus, at each interfaces point the chaser reaches the desired location with a desired attitude relative to the target. The velocity of the chaser is used as design variable to connect the different interface points minimising the overall Δv cost. It has been assumed to control the dynamics with impulsive manoeuvres and,

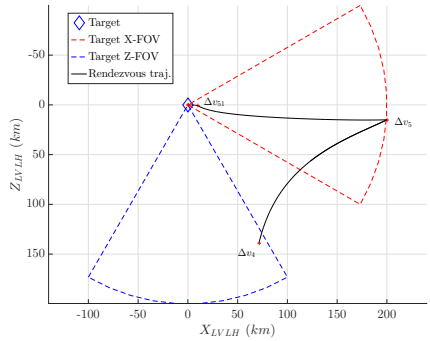

Figure 5.14: Proximity Operations in LVLH Frame, x-z view: Closing and final approach phase.

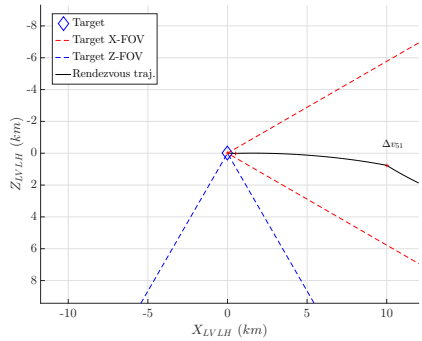

Figure 5.15: Final approach in LVLH Frame, x-z view.

therefore, the actual design variable is not directly the velocity of the chaser, but the instantaneous Δv that are applied at the interface points in order to control the chaser along the rendezvous trajectory with the minimum possible cost. If the optimisation algorithm converges to a feasible solution, the result is a trajectory that matches the final position vector of the target and minimises the Δv cost. The initial guesses at each interface point are obtained randomly. The linear programming optimisation algorithm chosen in this work is a particular version of the barrier method [83, 84], belonging to the class of the so-called interior point methods [85].

In figure 5.13 and figure 5.14 the proximity phases are shown in the synodic and in the LVLH frame. Both frames are useful to analyse the rendezvous, but the latter is more insightful when the distance between chaser and target is in the order of few hundreds of kilometers. In figure 5.14, it can be noted how the closing phase starts when the chaser enters in the field of view along the R-bar, then the following phases are maintained within the field of view in direction of

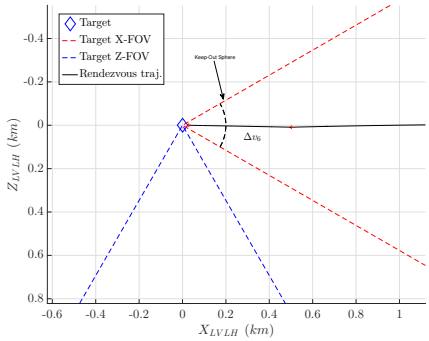

Figure 5.16: Mating phase in LVLH Frame, x-z view.

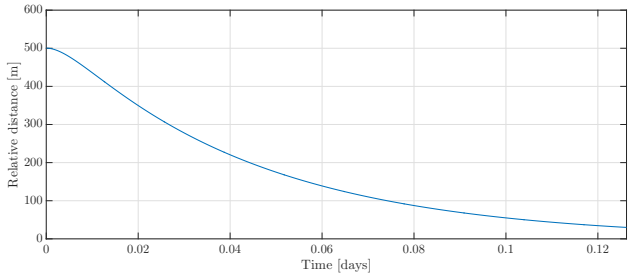

Figure 5.17: Relative distance during mating phase.

the docking axis. Moreover, in the same figure, the approach along the docking axis direction is evident; the interface points follows the approach axis that is changing in time because of the rotation of the space station.

In figure 5.15 is shown a more detailed view of the final approach phase, while the mating phase can be analysed in figure 5.16. In the aforementioned pictures the typical behaviour of relative motion in non-Keplerian orbits is confirmed: the approaching trajectories are almost rectilinear and the carving feature of LEO rendezvous trajectories is missing.

In figure 5.16, the interface point before Δv_6, 500 m from the target, is characterised by an hold in the procedures. In fact, for safety reasons, the chaser cannot enter in the Keep-Out sphere until the authority to proceed is obtained. After the final approach, the mating phase begins.

Table 5.4: Proximity Operations Parameters.

$t_{proximity}$ [d]	Δv_4 [m/s]	Δv_5 [m/s]	Δv_{51} [m/s]	Δv_6 [m/s]	$\Delta v_{proximity}$ [m/s]
3.36	1.27	3.41	2.52	0.44	7.64

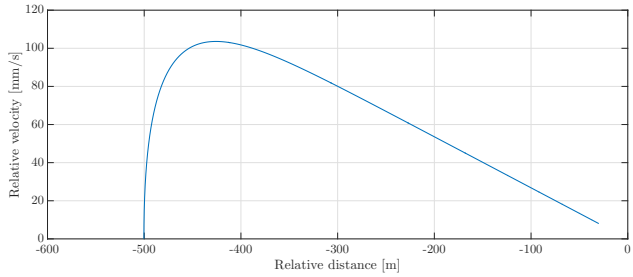

Figure 5.18: Relative velocity during mating phase as a function of relative distance.

In this example application scenario, the control during the mating phase is assumed to be continuous [11]. The final trajectory is here computed using a linear-quadratic regulator (LQR) and the linearised model of relative dynamics for the chaser, described in section 2.4. The relative distance between chaser and centre of mass of the target is reported in figure 5.17, as a function of the time of flight in the mating phase, which last for approximately 3 hours and brings the chaser few meters away from the docking port. In figure 5.18, the evolution of the relative velocity in this phase is presented as a function of the target-chaser distance. In table 5.4, time of flight and Δvs during the proximity operations are reported. Hence, remembering the data in table 5.3, the analysed rendezvous lasts for 29.5 d and requires a total Δv of 165.93 m/s.

Even if the two example applications are different, it should be noted how the current Δv is remarkably lower than the one for the rendezvous operations discussed in section 5.2.1, because of the exploitation of natural manifold dynamics in the Halo to Halo rendezvous. In the LLO to NRHO rendezvous, the transfer is obtained connecting the different transfer arcs with impulsive manoeuvres, resulting in a lower rendezvous efficiency.

5.2.3 NRHO to DRO Rendezvous

Rendezvous operations are influenced by several parameters and the set of possible solutions is wide. Hence, this last section presents additional rendezvous transfers between two non-Keplerian orbits, to better contextualise the rendezvous scenario in cislunar space. The example application considers a spacecraft that has to transfer between NRHOs and DROs.

The transfer phase begin at the perilune of the NRHO, when the chaser is injected into the unstable NRHO orbit-attitude manifold. After a certain time t_1, a first impulsive manoeuvre is performed to target the trajectory towards the DRO. A second impulsive manoeuvre is expected after an additional time

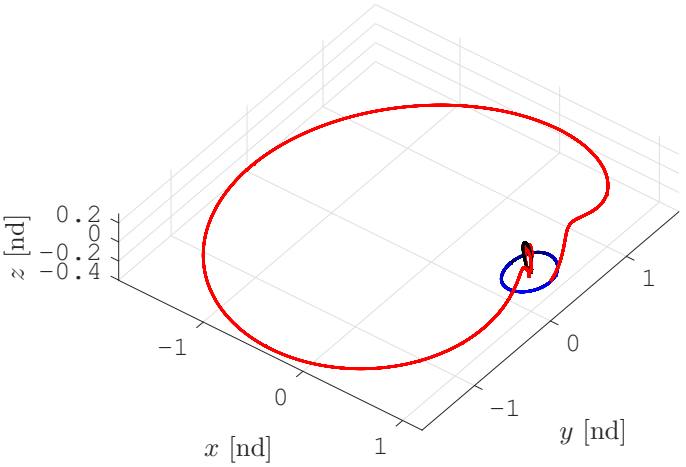

Figure 5.19: NRHO to DRO rendezvous transfer: orbital dynamics.

t_2, when the manifold intersects the operational DRO of the target. Hence, the full transfer time is equal to $t_1 + t_2$ and it is not constrained. For these cases, a multi-objective global optimisation method has been used in order to reduce the sum of the two Δv and to target the manifold to intersect the DRO. As already said, the times of the manoeuvres are completely free and the intersection point on the DRO has been chosen to have $y = 0$.

One example rendezvous trajectory is reported in figure 5.19. The spacecraft, after the injection in the unstable manifold trajectory, is dynamically driven along a natural trajectory that brings it behind the Earth and comes back after a retrograde revolution in the Earth-Moon system to the DRO. The time of flight is remarkably long, in the order of 90 d.

An additional example rendezvous is shown in figure 5.20. The differences in the trajectory are due to a different orbit-attitude manifold that is chosen to begin the manoeuvre. In this case, the rendezvous trajectory is contained within the DRO and the cost and time of the manoeuvres are obviously modified with respect to the previous case. In particular, the TOF is ~ 35 d.

In general, when dealing with large space structures, the design of cislunar rendezvous transfers and proximity operations share commonalities and problems between different orbital families. In fact, the considerations on the coupled orbit-attitude dynamics are always similar. For example, the perilune passage shall be carefully managed by choosing an appropriate attitude control system. Hence, what is most important to consider in designing GNC functions for rendezvous

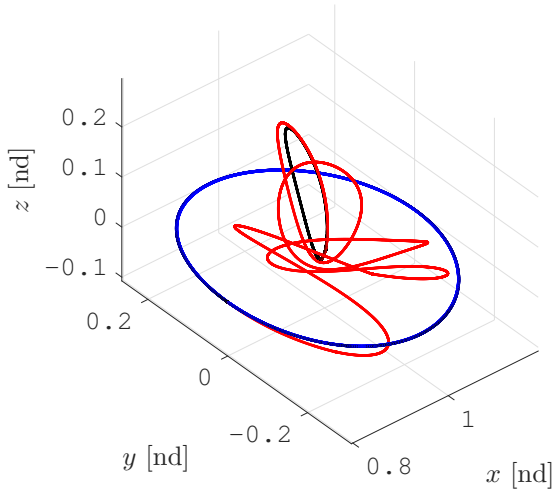

Figure 5.20: Alternative NRHO to DRO rendezvous transfer: orbital dynamics.

with large space structures in cislunar space, is the interaction between orbital and attitude dynamics.

CHAPTER 6

Flexible Dynamics

I would never work on flexible dynamics.

— Myself, *a few years ago ...*

Flexible dynamics of space structures interacts with the orbit-attitude motion, in particular when large space systems are considered. For this reason, this last part of the dissertation is dedicated to analyse the interactions between orbit-attitude and flexible dynamics. The rigid body dynamics assumption is discarded and the body B is assumed to be flexible. The outcomes of this investigation may be used to define the validity range in assuming rigid body motion while studying the dynamics of a large space structure in complex dynamical environments. Moreover, the acquired knowledge about orbit-attitude-flexible dynamics can be exploited to design guidance and control functions able to deal with flexible space systems.

This chapter discusses some analyses applied to flexible space structures in cislunar space, exploiting the available flexible models introduced in section 2.5. For instance, the distributed parameters model, based on the Ritz method, is exploited to simulate the dynamics of a body undergoing large overall motions,

comparing the obtained results with those available from the lumped parameters models. Generally, the two approaches can be used together to assemble and simulate complex flexible space structures, because they are developed utilising a multi-body formulation.

The presented investigations are also aimed in analysing, designing and testing the guidance and control (GC) functions for the attitude control of a spacecraft in Moon orbits, subject to environmental perturbations, internal fluid sloshing effects and flexibility coupling. As a matter of fact, the flexibility effects have a relevant influence mainly on rotational motion. The resulting coupled vibrational-attitude dynamics, with the inclusion of internal liquid sloshing, can reduce the achievable performances of the ACS. For this reasons, classical and alternative control methods are conscientiously applied in order to achieve a fully functional set of GC functions, capable to avoid dangerous resonances and vibrational excitation.

6.1 Comparison and Validation of Flexible Elements Models

The available flexible models require to be compared and validated for applicative purposes. In fact, DPM is surely the most accurate way to represent the vibrational dynamics, but it requires a high computational burden to be simulated. Moreover, the modelled effects may be overabundant for the purposes of these applications where, for example, the first natural modes are often sufficient to estimate the influence of the flexible-attitude coupling. Notwithstanding, LPM and LMM shall be accurately implemented and validated to acquire a confidence level sufficient for the considered applications. In particular, it shall be verified the correct representation of the main dynamical features.

The developed DPM is selected as a reference model to represent the dynamics of flexible structures undergoing large overall displacements. Hence, it is the first model to be validated according to the available literature results of Yoo [38]. The result reported in figure 6.1 shows a three-dimensional spin-up motion of a 10 m cantilever beam in free-space without any external force or torque. The beam is attached to a rigid base, with an angle of 45deg with respect to the spinning axis of the support, which undergoes a prescribed spin-up motion characterised by the parameters stated in the caption of figure 6.1. Many simulation, in different application scenarios, have been run and the available results are equivalent to the literature ones.

Then, the developed LPM is compared with respect to the DPM, and the behaviour of the simplified dynamics is reported as well in figure 6.1. The LPM dynamical evolutions are always analogous to those available with the more complex DPM, particularly for what concern the lowest vibrational modes, which have more impact on the attitude dynamics and the associated control

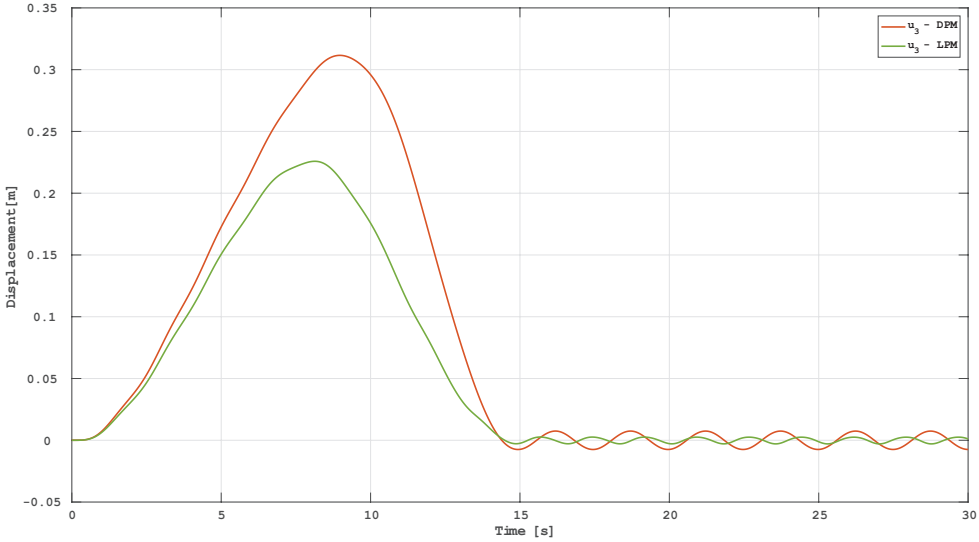

Figure 6.1: Lumped and Distributed Parameters Model Validation. (Cantilever beam with $l_b = 10\,\text{m}$, $m_b = 12\,\text{kg}$ and elastic modulus $E_b = 71\,\text{GPa}$. Spin-up motion: steady state angular speed $\Omega_s = 3\,\text{rad/s}$ and time constant $T_s = 15\,\text{s}$, as defined by Yoo [38]).

capabilities. Moreover, the time required to run the simulation in figure 6.1 is $t_{DPM} \simeq 8\,\text{s}$ for DPM and $t_{LPM} \simeq 3\,\text{s}$ for LPM, on a 2.5 GHz quad core processor. Thus, the analyses presented in this dissertation are conducted exploiting the lumped models, unless otherwise specified. Precisely, the LPM is used to simulate flexible appendages (e.g. solar panels, long beams), while the LMM is applied for the sloshing models. In fact, there is no relevant computational cost advantage of the LMM over LPM, but the accuracy of the last one is greater for flexible structures. On the other hand, LMM is perfect to be implemented as an equivalent mechanical sloshing model [72].

The developed flexible model described in section 2.5.3 is validated comparing its results with those obtained using an industrially validated simulator, implemented by the Spanish company Deimos Space S.L.U. [86], and referred in the dissertation as Functional Engineering Simulator (FES). This simulator performs 6DOF propagation of equations of motion. It includes, similarly to the coupled dynamics described in this research work in section 2.5, a model of sloshing and a model for flexible appendages (i.e. two solar panels). Furthermore, the perturbations that are modelled in are:

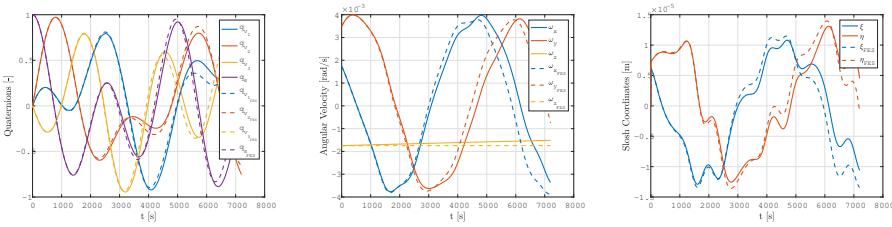

(a) Quaternions. **(b)** Angular Velocity. **(c)** Sloshing.

Figure 6.2: Flexible-attitude model compared to Deimos Space S.L.U. FES simulator.

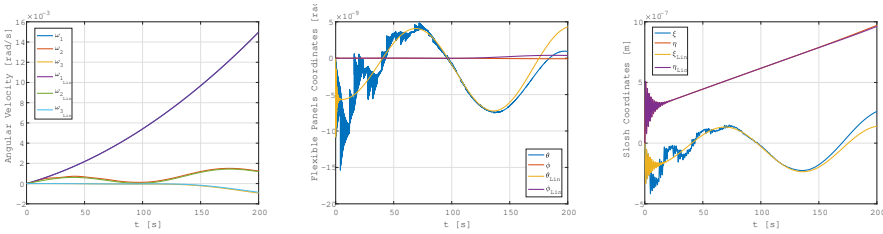

(a) Angular Velocity. **(b)** Flexible Appendages. **(c)** Sloshing.

Figure 6.3: Flexible-attitude linear model compared to full non-linear.

- ◇ Lunar Gravity Harmonics: LP75G;
- ◇ Sun and Earth four-body gravity, with gravity gradient;
- ◇ Solar Radiation Pressure: geometric model of spacecraft (S/C);
- ◇ Torque due to electric propulsion actuation.

The results in figure 6.2 show that the developed dynamics model produces valid results: the developed flexible-attitude dynamics is capable to correctly simulate all the relevant dynamical effects in cislunar space.

The validation of the flexible-attitude linear model, presented in section 2.5.3.1, is carried out comparing its result with respect to the developed full non-linear model, described in section 2.5.3. The validation results are presented in figure 6.3 and they confirm what already anticipated in chapter 2: the linear model loses some of the cross-coupling between slosh and flexible appendages, and it tends to smooth the flexible-sloshing dynamics. Nevertheless, it is very reliable in the attitude output, as evident in figure 6.3a. Thus, it is a valuable tool to support the design of GC functions for attitude control of large and flexible spacecraft with internal liquid sloshing.

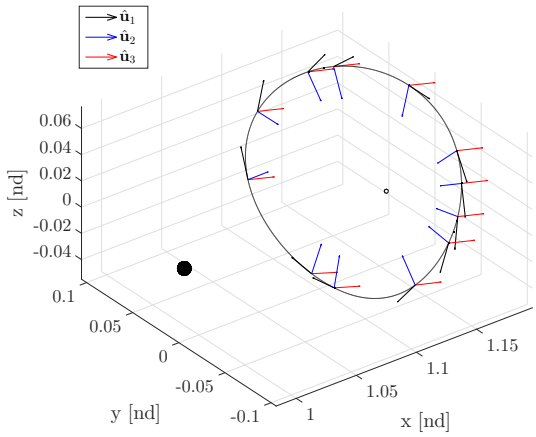

Figure 6.4: Orbit-Attitude motion on Halo orbit with $A_z = 30\,000\,\text{km}$.

6.2 Large Space Structures in Cislunar Environment

Research studies dealing with large space structures in cislunar space are of great interest in the scientific community of today, as explained in the introductory chapter of this dissertation. The present section presents some analyses that are carried out to have some preliminary insights on this modern and broad area of aerospace science.

Large space structures in cislunar space are subjected to non-Keplerian orbit-attitude dynamics, since they are moving in the Earth-Moon system, and to relevant flexible effects, because of their dimensions and of their low structural rigidity. When the flexible multi-body equations of motion are available, both for the distributed and the lumped parameters model, they are coupled with the periodic orbit-attitude dynamics transformed in the inertial non-rotating reference, and the orbit-attitude-flexible dynamics is propagated.

In figure 6.4 the attitude evolution of a large space structure is shown directly on the orbital path. The orbit-attitude periodic dynamics is analogous to those presented in chapter 3 for an EML2 Halo orbit, where the space station performs one overall rotation in a single orbital period. An analysis about the flexibility effects on four different periodic orbit-attitude dynamics of the same Halo family is reported in figure 6.5 and figure 6.6. The motion is propagated on four Halo orbits with diverse amplitude A_z, in a way that the influence between the orbital frequency and the structural frequency is highlighted. The LPM system attached to the centre of mass of the body B has a first mode natural frequency $\omega_{flex_1} = 50$ [nd]. The most elongated orbits have a particular influence on the oscillations of the Euler angles, while more the orbit is close to planar motion

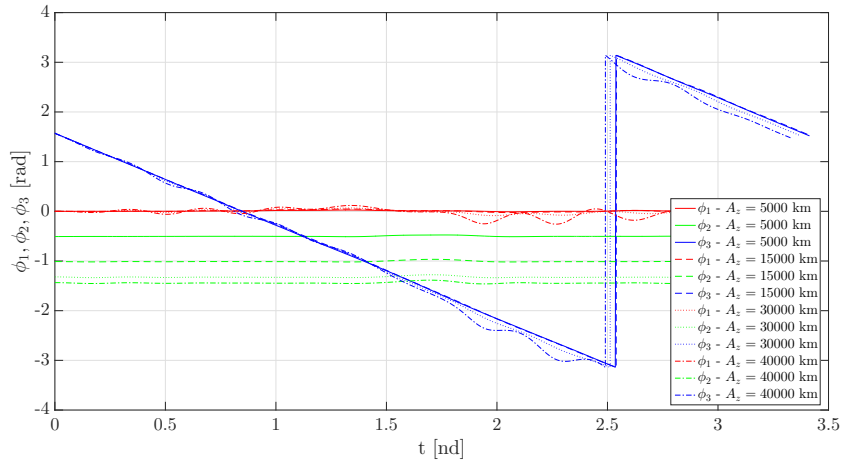

Figure 6.5: Euler angles evolution along one orbital period.

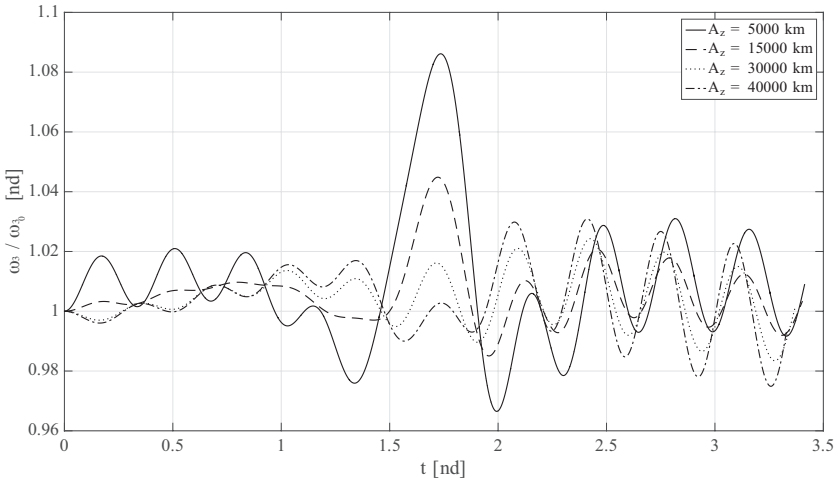

Figure 6.6: Angular velocity, ω_3, evolution along one orbital period.

more the variations are evident in ω_3. This results can be explained considering that in the limit of planar orbits all the torques are exerted along $\hat{\mathbf{b}}_3$.

A different simulation is targeted to point out the influence of the natural frequencies of the structure on the orbital motion. The difference in x, y and z of the coupled flexible model with respect to the point-mass dynamics is shown in figure 6.7. In this case, a unique trend does not exist among the different components and the different Halo orbits. Each orbit has its peculiar frequency in each spatial direction, and the influence on flexible systems with different

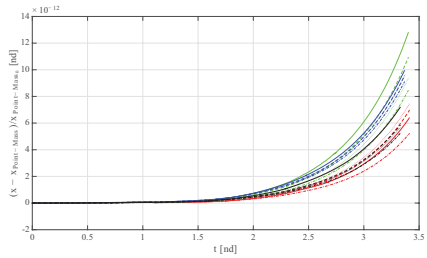

(a) x component.

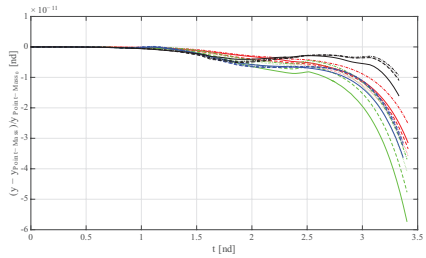

(b) y component.

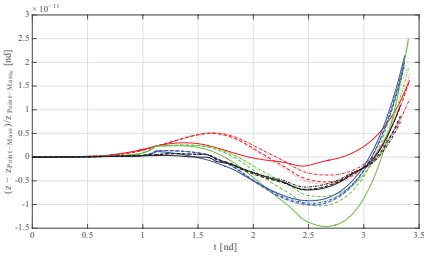

(c) z component.

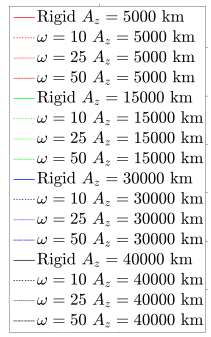

(d) Legend.

Figure 6.7: Difference with respect to the point-mass dynamics.

natural frequency must be analysed isolating each single effect and coupling term. However, the most important outcome from this analysis is that the flexible effects on the orbit motion are practically negligible, confirming the fact that vibrational dynamics is relevant mainly on the rotational motion. Hence, in the followings, the flexible-attitude coupling is investigated with particular attention.

One additional example simulation result is shown in figure 6.8, where the tip displacements of a distributed parameter beam (i.e. DPM) aligned with the principal inertia axes of m_B is plotted as a function of time. The coupled orbit-attitude dynamics that is taken as input, is related with a periodic solution similar to the one represented in figure 3.1 for a EML1 Halo orbit. The displacements u_1, u_2 and u_3 are labelled according to figure 2.5. Note that the displacements are large when compared to real conditions, but they are due to the characteristics of the selected beam, which are chosen to highlight the effects of flexibility. In fact, the beam is 100 m long, it has a square cross-section and it has the physical properties of a generic aerospace aluminium alloy ($\rho_{Al} = 2800\,\mathrm{kg/m^3}$ and $E_{Al} = 71\,\mathrm{GPa}$). The size of the cross-sectional area is derived imposing a target first bending natural frequency in the order of the lowest frequency of the International Space Station, approximately equal to 0.06 Hz. The flexible dynamics is therefore characterised by a quasi-static deformation due to the

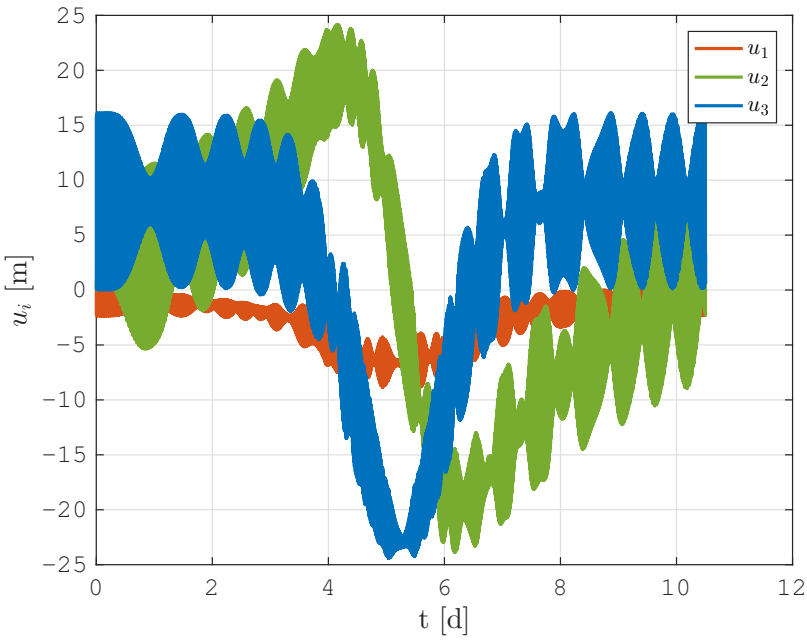

Figure 6.8: Flexible Dynamics in Halo Orbit. (EML1 Halo Orbit: $T_t = 10.5\,\mathrm{d}$ - $I_{max}/I_{min} = 1.5$. Distributed Parameters Beam: $l_b = 100\,\mathrm{m}$, $\rho_b = 2800\,\mathrm{kg/m^3}$, $E_b = 71\,\mathrm{GPa}$ and first bending natural frequency $\phi_{b_1} = 0.06\,\mathrm{Hz}$).

overall rotational motion, plus a superposition of the natural frequencies of the flexible structure. In fact, the dynamics in figure 6.8 is composed by a slow overall deformation and a fast sinusoidal oscillation with period of approximately 16 s, corresponding to the first bending natural frequency. The resulting flexible behaviour is due to a complex interaction with the full orbit-attitude dynamics in cislunar space.

The presented result is in agreement with other simulations that have been performed: a strong coupling between orbit-attitude dynamics and flexible dynamics seems to be not present. The flexibility properties of a space system may be selected independently from the planned orbit-attitude evolution. In fact, the dynamical response of the space structure is composed of a quasi-static term plus a superposition of natural modes, since there is a huge separation between typical lowest natural frequencies of real extended space systems and the one related with the non-Keplerian dynamics. This conclusion is valid in general also for other orbit-attitude periodic motions and extended structures with different physical properties, geometry and dimensions, as long as the natural frequencies of the extended structure stay well above the frequency content of the overall motion, which is true, in general, for actually feasible space

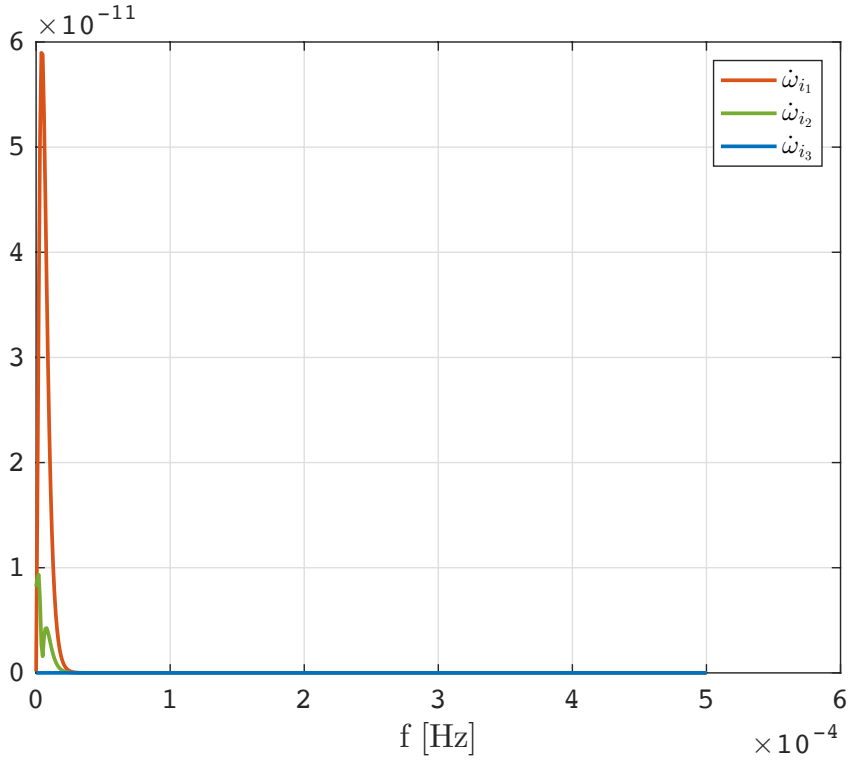

Figure 6.9: Frequency Content of Angular Acceleration in Halo Orbit. (EML1 Halo Orbit: $T_t = 10.5\,\mathrm{d}$ - $I_{max}/I_{min} = 1.5$).

systems. This statement can be explained looking at the frequency content of a periodic orbit-attitude dynamics; figure 6.9 shows a fast Fourier transform of the angular acceleration along a Halo orbit. Similar results are obtained considering various families of orbits and alternative dynamical quantities, such as the linear acceleration or the angular velocity.

The mutual influence of orbit-attitude and flexible dynamics should not be completely neglected, but seems to be reasonable to decouple the problem, at least for the investigations about natural dynamics. On the contrary, when the ACS is considered, the control bandwidth can overlap with certain natural frequencies of the system. In these cases, the orbit-attitude-flexible coupling in the dynamics shall not be neglected while designing GC functions, as discussed in section 6.3.

6.3 Flexible-attitude Guidance and Control Design

The purpose of the present section is to discuss the design of attitude guidance and control algorithms able to deal with the flexible-attitude dynamics described in sections 2.5.2 and 2.5.3. ACS design and development are carried out for different attitude modes, assuming the spacecraft able to detumble and to follow a reference attitude (i.e. pointing mode). An analysis of the intrinsic properties (e.g. stability margins) is presented, together with the extrinsic verification of the developed GC functions (e.g. one shot and Monte Carlo simulations).

The flexible-attitude guidance and control functions are designed, developed and validated in a major application scenario in lunar vicinity: a Moon circular orbit with radius 100 km. The ACS is based on reaction wheels, including saturation and bias. The sensors performance models are:

- ◇ Sun vector determination, including bias and noise;
- ◇ Angular velocity measurements, including bias, noise and random walk;
- ◇ Attitude Determination, including bias and noise equivalent angle.

The spacecraft to be controlled has a mass of 200 kg and moments of inertia in the order of $\sim 10^2\,\mathrm{kgm}^2$. The main sloshing frequency and the first natural frequency of the flexible appendages are in the order of $0.1\,\mathrm{Hz} \simeq 0.63\,\mathrm{rad/s}$.

Design and development of the flexible-attitude guidance and control subsystem are characterised by the following requirements:

- ◇ ACS performances shall be assessed assuming uncertainties of the critical parameters for sensors, actuators, spacecraft properties and environment;
- ◇ ACS shall be able to compensate for torques due to external and internal forces;
- ◇ ACS shall be able to avoid flexibility excitation, managing the flexible-attitude coupling;
- ◇ ACS shall work under the environmental perturbations characterising the cislunar environment, with reference to the operational orbit;
- ◇ ACS shall analytically be proven stable. The linear dynamics and kinematics shall be used to verify that 6 dB (i.e. gain) and 30 deg (i.e. phase) stability margins are respected.

Classical control methods (e.g. PID control) are used to have a fundamental development of the described ACS. Moreover, they are also employed as a reference comparison with respect to a wave-based (WB) attitude control algorithm [87]. In fact, such typology of simple but innovative control technique is especially suitable for mechanical systems that are inherently flexible and, thus, difficult

to be rapidly controlled, like a spacecraft with flexible parts and with internal liquid sloshing [88].

6.3.1 Guidance Functions

The first section to implement the GC system is the set of guidance functions. In particular, pointing mode guidance functions can be implemented independently from the employed control method; separately from a possible target for the guidance and a eventual tuning for the control. In fact, the guidance is based on a classical tracking regulator implementation [89]: the attitude trajectory follows a reference quaternion evolution, defining an error quaternion in time. The error angular velocity is obtained computing a reference angular velocity from the reference quaternion definition, in a way that guidance inconsistencies are avoided. The proportional command is finally computed from the quaternion vector part, multiplied by the modified sign of the scalar quaternion part (i.e. never equal to zero, but positive for values ≥ 0 and negative for values < 0). In this way, the shortest path to the reference is always commanded.

Detumbling and safe mode acquisition (i.e. Sun pointing) guidance is implemented only with classical control methods. In this ACS mode, the guidance is simply composed by a certain reference and target angular rate, followed by the acquisition of the Sun direction. Therefore, detumbling guidance is practically a PD control with respect to $\|\boldsymbol{\omega}\| \rightarrow \omega_{ref} = 0$, while the Sun acquisition guidance is determined from the Rodrigues' formula for the eigenaxis rotation between the actual Sun direction and the desired one [90]. Sun acquisition sub-mode starts when detumbling is considered finished: when the angular velocity is below a certain threshold, $\|\boldsymbol{\omega}\| \leq \omega_{treshold}$. The switching logic is one-way activation, detecting the first passage below the angular velocity threshold, without risk of mode flickering due to sensor noise. The proportional command for Sun acquisition is generated similarly to the pointing mode guidance, having the error quaternion available from the Rodrigues' rotation formula. The derivative command is computed from the measured angular rates of the spacecraft, after a proper low-pass filtering to reject noise. Note that also in this case, there is no need of a target angular velocity: the target angular rate is zero and, thus, during Sun acquisition, the angular rates behave has a good approximation of the derivative command.

6.3.2 Classical Control Methods

Classical control is implemented as a consistent GC block feedback to the flexible-attitude system dynamics. The development and design are carried out with the linear dynamics in section 2.5.3.1 and Linear Time Invariant (LTI)

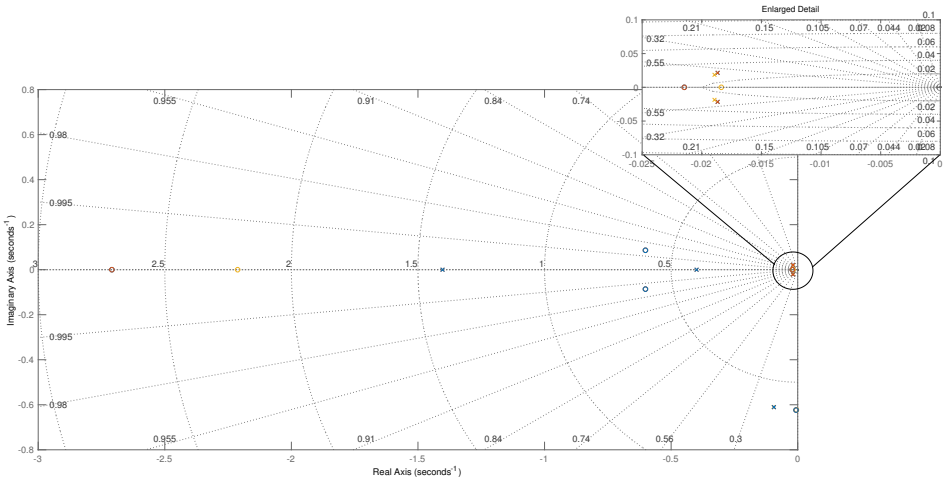

Figure 6.10: Pole-Zero map of the closed-loop system. (Poles: $\times$, Zeros: $\circ$).

plant dynamics, applied to the control analysis of the Single-Input and Single-Output (SISO)/Multiple-Input and Multiple-Output (MIMO) systems. Hence, the control design is performed through linear analyses, exploiting a LTI plant that is obtained linearising the system around a certain attitude equilibrium set point, defined by an equilibrium angular rate, $\boldsymbol{\omega}_{eq}$, as:

$$\boldsymbol{\omega} = \boldsymbol{\omega}_{eq} + \hat{\boldsymbol{\omega}}, \tag{6.1}$$

where $\hat{\boldsymbol{\omega}}$ are small rate perturbations around the equilibrium point. The full linearisation provides a linear time invariant system in state space formulation (e.g. A, B, C, D matrices). It should be reminded that this system is representative for the dynamics just around a single attitude equilibrium condition, with angular rates small enough to stay within the kinematics linearisation limits. Nevertheless, the output of the LTI plant is always validated by comparison with the results available from non-linear dynamics, simulated at the linearisation point.

Control actions are simply obtained with a PD logic from proportional and derivative commands computed by the aforementioned guidance functions. The integral action (i.e. I) is not inserted in the classical PD method, to avoid stability issues (e.g. additional poles in the controller) and numerical problems (e.g. integrator saturation): steady state error is assumed to be not a problem for the considered cislunar applications. The flexibility management is performed by filtering the whole control action with a band-stop filter (i.e. notch filter), which rejects a band around the main sloshing frequency and the first natural frequency of the flexible appendages. Higher natural flexible modes are considered to be

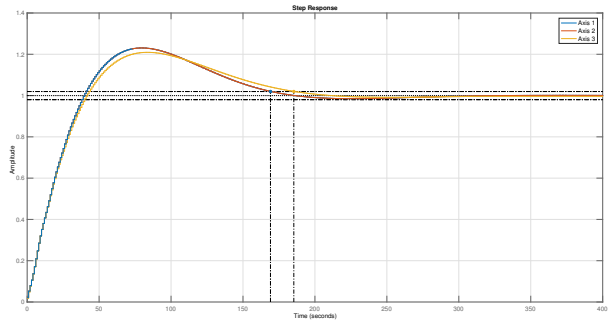

Figure 6.11: Step response of the closed-loop system.

out of the controller bandwidth and, thus, are not included in the GC functions implementation. The half-width of the rejection band in the band-stop filter is selected to be 15% of the central stop frequency. The filter section closes the GC sequence and, then, the control command is sent to the reaction wheels for the actuation. The controller is discretised for linear analyses and control implementation, with ACS frequency $f_{ACS} = 1\,\text{Hz}$.

The initial values for the gains are obtained with the Ziegler-Nichols tuning method, which assumes the system to behave as a second order closed-loop model, with its natural frequency ω_{2nd} and its damping factor ξ_{2nd}. They are applied in this high-order flexible-attitude system, because direct tuning methods are missing. The natural frequency is selected to be equal to twenty times the orbital frequency (i.e. $\omega_{2nd} = 20\,\omega_{LLO}$) and the damping coefficient is obtained to satisfy the requirement on settling time, $t_s \leq 200\,\text{s}$. In fact, for a second order system, the settling time is approximately equal to:

$$t_s \approx \frac{4}{\omega_{2nd}\xi_{2nd}}. \tag{6.2}$$

Hence, the first initial guesses for the PD control gains are:

$$k_{P_i} = I_i \omega_{2nd}^2, \tag{6.3}$$

$$k_{D_i} = I_i \omega_{2nd} \xi_{2nd}, \tag{6.4}$$

where I_i is the moment of inertia for each i-th principal axis. In figure 6.10 the Pole-Zero Map of the closed-loop system is reported and, given the presence of two dominant poles, the assumption to design the GC functions with a second order system method is confirmed to be valid.

Obviously, there are some differences with respect to a true second order linear system. Thus, the control tuning is verified also considering the output of the linear analysis to achieve stability margins and settling time according to the

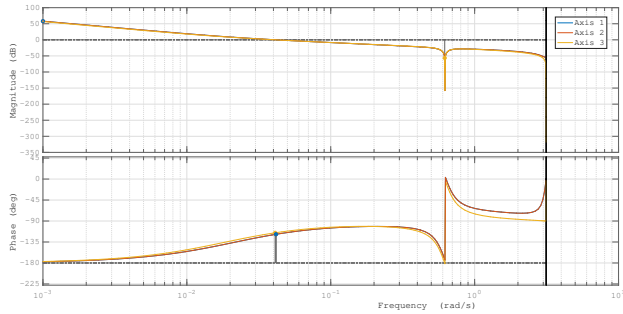

Figure 6.12: Bode plot of the open-loop system.

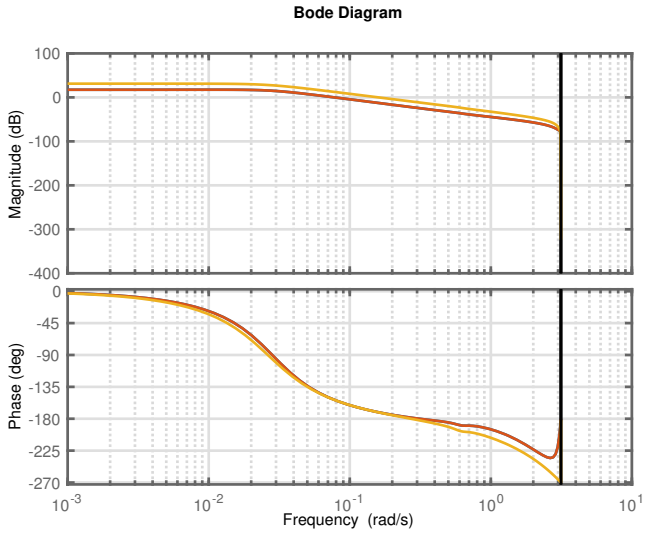

Figure 6.13: Bode plot of the external disturbance sensitivity function.

system requirements. The step response and the bode plot of the closed loop system are reported in figure 6.11 and figure 6.12: performance requirements are achieved on the three axes. In fact, the settling time is evident figure 6.11, with a closed loop step response with t_s lower than 200 s, in particular $t_s \simeq 175$ s. The stability margins are computed from the open loop system, which is stable on the 3-axes with a phase margin of $\sim 61.5°$, $\sim 61.5°$ and $\sim 64.7°$ respectively on $\hat{\mathbf{b}}_1$, $\hat{\mathbf{b}}_2$ and $\hat{\mathbf{b}}_3$. The gain margin is infinite since the phase never crosses the -180 axis. In figure 6.12, the effect of the filter to avoid flexibility coupling is evident; looking at the deep attenuation in magnitude, around the main flexible frequencies (i.e. ~ 0.63 rad/s), due to the dedicated ACS implementation. Note that $\hat{\mathbf{b}}_1$-axis plant is never visible in the plots because it is identical to the $\hat{\mathbf{b}}_2$-axis one. Therefore, $\hat{\mathbf{b}}_1$ plots are perfectly below $\hat{\mathbf{b}}_2$ plots.

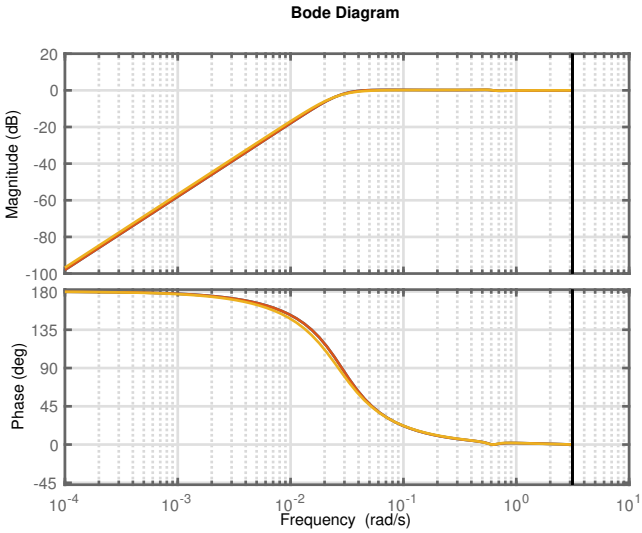

Figure 6.14: Bode plot of the sensitivity function.

From the sensitivity function, in figure 6.14, and the external disturbance sensitivity function, in figure 6.13, it was possible to check, respectively, the capability of the system to reject internal noise and external perturbations. With reference to the bode plot in figure 6.13, the high frequency external loads are correctly attenuated and the constant external loads produce a steady state error, due to the lack of integral control action, which is below 20 dB. Moreover, as expected, in figure 6.14 high frequency internal noise is not amplified, while steady state error in the sensor is attenuated, since the control is able to point according to the knowledge from the sensors' measurements.

MIMO results in figure 6.15 and figure 6.16 show that the system is stable also controlled around a steady condition with coupling between the axis due to spinning. The cross-talk between the axes is very limited and, consequently, there is a correct attenuation in all the non-diagonal bode plots. The diagonal bode plots, obviously, behave the same as the 3 SISO bode plots presented before in figure 6.12.

At this point, the output of the linear analysis design is completed and verified. But, when GC functions are applied to the full non-linear dynamics a gain tuning refinement is required. In particular, the PD gains are proportionally increased to reduce the steady state error, while maintaining stability and settling time requirements enforced. As a consequence, the proportional gain is selected according to the limit of the stability requirement (e.g. phase margin $\sim 30°$), which results in $k_P \simeq 1$. The derivative gain is scaled accordingly, resulting in $k_D \simeq 50$.

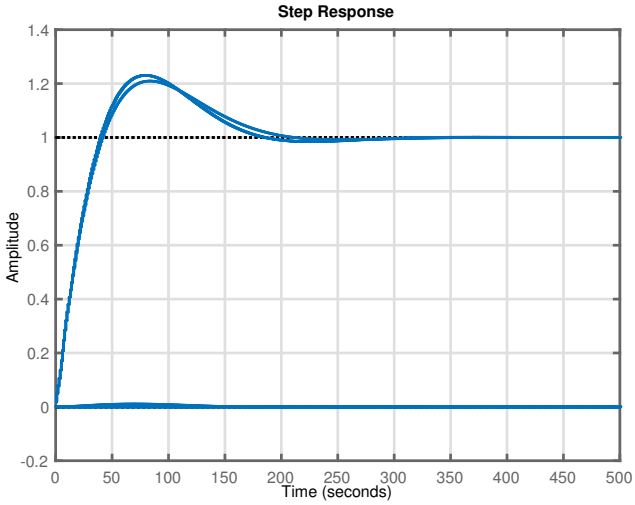

Figure 6.15: Step response of the MIMO closed-loop system.

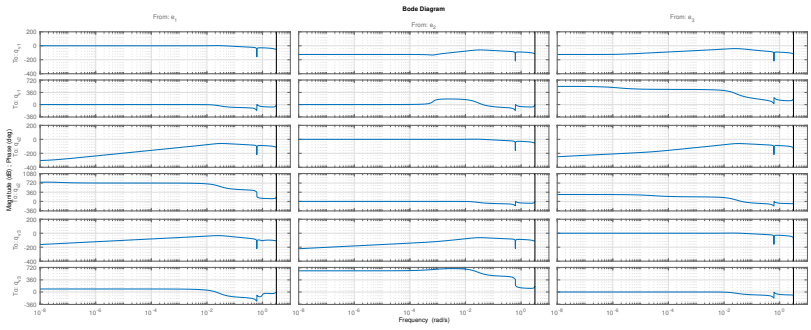

Figure 6.16: Bode plot of the MIMO closed-loop system.

The first evaluation of GC functions performances is conducted by means of numerical simulations without sensors noise and actuators errors. In figure 6.17 the angular velocity during detumbling and Sun acquisition mode is reported. Detumbling is completed in around 5000 s, followed by the Sun acquisition phase, which is very rapid. The flexibility excitement is not reflected in the dynamics, because there is not a diverging evolution of flexibility modes. In figure 6.18, the results of a pointing phase simulation are shown, from steady state null initial conditions (e.g. $\|\boldsymbol{\omega}\| = 0$ and identity quaternion). The final target quaternion is constant in time with value $\mathbf{q}_{ref} = [0.5, 0.5, 0.5, 0.5]^{\mathrm{T}}$.. Steady state conditions are reached in ~ 500 s, with a settling time in the order of ~ 200 s. The flexible dynamics is not excited unstably and the pointing is correctly achieved. The final resulting performances have the error rates and the error angles within the

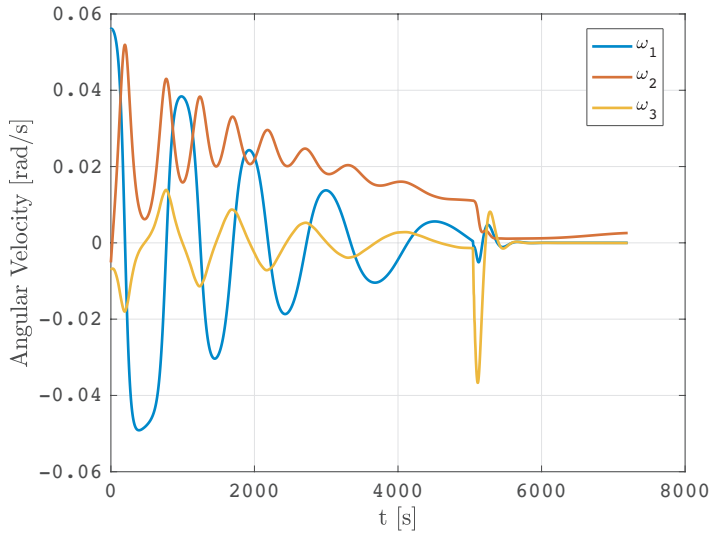

Figure 6.17: Angular velocity during detumbling and Sun acquisition mode.

imposed requirements. However, the actual verification of the ACS performances is discussed in section 6.3.4 through FES Monte Carlo simulations.

6.3.3 Wave-based Control Method

Wave-based control is a control technique introduced at the end of the last century, by O'Connor [87]. The flexibility and the fluid sloshing of the system are modelled with a linear second order system, which is used as a sort of model prediction to support the control functions. Even if a detailed model of the flexible dynamics within the system is not needed. The control action is then divided in two components: one travelling from the actuator into the system, and the other going from the system through the actuator. Practically, the actuator simultaneously launches mechanical waves into a system while it absorbs returning waves. The control system is therefore able to absorb the vibrations by means of destructive interference. The method has been applied in literature to 1 DOF systems with interesting results and, recently, the control technique has been extended to spacecraft in planar motion (e.g. 2 + 1 DOF) with preliminary results [88]. The possibility to control 6 DOF spacecraft or, namely, 3DOF coupled attitude, has not been tested yet and it is discussed in this section.

The peculiarity of wave-based control is the combination of position control and active vibration damping. As a matter of fact, the 1 DOF wave-based control implementation begins from the development of the wave model to

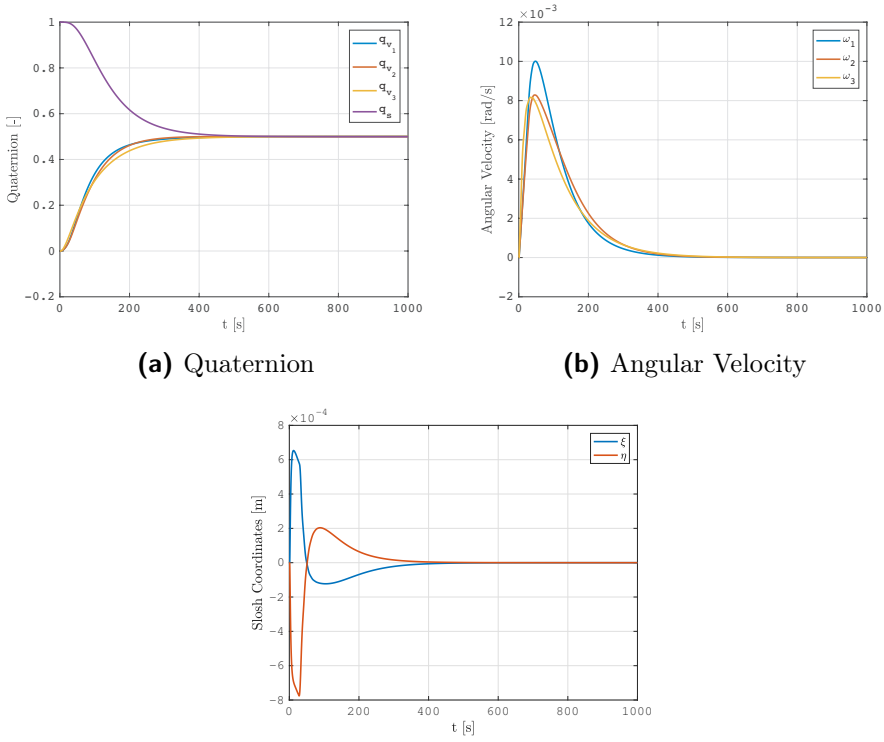

(a) Quaternion

(b) Angular Velocity

(c) Sloshing

Figure 6.18: Pointing mode with classical PD control.

represent the vibrations of the system. Ideal second order linear models are used (i.e. spring-mass-damper systems), through the associated approximating wave models:

$$G_0 = \frac{\omega_G^2}{s^2 + \omega_G s + \omega_G^2} \quad \text{with} \quad \omega_G = \sqrt{\frac{2k_0}{m_1}}, \tag{6.5}$$

$$H_0 = \frac{\omega_H^2}{s^2 + \omega_H s + \omega_H^2} \quad \text{with} \quad \omega_H = \sqrt{\frac{2k_0}{m_0}}, \tag{6.6}$$

where G_0 is the transfer function associated with the control output wave (i.e. the control wave), and H_0 is the transfer function associated with the returning wave (i.e. the approximated response of the systems). The associated angular frequencies (i.e ω_G and ω_H) should be tuned to have the desired behaviour of the controlled system. Therefore, the tuning parameters are the associated physical parameters k_0, m_0 and m_1. They are indicated in the conceptual representation of the wave-based control method, reported in figure 6.19, which shows the actuation mass, m_0, and spring, k_0, attached to the mechanical system to be controlled. Thus, the control action is generated by a hypothetical oscillating mass, m_0, which tries to create destructive interference on the returning wave,

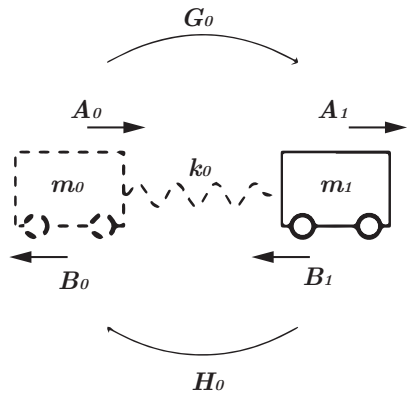

Figure 6.19: Wave-based control concept.

H_0, by means of a control wave, G_0. A reference actuation state, A_0, is computed in order to suppress vibrations, while commanding a certain position of the system, A_1. Hence, the control is actuated by the displacement of the fictitious mass m_0

In practice, the wave-based control launches a control wave equal to half of the reference 1 DOF state and to the 1 DOF returning wave. The measured values of the actual state and the commanded control are then used to evaluate the returning wave component at the actuator as:

$$B_{0_i} = H_0 \left(\frac{q_i - P_0 m_{C_i}}{1 - P_0 Q_0} \right), \tag{6.7}$$

where q_i and m_{C_i} are, respectively, the measured 1 DOF attitude state and the commanded 1 DOF control torque. P_0 and Q_0 are transfer functions defined as:

$$P_0 = \frac{G_0}{k_0(1 - G_0)}, \tag{6.8}$$

$$Q_0 = k_0(H_0 - 1). \tag{6.9}$$

The control is then actuated to match the returning wave component in equation (6.7) and, thereby, absorb it. When the absorbing is finished, the system will have been displaced by the specified launch wave (i.e. $0.5q_{ref_i} + B_{0_i}$), and it will be at the reference state (i.e. $0.5q_{ref_i} + B_{0_i} - q_i = 0$).

The 3 DOF ACS is obtained by a combination of three 1 DOF wave-based controls (i.e. 3 SISO systems). The development of a complete 3 DOF MIMO wave-based control requires further developments, which lead to a more complicated model-predictive wave-based control. However, this option is not considered in

this research work. In fact, the wave-based control has been chosen because of its simplicity and its robustness, without any prior knowledge of an exact modelling of the flexible system under control. The 3 DOF MIMO wave-based attitude control is considered to be out of the purpose of this investigation. The main difficulties in dealing with MIMO wave-based method are due to the fact that the attitude is fully coupled among the 3 axes, and to the fact that the attitude representation (i.e. quaternions) has a complex non-linear formulation to compute the errors with respect to a reference 3 DOF attitude state (i.e. non-linear formulation for the control wave). The fully coupled dynamics and the inherent non-linearities in the 3 DOF attitude control problems produce returning waves that enter 3 separate actuators. However, each control component can be absorbed only by the actuator that launched it into the system. In practice, it is not possible to distinguish proper returning waves to be absorbed and spurious returning waves coming from the coupling between different axes. The result is a non-working control that converges to the wrong target position, with weak stability properties.

The wave-based control method GC functions are designed with a preliminary tuning process on the linear system, followed by a fine tuning to achieve the desired performances on the full non-linear dynamics. The initial values for the control parameters are obtained from the real system characteristics, translated into the conceptual wave-based model, which is defined by k_0, m_0 and m_1. It is here reminded that the 3 SISO controllers and the lack of a non-linear wave model to handle 3 DOF attitude reference state make the implemented control algorithms to work well just in proximity of the reference target attitude (i.e. small error angles and small angular velocities). Again, this limitation is imposed by the difficulties to manage cross-coupling across the 3 body axes. Anyhow, the results are deemed relevant to be discussed since it is anyway possible to understand the capabilities of this control technique in damping out the sloshing and the internal vibrations connected with the spacecraft coupled dynamics during steady state pointing, which is relevant to achieve accurate control during the final phases of rendezvous operations in cislunar space.

The developed wave-based control has the transfer function associated with the control wave working in proximity to the main flexible frequencies: $\omega_G \sim 0.1\,\text{Hz}$ The returning wave is tuned to have enough control bandwidth; therefore, the returning wave is tuned to have a frequency that is almost double to the control wave: $\omega_H \sim 2\omega_G$. These control frequencies are obtained setting the control gain k_0 to be close to the value of the proportional gain in the classical control formulation: $k_0 \sim 1$. This is done to have similar stability properties and analogous behaviour to the controller described in section 6.3.2. The equivalent masses m_0, m_1 have been computed accordingly. The fine tuning of the gains is carried out to avoid excessive overshooting. At the end the control gain is

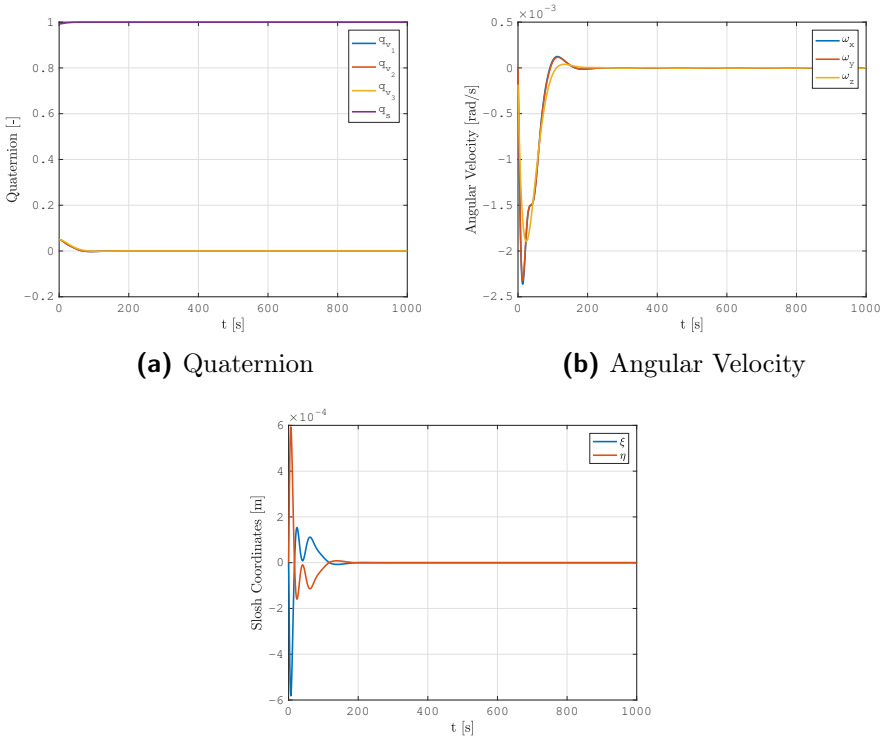

(a) Quaternion

(b) Angular Velocity

(c) Sloshing

Figure 6.20: Pointing mode with wave-based control.

$k_0 = 0.6$ and the returning wave frequency is lowered to $\omega_H = 1.75\omega_G$ to reduce the control oscillation before convergence.

A pointing mode simulation is reported in figure 6.20. It is initialised with steady state initial conditions (e.g. $\|\boldsymbol{\omega}\| = 0$) and random error angles with respect to the target final state in the order of $\sim 5°$. The final target quaternion is imposed to be the identity quaternion, with null vector part. Steady state conditions are reached in $\sim 200\,\text{s}$. The sloshing is not excited unstably and the pointing is achieved correctly. The capabilities and performances of this control technique are similar to those achievable with the PD control with notch filter. The rejection of external disturbances is better than classical control methods, and it is remarkable to note the different suppression of the sloshing effect, comparing figure 6.18c and figure 6.20c: wave-based control creates a controlled periodic oscillation which is suppressed by a destructive interference, while the PD control does not generate any periodic oscillation, because of the notch filter, and the only sloshing evolution is directly related to the control acceleration damped by the PD action.

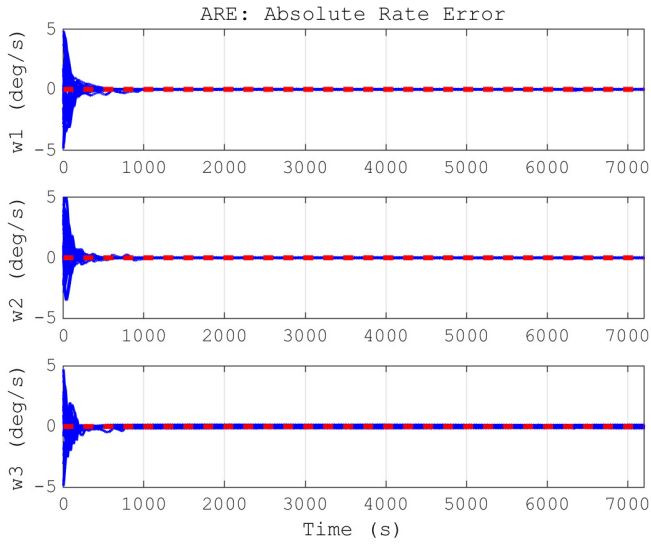

Figure 6.21: Monte Carlo analysis: Detumbling mode (50 runs).

6.3.4 Numerical Verification

The verification of the ACS performances is conducted by means of multiple Monte Carlo simulations, executed with the FES simulator. The Monte Carlo dispersions are defined with respect to all the system parameters, from sensors noise specifications, to actuation errors, passing through the physical characteristics of the spacecraft (e.g. position of the centre of mass, moments of inertia, area of surfaces). Notwithstanding, these engineering details are not discussed further in this dissertation. In fact, the purpose of this section is to highlight the global validity of the developed set of GC functions in real operations scenarios in lunar vicinity. In particular, practical attitude modes are simulated considering, for example, the problem of rendezvous from a LLO to NRHO. Let's assume that a flexible spacecraft, ascending from the lunar surface, is inserted into a LLO with a large spinning motion. The first necessary attitude operation is the detumbling, followed by a Sun acquisition attitude manoeuvre to orient the solar panels and charge the batteries before the continuation of the rendezvous mission. Then, let's suppose that the set of proximity operations are continued with an attitude trajectory similar to those discussed in chapters 4 and 5. In these cases, the guidance is defined as a quaternion evolution in time, $\mathbf{q}_{ref} = \mathbf{q}(t)$, and the implemented attitude tracking regulator tries to follow the reference path. Therefore, the aforementioned pointing mode can be simulated to verify the ACS performances. In both case, the focus is on the flexible-attitude coupling during controlled dynamics. The main verification point is to check the lack of any unstable flexible excitation, leading to resonant vibrations.

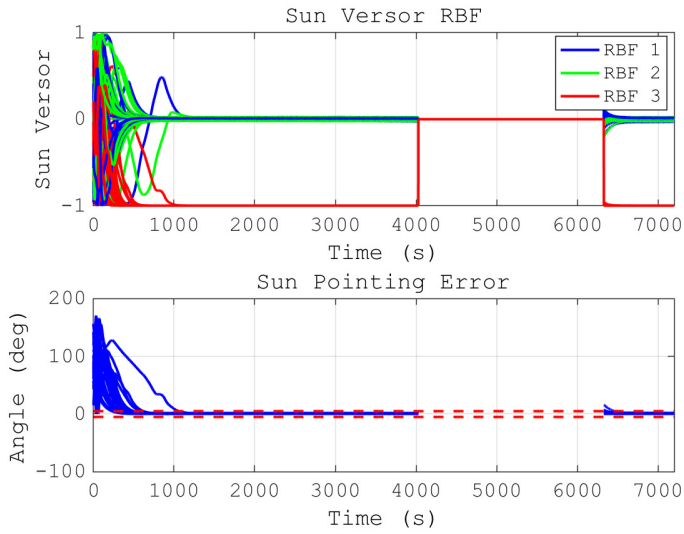

Figure 6.22: Monte Carlo analysis: Sun acquisition mode (50 runs).

In figure 6.21, the verification of detumbling and Sun acquisition GC functions confirms that the developed ACS is able to detumble the spacecraft within 20 min. Soon after detumbling the Sun acquisition mode is automatically and irreversibly switched on. The Sun is acquired and pointed within specifications. In fact, in figure 6.22, it is possible to see that the Sun is always correctly acquired along $-\hat{\mathbf{b}}_3$. There is no evidence of flexibility excitation and the average momentum storage level in the reaction wheels is always contained below 5 Nms in all the axes.

In figure 6.23 Monte Carlo simulations for pointing mode are shown. Maximum steady state error in error angles is 1° ($\hat{\mathbf{b}}_1$ and $\hat{\mathbf{b}}_2$) and 0.5° ($\hat{\mathbf{b}}_3$). Steady state is achieved in $\sim$ 300 s and the slower behaviour, with respect to the original design analyses, is due to Monte Carlo dispersion computed with the Deimos Space S.L.U. FES simulator and to the fact that the tracking is performed with respect to a quaternion trajectory in time. The lower pointing error in $\hat{\mathbf{b}}_3$ is due to the fact that the sloshing is acting mainly in the $\hat{\mathbf{b}}_1 - \hat{\mathbf{b}}_2$ plane, while the effect of the flexible appendages has a weaker effect on the attitude dynamics. The pointing errors is the order of $\sim 1°$ are due to friction torques in the reaction wheels, which are assumed to be in the order of 10% of the maximum actuation torque. However, again, the stability performances are here preferred with respect to high disturbance rejection. In fact, the increase in the required proportional gain is limited by the stability properties and the inclusion of an integral action (i.e. PID control) is avoided for the previously discussed stability reasons. One alternative solution to reduce steady state pointing error can be sought in the inclusion of a control loop on the wheels management. In this

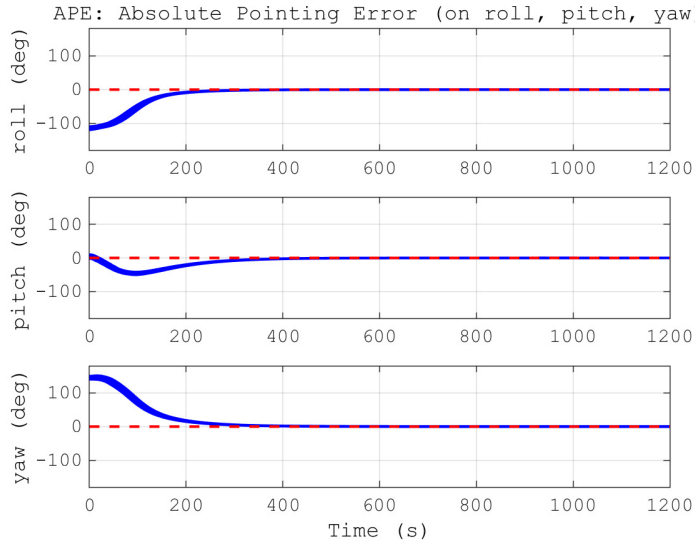

(a) Angular Pointing Error

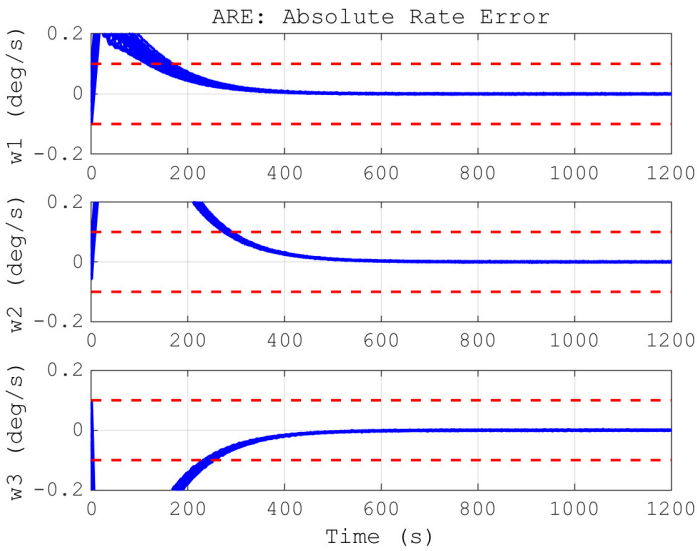

(b) Angular Rates Error

Figure 6.23: Monte Carlo analysis: Pointing mode (50 runs).

way, the friction of the wheels can be controlled in order to reduce the actuation disturbances. Additional Monte Carlo simulations, with a 90% reduction in the wheels disturbances, proved that in these cases maximum pointing errors are always in the order of $\sim 0.1°$.

Monte Carlo simulations performed with the FES simulator are applied to verify classical control methods. The wave-based control has been verified by means of several one-shot simulations, similar to the one in figure 6.20 using the flexible non-linear dynamics discussed in section 2.5.3.1. The verification of flexible-attitude guidance and control functions proved the fulfilment of the requirements introduced in the beginning of this section.

As a matter of fact, the ACS is able to avoid flexibility excitation and to manage the flexible-attitude coupling. Intrinsic properties analysis, such as stability margins, settling time or sensitivity to noise and external disturbances, supported the development of the ACS algorithms, extracting all intrinsic properties of the system. The flexibility coupling is managed mainly exploiting the results of the linear analyses carried out. Extrinsic verification with numerical simulations, in both one shot and Monte Carlo runs, provides full insight in the operation of the GC functions in the two example scenarios: detumbling and sun acquisition mode and pointing mode. The numerical simulations in FES for classical control methods are complete, considering all the real effects acting on a space system in lunar vicinity. Numerical verification proved the validity of the whole set of GC functions.

The on-board guidance and control for Detumbling and Sun Acquisition mission phases is implemented and tested only with classical control methods, due to the discussed limitation of the wave-based control. On the contrary, the controller for pointing mode is implemented with two different structures: PD control and wave-based control. Guidance profile generation and on-board control for pointing mission phases are properly filtered to consider flexibility and sloshing constraints, reducing possible tracking errors due to the internal vibrations.

CHAPTER 7

Conclusion

> This is the end, beautiful friend
> This is the end, my only friend
> The end.
>
> — Jim Morrison

This dissertation deals with 6DOF dynamics, guidance and control for large space structures in cislunar space, analysing both absolute and relative motion. The performed analyses and the set of developed tools and GC functions are helpful to drive the design of a large space system in lunar vicinity, such as the proposed cislunar space station. In particular, the research work presented in this thesis is focused on possible rendezvous and proximity operations, defining practical strategies that can be exploited to deal with the assembly and the management of the cislunar space station.

This final chapter summarises the major findings and outcomes of this research work, by recalling the performed investigations and their relevance when associated to practical mission applications. The elements of innovations with respect

to existing knowledge and previous works in the field are highlighted. Moreover, possible opportunities and suggestions for future works are finally discussed.

The presented results highlight the importance of the coupling between orbital and attitude dynamics. The primary coupling is related to the effect of the orbital dynamics on the associated naturally periodic rotational motion. In the other way around, the influence of the attitude dynamics on the orbit has a lower magnitude. In fact, the gravitational attraction deviation due to the rotational motion is, for realistic bodies, 4 to 5 orders of magnitude smaller than the one determined by the other perturbations. Therefore, the main coupling from the attitude to the orbital dynamics is related to orientation-dependent perturbations, like the SRP.

The best orbit to host a large space structures in the vicinity of the Moon, together with the related coupled attitude dynamics, is not completely defined. Then, despite the focus of the discussed analyses is on certain orbital families, an important remark can be structured and applied to all the classes of non-Keplerian orbits: when dealing with large space structures, there is an upmost need to consider not only the orbital dynamics but also the rotational motion. This necessity is not only related to the accuracy of the simulations, but also to the fact that the study of coupled orbit-attitude dynamics gives an extensive knowledge about the 6DOF space of solutions, which can be positively leveraged to design future missions and operations. Furthermore, the flexibility of a large space system should not be neglected, even if its influence seems to be not strongly coupled with the natural dynamics. This is because, attitude dynamics associated with particular operational activities and manoeuvres, or the presence of an active control system, as the one discussed in section 6.3, can introduce higher frequency phenomena that can interact with the flexibility of the space system.

As a matter of fact, the main innovation aspect of this research work is related with the extensive investigation about coupled orbit-attitude-flexible dynamics in non-Keplerian cislunar environment, and its application to guidance and control problems for absolute and relative dynamics. Moreover, particular attention is dedicated to periodic non-Keplerian orbit-attitude solutions with applicative relevance, such as NRHOs and DROs. They are currently considered as optimal staging location for the future modular infrastructure in lunar proximity and, thus, their complete characterisation, including natural and controlled 6DOF absolute and relative dynamics, is interesting and innovative in the framework of non-Keplerian dynamics research.

The orbit-attitude spin stabilised solutions presented in chapter 3 laid the foundation for a simple and effective control of modular and extended space structures in cislunar environment. The attitude stabilisation techniques help the design of the considered space system, broadening the space of periodic

orbit-attitude solutions that are stable enough to host an extended spacecraft with minimum active control effort. Furthermore, spin stabilisation techniques offer possibility to manage situations in which the inertia properties and the configurations of the space system change in time. This is guaranteed by small on-line adjustments to the attitude stabilisation parameters, which are extremely efficient in terms of energy consumption. This aspect is extremely important for a modular structure that is assembled on-orbit by means of many automated operations. In fact, the attitude control technique should be as simple and efficient as possible since, while designing this kind of space missions, the main driver that must be followed is the minimisation of maintenance and station-keeping costs. The attitude stabilisation methods presented in this dissertation, with single-spinning spacecraft or constant speed spinning devices, showed a positive and innovative result in this direction.

Natural dynamics existing in non-Keplerian environment is well known from classical literature. Nevertheless, its 6DOF formulation and its application to relative dynamics problems offer new results that are relevant in the framework of applications to the cislunar space station. The design and optimisation of a whole rendezvous mission can be particularly enhanced by the exploitation of these orbit-attitude natural trajectories. They can be designed to have a full connection of orbit and attitude states from the departure point to the final rendezvous approach. Again, during the design of cislunar operation, the main driver to be followed is the minimisation of transfer and control costs. Thus, natural rendezvous trajectories are extremely beneficial in this direction. Moreover, the attitude control design is integrated, and the attitude stabilisation techniques allow to tune and stabilise the natural attitude motion with little influences on the orbital motion. The proposed 6DOF natural and controlled rendezvous design guarantees effective and efficient solutions for the design and implementation of the considered space system.

Rendezvous control techniques presented and analysed in this dissertation are based on a complete set of GC functions for transfer operations in the Earth-Moon system. In these regards, the cislunar space station project is a perfect application scenario for the developed methods and tools. In fact, this ambitious space mission requires a careful planning of all the rendezvous operations and, due to the dimensions of the space system itself, the attitude coupling is of primary relevance; in particular, when considering relative dynamics. Extensive knowledge of orbit-attitude relative dynamics in cislunar space is fundamental to design proper GC functions and to exploit natural dynamics in helping the rendezvous design process. Moreover, the analyses about relative dynamics guidance and control further emphasise the importance in studying the fully coupled orbit-attitude dynamics while designing the architecture to build and operate a large and modular space structure in cislunar orbits. In particular, the coupling with the structural flexibility is extremely important during controlled

operations, because the structural dynamics of extended space infrastructures could be excited by the active control system and, thus, it could generate non-nominal situations during rendezvous phases. The examples of possible rendezvous scenarios with very large and flexible spacecraft in cislunar space addressed in this dissertation can be used to show the capabilities of the developed analyses and design tools. Moreover, some reference parameters for typical rendezvous missions are presented, and they can be exploited to assess the feasibility of the entire network of missions and operations in lunar vicinity. In particular, the exploitation of optimal energy controls and the application of natural motions to satisfy operational requirements are presented to report which are the design methods that can facilitate the implementation of such advanced space systems. Furthermore, the coupled investigation gives the possibility to set few preliminary system requirements. For example, NRHO's perilune is not convenient for proximity operations and delicate manoeuvres: NRHO's apolune is the safe region where complex operations shall take place.

The present research work provides also a detailed discussion about the fidelity of cislunar dynamics modelling. In fact, the design of applied operations shall rely on accurate simulation, in order to test the performances of the implemented GNC functions. Actually, circular restricted and other approximated models (i.e. ER3BP) are beneficial for preliminary analysis of non-Keplerian environment. Still, the peculiarities of the Earth-Moon system are strongly dependent from the true motion of Earth and Moon, since their orbital eccentricity is not negligible in dictating the force field that maintains the periodicity of non-Keplerian orbits. In addition, the gravitational attraction due to the Sun plays a non- negligible role as well; in fact, the periodic oscillations of the cislunar orbits due to the Sun's pull are missed out in a CR3BP model. In particular, for what concern relative dynamics, even in the short period, the ephemeris four-body model is the model to correctly represent the peculiar regime of relative motion in cislunar space. Relative GNC functions designed in a simplified model of the Earth-Moon system are in general not valid for practical applications. This is particularly true when high precision is sought, like during close-proximity operations.

The space structure flexibility is investigated as a last part of the dissertation. In fact, analysing unforced motion in cislunar space, there is no a strong coupling between orbit-attitude dynamics and flexible dynamics. As a consequence, the structural dynamics of a space system may be investigated almost independently from the planned orbit-attitude evolution, and the dynamical response of the space structure is composed of a quasi-static term plus a superposition of natural modes. This is due to the large separation between typical lowest natural frequencies of real extended space systems and the ones related with the free non-Keplerian dynamics. Therefore, even if the complete orbit-attitude-flexible coupling should not be completely neglected, it is reasonable to decouple the natural orbit-attitude dynamics from the flexible effects. Still, when an ACS is

considered and the study is focused on forced dynamics, this assumption is not valid anymore. Under these conditions, the forcing frequencies or the control bandwidth can overlap the natural modes of the structures. Indeed, the higher frequencies associated with an active control system can be more dangerous with respect to possible resonances of the flexible system. Then, the GC functions design shall consider the flexibility, avoiding possible vibration excitation. In these regards, the vibrational dynamics is mainly relevant on the attitude motion, since the flexible perturbations on the orbit motion are typically few order of magnitudes lower than other perturbing forces. So, the implementation of GC algorithms is conducted taking into account the flexible-attitude coupling. The developed ACS exploiting classical PD control proved its validity in suppressing vibrations resonance whilst the spacecraft is manoeuvred to acquire the desired rotational state. Alternatively, the application of wave-based control is powerful in containing internal vibrations and structural excitations, but the range of applications is limited to pointing mode by cause of the difficulties in managing coupled 3 DOF MIMO dynamics.

7.1 Future Works

The research work presented in this dissertation is obviously not all-encompassing the vast topic of dynamics, guidance and control of large and flexible space structures in cislunar space. For sure the present research can be extended and generalized to include more mission scenarios and GNC design solutions. For example, the coupling between orbital and attitude dynamics should be further investigated. In particular, dedicated analyses are needed to highlight the effects of perturbations in long term simulations. In the direction of the cislunar space station program, this is needed to evaluate station-keeping cost and long-term stability performances on the selected staging periodic orbit-attitude dynamics.

Moreover, varying in time configurations and different mechanical properties of the extended space structure can have a strong effect on the coupled orbit-attitude dynamics. For this reason, the study of the effect of changing mass distribution on the periodic dynamics is important. As example, the sequence in which a future space station will be assembled is of a maximum relevance. In that case, the inertia moments will vary in time, as docking operations are performed and independent modules are attached and detached from the main structure. These operations will have to be carefully planned to avoid the departure from a stable periodic dynamics or to minimise the station-keeping effort. Therefore, the complete assembly sequence need to be designed and optimised. Such a research work could begin exploiting the solid foundation of analyses and tools presented and discussed in this dissertation.

Further investigations are suggested also about spin stabilisation methods. In particular, passive single or dual-spin attitude stabilisation methods, analysed in section 3.4, can be integrated with the currently proposed active attitude control system in section 6.3. As a consequence, the range of the proposed results can be extended, and the investigation of an active control system with variable stored angular momentum is of interest.

Finally, a methodical applications of the methods and the tools presented in this dissertation for a complete survey of the cislunar space environment can extend the range of selection for the nominal staging orbit. For example, an orbit with a higher perilune altitude can be helpful to extend the available time window to perform rendezvous operations. Moreover, further investigations on the entire system configuration and on the assembly strategy may highlight some additional drivers for the cislunar infrastructure design and implementation.

Even though the best orbit-attitude periodic motion and configuration of a large space structure in the vicinity of the Moon is not completely defined, this Ph.D. research is intended to underline some relevant and essential conclusions in the field of dynamics, guidance and control of extended and flexible bodies in cislunar environment. The presented investigations emphasises the importance in studying the fully coupled orbit-attitude dynamics and in implementing GC functions able to deal with the intrinsic flexibility of the system. The acquired knowledge is applied to rendezvous and proximity operations, having in mind the on-orbit assembly of a cislunar space station. However, it shall not be limited to the current applications: future research endeavours will pursue for something that is still unknown.

Research without research is, tautologically, pointless.

Bibliography

[1] International Space Exploration Group (ISECG), "The Global Exploration Roadmap", Tech. Rep., 2018.

[2] R. Whitley and R. Martinez, "Options for Staging Orbits in Cislunar Space", in *Proceedings of the 2016 IEEE Aerospace Conference, Big Sky, Montana, US, 5-12 March*, 2016.

[3] N. Copernicus, *De Revolutionibus Orbium Coelestium*. 1543.

[4] G. Galilei, *Sidereus Nuncius*. 1610.

[5] J. Kepler, *Astronomia Nova*. 1609.

[6] I. Newton, *Philosophiae Naturalis Principia Mathematica*. 1687.

[7] J. L. Lagrange, *Essai sur le Problème des Trois Corps*. 1772.

[8] H. Poincaré, *Les Méthodes Nouvelles de la Mécanique Céleste*. 1899.

[9] F. R. Moulton, D. Buchanan, T. Buck, F. L. Griffin, W. R. Longley, and W. D. MacMillan, *Periodic Orbits*. Carnegie institution for science, Washington, DC, US, 1920.

[10] V. Szebehely, *Theory of Orbits: the Restricted Problem of Three Bodies*. Academic Press, Cambridge, Massachusetts, US, 1967.

[11] R. W. Farquhar, "The Control and Use of Libration-point Satellites", Ph.D. Dissertation, Stanford University, Department of Aeronautics and Astronautics, Stanford, California, US, 1968.

[12] R. W. Farquhar and A. A. Kamel, "Quasi-periodic Orbits about the Translunar Libration Point", *Celestial mechanics*, vol. 7, no. 4, pp. 458–473, 1973.

[13] J. V. Breakwell and J. V. Brown, "The 'Halo' Family of 3-dimensional Periodic Orbits in the Earth-Moon Restricted 3-body Problem", *Celestial Mechanics*, vol. 20, no. 4, pp. 389–404, 1979.

[14] K. C. Howell, "Three-dimensional Periodic 'Halo' Orbits", *Celestial mechanics*, vol. 32, no. 1, pp. 53–71, 1984.

[15] ——, "Families of Orbits in the Vicinity of the Collinear Libration Points", *The Journal of the astronautical sciences*, vol. 49, no. 1, pp. 107–125, 2001.

[16] K. C. Howell and J. V. Breakwell, "Almost Rectilinear Halo Orbits", *Celestial mechanics*, vol. 32, no. 1, pp. 29–52, 1984.

[17] D. L. Richardson, "Analytic Construction of Periodic Orbits about the Collinear Points", *Celestial mechanics*, vol. 22, no. 3, pp. 241–253, 1980.

[18] M. Hénon, "Numerical Exploration of the Restricted Three-body Problem", in *Proceedings of the Theory of Orbits in the Solar System and in Stellar Systems, Thessalonki, Greece, 17-22 August*, 1966.

[19] T. R. Kane and E. Marsh, "Attitude Stability of a Symmetric Satellite at the Equilibrium Points in the Restricted Three-body Problem", *Celestial mechanics*, vol. 4, no. 1, pp. 78–90, 1971.

[20] W. Robinson, "Attitude Stability of a Rigid Body Placed at an Equilibrium Point in the Restricted Problem of Three Bodies", *Celestial Mechanics and Dynamical Astronomy*, vol. 10, no. 1, pp. 17–33, 1974.

[21] A. Abad, M. Arribas, and A. Elipe, "On the Attitude of a Spacecraft Near a Lagrangian Point", *Bulletin of the Astronomical Institutes of Czechoslovakia*, vol. 40, no. 1, pp. 302–307, 1989.

[22] E. Brucker and P. Gurfil, "Analysis of Gravity-gradient-perturbed Rotational Dynamics at the Collinear Lagrange Points", *The Journal of the Astronautical Sciences*, vol. 55, no. 3, pp. 271–291, 2007.

[23] J Peláez, M Sanjurjo, F. Lucas, *et al.*, "Dynamics and Stability of Tethered Satellites at Lagrangian Points", ESA ACT Report, Tech. Rep., 2008.

[24] B. Wong, R. Patil, and A. Misra, "Attitude Dynamics of Rigid Bodies in the Vicinity of the Lagrangian Points", *Journal of guidance, control, and dynamics*, vol. 31, no. 1, pp. 252–256, 2008.

[25] D. Guzzetti and K. C. Howell, "Coupled Orbit-Attitude Dynamics in the Three-Body Problem: a Family of Orbit-Attitude Periodic Solutions", in *Proceedings of the AIAA/AAS Astrodynamics Specialist Conference, San Diego, California, US, 4-7 August*, 2014.

[26] ——, "Natural Periodic Orbit-Attitude Behaviors for Rigid Bodies in Three-body Periodic Orbits", *Acta Astronautica*, vol. 130, no. 1, pp. 97–113, 2017.

[27] D. Guzzetti, "Coupled Orbit-attitude Mission Design in the Circular Restricted Three-body Problem", Ph.D. Dissertation, Purdue University, School of Aeronautics and Astronautics, West Lafayette, Indiana, US, 2016.

[28] D. Guzzetti and K. C. Howell, "Attitude Dynamics in the Circular Restricted Three-body Problem", *Astrodynamics*, vol. 2, no. 2, pp. 87–119, 2018.

[29] Y. Meng, R. Hao, and Q. Chen, "Attitude Stability Analysis of a Dual-spin Spacecraft in Halo Orbits", *Acta Astronautica*, vol. 99, no. 1, pp. 318–329, 2014.

[30] A. J. Knutson and K. C. Howell, "Application of Kane's Method to Incorporate Attitude Dynamics into the Circular Restricted Three-body Problem", in *Proceedings of the AIAA/AAS Astrodynamics Specialist Conference, Minneapolis, Minnesota, US, 13-16 August*, 2012.

[31] A. J. Knutson, D. Guzzetti, K. C. Howell, and M. Lavagna, "Attitude Responses in Coupled Orbit-sttitude Dynamical Model in Earth–Moon Lyapunov Orbits", *Journal of Guidance, Control, and Dynamics*, vol. 38, no. 7, pp. 1264–1273, 2015.

[32] D. Guzzetti, R. Armellin, and M. Lavagna, "Coupling Attitude And Orbital Motion Of Extended Bodies in the Restricted Circular 3-body Problem: a Novel Study on Effects and Possible Exploitations", in *Proceedings of the 63rd International Astronautical Congress, Naples, Italy, 1-5 October*, 2012.

[33] J. Ho, "Direct Path Method for Flexible Multibody Spacecraft Dynamics", *Journal of Spacecraft and Rockets*, vol. 14, no. 2, pp. 102–110, 1977.

[34] V. Modi, "Attitude Dynamics of Satellites with Flexible Appendages:a Brief Review", *Journal of Spacecraft and Rockets*, vol. 11, no. 11, pp. 743–751, 1974.

[35] V. Modi and A. Ibrahim, "A general Formulation for Librational Dynamics of Spacecraft with Deploying Appendages", *Journal of Guidance, Control, and Dynamics*, vol. 7, no. 5, pp. 563–569, 1984.

[36] V. Modi, A Suleman, A. Ng, and Y Morita, "An Approach to Dynamics and Control of Orbiting Flexible Structures", *International Journal for Numerical Methods in Engineering*, vol. 32, no. 8, pp. 1727–1748, 1991.

[37] T. R. Kane, R. Ryan, and A. Banerjee, "Dynamics of a Cantilever Beam Attached to a Moving Base", *Journal of Guidance, Control, and Dynamics*, vol. 10, no. 2, pp. 139–151, 1987.

[38] H. Yoo, R. Ryan, and R. Scott, "Dynamics of Flexible Beams Undergoing Overall Motions", *Journal of Sound and vibration*, vol. 181, no. 2, pp. 261–278, 1995.

[39] D. Invernizzi, "A Foreshortening Formulation for Flexible Structures Undergoing Large Overall Motions", Master's thesis, Politecnico di Milano, Department of Aerospace Science and Technology, Milano, 2014.

[40] F. Liu, B. Yue, and L. Zhao, "Attitude Dynamics and Control of Spacecraft with a Partially Filled Liquid Tank and Flexible Panels", *Acta Astronautica*, vol. 143, no. 1, pp. 327–336, 2018.

[41] R. Gerding, "Rendezvous Equations in the Vicinity of the Second Libration Point", *Journal of Spacecraft and Rockets*, vol. 8, no. 3, pp. 292–294, 1971.

[42] P. Gurfil and N Kasdin, "Dynamics and Control of Spacecraft Formation Flying in Three-body Trajectories", in *Proceedings of the AIAA Guidance,*

Navigation, and Control Conference and Exhibit, Montreal, Canada, 6-9 August, 2001.

[43] B. Marchand and K. Howell, "Control Strategies for Formation Flight in the Vicinity of the Libration Points", *Journal of guidance, control, and dynamics*, vol. 28, no. 6, pp. 1210–1219, 2005.

[44] A. Héritier and K. C. Howell, "Dynamical Evolution of Natural Formations in Libration Point Orbits in a Multi-body Regime", *Acta Astronautica*, vol. 102, no. 1, pp. 332–340, 2014.

[45] S. Lizy-Destrez, "Rendezvous Optimization with an Inhabited Space Station at EML2", in *Proceedings of the 25th International Symposium on Space Flight Dynamics, Munich, Germany, 19-23 October*, 2015.

[46] N. Murakami, S. Ueda, T. Ikenaga, M. Maeda, T. Yamamoto, and H. Ikeda, "Practical Rendezvous Scenario for Transportation Missions to Cis-Lunar Station in Earth–Moon L2 Halo Orbit", in *Proceedings of the 25th International Symposium on Space Flight Dynamics, Munich, Germany, 19-23 October*, 2015.

[47] S. Ueda and N. Murakami, "Optimum Guidance Strategy for Rendezvous Mission in Earth-Moon L2 Halo Orbit", in *Proceedings of the 25th International Symposium on Space Flight Dynamics, Munich, Germany, 19-23 October*, 2015.

[48] K. Mand, "Rendezvous and Proximity Operations at the Earth-Moon L2 Lagrange Point: Navigation Analysis for Preliminary Trajectory Design", Master's thesis, Rice University, Department of Aerospace Engineering, Houston, 2014.

[49] L. Bucci and M. Lavagna, "Coupled Dynamics of Large Space Structures in Lagrangian Points", in *Proceedings of the 6th International Conference on Astrodynamics Tools and Techniques, Darmstadt, Germany, 14-17 March*, 2016.

[50] L. Bucci, A. Colagrossi, and M. Lavagna, "Rendezvous in Lunar Near Rectilinear Halo Orbits", *Advances in Astronautics Science and Technology*, vol. 1, no. 1, pp. 39–43, 2018.

[51] A. Colagrossi and M. Lavagna, "Preliminary Results on the Dynamics of Large and Flexible Space Structures in Halo Orbits", *Acta Astronautica*, vol. 134, no. 1, pp. 355–367, 2017.

[52] ——, "Dynamical Analysis of Rendezvous and Docking with Very Large Space Infrastructures in non-Keplerian Orbits", *CEAS Space Journal*, vol. 10, no. 1, pp. 87–99, 2018.

[53] ——, "Cislunar non-Keplerian Orbits Rendezvous & Docking: 6DOF Guidance and Control", in *Proceedings of the 69th International Astronautical Congress, Bremen, Germany, 1-5 October*, 2018.

[54] ——, "Assembly and Operations for a Cislunar Orbit Space Station", in *Proceedings of the 68th International Astronautical Congress, Adelaide, Australia, 25-29 September*, 2017.

[55] ——, "Dynamics and Control of Modular and Extended Space Structures in Cislunar Environment", in *Proceedings of the 26th International Symposium on Space Flight Dynamics, Matsuyama, Japan, 3-9 June*, 2017.

[56] ——, "Preliminary Results on the Dynamics of Large and Flexible Space Structures in Halo Orbits", in *Proceedings of the 67th International Astronautical Congress, Guadalajara, Mexico, 26 - 30 September*, 2016.

[57] ——, "Dynamical Analysis of Rendezvous and Docking with Very Large Space Infrastructures in Non-Keplerian Orbits", in *Proceedings of the 6th International Conference on Astrodynamics Tools and Techniques, Darmstadt, Germany, 14-17 March*, 2016.

[58] H. Goldstein, *Classical Mechanics*. Pearson Education, London, UK, 1962.

[59] T. R. Kane, P. W. Likins, and D. A. Levinson, *Spacecraft Dynamics*. McGraw-Hill Book Co., New York, New York, US, 1983.

[60] P. Flores, "Euler Angles, Bryant Angles and Euler Parameters", in *Concepts and Formulations for Spatial Multibody Dynamics*, Springer, New York, New York, US, 2015, pp. 15–22.

[61] A. D. Dei Tos, "Trajectory optimization of limited control authority spacecraft in high-fidelity models", Ph.D. Dissertation, Politecnico di Milano, Department of Aerospace Science and Technology, Milano, Italy, 2018.

[62] M. J. Sidi, *Spacecraft Dynamics and Control: A Practical Engineering Approach*. Cambridge university press, Cambridge, UK, 2000.

[63] J. R. Wertz, *Spacecraft Attitude Determination and Control*. Kluwer Academic Publishers, Dordrecht, NL, 1990.

[64] A. Colagrossi, F. Ferrari, and M. Lavagna, "Asteroids Coupled Dynamics Analysis by Means of Accurate Mass Distribution and Perturbations Modeling", in *4th IAA Planetary Defense Conference, Frascati, Italy, 13-17 April*, 2015.

[65] A. Colagrossi, F. Ferrari, and M. Lavagna, "Coupled Dynamics Analysis Around Asteroids by Means of Accurate Shape and Perturbations Modeling", in *Proceedings of the 66th International Astronautical Congress, Jerusalem, Israel, 12-16 October*, 2015.

[66] W. S. Koon, M. W. Lo, J. E. Marsden, and S. D. Ross, *Dynamical Systems, the Three-body Problem and Space Mission Design*. California Institute of Technology, Pasadena, California, US, 2008.

[67] G. Q. Xing and S. A. Parvez, "Alternate Forms of Relative Attitude Kinematics and Dynamics Equations", in *Proceedings of the 2001 Flight Mechanics Symposium, Greenbelt, Maryland, US, 19-21 June*, 2001.

[68] R. J. Luquette, "Nonlinear Control Design Techniques for Precision Formation Flying at Lagrange Points", Ph.D. Dissertation, University of Maryland, Department of Aerospace Engineering, College Park, Maryland, US, 2006.

[69] A. A. Shabana, *Dynamics of Multibody Systems*. Cambridge university press, Cambridge, UK, 2013.

[70] L. Meirovitch, *Fundamentals of Vibrations*. Waveland Press, Long Grove, Illinois, US, 2010.

[71] J. L. Junkins, *Introduction to Dynamics and Control of Flexible Structures*. AIAA Education Series, Reston, Virginia, US, 1993.

[72] F. T. Dodge, *The new dynamic behavior of liquids in moving containers*. Southwest Research Institute, San Antonio, Texas, US, 2000.

[73] R. A. Ibrahim, *Liquid sloshing dynamics: theory and applications*. Cambridge university press, Cambridge, UK, 2005.

[74] H. B. Keller, "Numerical solution of bifurcation and nonlinear eigenvalue problems", *Application of bifurcation theory*, vol. 1, no. 38, pp. 359–384, 1977.

[75] L. Perko, *Differential Equations and Dynamical Systems*. Springer, New York, New York, US, 2001.

[76] C. W. H. and W. R. S., "Terminal Guidance System for Satellite Rendezvous", *Journal of the Aerospace Sciences*, vol. 27, no. 9, pp. 653–658, 1960.

[77] L Bucci, M Lavagna, R Jehn, *et al.*, "Station Keeping Techniques for Near Rectilinear Orbits in the Earth-Moon System", in *Proceedings of the 10th international ESA conference on GNC systems, Salzburg, Austria, 29 May–2 June*, 2017.

[78] W. Fehse, *Automated Rendezvous and Docking of Spacecraft*. Cambridge university press, Cambridge, UK, 2003.

[79] L. Bucci, M. Lavagna, and F. Renk, "Phasing and Rendezvous Operations on non-Keplerian Orbits in the Earth-Moon System", in *Proceedings of the 69th International Astronautical Congress, Bremen, Germany, 1-5 October*, 2018.

[80] ——, "Relative Dynamics Analysis and Rendezvous Techniques for Lunar Near Rectilinear Halo Orbits", in *Proceedings of the 68th International Astronautical Congress, Adelaide, Australia, 25-29 September*, 2017.

[81] F Bernelli, F Topputo, and M Massari, "Assessment of Mission Design Including Utilization of Libration Points and Weak Stability Boundaries", ESA ACT Report, Tech. Rep., 2004.

[82] T. A. Pavlak, "Trajectory Design and Orbit Maintenance Strategies in Multi-Body Dynamical Regimes", Ph.D. Dissertation, Purdue University, School of Aeronautics and Astronautics, West Lafayette, Indiana, US, 2013.

[83] R. H. Byrd, J. C. Gilbert, and J. Nocedal, "A Trust Region Method Based on Interior Point Techniques for Nonlinear Programming", *Mathematical Programming*, vol. 89, no. 1, pp. 149–185, 2000.

[84] R. A. Waltz, J. L. Morales, J. Nocedal, and D. Orban, "An Interior Algorithm for Nonlinear Optimization that Combines Line Search and Trust Region Steps", *Mathematical programming*, vol. 107, no. 3, pp. 391–408, 2006.

[85] J. Nocedal and S. Wright, *Numerical Optimization*. Springer, New York, New York, US, 2006.

[86] V Fernandez, G De Zaiacomo, A Mafficini, D. Mostaza, M. Kerr, and L. F. Peñín, "The IXV GNC Functional Engineering Simulator", in *Proceedings of the 11th International Workshop on Simulation & EGSE facilities for Space Programmes, ESTEC, Netherlands, 28-30 September*, 2010.

[87] W. J. O'Connor, "Wave-based Control of Flexible Mechanical Systems", in *Informatics in Control Automation and Robotics*, Springer, New York, New York, US, 2008, pp. 25–34.

[88] J. W. Thompson and W. O'Connor, "Wave-based Attitude Control of Spacecraft with Fuel Sloshing dynamics", *Archive of Mechanical Engineering*, vol. 63, no. 2, pp. 263–275, 2016.

[89] F. L. Markley and J. L. Crassidis, *Fundamentals of Spacecraft Attitude Determination and Control*. Springer, New York, New York, US, 2014.

[90] A. Colagrossi and M. Lavagna, "Fully Magnetic Attitude Control Subsystem for Picosat Platforms", *Advances in Space Research*, vol. 62, no. 12, pp. 3383–3397, 2018.

Colophon

This thesis was typeset with LaTeX and BibTeX, using a typographical look-and-feel created by Andrea Colagrossi. The style was inspired by D.A. Dei Tos `PhD_Dis` and by J. Stevens, L. Fossati `phdthesis` styles.